

Experimental
Study
of Shock Wave /
Boundary-Layer
Interactions over
Fluttering Panels

Master of Science Thesis
Abhyuday Aditya

Experimental Study of Shock Wave / Boundary-Layer Interactions over Fluttering Panels

Master of Science Thesis

by

Abhyuday Aditya

to obtain the degree of Master of Science
at the Delft University of Technology
to be defended publicly on Monday, February 28, 2022 at 10:00.

Student Number:	5009332	
Thesis committee:	Dr. ir. B. W. (Bas) van Oudheusden	TU Delft, Chair
	Dr. ir. F. F. J. (Ferry) Schrijer	TU Delft, Responsible Supervisor
	J. (Jane) Bulut	TU Delft, PhD Supervisor
	Dr. F. (Francesco) Avallone	TU Delft, External Examiner
	Dr. ir. W. J. (Woutijn) Baars	TU Delft, Additional Examiner

An electronic version of this thesis is available at <http://repository.tudelft.nl/>.

Abstract

The flutter of thin flexible panels exposed to supersonic flows, characterized by out-of-plane panel deflections reaching the order of the panel thickness itself, is a notorious aeroelastic phenomenon that increases the risk of fatigue failure of the flexible panel due to its highly unsteady nature. Flutter is known to be exacerbated when a shock wave impinges on the panel, creating a shock wave/boundary-layer interaction (SWBLI) which promotes separation of flow and leads to increased aerodynamic and thermal loading on the panel. This novel fluid-structure interaction (FSI) is known as shock-induced panel flutter, and it poses a risk to the structural integrity of components involved in constructing high-speed aerial vehicles, such as rocket nozzle and supersonic engine inlets. The exact physical nature of this FSI is still an open question, as an investigation is still necessary into how the strength and location of the impinging shock over the panel affects the SWBLI and flutter dynamics. Progress has been made in the study of shock-induced panel flutter in the ST-15 supersonic wind tunnel facility at TU Delft, and the phenomenon has been shown to be periodic and repeatable with non-intrusive optical techniques like Schlieren, Particle Image Velocimetry (PIV) and Digital Image Correlation (DIC) proving to be reliable measurement methods. However, challenges outlined in experimentally recreating shock-induced flutter in ST-15 include the possible existence of spurious vibrations in certain parts of the wind tunnel test section, which leads to resonance between the frequency of the aforementioned vibrations and the panel flutter frequency.

The objective of the current study is to delve deeper into the origin of external vibrations in ST-15 that could potentially affect the recreation of flutter in the same facility and conduct an investigation into the effect of impinging shock strength and location on the shock-induced flutter of the panel. Tests are carried out at a freestream Mach number of 2.0 and a total freestream pressure of 2.5 bar, in ST-15. Two different shock generators with 12° and 15° ramp angles are used, with the latter producing the stronger impinging shock, and the impingement locations are varied from 30% to 80% of the panel length in steps of 10%. To address the wind tunnel vibrations, simultaneous measurements of vibrations through accelerometers and temperatures through thermocouples are made around various parts of the test section. The temperature measurements are used to check whether rapid convective cooling due to high speeds of the wind tunnel leads to an increase in the spurious vibrations, possibly by causing contraction of parts of the wind tunnel. Since shock-induced flutter was already proven to possess a repeatable and periodic nature, flow and structural measurements are done non-simultaneously for the first time, to alleviate the problems caused by the sheer complexity of simultaneous measurement setups attempted by previous studies in ST-15. For the current study, flow measurements are done using high-speed Schlieren imaging, a robust optical non-intrusive technique that is sufficient to provide all necessary information on the SWBLI, such as shock-induced separation size and unsteadiness of the shock waves. In a separate campaign, measurements of the out-of-plane panel displacements to characterize the panel flutter behaviour are made using a stereographic DIC setup with 2 cameras for recording and a white LED for illumination.

Initial tests to detect wind tunnel vibrations are done without any shock generator installed in the test section and with a rigid plate instead of a flexible panel, to eliminate any effect the flutter of the panel might have. The accelerometers in the lower part of the test sections exhibited vibrations at the frequency of 770 Hz in this case, and when the rigid plate was replaced with a flexible panel, the same frequency existed in both the flutter of the panel (measured using DIC) as well as the spurious vibrations, showing a resonance between the two. When a shock generator is installed, the dominant frequency of these spurious vibrations shifts to a lower value, varying in the range of 620 ± 20 Hz for different combinations of impinging shock strength and location. Again, these vibrations exist regardless of the type of panel used: rigid or flexible - the flutter frequency of the latter resonating with the vibrations - proving that the problem is inherent to the facility. No direct correlation is established between the drop in tunnel temperature and the growth in the severity of the spurious vibrations.

With an impinging shock of higher strength, the boundary-layer separation over the panel is exacerbated, leading to higher SWBLI interaction lengths and higher post-shock pressure jump. The inviscid shock impingement location over the flexible panel is varied and it is observed that if the separation shock foot originates over the flexible panel, the resulting interaction length is always greater than the SWBLI interaction length over a rigid panel with the same shock generator, showing that using flexible fluttering panels is not a viable method for shock-induced separation control. For two exceptional cases, the separation shock is seen to originate upstream of the flexible panel leading edge, and the resulting SWBLI interaction lengths are found to be less compared to the rigid plate. The fluttering panel without an impinging shock shows a mean shape like an upward bump, in contrast to shock-induced panel flutter which shows an upstream crest-downstream trough separated by a node as its mean shape, with the higher shock strength resulting in a smaller crest and a larger trough due to a bigger extent of the panel being influenced by the post-shock high-pressure region. With increased shock strength, the fluctuations about the mean shape of the panel are subdued because of a combination of the fully-clamped edges and the higher pressure experienced by the top of the panel. For the same shock generator, varying the impinging shock location downstream causes an increase in crest amplitude alongside a decrease in the trough amplitude.

Except for a few cases when the separation shock is located either upstream of or close to the leading edge, its characteristic frequency is always coupled with the dominant frequency of the panel flutter, which is found to be constantly driven by the aforementioned spurious wind tunnel vibrations at 620 ± 20 Hz for all tested combinations of shock strengths and impingement locations, except for the most downstream impingement location at the higher shock strength. From energies of the separation shock motion and panel flutter, it is found that an inviscid shock impingement location at 60% of the panel length produces the most energetic flutter for both shock strengths, closely followed by the case of 70% impingement location. Proper Orthogonal Decomposition (POD) is employed to differentiate the most energetic mode shapes defining the dynamics of the panel flutter, and the flutter with no shock generator is found to exhibit a (1,2) shape as its dominant mode with two out-of-phase peaks in the streamwise direction, while the shock-induced panel flutter produces a (1,1) shape, i.e., a solitary peak, as its dominant mode in terms of energy, consistent for all shock impingement locations and both shock strengths considered. A low-order model of the flutter is tested using the first few POD modes, and it is found that when the overall flutter energy is low at the most upstream and downstream shock impingement locations with both shock generators, even the first 2 POD modes are able to provide a good approximation of the actual shape, whereas when flutter energy is highest at the 60% shock impingement location with respect to the panel length, at least 6 POD modes are needed to build a reasonably accurate estimation of the instantaneous panel shapes.

Acknowledgements

As I attempt to fill out this page, I am trying hard to recall every single seemingly trivial moment that made the whole 2+ year journey as a student of TU Delft memorable. I am a nostalgic person, and I firmly believe that it is the people who create the strong attachment that one feels to places: be it cities, houses, or even classrooms. This is my chance to properly thank everyone who helped me form an attachment to Delft and, deliberately or otherwise, made the challenge of pursuing a Master's degree in a foreign land - with the constant gloom caused by a once-in-a-century pandemic - a little more bearable, day after day.

After a lengthy period of contemplation, I decided to pursue my thesis in an experimental (rather than computational) area, which I had always wanted, and looking back now, I am delighted to write that not even once did I regret that decision. The primary reason behind that is the unqualified support I received from my supervisors: Ferry and Bas. I am grateful to both of them for allowing me the freedom to learn, fail, and re-learn without constraints, for the calmness and friendliness they exuded in every meeting, and their invaluable inputs that served as the guiding force for this mammoth endeavour (from my perspective). I am also thankful to my internship supervisor at DAF Trucks: Jemil, for his kind words and constant encouragement during confusing times (personally) that instilled the self-belief in me to pursue the path that I finally chose for my thesis.

Productive work in a lab is just not possible without the hands-on support of others, and there are a lot many people to thank for the same, starting with Jane and Alessandro. I thank them for their advice, constant support, and especially their endless reservoir of patience when dealing with the silliest of my doubts. I could never have executed everything in the limited time-frame had it not been for your mentoring. A special thanks to Giulio, Edou, and Gabriel (along with Jane and Alessandro, of course) for saving my DIC campaign. It was always a pleasure chatting with you guys and being a bother when you were trying to enjoy your coffee breaks. Finally, thanks to Lucas: *"better late than never"* is how I would describe the help and advice you provided, apart from vital and invaluable.

I would also like to express my appreciation for the truly kind and helpful staff at HSL: Dennis, Frits, Peter, Henk-Jan and Niko. I am grateful to all of them their expert handling of all possible technical problems, be it finding the right paint thinner (turned out to be water but still counts), forcibly removing a damaged screw, helping with the thermocouple setup or running the tunnel. A special thanks to Dr. Jurij Sodja for lending me the accelerometers from the Aircraft hall, and also for his forgiveness when I accidentally broke a couple of them.

I am grateful to my wonderful housemates during the thesis period: Abhinand and Sanjeet, for making the weekends relaxing and energizing after each gruelling week of work. Thanks so much for the most sumptuous home-cooked Indian food that my gluttonous self could ever have yearned for, and not to forget the movie/pizza/twister-fries nights that were the perfect recipe for unwinding. Also, I would like to thank Bithin Da and Aneek, for bringing the Jadavpur vibe - that I had sorely missed in my first year - with their company during the gloomy, rainy days we suffered in Delft.

I would like to thank a bunch of people who I bonded with through the shared labour of completing assignments on time during our first year: Sophie, Nivi, Vadim, Aniketh, Anand, Ramu, Sid. Too bad the pandemic cut short the fun we used to have on the campus and outside. I am also thankful to my on-campus Aero "neighbour" Muaaz, for his brilliant biryanis, fatty-patty kebabs, his immense help and the inspiration he radiated through his hard work and diligence in every task, and for introducing me to anime - exposing me to some of the best stories I have ever known - they certainly helped a lot when we were locked up in our rooms indefinitely.

My penultimate expression of gratitude is reserved for Parv and Uttam. I was able to be myself and still be productive at the same time around the both of you, which is kind of an anomaly, but also a testament to our bond. Assignments, football matchdays, FIFA competitions, cooking, midnight runs to the Döner shop, or random chill-out sessions, it was an absolute pleasure hanging out together and learning from you both. Life in Delft seems unimaginably tough in retrospect without your company and support. Hopefully, this "jawk" (translation from Punjabi: kid) was also able to teach you a thing or two.

Finally, I would like to thank my parents. Maa and Papa, I am always grateful for your unconditional love, your teachings, and the sacrifices you have made so that I could afford the freedom to pursue my dreams. In return, I only hope that you feel as proud of me as I feel fortunate to have you both as my guiding light in life.

*Abhyuday Aditya
Kolkata, February 2022*

Contents

Abstract	iii
Acknowledgments	v
List of Figures	xi
List of Tables	xvii
List of Symbols and Abbreviations	xix
1 Introduction	1
1.1 When Shock Waves meet Boundary Layers	1
1.2 The Problem of Flutter	2
1.3 Research Questions	5
1.4 Structure of Report	5
2 Literature Survey	7
2.1 Panel Flutter	7
2.1.1 Physical Nature	8
2.1.2 Effect of Dynamic Pressure	9
2.1.3 Effect of Static Pressure Differential	10
2.1.4 Effect of Thermal Loading	11
2.1.5 Effect of Geometry	12
2.1.6 Effect of Edge Boundary Conditions	12
2.1.7 Three-dimensional Effects	14
2.2 Shock Wave/Boundary-Layer Interactions	14
2.2.1 Structure of SWBLIs	15
2.2.2 Unsteadiness of SWBLIs	15
2.2.3 Techniques to study SWBLIs	16
2.3 Shock-induced Panel Flutter	19
2.3.1 Effect of Impinging Shock on Panel Flutter	19
2.3.2 Effect of Panel Motion on SWBLI	22
2.3.3 Effect of Shock Impingement Location	24
2.3.4 Effect of Cavity Pressure	25
2.3.5 Effect of Reynolds Number	27
2.3.6 Effect of Geometrical Parameters	27
2.3.7 Three-dimensional Effects	28
2.3.8 Techniques to study Shock-induced Panel Flutter	29
2.4 Recent Investigation at TU Delft	32
2.4.1 Experimental Setup	32
2.4.2 Wind Tunnel Vibrations	34
2.4.3 Effect of SWBLI on Panel Flutter	35
2.4.4 Effect of Panel Flexibility on SWBLI	36
2.4.5 Fluid-Structure Correlation	37
2.4.6 Parametric Study	38
2.5 Motivation for Current Study	39
3 Measurements & Processing	41
3.1 Supersonic Wind Tunnel	41
3.1.1 Principle of operation	41
3.1.2 ST-15	43

3.2	Test Section Setup	44
3.2.1	Shock Generation	44
3.2.2	Panels.	45
3.3	Thermocouples and Accelerometers	46
3.3.1	Principle of operation: Thermocouples	46
3.3.2	Principle of operation: Accelerometers	46
3.3.3	Experimental Setup	47
3.4	Schlieren	48
3.4.1	Principle.	48
3.4.2	Z-type Schlieren setup in ST-15	49
3.4.3	Shock Detection Methodology	51
3.5	Digital Image Correlation	53
3.5.1	Principle.	53
3.5.2	Optical Markers	53
3.5.3	Subset Size	55
3.5.4	Illumination	55
3.5.5	Recording	56
3.5.6	Processing and Evaluation.	56
3.5.7	Experimental Setup and Pre-Processing	59
3.6	Test Conditions	61
3.7	Measurement Repeatability	62
3.7.1	Repeatability of Schlieren	62
3.7.2	Repeatability of DIC	62
3.8	Uncertainty Analysis	63
4	Investigation of Wind Tunnel Vibrations	65
4.1	Previous Investigation in ST-15	65
4.2	Relation to Temperature Change	65
4.2.1	Without Shock Generator	68
4.2.2	With Shock Generator	69
4.3	Schlieren with Accelerometers.	72
4.4	DIC with Accelerometers.	75
4.5	Note on Fluid-Structure Interaction	77
5	Effect of Shock Strength and Shock Location	79
5.1	Effect of Shock Strength on SWBLI	79
5.1.1	SWBLI Interaction Length	79
5.1.2	SWBLI Characteristic Frequencies	80
5.2	Effect of Shock Strength on Panel Flutter	81
5.2.1	Panel Shapes.	81
5.2.2	Flutter Characteristic Frequencies.	84
5.2.3	Flutter POD Modes.	86
5.3	Coupling of Panel and Separation Shock Motion	92
5.4	Effect of Shock Location on SWBLI	93
5.4.1	SWBLI Interaction Lengths.	95
5.4.2	SWBLI Characteristic Frequencies	96
5.5	Effect of Shock Location on Panel Flutter	97
5.5.1	Panel Shapes.	98
5.5.2	Flutter Characteristic Frequencies.	100
5.5.3	Flutter POD Modes.	106
6	Conclusions and Recommendations	111
6.1	Conclusions of Current Study	111
6.2	Recommendations for Future Studies.	114

Bibliography	117
A Experimental Campaign Test Matrices	123
B Technical Drawing	127

List of Figures

1.1	A typical impinging shock wave/boundary-layer interaction (Anderson Jr, 2010)	2
1.2	Panel failure due to dynamic resonant fatigue (Spottswood et al., 2019)	3
1.3	Schematic showing flow features, including SWBLIs, inside a scramjet (supersonic combustion ramjet) engine used for hypersonic vehicles (Quan et al., 2016)	3
2.1	Panel response to dynamic pressure (Dowell, 1974)	8
2.2	Different flutter regimes, depending on Mach number and aspect ratio (Dowell, 1970)	9
2.3	Peak panel response as a function of dynamic pressure (Dowell, 1974)	10
2.4	Schematic of typical panel flutter problem (Dowell and Bendiksen, 2010)	10
2.5	Critical dynamic pressure vs. static pressure differential (Dowell, 1970)	11
2.6	Dynamic limit cycle amplitude vs. static pressure differential (Dowell, 1970)	11
2.7	PSD of panel velocity at $x/a = 0.75$ at different pressure and temperature differentials (Brouwer et al., 2021a)	11
2.8	Effect of length-to-width ratio on flutter	12
2.9	Flutter dynamic pressure vs. static pressure differential for different edge restraints (Ventres and Dowell, 1970)	13
2.10	Flutter amplitude vs. dynamic pressure for different edge restraints	13
2.11	Flutter dynamic pressure vs. support stiffness (Dowell and Bendiksen, 2010)	14
2.12	Structure of a separation-inducing SWBLI (Babinsky and Harvey, 2011)	15
2.13	Wall pressure distribution along a strong SWBLI (Babinsky and Harvey, 2011)	16
2.14	Regions of unsteadiness in a strong SWBLI (Babinsky and Harvey, 2011)	17
2.15	Schlieren image of obliques shock reflection (Babinsky and Harvey, 2011)	17
2.16	Spanwise variation of mean flow organisation in SWBLI (Humble et al., 2007)	18
2.17	Instantaneous flow organisation of a SWBLI visualized using tomographic PIV measurements (Humble et al., 2009)	19
2.18	Peak panel displacement, with shock (green) and without shock (blue) (Beberniss et al., 2016)	20
2.19	Displacement PSD at center chord position (Beberniss et al., 2011)	20
2.20	Displacement spectra at three-quarter chord location (Visbal, 2014)	20
2.21	Dominant spatial modes in shock-induced panel flutter	21
2.22	x-t diagrams of two-dimensional panel displacement (Visbal, 2014)	21
2.23	Effect of shock impingement on surface pressure	22
2.24	Temperature field over flexible panel with shock impingement location indicated by black vertical line (Beberniss et al., 2011)	22
2.25	Time-averaged separation zone of SWBLI over (a) rigid plate and (b) flexible panel (Visbal, 2014)	23
2.26	Schlieren images of SWBLI, leading and trailing edges of panels indicated by white dashed lines (Neet and Austin, 2020)	23
2.27	Wall pressure PSD at mid-span location (Shinde et al., 2018)	24
2.28	Wall pressure PSD at mid-span location for a transitional SWBLI (Shinde et al., 2019a)	24
2.29	Effect of shock impingement location for inviscid interaction on (a) time-averaged panel deflection (b) time averaged surface pressure (c) oscillation frequency spectra at $x/a = 0.75$ location, and x-t diagram of panel fluctuations for (d) $x_i/a = 0.5$ and (e) $x_i/a = 0.18$ (Visbal, 2014)	25
2.30	For different shock impingement locations (1-4 from leading edge towards trailing edge): (a) Static deflection of plate (b) Deflection PSD (Willems et al., 2013)	25
2.31	SWBLI interaction length vs. shock impingement location from experimental results (Gomez-Vega et al., 2020)	26
2.32	Effect of cavity pressure on static deflection and wall pressure (Gramola et al., 2020)	26

2.33 Panel velocity PSD for changing cavity pressure and temperature differential (Brouwer et al., 2021a)	26
2.34 Schlieren images of SWBLI over flexible panels for different Re per unit length (Tripathi et al., 2020)	27
2.35 Panel deflection over time	27
2.36 Effect of panel aspect ratio (Shinde et al., 2019b)	28
2.37 Mean and SD of panel deflection at 3/4-chord location for different thicknesses	28
2.38 Effect of panel thickness (Shinde et al., 2019b)	28
2.39 Shock shape from (a) 3D simulation and (b) oil-flow image for rigid (left) and flexible panel (right) (Willems et al., 2013)	29
2.40 Wall pressures for different edge boundary conditions: (a) all edges clamped and (b) free side edges	30
2.41 Oil flow visualisation of SWBLI surface flow over a flexible panel, cavity pressure decreasing from left to right (Tripathi et al., 2021)	30
2.42 DIC displacement PSD from (a) 1 second 5000 frame time record (b) 2 second 10,000 frame time record and (c) 20.8 second 101,661 frame time record (Beberniss et al., 2011)	32
2.43 Experimental setup used by Allerhand (2020)	33
2.44 Emission/transmission spectra of the employed light sources (Allerhand, 2020)	34
2.45 Timing diagram of simultaneous PIV/DIC measurements (Allerhand, 2020)	34
2.46 Accelerometer readings on lower Mach block for early run (blue) and late run (orange) on the same day (Allerhand, 2020)	35
2.47 Accelerometer readings on lower Mach block before (blue) and after (orange) tightening the lower Mach block (Allerhand, 2020)	35
2.48 (a) Mean and (b) standard deviation of panel displacements at the midspan of the panel without shock impingement (Allerhand, 2020)	36
2.49 (a) Mean and (b) standard deviation of panel displacements at the midspan of the panel with shock impingement (Allerhand, 2020)	36
2.50 Energy spectral density at $x/a = 0.75, y/a = 0.0$ with and without impinging shock (Allerhand, 2020)	37
2.51 Energy spectral density of reflected shock oscillations for (a) rigid plate and (b) flexible panel (Allerhand, 2020)	37
2.52 Spatial distribution of the zero-lag correlation coefficient between the vertical velocity vector component and the out-of-plane panel displacement at the position $x/a = 0.25$ (Allerhand, 2020)	38
2.53 Spatial distribution of the correlation coefficient between the vertical velocity vector component and the out-of-plane panel displacement at the position $x/a = 0.25$ with a lag of 0.6 ms (Allerhand, 2020)	38
2.54 PSD of reflected shock oscillations for different a/b and CCF boundaries (Allerhand, 2020)	39
3.1 General structure of a supersonic wind tunnel (Anderson Jr, 2010)	42
3.2 Schematic of the ST-15 supersonic wind tunnel at TU Delft (Sun, 2014)	43
3.3 Photograph showing the ST15 with different parts labelled	44
3.4 Representation of the flow in the test section with a shock generator of ramp angle θ installed, resulting in an oblique shock wave of angle β impinging at location x_i from the leading edge of the panel	45
3.5 Schematic of the designed panel insert, blue lines showing the actual flexible panel cutout (Allerhand, 2020)	46
3.6 Photo of ST-15 showing Mach blocks, shock generator and panel insert	46
3.7 From Rao and Yap (2010)	47
3.8 Accelerometer (circled in blue) and thermocouple (circled in red) setup around the test section	48
3.9 Deflection of a light ray in the presence of gradient of refractive index	49
3.10 Light deflection at the knife-edge filter of a Schlieren system	50

3.11 Z-type Schlieren system description: 1. Light source 2. Collimating lens 3. Converging lens 4. Pinhole 5. Plane mirror 6. & 7. Parabolic mirrors 8. Plane mirror 9. Knife-edge 10. Converging lens 11. Sensor	50
3.12 Pictures of the Z-type Schlieren setup in ST-15	50
3.13 Average Schlieren image and definition of shock detection regions for imping shock (red) and separation shock (cyan)	52
3.14 Detected shock edges and shock foots from instantaneous Schlieren images	52
3.15 Shock foots and definition of interaction length	53
3.16 The problem of aliasing (Reu, 2014a)	54
3.17 Typical correlation function peaks for speckle size of (a) 3 pixels and (b) 8 pixels (Crammond et al., 2013)	54
3.18 Error levels for different speckle patterns at (a) 1% strain and (b) 2% strain (Crammond et al., 2013)	54
3.19 Standard deviation of in-plane displacement for different subset sizes (Pan et al., 2008)	55
3.20 A typical correlation map from the cross-correlation operation (Raffel et al., 2018)	57
3.21 Camera, lens and LED arrangement for DIC	59
3.22 Test section showing shock generator and speckle pattern on panel	59
3.23 Illuminated test section during DIC	60
3.24 Comparison of mean displacement fields between different runs for a CCCC1.5 panel with $\theta_{SG}=12^\circ$ and $x_i/a=0.6$	63
3.25 Comparison of STD displacement fields between different runs for a CCCC1.5 panel with $\theta_{SG}=12^\circ$ and $x_i/a=0.6$	63
4.1 Temperature variation in various parts of the test section during tunnel run	66
4.2 Distinction between PSD and total energy	67
4.3 Wind tunnel vibrations with no shock generator in test section. See Table 4.2 for accelerometer locations.	68
4.4 Mean plate temperature variation for runs 9 to 11	69
4.5 Accelerometer response for runs 9 to 11. See Table 4.2 for accelerometer locations.	69
4.6 Mean plate temperature variation for runs 12 to 14	70
4.7 Accelerometer response for runs 12 to 14. See Table 4.2 for accelerometer locations.	71
4.8 Wind tunnel vibrations during the last runs of the day. See Table 4.2 for accelerometer locations.	72
4.9 Wind tunnel vibrations for a rigid plate with no shock generator	73
4.10 Wind tunnel vibrations for a SWBLI over a rigid plate	74
4.11 Wind tunnel vibrations in free flutter of a CCCC1.5 flexible panel	74
4.12 Wind tunnel vibrations in shock-induced flutter of a CCCC1.5 flexible panel	75
4.13 Wind tunnel vibrations with DIC measurements in free flutter of a CCCC1.5 flexible panel	76
4.14 Wind tunnel vibrations with DIC measurements in shock-induced flutter of a CCCC1.5 flexible panel	76
4.15 Wind tunnel vibrations with DIC measurements for SWBLI on rigid panel	77
4.16 Comparison of frequencies for shock-induced flutter of a CCCC1.5 panel with 12° shock generator and inviscid shock location of $x_i/a=0.5$	78
5.1 Average Schlieren images for different shock strengths	80
5.2 Frequency response of impinging and separation shock foot locations for CCCC1.5 flexible panel	81
5.3 Frequency response of impinging and separation shock foot locations for rigid plate	81
5.4 Mean panel shapes for different shock strengths	82
5.5 STD panel shapes for different shock strengths	82
5.6 Mean and STD shapes at midspan of the CCCC1.5 flexible panel	83
5.7 Displacements about the mean at the maximum STD locations	83
5.8 Correlation maps with respect to displacement at maximum STD location for different shock strengths	84
5.9 Characteristic frequencies from DIC and accelerometers	85
5.10 Spectrograms along panel chord from DIC along panel midspan ($y/b=0$)	85

5.11 Spectrograms along panel chord from DIC away from panel midspan ($y/b=0.25$)	86
5.12 (a) POD modes and (b) corresponding frequencies for flexible panel with no SG	87
5.13 Effect of POD mode 1 on the mean shape at midspan of CCCC1.5 flexible panel with no SG	87
5.14 (a) Actual panel shapes (solid lines) at time instants when displacement at max STD location is maximum (blue) and minimum (red) compared to shapes predicted using first k POD modes: $k=2$ (dashed lines), $k=6$ (long dash-short dash lines), $k=10$ (dotted lines) and (b) cross-correlation between pairs of first 3 POD time coefficients for flexible panel with no SG	88
5.15 (a) POD modes and (b) corresponding frequencies for flexible panel with $\theta_{SG}=12^\circ$, $x_i/a=0.6$	89
5.16 (a) POD modes and (b) corresponding frequencies for flexible panel with $\theta_{SG}=15^\circ$, $x_i/a=0.6$	90
5.17 Effect of POD mode 1 on the mean flutter shape at midspan of CCCC1.5 flexible panel with (a) $\theta_{SG}=12^\circ$, $x_i/a=0.6$ and (b) $\theta_{SG}=15^\circ$, $x_i/a=0.6$	90
5.18 (a) Actual panel shapes (solid lines) at time instants when displacement at max STD location is maximum (blue) and minimum (red) compared to shapes predicted using first k POD modes: $k=2$ (dashed lines), $k=6$ (long dash-short dash lines), $k=10$ (dotted lines) and (b) cross-correlation between pairs of first 3 POD time coefficients for flexible panel with $\theta_{SG}=12^\circ$, $x_i/a=0.6$	91
5.19 (a) Actual panel shapes (solid lines) at time instants when displacement at max STD location is maximum (blue) and minimum (red) compared to shapes predicted using first k POD modes: $k=2$ (dashed), $k=6$ (large dash-small dash), $k=10$ (dotted) and (b) cross-correlation between pairs of first 3 POD time coefficients for flexible panel with $\theta_{SG}=15^\circ$, $x_i/a=0.6$	92
5.20 SWBLI organization at different time instances when separation shock originates (a) more downstream and (b) more upstream for flexible panel with $\theta_{SG}=12^\circ$, $x_i/a=0.6$	93
5.21 Errors in shock impingement location values achieved in practice for both $\theta_{SG}=12^\circ$ (in blue) and $\theta_{SG}=15^\circ$ (in red)	94
5.22 Mean location of separation shock foot at panel height for different shock impingement locations, for both $\theta_{SG}=12^\circ$ (in blue) and $\theta_{SG}=15^\circ$ (in red)	94
5.23 Mean interaction lengths on flexible and rigid panels at different shock impingement locations for both $\theta_{SG}=12^\circ$ (in blue) and $\theta_{SG}=15^\circ$ (in red)	95
5.24 Energy of separation shock characteristic frequency bandpassed at 620 ± 20 Hz at different shock impingement locations for both $\theta_{SG}=12^\circ$ (in blue) and $\theta_{SG}=15^\circ$ (in red)	97
5.25 (a) Mean and (b) STD panel shapes based on out-of-plane displacements for $\theta_{SG}=12^\circ$ at different inviscid shock impingement locations	98
5.26 (a) Mean and (b) STD panel shapes based on out-of-plane displacements for $\theta_{SG}=15^\circ$ at different inviscid shock impingement locations	99
5.27 Variation in location of maximum STD point of panel flutter at different shock impingement locations for both $\theta_{SG}=12^\circ$ (in blue) and $\theta_{SG}=15^\circ$ (in red)	99
5.28 Variation in amplitude of maximum STD point of panel flutter at different shock impingement locations for both $\theta_{SG}=12^\circ$ (in blue) and $\theta_{SG}=15^\circ$ (in red)	100
5.29 Comparison of frequency responses from (a) DIC measurements on the flexible panel and accelerometers (b) DIC measurements on rigid points beside the flexible panel for $\theta_{SG}=12^\circ$ and $x_i/a=0.4$	102
5.30 Comparison of frequency responses from (a) DIC measurements on the flexible panel and accelerometers (b) DIC measurements on rigid points beside the flexible panel for $\theta_{SG}=15^\circ$ and $x_i/a=0.5$	103
5.31 Energy of flutter characteristic frequency at maximum STD location on panel, bandpassed at 620 ± 20 Hz for different shock impingement locations for both $\theta_{SG}=12^\circ$ (in blue) and $\theta_{SG}=15^\circ$ (in red)	103
5.32 Spectrograms over panel length at different spanwise locations: (a) $y/b=-0.25$, (b) $y/b=0$, (c) $y/b=0.25$ for $\theta_{SG}=12^\circ$, $x_i/a=0.4$	104
5.33 Spectrograms over panel length at different spanwise locations: (a) $y/b=-0.25$, (b) $y/b=0$, (c) $y/b=0.25$ for $\theta_{SG}=12^\circ$, $x_i/a=0.6$	104
5.34 Spectrograms over panel length at different spanwise locations: (a) $y/b=-0.25$, (b) $y/b=0$, (c) $y/b=0.25$ for $\theta_{SG}=15^\circ$, $x_i/a=0.5$	105

5.35 Spectrograms over panel length at different spanwise locations: (a) $y/b=-0.25$, (b) $y/b=0$, (c) $y/b=0.25$ for $\theta_{SG}=15^\circ$, $x_i/a=0.6$	105
5.36 First two POD mode shapes and corresponding relative energies at different shock impingement locations for $\theta_{SG}=12^\circ$	106
5.37 First two POD mode shapes and corresponding relative energies at different shock impingement locations for $\theta_{SG}=15^\circ$	108
5.38 Comparison of instantaneous panel shapes (solid lines) with predicted shapes from first k POD modes: $k=2$ (dashed lines), $k=6$ (long dash-short dash lines), $k=10$ (dotted lines) at (a) most upstream and (b) most downstream shock impingement locations for flexible panel with $\theta_{SG}=12^\circ$	109
5.39 Comparison of instantaneous panel shapes (solid lines) with predicted shapes from first k POD modes: $k=2$ (dashed lines), $k=6$ (long dash-short dash lines), $k=10$ (dotted lines) at (a) most upstream and (b) most downstream shock impingement locations for flexible panel with $\theta_{SG}=15^\circ$	110
B.1 Technical drawing of the CCCC1.5 panel (Allerhand, 2020)	128

List of Tables

3.1	Properties and achievable test conditions in ST-15	44
3.2	Accelerometer and Thermocouple specifications	47
3.3	Schlieren equipment used (see Figure 3.11)	51
3.4	Schlieren camera technical details	51
3.5	Technical details of DIC equipment used	61
3.6	Governing parameters of tests	62
3.7	Comparison of interaction lengths calculated from Schlieren of a CCCC1.5 panel with $\theta_{SG}=12^\circ$ and $x_i/a=0.6$	62
3.8	Uncertainty values from various sources in different measurements	64
4.1	Test conditions for particular runs in the first campaign. For some runs, no changes were made in between to the setup to allow for drastic change in temperatures. In others, bolts were tightened to try and eliminate vibrations.	67
4.2	Accelerometer locations for Figures 4.3, 4.5, 4.7, 4.8. See Figure 3.8 for more details.	67
5.1	Mean SWBLI interaction lengths for different cases	80
5.2	Characteristic frequencies (in Hz) detected in separation shock foot motion from Schlieren based on $f \cdot E(f)$	96
5.3	Characteristic frequencies (in Hz) detected at the maximum STD location of panel from DIC and accelerometers in LMB based on $f \cdot E(f)$ for $\theta_{SG}=12^\circ$ at different inviscid shock impingement locations	101
5.4	Characteristic frequencies (in Hz) detected at the maximum STD location of panel from DIC and accelerometers on LMB based on $f \cdot E(f)$ for $\theta_{SG}=15^\circ$ at different inviscid shock impingement locations	101
5.5	Characteristic frequencies (in Hz) detected from the time coefficients of the first two POD modes based on $f \cdot E(f)$ for $\theta_{SG}=12^\circ$ at different inviscid shock impingement locations	107
5.6	Characteristic frequencies (in Hz) detected from the time coefficients of the first two POD modes based on $f \cdot E(f)$ for $\theta_{SG}=15^\circ$ at different inviscid shock impingement locations	108
A.1	All runs using rigid plate. θ_{SG} = shock generator angle. x_i/a = inviscid shock impingement location as fraction of chord.	123
A.2	θ_{SG} = shock generator angle. x_i/a = inviscid shock impingement location as fraction of chord. RP = rigid plate. CCCC1.5 = fully clamped flexible panel of aspect ratio 1.5.	124
A.3	θ_{SG} = shock generator angle. x_i/a = inviscid shock impingement location as fraction of chord. RP = rigid plate. CCCC1.5 = fully clamped flexible panel of aspect ratio 1.5. T_{amb} = ambient temperature.	125

List of Symbols and Abbreviations

Abbreviations

CCCC	Panel with all edges fully camped
CCFF	Panel with free side edges, other two clamped
DEHS	Di-ethyl-hexyl-sebacate
DES	Detached Eddy Simulation
DIC	Digital Image Correlation
DMD	Dynamic Mode Decomposition
DNS	Direct Numerical Simulation
FEM	Finite Element Method
FOV	Field-of-view
FSI	Fluid-structure Interaction
IRT	Infrared Thermography
LCO	Limit Cycle Oscillations
LE	Leading edge
LED	Light Emitting Diode
LES	Large Eddy Simulation
LMB	Lower Mach block
PIV	Particle Image Velocimetry
POD	Proper Orthogonal Decomposition
PSD	Power Spectral Density
PSP	Pressure-sensitive paint
RANS	Reynolds-averaged Navier-Stokes
ROM	Reduced-order model
RP	Rigid plate
SG	Shock generator
SNR	Signal-to-noise ratio
STD	Standard Deviation
SVD	Singular Value Decomposition
SWBLI	Shock wave/boundary-layer interaction
TE	Trailing edge

TSP Temperature-sensitive paint

UMB Upper Mach block

URANS Unsteady RANS

Greek Symbols

β Shock angle

$\delta_{99,\infty}$ Freestream boundary layer thickness

γ Specific heat ratio

λ Wavelength / Non-dimensional dynamic pressure

λ_f Flutter dynamic pressure

ρ Density

Σ POD mode energy

σ Standard Deviation

θ Local surface inclination angle

θ_{SG} Shock generator ramp angle

Latin Symbols

a Panel length/chord

a/b Panel length-to-width ratio

b Panel width

D Panel Flexural Rigidity

$E(f)$ Power Spectral Density

$f \cdot E(f)$ Total Spectral Power

f Frequency

$f_{\#}$ Camera f-stop number

h Panel thickness

L_{int} Interaction length

L_{sep} Separation length

M Mach number

M_{∞} Freestream Mach number

p Static pressure

p_0 Total pressure

p_c Cavity pressure

q Dynamic pressure

q_f Flutter dynamic pressure / Flutter boundary

Re Reynolds number

St	Strouhal number
t	Time
U	POD spatial mode
V	POD time coefficient
w	Panel out-of-plane displacement
x	Longitudinal / chordwise / streamwise location on panel
x_i	Inviscid shock impingement location
x_i/a	Inviscid shock impingement location as fraction of chord
$x_{sep,foot}$	Chordwise location of separation shock foot
y	Spanwise location on panel
z	Out-of-plane panel displacement

Subscripts

0	Total/stagnation property
∞	Freestream property

Superscripts

'	Fluctuations about mean
–	Mean/time-average

Introduction

Supersonic and hypersonic regimes of flow have increasingly become crucial areas of research for developing manned and unmanned flying machines since the technological growth spurred by the advent of World War Two, followed by the first manned flight to break the "sound barrier" in 1947, and subsequently the Space Race of the 1960s and 70s. The regimes pose a unique engineering challenge due to the existence of features like shock and expansion waves. Compared to the subsonic flow regime, vehicles operating in the supersonic regime experience higher mechanical and thermal loading, hence their design must factor in the same. With spacecrafts getting lighter and faster while payloads get heavier, and progress in supersonic commercial flight making a comeback to enable faster global commute, there is an increased focus on making supersonic flight more durable. Thus, it is crucial to gain insight into the physics of the processes that dominate these regimes in order to design safer and more efficient vehicles.

1.1. When Shock Waves meet Boundary Layers

Nature's mechanism of informing the faster-than-sound flow about obstacles and deflections in the flowfield is through the creation of shock waves and expansion waves. Thus, for supersonic flight, shock waves are inevitable. These are thin regions in the flowfield across which supersonic flow reduces its high kinetic energy through converting part of it into increased pressure, temperature, and density. Stronger the shock, higher is the jump in pressure/temperature/density across it. Although shock waves are regions with a very high viscosity and result in an entropy jump, the flow across them can still be treated free of viscous effects as long as it is sufficiently far from walls.

Flow sticks to walls as the relative velocity between them has to be zero. In a direction normal to the wall, flow velocity gradually increase from its value at the wall to its value in the freestream, thus forming a region known as the "boundary layer", where viscous effects are dominant as the flow velocity exhibits a gradient. When the boundary layer experience a positive streamwise pressure gradient, it becomes prone to separating from the wall. In turn, when flow (or the boundary layer) separates from a surface, it leads to an increase in the overall pressure drag, as the pressure downstream decreases due to the separation.

In several high-speed applications, such as inside engine inlets or rocket nozzles, shock waves impinge on the walls. As mentioned earlier, the pressure across the shock increases, and the boundary layer at the wall experiences this as an adverse pressure gradient. Since the relative flow velocity at the wall has to be zero regardless of its value in the freestream, the region of the boundary layer closest to the wall is always subsonic. The adverse pressure gradient imposed by the shock gets transmitted upstream through this subsonic region, and, if the shock is strong enough resulting a sufficiently large adverse pressure gradient, the boundary layer separates from the wall even upstream of the impinging shock (also called incident shock) location (Babinsky and Harvey, 2011). This is illustrated in Figure 1.1. Needless to say, this separation is undesirable as it induces increases aero-thermal loading. Hence,

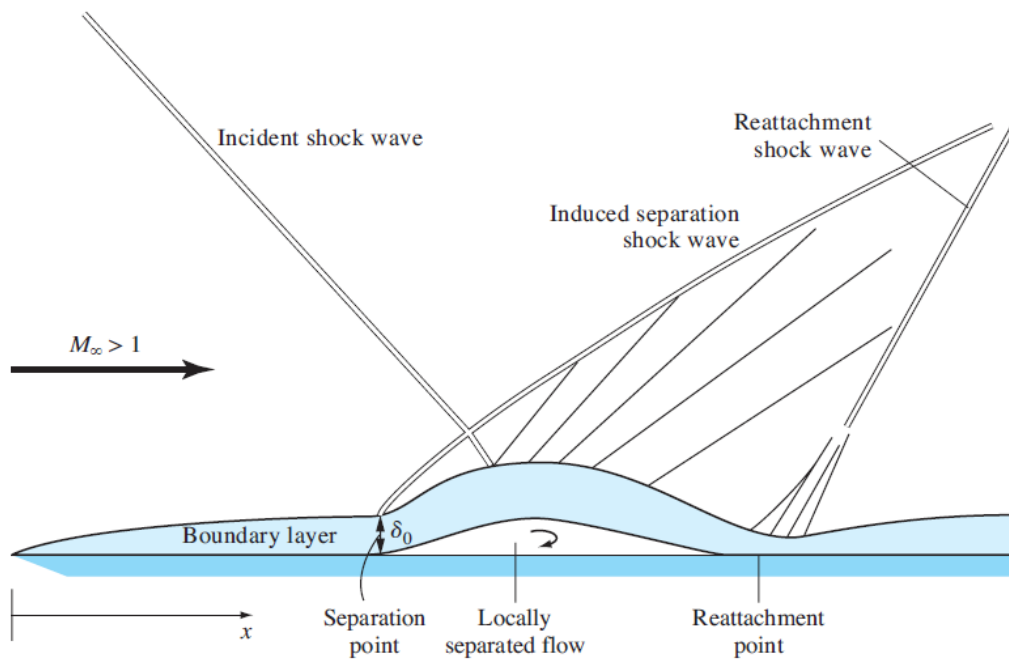


Figure 1.1: A typical impinging shock wave/boundary-layer interaction (Anderson Jr, 2010)

it is a constant endeavour in related research to devise methods to control shock-induced separation. The flow separation also results in compression waves emanating from the separation point to coalesce into another shock wave, labelled as "induced separation shock" in Figure 1.1. Additionally, when the flow reattaches, yet another shock emerges from the resulting compression waves, known as "reattachment shock". Thus, when shock waves meet boundary layers, known as shock wave/boundary layer interactions (SWBLIs), it leads to flow separation and a system of 3 shock waves instead of just the one.

The physics of SWBLIs is still an area of active research. Although its mean organization is well-understood, its significant three-dimensionality, unsteady nature, and sensitivity to factors such as incoming boundary layer properties still pose challenging questions to researchers. The origin of a characteristic low frequency unsteadiness of the SWBLI is an open research question, and recent studies (Clemens and Narayanaswamy, 2014, Ligrani et al., 2020) have revealed that its actual origin depends even on the strength of the SWBLI, and that the low-frequency unsteadiness can either be due to only upstream flow influences, or a combined upstream/downstream influence.

1.2. The Problem of Flutter

Panel flutter is a phenomenon that is unique to thin panels exposed to supersonic (or hypersonic) flows, occurring as a result of the dynamic coupling between the panel's out-of-plane motion and the pressure fluctuations in the flow boundary layer next to the panel. Random pressure fluctuations in the boundary layer excite flexible panels, and as dynamic pressure is increased, a dynamic instability arises due to a feedback loop being created between the panel oscillations and boundary layer pressure fluctuations that influence each other, essentially forming what is broadly known as a fluid-structure interaction (FSI). It was detected as early as during World War Two in the skin panels of the ballistic missile V-2, and efforts were made to characterize its behaviour by studies on the experimental hypersonic aircraft X-15 followed by subsequent space missions and projects around the world, including the famous Apollo missions (Dowell and Bendiksen, 2010). Since the development of high-speed vehicles, minimizing their weight has been a crucial aspect towards improving their efficiency, which has led to thinner panels being used to form the bodies, which leads to a drawback by increasing the susceptibility of the panels to flutter. Since panels used to build aircraft structures primarily carry load, prolonged flutter increases the risk of fatigue failure due to its high-amplitude oscillatory nature. Examples of fatigue failure of thin panels are shown in Figure 1.2.

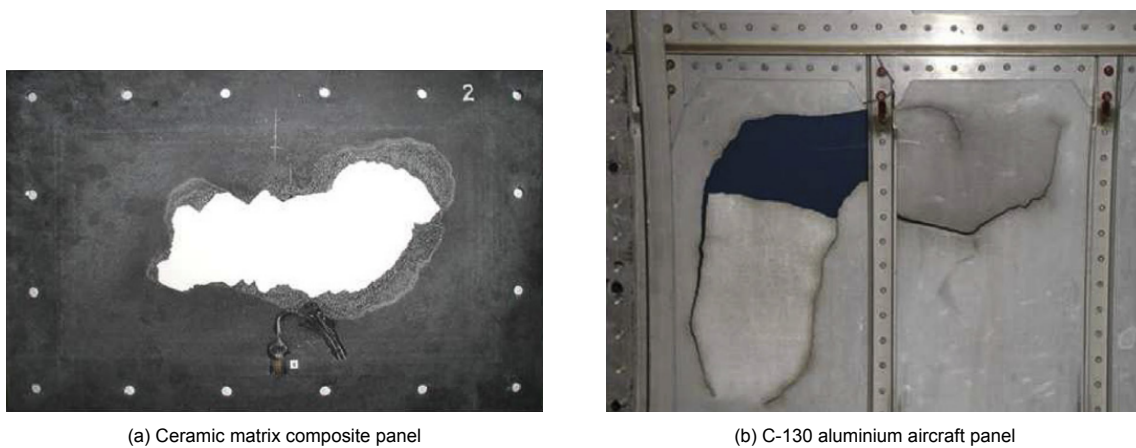


Figure 1.2: Panel failure due to dynamic resonant fatigue (Spottswood et al., 2019)

Supersonic panel flutter is characterized by out-of-plane panel deformations of the order of the panel thickness. While dynamic pressure is the primary parameter used to identify the flutter boundary (Dowell, 1974), other parameters like pressure differential across the panel thickness and thermal loading on the panel also influence the panel response and flutter boundary through an imposed static deformation of the panel.

In supersonic engine inlets or under-expanded rocket nozzles, oblique shock waves form when the supersonic flow interacts with surrounding components on such vehicles lead to the formation of shock waves, which can then impinge on the thin panels used to form the bodies. The impinging shock on a flexible panel creates a novel dynamic instability, called "shock-induced panel flutter" (Boyer et al., 2018), and it has been shown by multiple studies that the resulting oscillations are more severe compared to coalescent flutter, likely due to increased pressure and thermal loading created by the shock (Dolling, 2001). Again, it is a type of FSI and is an interesting phenomenon from both points of view - flow: how flexibility of the panel affects the SWBLI formed on top, and structural: how an impinging shock wave modifies a flexible panel's flutter response.

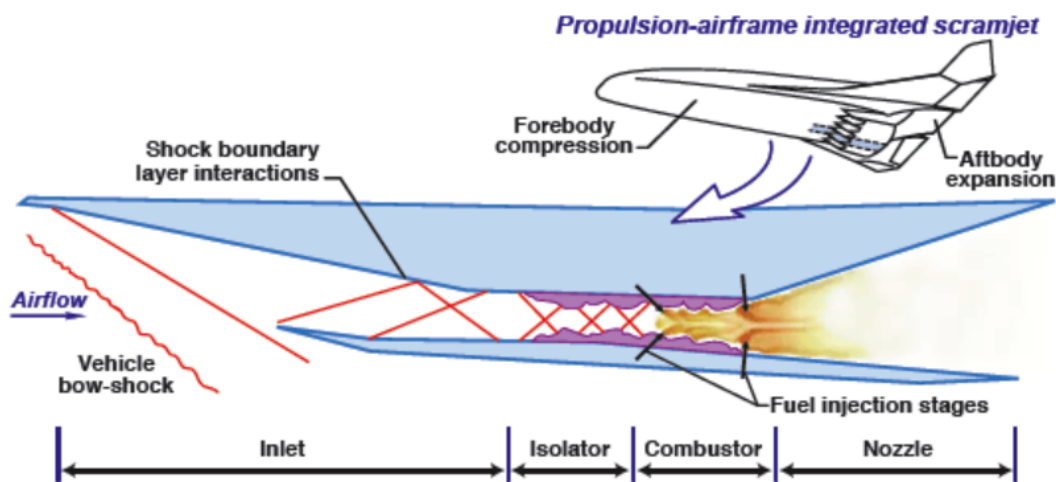


Figure 1.3: Schematic showing flow features, including SWBLIs, inside a scramjet (supersonic combustion ramjet) engine used for hypersonic vehicles (Quan et al., 2016)

In terms of structural response, shock-induced panel flutter has been found to cause an increase in thermal and structural loading on a thin panel when compared to the case of free flutter (Bebemiss

et al., 2016, Spottswood et al., 2019). In fact, it has also been suggested that the low frequency characteristic unsteadiness of SWBLIs, as mentioned earlier, could be the primary physical mechanism behind establishment of the fluid-structure interaction between a fluttering panel and the separation shock motion. As per expectations, the increased loading on thin panels results in an increased susceptibility to fatigue failure too (Spottswood et al., 2019). Interestingly, increasing the stiffness of panel only serves to shift the increased loading to another location, rather than suppressing it. Thus, a potential solution to reducing the severe loading imposed by an impinging shock on a fluttering panel might actually involve an aspect of flow control (Spottswood et al., 2019). However, some numerical studies (Boyer et al., 2021) have also suggested that shock strength plays an important role in determining whether the resulting flutter from shock impingement has increased severity in terms of loading than a case of flutter without an impinging shock, and it seems weak shocks result in lower flutter amplitude compared to free flutter.

A potentially useful result from some early numerical studies of shock-induced flutter (Visbal, 2014) has been reduction in the size of separation region of SWBLIs on flexible panels with respect to SWBLIs on rigid panels. This suggests that flexible panels could be used for SWBLI control, as separation is undesirable. While this observation was experimentally confirmed for flutter-free flexible panels, i.e., statically deformed panels under loading (Gomez-Vega et al., 2020), other experimental studies on shock-induced panel flutter have suggested otherwise, showing that the fluttering panels actually results in an increased size of the separation region (Daub et al., 2016a, Neet and Austin, 2020). To make matters more interesting, a recent numerical study actually confirmed the aforementioned observation of experiments, that fluttering panels do lead to exacerbation of shock-induced separation compared to rigid plates (Hoy and Bermejo-Moreno, 2021). Thus, there still remains a discrepancy between the observations of some numerical studies and experimental studies, and it is likely that factors like shock strength, shock location, cavity pressure, geometrical features, etc. have an important role to play in determining the change in separation region size, requiring a deeper and more comprehensive investigation.

Early studies of flutter relied on analytical methods (Dowell, 1970, Kordes et al., 1960) and experiments (Anderson, 1962, Dowell and Voss, 1965), the latter limited to point-based measurement techniques. Due to the nonlinear nature of flutter, it became difficult to model using analytical models and lead to large discrepancies between analytical predictions and experimental observations. With the advent of powerful computers, numerical methods became the tool of choice, due to the ability to obtain full-field space and time-resolved data while avoiding the cumbersomeness of carrying out supersonic wind tunnel experiments. The high-fidelity Computational Fluid Dynamics (CFD) methods of present day, such Large Eddy Simulation (LES) and Direct Numerical Simulation (DNS) are now powerful enough to possess the ability to simulate the physics involved in complex processes like SWBLIs with high-accuracy at the smallest and largest of spatio-temporal scales. Recent studies have employed both DNS (Shinde et al., 2019a) and LES (Shinde et al., 2021) to simulate shock-induced panel flutter. Unfortunately, most of high-fidelity simulations are limited to two-dimensional panels and miss out on the complexities of 3D effects in shock-induced flutter, as the associated computational costs are too high even for the computational power available in present times. While low-fidelity CFD methods like RANS or hybrid LES/RANS have considerably lower computational requirements, their accuracy in simulating unsteady, 3D phenomena like shock-induced flutter is questionable.

Even with the rapid development in numerical techniques, high-quality experimental data is often a necessity for validation of any computational simulations. In recent times, powerful non-intrusive, optical techniques have come to the fore that allow for full-field measurements of both flow and structural behaviour of FSIs. Techniques like Particle Image Velocimetry (PIV) and Schlieren imaging have been extensively employed for experimental studies of SWBLIs (Humble et al., 2009), while Digital Image Correlation (DIC) is a popular technique when it comes to measuring space and time-resolved structural deformations in shock-induced flutter (Brouwer et al., 2021b, Spottswood et al., 2019). Combining these techniques makes it possible to carry out a comprehensive study of a SWBLI on a fluttering panel reproduced in a supersonic wind tunnel and explore the effects that crucial defining parameters like impinging shock strength and impinging shock location have on the SWBLI and flutter behaviour.

1.3. Research Questions

Based on the identified knowledge gaps from existing literature and previous studies in the same facility, a research objective was devised, broadly stated as follows:

Conduct an investigation of shock-induced panel flutter using full-field experimental measurements of flow and structural aspects, and study the influence of impinging shock strength and location on the SWBLI and panel flutter behaviour.

To fulfill the research objective, a set research questions have been formulated to serve as a guide throughout the progress of the current study. These take into account what previous studies at the same facility have revealed, as well as keep the larger research objective in context. The research questions are stated below:

1. Which external sources of vibrations influence the fluid-structure interaction in the ST-15 supersonic wind tunnel facility?
 - (a) How does cooling of the wind tunnel during runs affect the external vibrations?
 - (b) How does change in flow conditions affect the external vibrations?
 - (c) Can the external vibrations be eliminated or minimized without major modifications in the current setup?
2. How can the existence of fluid-structure interaction in case of shock-induced panel flutter be established when fluid and structural measurements are done separately instead of simultaneously?
3. How do the shock strength and shock impingement location affect the shock-induced flutter characteristics?
 - (a) How is the separation zone affected in terms of its size? How does it compare to the size of the separation zone created by an impinging shock on a rigid plate?
 - (b) What are the effects on impinging shock and separation shock dynamics?
 - (c) How is the panel flutter affected in terms of mode shapes and characteristic frequencies?

Throughout the rest of the report, the discussion will reveal how the investigations carried out during the period of the work help make progress towards answering the aforementioned research questions.

1.4. Structure of Report

In Chapter 2, a literature review on the topics of panel flutter, SWBLIs, and shock-induced panel flutter is presented. With the latter two, experimental techniques commonly used for their investigation are also discussed. In Chapter 3, background on the chosen experimental techniques for the current study is given. This includes a description of the physical principles behind the measurement techniques employed in the study, including operation of supersonic wind tunnels, accelerometer and thermocouples, Schlieren imaging, and Digital Image Correlation. Also, the corresponding experimental arrangements used are detailed, along with data processing techniques employed to extract meaningful results from the measurements. In Chapter 4, major findings from an investigation of spurious vibrations in the used wind tunnel facility are discussed, with an analysis of their influence on the fluid-structure interaction established in the wind tunnel for the study. Chapter 5 presents the results describing the effect of shock strength and location on characteristics of the SWBLI, like its interaction length and frequencies dominating its motion, and panel flutter, including the different panel shapes, dominant frequencies, POD modes. Finally, major conclusions are drawn regarding the work done in the thesis in Chapter 6, followed by recommendations for future studies on the same phenomenon and/or in the same facility.

2

Literature Survey

In this chapter, background on the phenomena of supersonic panel flutter and shock-induced panel flutter will be explored, to provide a foundation based on which further investigations are carried out as part of the current study. Based on the knowledge gaps identified as a result of the literature review, the research questions presented in section 1.3 were formulated.

Starting off in section 2.1, the general nature of supersonic panel flutter will be described, including the influence of some important parameters that determine flutter boundary such as dynamic flutter, geometry and static pressure differential. Next, section 2.2 will be dedicated to forming a comprehensive understanding of SWBLIs, mainly the physical mechanism underlying the phenomenon. Additionally, a short overview of most used techniques to study SWBLIs will also be included. In section 2.3 will focus on the phenomenon of shock-induced panel flutter. Here, the coupling between the shock and flutter behaviour will be described, through an analysis of the most important parameters that influence the resulting FSI. Most frequently used techniques to investigate shock-induced panel flutter will also be included, with a spotlight on experimental techniques. Finally, section 2.4 will discuss notable results from an experimental investigation of shock-induced panel flutter conducted recently in TU Delft (Allerhand, 2020).

2.1. Panel Flutter

Flutter is a dynamic instability unique to thin panels immersed in supersonic flow, and has been an area of interest since the 1950s due to the failure of classical aerodynamic theories to reconcile with experimental results Dowell (1974). The importance of nonlinear effects in predicting flutter were eventually identified, and to this day interest remain in improving analytical, numerical and experimental techniques to study flutter. In literature, the book by Dowell (1974) presents a comprehensive overview of physical aspects and theoretical modelling of flutter. Following that, Mei et al. (1999) provides a thorough review of the work done in theoretical modelling techniques of panel flutter in the 20th century.

Early work in studying panel flutter involved experiments by Kordes et al. (1960), who studied the effects of Mach number, panel aspect ratio, static pressure differential on flutter boundaries. A similar parametric study was undertaken by Dowell and Voss (1965), who also tested predictions of different theoretical approaches with experiments, Anderson (1962) studied flutter of flat and curved panels with free side edges using point-wise measurement techniques. Fung (1963) and Olson and Fung (1967) made attempts at reconciling theory and experiments on supersonic panel flutter of flat panels and cylindrical shells, and highlighted the importance of accounting for the effect of boundary layer for accurately predicting flutter. Muhlstein (1968) and Gaspers (1970) also investigated the influence of boundary layer on supersonic panel flutter using experimental techniques.

Numerical studies of panel flutter have been ongoing since the work of Hedgepeth (1957), possibly even earlier, who employed aerodynamic strip theory on flat panels, followed by Cunningham (1963), who used linearized potential flow theory. Bohon and Dixon (1964) reviewed and compared the prevail-

ing numerical techniques to predict flutter at that time and showed that for rectangular isotropic panels, simpler aerodynamic theories were reasonably accurate. Oyibo (1983) used the technique of affine transformation to unify the flutter prediction model for both isotropic and orthotropic panels, as earlier the latter had required a more rigorous treatment than the former. More recently, Gordnier and Visbal (2002) developed a three-dimensional viscous aeroelastic solver using the full Navier-Stokes equations coupled with von Kàrmàn plate equations, Hashimoto et al. (2009) used RANS equations to investigate the stabilizing effect of turbulent boundary layer on panel flutter at different Mach numbers, Shitov and Vedenev (2017) developed a model for predicting the single mode panel flutter that is predominant at low supersonic speeds, and Amirzadegan and Dowell (2019) computed theoretical results for flutter of curved panels to compare with the experimental results of Anderson (1962).

In subsequent sections, the physical nature of panel flutter will be explored, the effects of dynamic pressure, static pressure differential, thermal loading, geometry, edge boundary conditions will be discussed along with three-dimensional effects as well.

2.1.1. Physical Nature

Panel flutter occurs when thin panels with fixed leading and trailing edges are subjected to supersonic flow. It is characterized by dynamic behaviour with out-of-plane deformations of the order of the panel thickness. Before the onset of flutter, the panel experiences random oscillations as a reaction to pressure fluctuations in the turbulent boundary layer (Dowell, 1970). The flutter boundary is determined at a critical value of the dynamic pressure, beyond which the oscillation amplitudes are seen to increase to the order of the panel thickness.

As shown in Figure 2.1, when conditions approach the flutter boundary amplitude of panel oscillations keeps increasing, which leads to a coupling with the boundary layer pressure fluctuations: larger deformations lead to larger pressure fluctuations in the boundary layer, which in turn exert increased influence over the panel motion. The aeroelastic feedback loop thus formed is the primary source of panel flutter, and may occur in flat panels, curved panels, and cylindrical flexible shells (Dowell, 1974). For the current study, only flat panels with fixed leading and trailing edges are considered.

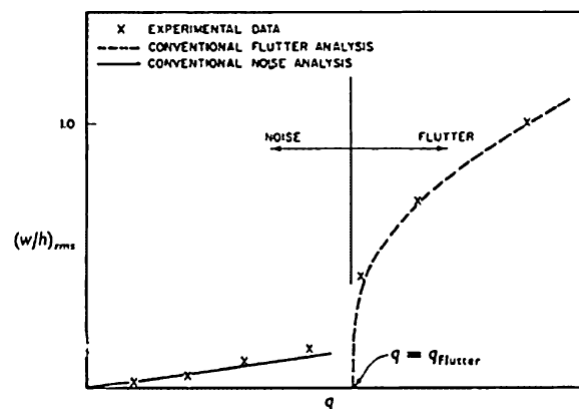


Figure 2.1: Panel response to dynamic pressure (Dowell, 1974)

The large deformations lead to nonlinear structural forces, which cause stiffening and eventually result in limit cycle oscillation (LCO) when moving further beyond the flutter boundary (Dowell and Bendiksen, 2010). During LCO, periodic exchange of energy takes place between the fluid and the structure, such that self-sustained constant amplitude and constant frequency oscillations of the panel take place. For a fixed geometry, the phenomenon is highly influenced by the dynamic pressure, static pressure differential, and thermal loading; often, the latter leads to thermal buckling which alters the flutter response (Dowell and Bendiksen, 2010).

As described by Dowell and Bendiksen (2010), panel flutter is distinct from the classical flutter experienced by airplane wings in the following aspects:

- stream-wise bending deformations are significantly greater than span-wise bending
- nonlinear structural forces are much more significant due to large deformations
- viscous boundary layer effects are crucial in the higher speed regimes

Depending on the geometry (length-to-width ratio, specifically) and freestream Mach number, different regimes of flutter exist, as shown in Figure 2.2. A high supersonic Mach number (near 2.0) and a relatively low length-to-width ratio results in the coupled mode flutter, or coalescent panel flutter, which will be the subject of interest throughout this study. It is called so because the first and second natural modes contribute equally to the oscillation, with the frequency being somewhere in between the first two natural frequencies (Dowell, 1970). Other variations include "flag" flutter, which happens in panels with 3 free edges and can even occur at subsonic speeds. Finally, shock-induced panel flutter is the phenomenon of interest, but is only discussed in Chapter 2.3. The focus in this chapter is only on coalescent or coupled mode panel flutter.

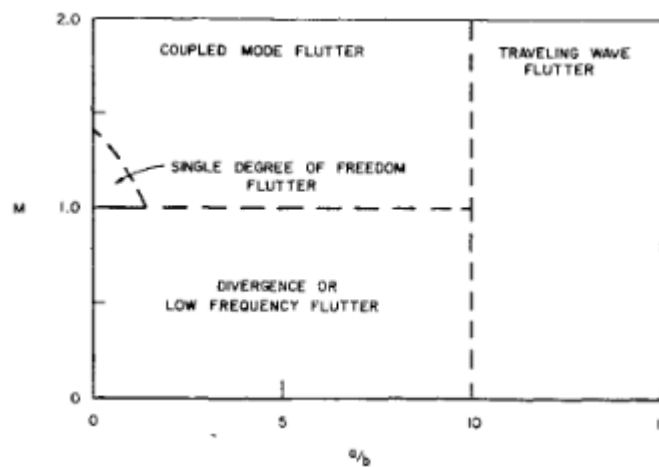


Figure 2.2: Different flutter regimes, depending on Mach number and aspect ratio (Dowell, 1970)

2.1.2. Effect of Dynamic Pressure

The parameter most often used to extract the flutter boundary is the dynamic pressure, defined as $q = \frac{1}{2}\rho U^2$. Often in literature, a non-dimensional form of dynamic pressure is used (Dowell, 1970):

$$\lambda = \frac{2qa^3}{D} = \frac{\rho U^2 a^3}{D} \quad (2.1)$$

where a is the panel length and D is the plate stiffness, based on material properties and thickness.

Pre and post-flutter characteristics can be determined based solely on the dynamic pressure, and are described as follows:

- Pre-flutter ($q < q_f$): For dynamic pressures less than the critical dynamic pressure (q_f), the panel response shows random fluctuations low in amplitude (fraction of panel thickness) and mainly due to pressure fluctuations in the turbulent boundary layer (Dowell and Bendiksen, 2010). The frequency is close to the first natural frequency (Dowell, 1974).
- $q \rightarrow q_f$: As dynamic pressure approaches the critical value, the aeroelastic feedback loop kicks in. The panel response amplitude becomes large enough to influence the boundary layer pressure fluctuations, and vice-versa. Thus, panel response increases significantly, and becomes of the same order as the panel thickness (see Figure 2.3). Furthermore, the oscillations become periodic rather than random as observed earlier. The frequency, specifically, for coupled mode flutter lies between the first two natural frequencies, but close to the second (Dowell, 1974).

- Post-flutter ($q > q_f$): At higher dynamic pressures, nonlinear structural coupling happens between bending and stretching of the panel, leading to an increase in the effective panel stiffness (Dowell, 1974). The stiffening leads to no further increase in amplitude of oscillations and is the main cause of LCO (Dowell and Bendiksen, 2010).

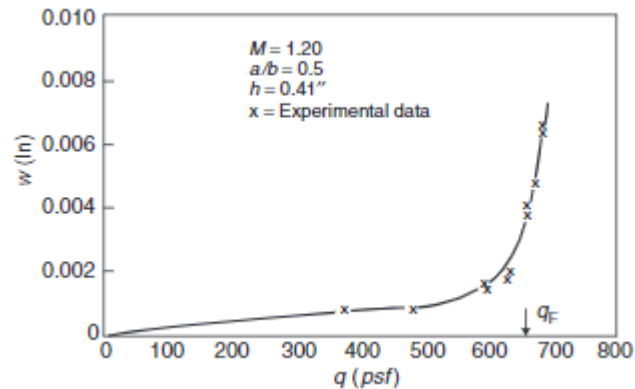


Figure 2.3: Peak panel response as a function of dynamic pressure (Dowell, 1974)

2.1.3. Effect of Static Pressure Differential

A typical setup for studying panel flutter is shown in Figure 2.4. There is a cavity present below the panel of length ' a ', and difference between the flow static pressure and the cavity pressure (called static pressure differential) also plays an important role in flutter behaviour.

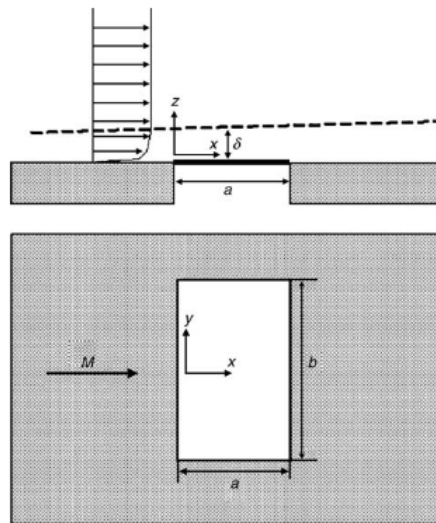


Figure 2.4: Schematic of typical panel flutter problem (Dowell and Bendiksen, 2010)

In general, static pressure differential create a transverse loading that creates a static deformation of the plate. At high enough dynamic pressure, the panel will exhibit flutter about the static equilibrium position established as a result of the static pressure differential Dowell (1970). The tensile loading caused due to the static deflection is the cause of an increase in the stiffness and natural frequency of the panel (Dowell and Bendiksen, 2010), which has an effect on the flutter boundary, as seen in Figure 2.5. It is observed that irrespective of the sign of pressure differential (i.e., whether pressure is higher above or below the panel), a stabilizing effect is seen as an increase in critical dynamic pressure when static pressure differential increases. The stabilizing effect is confirmed in terms of LCO amplitude, which is seen to decrease with increase in static pressure differential for a fixed dynamic pressure, as shown in Figure 2.6.

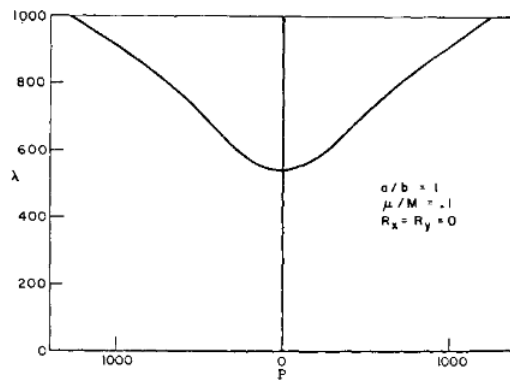


Figure 2.5: Critical dynamic pressure vs. static pressure differential (Dowell, 1970)

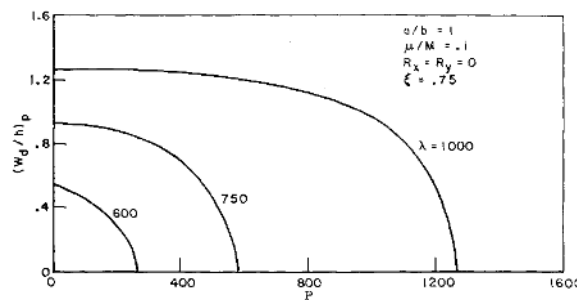


Figure 2.6: Dynamic limit cycle amplitude vs. static pressure differential (Dowell, 1970)

2.1.4. Effect of Thermal Loading

Thermal stresses as a result of the temperature differential between panel and supports creates in-plane loading, which may or may not lead to buckling (Dowell, 1970), depending on the magnitude of the differential. In case the panel does not buckle, the increased stiffness due to the in-plane loading alters flutter characteristics as discussed before. However, if compressive thermal stresses are large enough and the panel buckles, then the response may even change from periodic to chaotic (Dowell and Bendiksen, 2010). Experiments conducted by Brouwer et al. (2021a) do show chaotic behaviour of the panel response (characterized by a single prominent peak in the power spectral density) at higher temperature differential between panel and support, compared to a more periodic response at lower temperature differential, shown in Figure 2.7. However, the temperature differential decreased naturally in the experiments due to the different rates of temperature rise of the panel and the wind tunnel walls. Simultaneously, the static pressure differential was being varied in a cyclic fashion in order to expose hysteresis effects. Thus, it is not conclusive whether the change in temperature differential or hysteresis effect is the dominant factor in producing the periodic response subsequently following the initial chaotic behaviour.

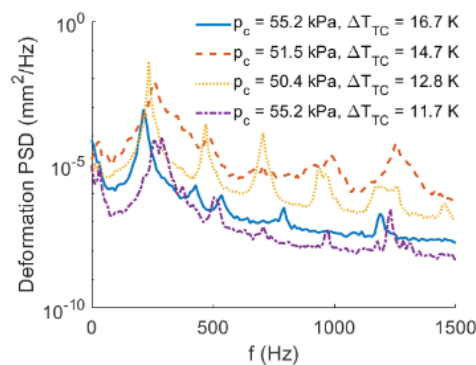
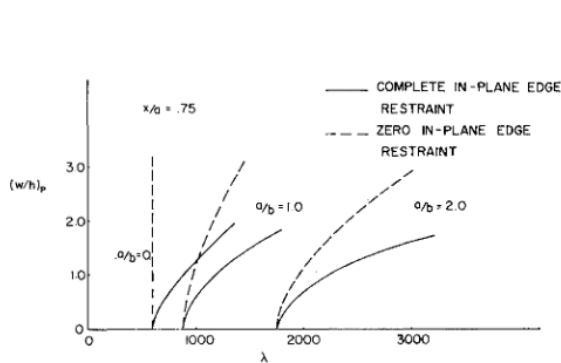


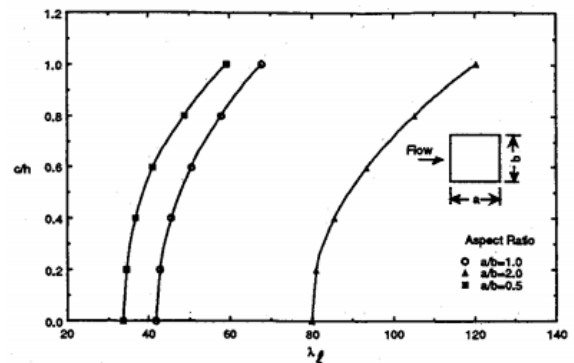
Figure 2.7: PSD of panel velocity at $x/a = 0.75$ at different pressure and temperature differentials (Brouwer et al., 2021a)

2.1.5. Effect of Geometry

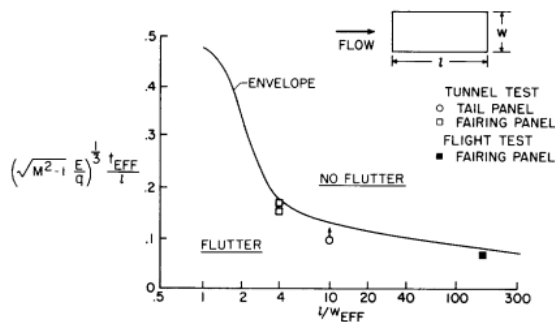
Since flutter of flat panels only is being discussed, the main geometrical parameter of interest is the length-to-width ratio a/b . The basic result of flutter regime being dependent on a/b (along with Mach number) was presented in Figure 2.2. For coupled mode flutter specifically, increasing a/b is found to have a stabilizing effect. In Figure 2.8a it is seen that even though the presence of in-plane edge restraint does not affect flutter boundary, a larger a/b increases the flutter boundary, i.e., dynamic pressure at which flutter is first observed, from the theoretical predictions of Ventres and Dowell (1970). Similar observations were made by Gray Jr and Mei (1993) where the flutter boundary is seen to increase as a/b is increased, shown in Figure 2.8b. Kordes et al. (1960) experimentally studied panels of the hypersonic test vehicle X-15, and observed that the minimum thickness required to prevent flutter was lower for higher length-to-width ratios, as shown in Figure 2.8c. This was also confirmed by the theoretical and experimental data of Dowell (1974), as shown in Figure 2.8d. Both the studies confirm the stabilizing effect of increasing a/b .



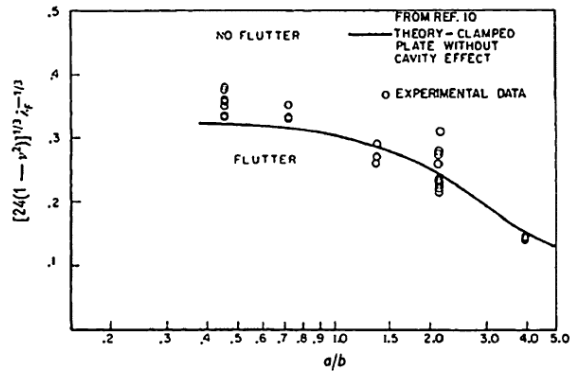
(a) Flutter amplitude vs. dynamic pressure for different length-to-width ratios and in-plane edge restraints (Ventres and Dowell, 1970)



(b) Limit cycle amplitude vs. dynamic pressure for different length-to-width ratios (Gray Jr and Mei, 1993)



(c) Flutter thickness vs. length-to-width ratios (Kordes et al., 1960)



(d) Flutter thickness vs. length-to-width ratios (Dowell, 1974)

Figure 2.8: Effect of length-to-width ratio on flutter

2.1.6. Effect of Edge Boundary Conditions

Any of the panel edges may have one of three possible boundary conditions, mathematically described below (Gibbs et al., 2012):

- Free boundary: $\frac{\partial^2 w}{\partial x^2} \Big|_{x=x_b} = 0, \frac{\partial^3 w}{\partial x^3} \Big|_{x=x_b} = 0$
- Pinned boundary: $w \Big|_{x=x_b} = 0, \frac{\partial^2 w}{\partial x^2} \Big|_{x=x_b} = 0$
- Clamped boundary: $w \Big|_{x=x_b} = 0, \frac{\partial w}{\partial x} \Big|_{x=x_b} = 0$

where w is the out-of-plane displacement and x_b is the longitudinal location of the boundary. Physically, a free edge has no restrictions on displacement or rotation, pinned edge has zero displacement but

no restrictions on rotation, and clamped edge has both zero displacement and zero rotation. Having only one fixed (pinned or clamped) with three free edges leads to lag flutter (Dowell and Bendiksen, 2010), which is not of interest currently as discussed before. Additional restraints may be imposed on the boundaries in the form of complete in-plane edge restraint ($\delta y=0$) or zero in-plane edge restraint ($\delta y \neq 0$), which is common in experimental studies of panel flutter (Dowell and Bendiksen, 2010).

As seen in Figure 2.8a, the type of in-plane edge restraint created an effect on the flutter amplitude; specifically, zero in-plane edge restraint resulted in higher flutter amplitude than complete in-plane edge restraint (Ventres and Dowell, 1970). In the same study, the effect of in-plane edge restraint was observed in the presence of static pressure differential, as shown in Figure 2.9. For the lower a/b , type of in-plane edge restraint did not make a difference to the stabilizing effect of static pressure differential, according to both theory and experiments. But, for the higher a/b , theory predicted a destabilizing effect when complete in-plane edge restraint was used, i.e., flutter boundary decreased with increase in static pressure differential. This is attributed to zero in-plane edge restraint being more representative of actual panels used in experiments (Dowell and Bendiksen, 2010).

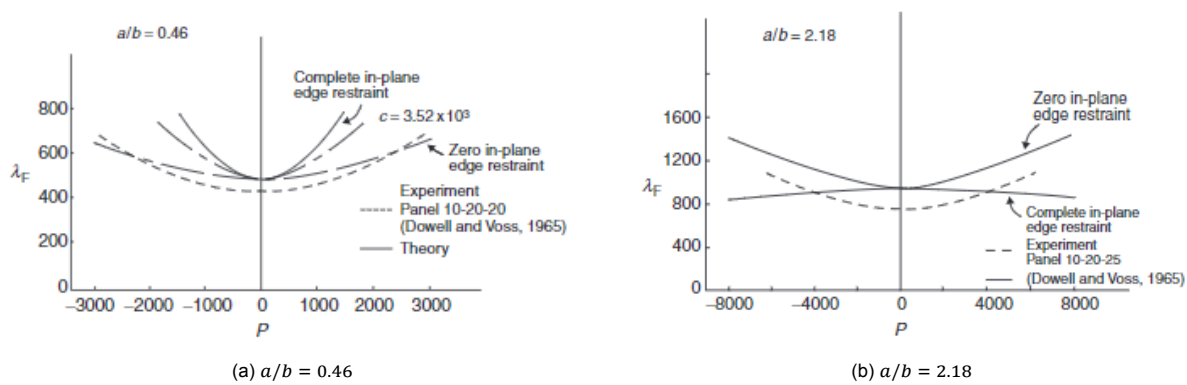


Figure 2.9: Flutter dynamic pressure vs. static pressure differential for different edge restraints (Ventres and Dowell, 1970)

Gray et al. (1991), using the same Finite Element formulation as Mei (1977), numerically investigated two-dimensional panel flutter. and found that both clamped edges had the greatest flutter boundary while both pinned edges showed the least, as reflected in Figure 2.10a. The Finite Element formulation to was extended to three-dimensional composite panels by Gray Jr and Mei (1993), and it was shown that if all four edges were clamped, then the critical dynamic pressure would be the highest, whereas it would be lowest if pinned boundary conditions were used at all the edges (see Figure 2.10b).

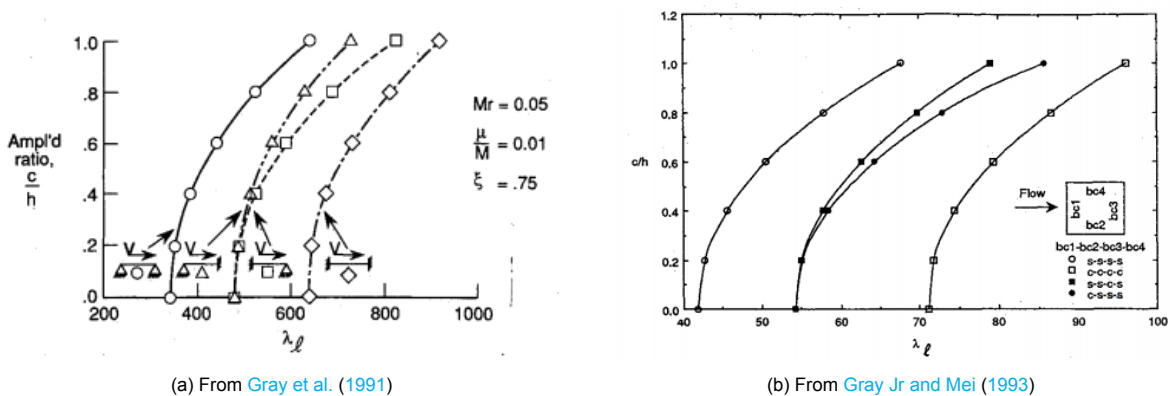


Figure 2.10: Flutter amplitude vs. dynamic pressure for different edge restraints

Gordnier and Visbal (2002) developed a three-dimensional viscous aeroelastic solver for nonlinear flutter, confirmed the aforementioned result of clamped edges leading to higher flutter boundary

compared to pinned edges. Similar observations were made also by [Dugundji \(1966\)](#), who theoretically modelled three-dimensional flutter using linear plate theory and two-dimensional aerodynamics. Experimental and theoretical studies done by [Kobett \(1966\)](#) and [Bohon et al. \(1969\)](#) on the effect of degree of rigidity of panel supports also gave rise to interesting observations, as seen in 2.11. K_d represents non-dimensional support stiffness such that $K_d \rightarrow 0$ represents a free edge while $1/K_d \rightarrow 0$ is a simply-supported edge. It is clear that with increased edge support rigidity (i.e., going from free to simply-supported edge), flutter boundaries are found to increase.

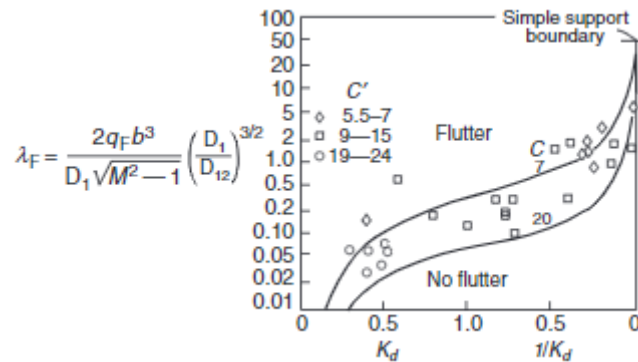


Figure 2.11: Flutter dynamic pressure vs. support stiffness ([Dowell and Bendiksen, 2010](#))

2.1.7. Three-dimensional Effects

[Hedgepeth \(1957\)](#) showed that when using Aerodynamic surface theory to study three-dimensional panel flutter, the governing equations can be reduced to a form that is representative of two-dimensional behaviour counterparts in case $\beta \cdot b/a > 1$, where $\beta = \sqrt{M^2 - 1}$, a and b are the length and width of the panel respectively, while M is the freestream Mach number. Similarly, [Dowell \(1970\)](#) stated that for the quasi-steady approach of piston theory to hold, $\beta > a/b$ is a requirement. Essentially, for any given M , lower the a/b , more is the two-dimensionality of the flutter behaviour. Physically, if one were taking measurements at the mid-span of the panel, then a higher length-to-width ratio ensures that three-dimensional effects at the edges are less influential. This was observed in the experiments conducted by [Willems et al. \(2013\)](#), where the effects if the wind tunnel walls was seen to cause variations at the edges of the panel.

The aforementioned considerations are from the aerodynamic point-of-view only. In fact, [Currao et al. \(2019\)](#) observed that panels with lower length-to-width ratio actually exhibited higher three-dimensionality due to higher contribution of the first torsional mode to the flutter, thus giving rise to span-wise variations. However, this was observed in case of a shock-induced panel flutter case with a single clamped edge, thus it is not conclusive that the same effect would be observed in case of coalescent panel flutter with different edge boundary conditions.

2.2. Shock Wave/Boundary-Layer Interactions

Shock waves are a natural occurrence in the presence of supersonic flows, and are formed with a change in slope of a surface, a downstream obstacle, or with back pressure that forces flow to become subsonic ([D elery and Dussauge, 2009](#)). The jump discontinuity established by a shock wave causes a rise in pressure, temperature, density and decreased velocity of the flow crossing it. The shock wave itself is a thin region (10-20 times the molecular mean free path) of high viscosity, as evidenced by the rise in entropy of an adiabatic, non-reacting flow crossing it ([Babinsky and Harvey, 2011](#)). In the presence of walls, as is often the case when studying external aerodynamics, the effect of boundary layer flow is most influential on quantities of interest such as shear stress and heat transfer. The meeting of these two phenomena may occur in a variety of cases that include supersonic mean flow and presence of a wall: oblique shock reflections, ramp flow, imposed pressure jump, forward facing jump, etc. ([Babinsky and Harvey, 2011](#)), and is termed as a shock wave/boundary layer interaction (SWBLI). For this study, only the first case, i.e., oblique shock reflection, is of interest, and the following

discussion will be limited to the same.

2.2.1. Structure of SWBLIs

The exact structure of SWBLIs is dependent on the properties of the boundary layer as well as the shock strength. For e.g., an SWBLI may or may not lead to separation of flow, and is termed strong or weak depending on that, respectively. However, the general mechanism of the interaction remains the same regardless of exact properties, and are described with respect to strong SWBLI.

Although SWBLIs are highly three-dimensional due to the nature of separated flows, sufficiently high ratio of test section width to freestream boundary layer thickness decreases the influence of three-dimensional effects on mid-plane flow characteristics (Babinsky and Harvey, 2011). In Figure 2.12, a two-dimensional sketch of a separation-inducing SWBLI is shown. Here, the oblique shock C_1 is called the incident shock. The presence of the shock wave leads to a pressure rise, that can only be transmitted upstream in the subsonic region of the boundary layer. This adverse pressure gradient is established in the subsonic region of the boundary layer much upstream of the point of impingement of C_1 in the absence of boundary layer, and leads to dilatation of the boundary layer, resulting in formation of compression waves due to flow being turned into itself that eventually coalesce into a second oblique shock wave C_2 , called the reflected shock or separation shock. The adverse pressure gradient is also the initiator of boundary layer separation at point **S**. The shock-shock interaction of C_1 and C_2 leads to creation of C_4 and C_3 , and eventually expansion waves are generated due to reflection of C_4 off the separation bubble. The penetration of C_4 into the boundary layer also results in deflection of the separated shear layer such that it reattaches downstream. The deceleration of flow as it stagnates at the reattachment point **R** leads to compression waves that result in the reattachment shock in the outer flow region.

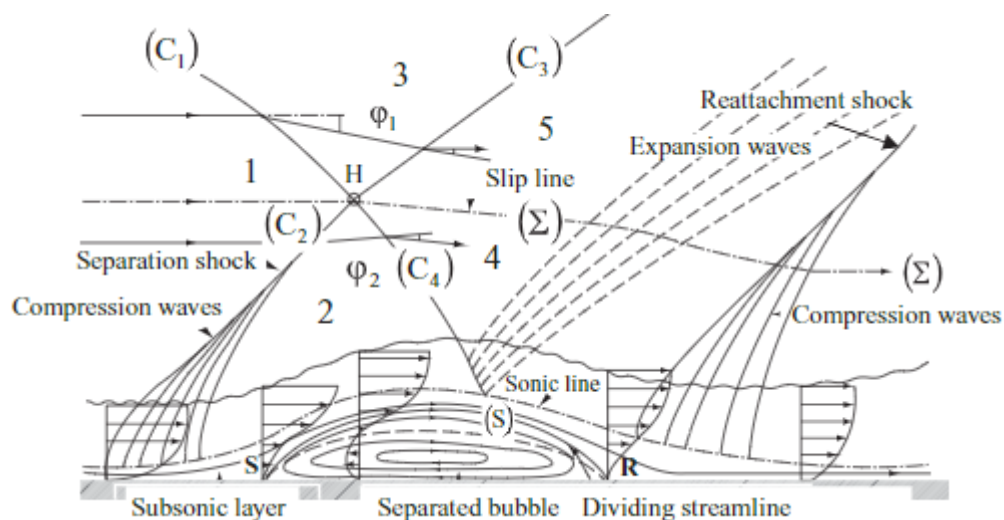


Figure 2.12: Structure of a separation-inducing SWBLI (Babinsky and Harvey, 2011)

The wall pressure distribution shown in Figure 2.13 illustrates an important difference between inviscid and viscous shock reflections: an inviscid system would only consist of two shocks, the incident and the reflected that would result in a jump discontinuity in the wall pressure distribution (marked as "inviscid solution"), whereas viscous effects result in 5 shocks and a centered expansion wave with two separate instances of pressure rise, at separation and reattachment, conjoined by a pressure plateau in the separated region.

2.2.2. Unsteadiness of SWBLIs

Dolling (2001), in his review of half-a-century of SWBLI research, noted that unsteadiness in SWBLIs was dominant to such an extent that even predicting mean properties required some knowledge of the unsteadiness. Although the characteristic low frequency unsteadiness of the SWBLI has been known for a long time, its origin has been, and continues to be, the subject of debate despite consistent efforts

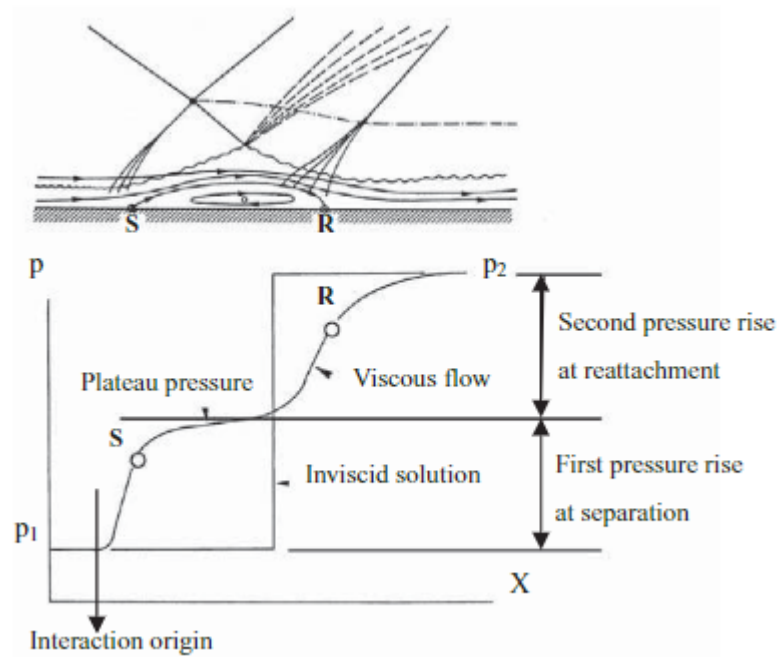


Figure 2.13: Wall pressure distribution along a strong SWBLI (Babinsky and Harvey, 2011)

which have led to significant breakthroughs (Gaitonde, 2015). Particularly, the dominant frequencies of separation shock foot motion being generally much lower than frequencies of the incoming turbulent boundary layer fluctuations and even the downstream fluctuations is the main issue in need of resolution (Dussauge et al., 2006). In general, unsteady characteristics are split into three different regions, as shown in Figure 2.14: a region of high frequency content upstream of the separation shock foot that originates from the incoming turbulent boundary layer, low frequency content associated with the reflected shock motion and the separated region, followed by another region of high frequency content post-reattachment once the boundary layer is recovered. The separated region consists of large-scale unsteadiness (influential over a large region) that is transmitted upstream through the subsonic part of the boundary layer and thus forms a feedback loop that increases the overall fluctuation levels (Babinsky and Harvey, 2011). Competing theories to explain the origin of the low frequency unsteadiness rely on the influence of either upstream or downstream unsteadiness. However, recent studies have suggested that in strong SWBLIs, downstream unsteadiness is the main driver of low frequency shock foot motion, while in weak SWBLIs, it is a combination of upstream and downstream unsteadiness (Clemens and Narayanaswamy, 2014). Further, under experimental conditions, three-dimensionality is also a major consideration for explaining the unsteadiness: both Dupont et al. (2005) and Bruce et al. (2011) have confirmed the influence of corner effects and wind tunnel wall interacting with the SWBLI on the unsteadiness. A recent comprehensive review of the current state of knowledge on the unsteadiness mechanisms can be found in Ligrani et al. (2020).

2.2.3. Techniques to study SWBLIs

Numerical techniques

Usage of RANS turbulence models for simulating SWBLIs usually leads to considerable inaccuracies due to their treatment of the turbulence transport term and inherent assumption of isotropic diffusion (Morgan et al., 2013). Special modifications made to these models, such as the shock-unsteadiness model by Pasha and Sinha (2012), leads to more accurate results in specific cases. Thus, only high-fidelity techniques such as Large Eddy Simulation (LES) and Direct Numerical Simulation (DNS) are viable options for numerically investigating the physics of SWBLIs. Their prowess is demonstrated by the work of Génin and Menon (2010), Pasquariello et al. (2015, 2017) (LES), Pirozzoli and Grasso (2006), Priebe et al. (2009) (DNS).

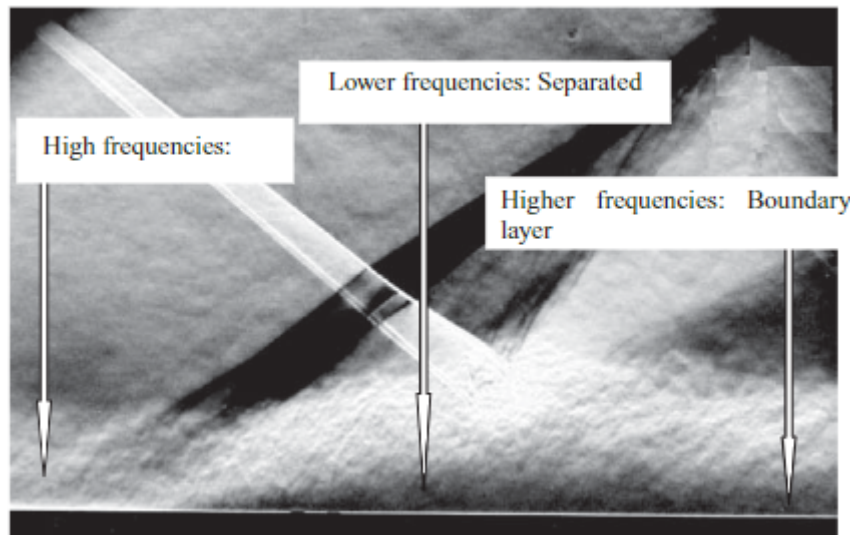


Figure 2.14: Regions of unsteadiness in a strong SWBLI (Babinsky and Harvey, 2011)

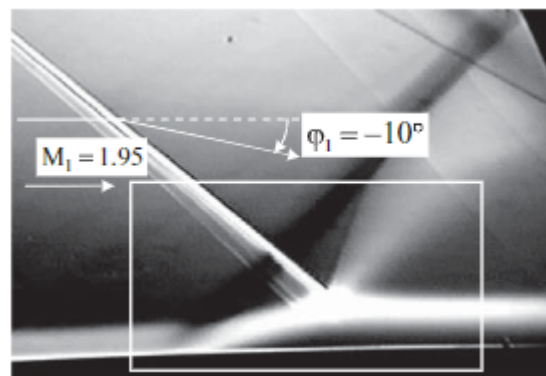


Figure 2.15: Schlieren image of oblique shock reflection (Babinsky and Harvey, 2011)

Experimental techniques

Given the inherently unsteady nature of SWBLIs, experimental methods used to study them need to have sufficient sampling rate, in accordance with the Nyquist-Shannon theorem (Jerri, 1977), as well as high sensitivity. Thus, fast-response pressure measurements and high-speed, non-intrusive optical imaging methods are often used.

Shadowgraph and Schlieren (see Figure 2.15) techniques have been very commonly employed to study SWBLIs in terms of mean flow and unsteadiness (Dolling, 2001). The main advantage is their non-intrusive measurement, and they rely on the density variations in the flowfield to capture essential features such as shock and expansion waves that result in strong density gradients. However, they are not capable of obtaining full-field quantitative information in terms of quantity of interest such as velocity, pressure, density, because the quantity measured is the first or second gradient of density. Another disadvantage is that these techniques are limited to span-averaged details of the flowfield as they provide an integral measurement over the depth of medium, hence it is not possible to detect three-dimensional features of the flow. What can be measured are quantities such as shock angles (an indication of shock strength) and separation length, which is why these techniques still prove useful for SWBLI research (Estruch et al., 2008, Sun et al., 2020).

State-of-the-art Particle Image Velocimetry (PIV) techniques are the most powerful tool available for studying any flows in general. They offer non-intrusive, full-field quantitative measurements and can be used to measure in quasi two-dimensional planes (planar PIV) or full three-dimensional volumes

(tomographic PIV). The quantitative nature of the data ensures more accurate determination of SWBLI features such as shock location, separation bubble, boundary layer profile, etc.

Humble et al. (2007) used planar PIV measurements at multiple spanwise locations to determine the three-dimensional nature of oblique SWBLIs. In Figure 2.16, the velocities of the mean streamtubes clearly show span-wise variation of the SWBLI. The instantaneous flowfields also allowed an investigation into the unsteady and turbulent features.

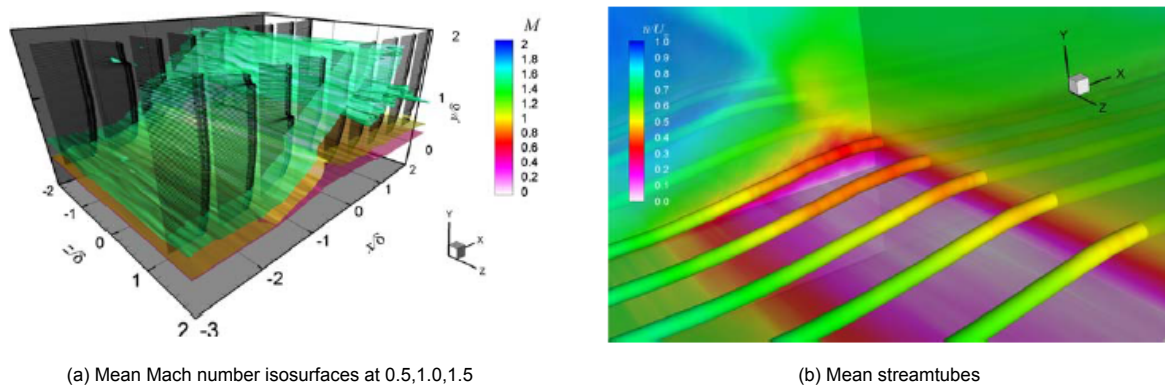


Figure 2.16: Spanwise variation of mean flow organisation in SWBLI (Humble et al., 2007)

The study by Beresh et al. (2002) used PIV and wall pressure measurement and established a clear relationship between velocity fluctuations in the boundary layer upstream of the shock impingement and the reflected shock foot position in a SWBLI. Souverein et al. (2010) suggested the presence of both upstream and downstream mechanisms in creating the low frequency unsteadiness of SWBLIs, the dominant one depending upon the incident shock strength, using measurements from a two-component planar PIV. Van Oudheusden et al. (2011) also employed high-speed planar PIV to study an intermittently separated SWBLI. The data analysis to establish correlation between different features of the interaction suggested a strong influence of incoming boundary layer on the dynamics of the separation bubble. Evidence of the influence of the incoming boundary layer was also made by Baidya et al. (2020), who employed planar PIV in wall-normal and wall-parallel conditions to study the stream-wise and span-wise characteristics of SWBLIs, respectively. Further, the use of PIV also makes it possible to obtain pressure fields of SWBLIs from the velocity data, as demonstrated by van Oudheusden et al. (2019). Finally, the three-dimensional tomographic PIV has also proved a useful tool for studying the instantaneous nature of SWBLIs, as done by Humble et al. (2009). Figure 2.17 shows in detail the various flow features of a SWBLI induced by shock impingement, highlighting the strong three-dimensional behaviour of the instantaneous flowfield.

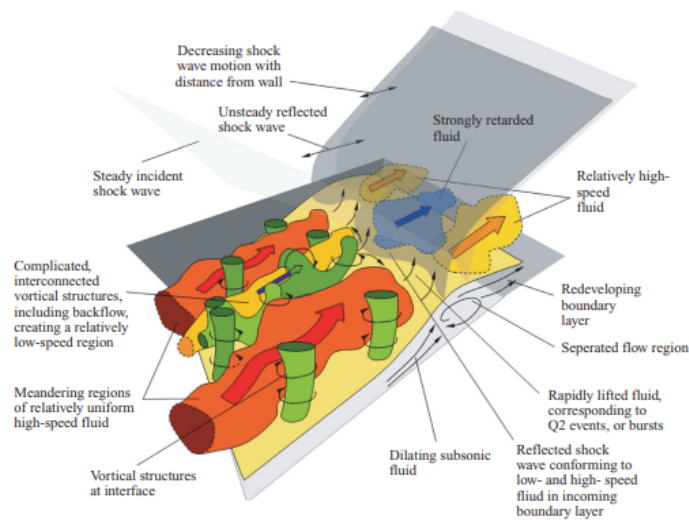


Figure 2.17: Instantaneous flow organisation of a SWBLI visualized using tomographic PIV measurements (Humble et al., 2009)

2.3. Shock-induced Panel Flutter

Shock-induced panel flutter is a subset of panel flutter, as mentioned in Chapter 2.2. Along with being immersed in supersonic flow, an oblique shock impingement creates this dynamic instability on a flexible panel. While for coalescent panel flutter, the viscous effects of the boundary layer were important in creating a self-sustained oscillation through an aerodynamic feedback loop, in shock-induced panel flutter, the interaction of the impinging shock with the boundary layer gives rise to a new phenomenon. Studies as early as the one by Maestrello and Linden (1971) experimentally confirmed that the flutter resulting from impinging shock gives rise to higher wall pressure fluctuations as well as higher panel deflections, compared to coalescent panel flutter. Thus, shock-induced panel flutter can be seen as a "combination" of the phenomena discussed in the preceding chapters, i.e., coalescent panel flutter and SWBLIs. The characteristic low-frequency unsteadiness of SWBLIs is believed to play an important role in creating this new instability as a result of the fluid-structure interaction (Shinde et al., 2019a).

In the first couple of sections, the effect of an SWBLI on flutter, and vice-versa, will be discussed. Following that, a range of parameters that influence shock-induced panel flutter, including static pressure differential, temperature differential, geometrical aspects, Reynolds number, and three-dimensional effects, will be discussed. To conclude with, the techniques used to study the phenomenon with a focus on experimental considerations will also be discussed.

2.3.1. Effect of Impinging Shock on Panel Flutter

The numerical study by Visbal (2012) on flutter produced by an impinging shock wave using compressible Euler equations and von Kármán plate equations, even without considering the effect of viscosity (i.e., boundary layer), suggested that a new form of instability resulted from such an interaction, that was different from coalescent panel flutter. Specifically, flutter boundaries were found to decrease compared to coalescent panel flutter, and LCO amplitude was found to be higher than without the shock and increasing with greater shock strength. Interestingly, Boyer et al. (2021) simulated laminar SWBLI on a flexible panel and noted that weak impinging shocks actually reduced flutter amplitude, only strong shocks were able to raise it, with increased frequency in both cases, with respect to coalescent flutter.

Effect on Response Amplitude

Both asymmetric static and dynamic components of displacement were detected by Willems et al. (2013), Visbal (2014), Daub et al. (2016a), and Shinde et al. (2019a). The asymmetry was attributed to the pressure distribution imposed by the SWBLI, and the maximum location of displacement was found to be three-quarter chord length, as noted by Shinde et al. (2019a), Spottwood et al. (2012). The observed location of maximum displacement at three-quarter chord position in engineering investigations

was established theoretically by Meng et al. (2020), using numerical investigations and a theoretical derivation. Bebernis et al. (2016) measured peak displacements with and without shock in an experimental setup and found that an impinging shock resulted in a clear rise in displacement amplitude, as shown in Figure 2.18. In fact, in the presence of the shock impinging at quarter chord location, the peak displacement doubled to the order of the panel thickness. The only exception to these observations seems to be in the case of weak shocks (pressure ratio across shock ≈ 1.2), where the flutter amplitude is found to decrease (Boyer et al., 2021).

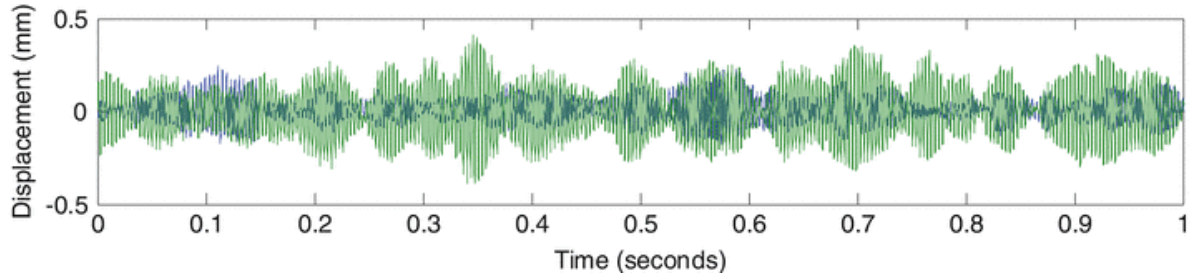


Figure 2.18: Peak panel displacement, with shock (green) and without shock (blue) (Bebernis et al., 2016)

Effect on Response Frequency

Bebernis et al. (2011) detected a positive shift in frequency of the dominant modes and widening of the dominant peak with an impinging shock (Figure 2.19), suggesting increased stiffness in presence of the shock. Visbal (2014) found a single dominant peak for two-dimensional panel flutter with only a laminar boundary layer, but multiple peaks with the dominant peak at a lower Strouhal number for an impinging shock on the panel, suggesting a more chaotic response in presence of the shock (Figure 2.20).

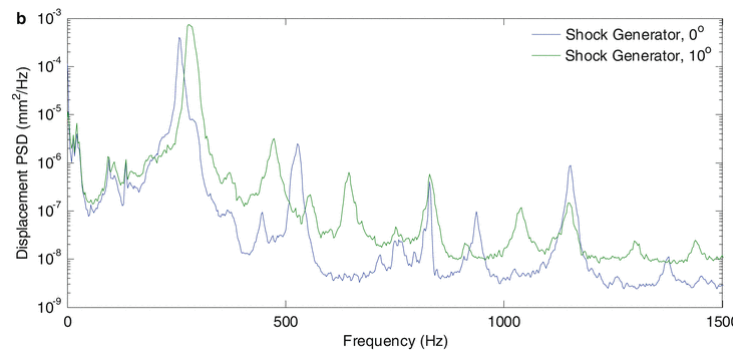


Figure 2.19: Displacement PSD at center chord position (Bebernis et al., 2011)

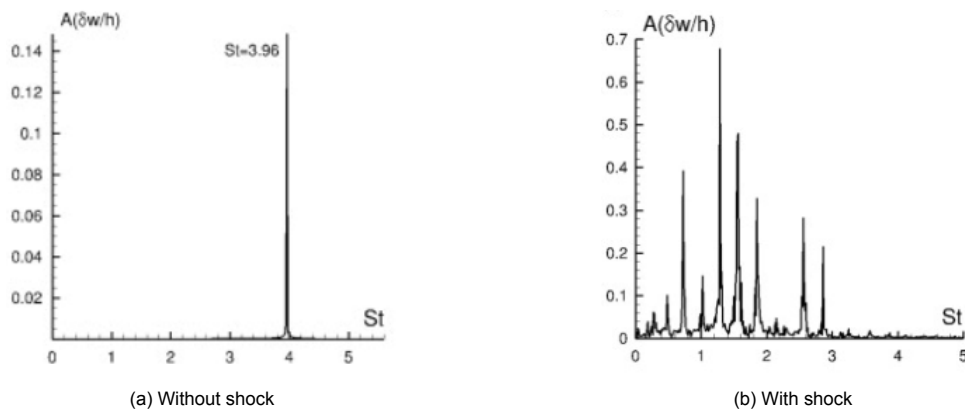


Figure 2.20: Displacement spectra at three-quarter chord location (Visbal, 2014)

Effect on Mode Shapes

Spottswood et al. (2012) employed operational modal analysis on the full-field 3D DIC measurements made on a shock-induced fluttering panel with all four edges clamped, and the dominant mode shapes are shown in Figure 2.21a. The symmetry about the mid-span suggests absence of torsional modes in the flutter. In the following study done (Spottswood et al., 2013), side edges were left free and Proper Orthogonal Decomposition (POD) was employed on the 3D DIC data to determine the most energetic mode shapes, the first 9 modes shown in Figure 2.21b.

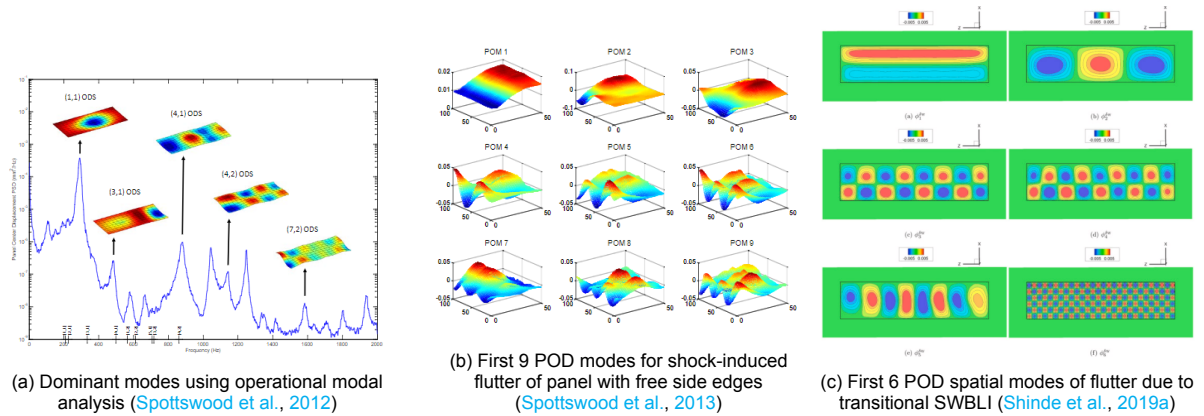


Figure 2.21: Dominant spatial modes in shock-induced panel flutter

Shinde et al. (2019a) performed DNS of a 3D transitional boundary layer interacting with an oblique shock impinging on the mid-chord location of a flexible panel, and extracted the dominant POD spatial mode shapes as shown in Figure 2.21c. While the first mode represent the mean deflection of the panel, the other modes contribute to the unsteadiness of flutter. The 6th POD mode (which also has highest Strouhal number among the dominant modes shown) is found to be excited by high frequency events of the flow transition. Visbal (2014) conducted simulations on a two-dimensional panels, hence presented the behaviour of flutter on the x-t plane, as shown in Figure 2.22. With no shock impinging on the panel, the flutter behaviour exhibits spatially stationary deflection behaviour. When a SWBLI is formed over the panel, a significant rise in peak amplitude of deflection is seen with disturbances moving back and forth across the panel in time.

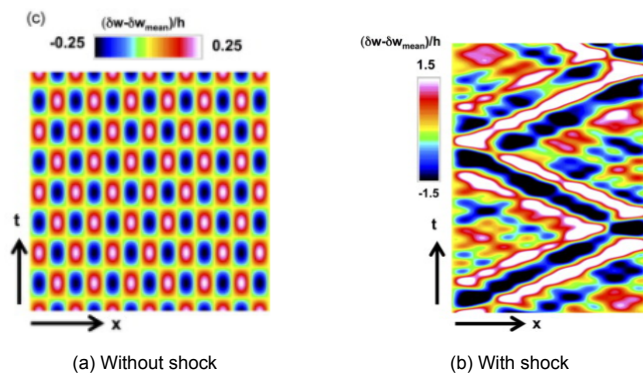


Figure 2.22: x-t diagrams of two-dimensional panel displacement (Visbal, 2014)

Effect on Pressure

Spottswood et al. (2012) measured the panel center displacements and used pressure-sensitive paint (PSP) to obtain the pressure field over the entire panel (Figure 2.23a). While the displacement spectra at the center showed a positive shift in dominant frequencies, confirming the increase in stiffness as also observed by Bebernis et al. (2011), the peak pressure load was found to have doubled due to

the shock impingement. Similar observations are made by the experiments of [Beberriss et al. \(2016\)](#), as seen in [Figure 2.23b](#), and once again pressure load is seen to have doubled or at least increased substantially in extensive regions near the shock impingement.

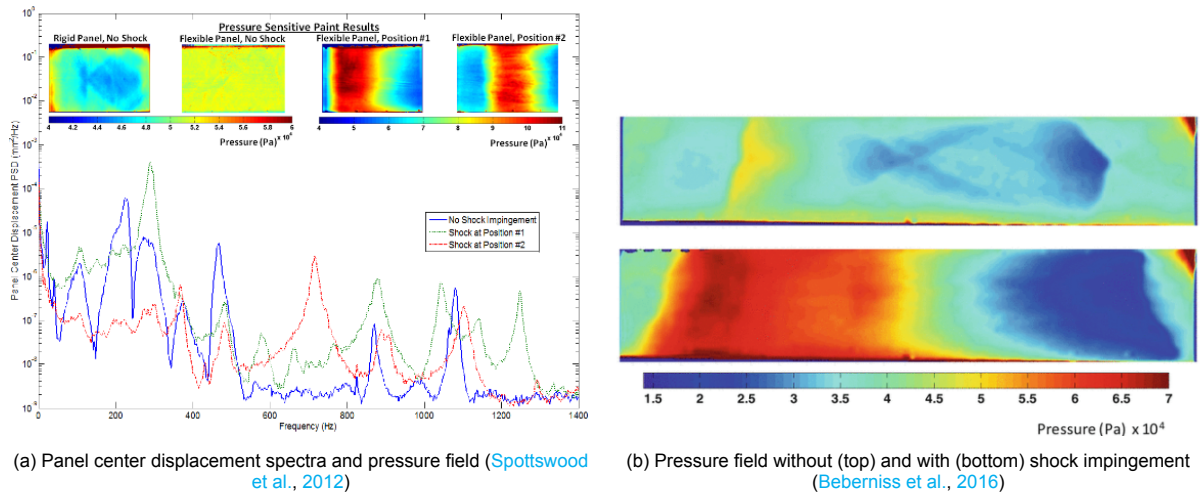


Figure 2.23: Effect of shock impingement on surface pressure

Effect on Temperature

Experiments by [Beberriss \(2017\)](#) used temperature-sensitive paint (TSP) to obtain temperature distribution over the entire panel. In [Figure 2.24](#), the highly non-uniform temperature field, with high temperatures near the shock impingement location (marked by the black line), show that the shock impingement causes local heating thus creating strong thermal gradients that influence the mechanical behaviour and flutter dynamics of the panel. The local heating caused by shock impingement was also confirmed by the TSP measurements of [Spottswood et al. \(2019\)](#) and IRT measurements of [Daub et al. \(2019\)](#), although the both measurements were made over a rigid plate so were more representative of a canonical SWBLI. Experiments by [Daub et al. \(2020\)](#) of full-field displacement and temperature of a buckled panel in hypersonic flow showed a clear correlation between regions of positive gradient in displacement and regions of high temperature.

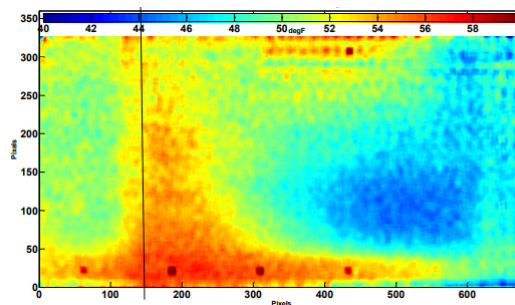


Figure 2.24: Temperature field over flexible panel with shock impingement location indicated by black vertical line ([Beberriss et al., 2011](#))

2.3.2. Effect of Panel Motion on SWBLI

Size of separation region

The computations of [Visbal \(2014\)](#) suggested that an elastic panel was able to reduce the size of the separation zone of the SWBLI for the same shock strength and location, both in terms of length and height compared to a rigid panel, as shown in [Figure 2.25](#), suggesting that flexible panels could be used as a method for SWBLI control to mitigate its adverse effects. However, the experimental results of [Daub et al. \(2016a\)](#) showed an increase in the size of the separation region when a flexible panel

was used instead of a rigid plate. Recently, experiments conducted by [Neet and Austin \(2020\)](#) of a SWBLI created by mid-panel shock impingement resulted in an increase in separation length and a decrease in separation height when a flexible panel was used instead of a rigid plate ([Figure 2.26](#)), suggesting that use of flexible panels for shock control may not be as straightforward and depends on other factors as well. [Hoy and Bermejo-Moreno \(2021\)](#) used a coupled FSI solver with wall-modelled LES (helps achieve longer duration simulation) to replicate the experiments of [Daub et al. \(2016a\)](#), and found that SWBLI separation region was considerably larger in case of a flexible panel with respect to rigid plate, in terms of both length and volume, with the chord-wise centroid of the separation bubble only showing a minor change as a result of flexibility.

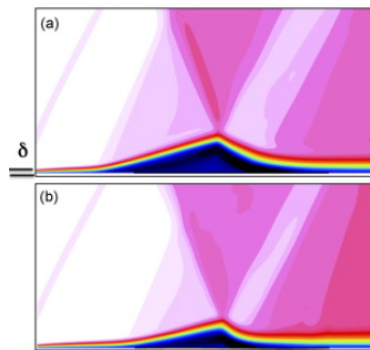
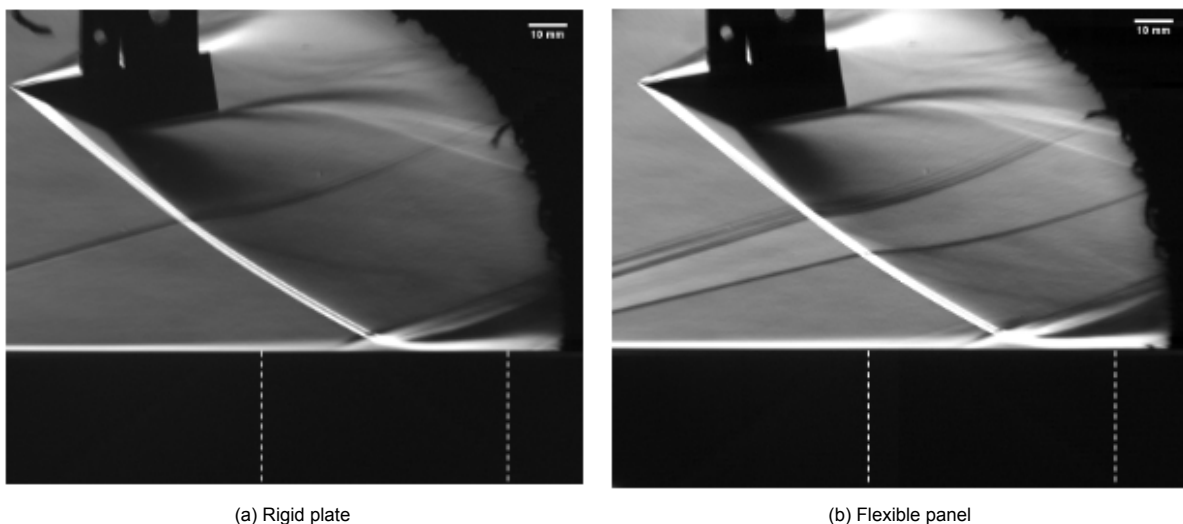


Figure 2.25: Time-averaged separation zone of SWBLI over (a) rigid plate and (b) flexible panel ([Visbal, 2014](#))



(a) Rigid plate

(b) Flexible panel

Figure 2.26: Schlieren images of SWBLI, leading and trailing edges of panels indicated by white dashed lines ([Neet and Austin, 2020](#))

SWBLI Dynamics

Wall pressure PSD was used as an indication of the SWBLI dynamics by [Shinde et al. \(2018\)](#) and [Shinde et al. \(2019a\)](#). In [Figure 2.27](#), the low frequency content ($St \approx 0.04 - 0.08$) present near the separation region for the rigid plate was found to be absent in case of a flexible panel. In fact, with the flexible panel, all the spectral content now existed in the reattachment region only, and the high frequency peaks were also found to be sharper, indicative of the decreased rigidity. From [Figure 2.28](#), again the spectral content of the wall pressure PSD as found to be considerably altered in the presence of a flexible panel. While for the rigid plate, low frequency content ($St < 0.1$) was found near separation and reattachment locations, with the flexible panel the frequencies near the separation zone were found to be higher ($St \approx 0.1 - 0.3$), and the peaks near the reattachment region were now at higher frequencies and at much higher PSD as well. Experiments by [Neet and Austin \(2020\)](#) and simulations by [Hoy and](#)

Bermejo-Moreno (2021) both confirm a considerable decrease in peak pressure fluctuations on the panel due to flexibility.

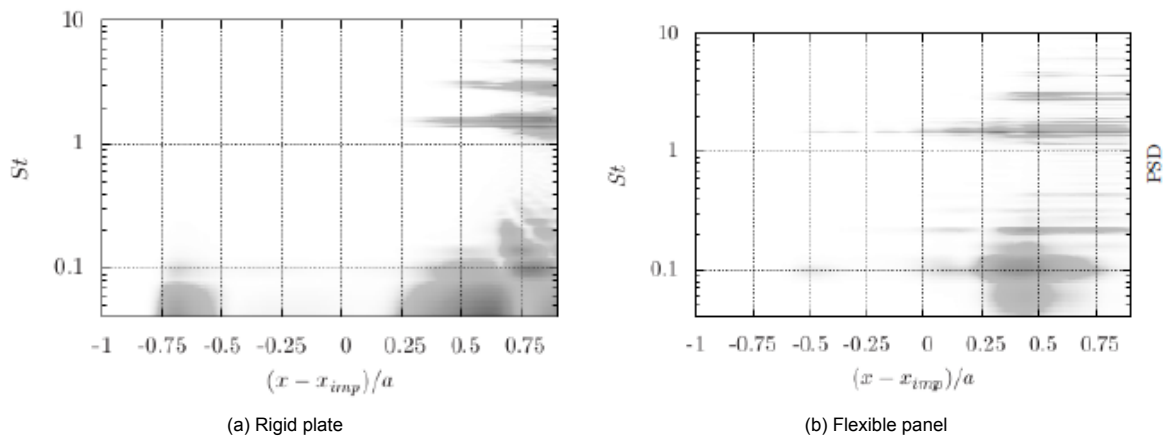


Figure 2.27: Wall pressure PSD at mid-span location (Shinde et al., 2018)

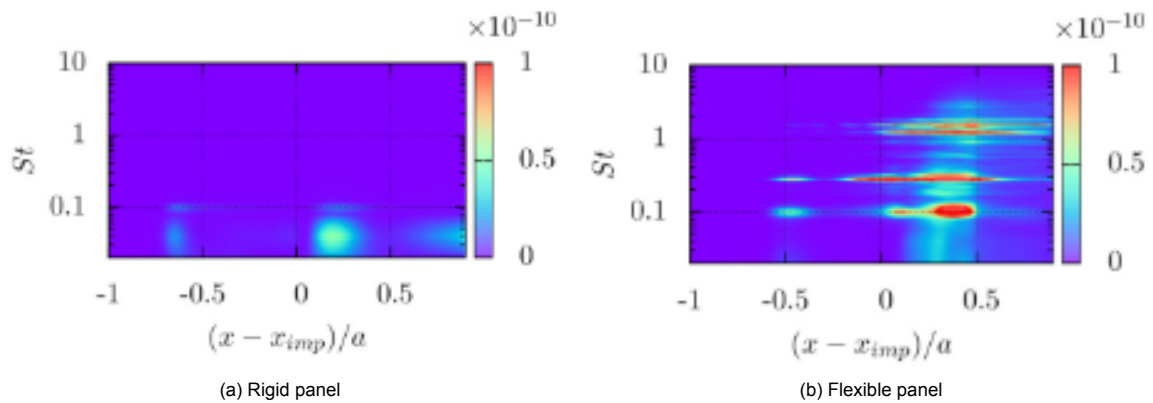


Figure 2.28: Wall pressure PSD at mid-span location for a transitional SWBLI (Shinde et al., 2019a)

2.3.3. Effect of Shock Impingement Location

Visbal (2014) studied the effect of varying shock impingement location x_i , while maintaining a net zero transverse loading condition by varying the static pressure ratio across the panel in each case. Results are shown in Figure 2.29. The shock impingement locations considered were $x_i/a = 0.5, 0.43, 0.38, 0.25, 0.18$. For $x_i/a = 0.43$, there is not much effect on the dominant frequency compared to $x_i/a = 0.5$. At locations $x_i/a = 0.25$ and 0.28 , the LCO disappeared and instead a static displacement of the panel was observed. However, at $x_i/a = 0.18$ the LCO re-emerges at a much higher frequency. The x-t diagrams show that a higher spatial mode of oscillations exists when the shock impinges near the leading edge, compared to mid-chord impingement. Experimental study of shock-induced panel flutter by Willems et al. (2013) also evaluated the effect of shock-impingement location. The static deflection is clearly very different depending on the impingement location, with the maximum deflection seen for the most upstream impingement location. The different maximum deflections are manifested in the shift in frequencies of the dominant modes, due to the variation in tensile stresses.

More recently, Gomez-Vega et al. (2020) conducted an experimental investigation as well as RANS simulations on the effect of shock impingement location on the separation/interaction length of an SWBLI, albeit on a flexible panel designed against flutter. Still, the results found were interesting from the perspective of shock control. In Figure 2.31, the interaction lengths of the SWBLI as measured using the Schlieren images, follows a decreasing-increasing trend as the shock impingement location (x_1) is varied from the leading edge to the trailing edge, and a minima exists near the three-quarter-chord location. This trend is also confirmed by the RANS simulation results, indicating that optimizing

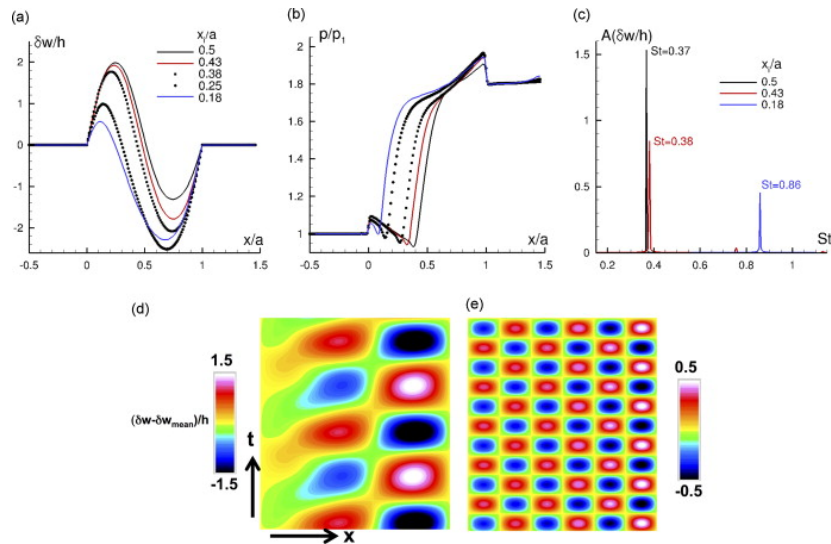


Figure 2.29: Effect of shock impingement location for inviscid interaction on (a) time-averaged panel deflection (b) time averaged surface pressure (c) oscillation frequency spectra at $x/a = 0.75$ location, and x-t diagram of panel fluctuations for (d) $x_i/a = 0.5$ and (e) $x_i/a = 0.18$ (Visbal, 2014)

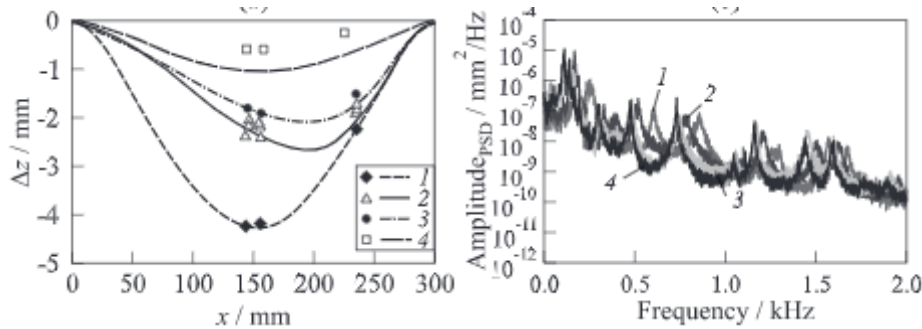


Figure 2.30: For different shock impingement locations (1-4 from leading edge towards trailing edge): (a) Static deflection of plate (b) Deflection PSD (Willems et al., 2013)

the shock impingement location on a flexible panel might lead to a shorter separation region compared to a rigid plate.

2.3.4. Effect of Cavity Pressure

Various studies have highlighted the influence of the cavity pressure, which creates a pressure differential across the panel thickness, on the dynamics. The study by Visbal (2014) established the impact of the dimensionless pressure differential, p_c/p_1 , where p_c is the cavity pressure and p_1 is the static pressure in the freestream. When the pressure differential is maintained to keep a net-zero loading, then LCO is observed. However, both positive and negative pressure differentials result in a steady deflection component of the first-mode nature, about which the flutter may occur. Experiments by Gramola et al. (2020) focused on the effect of cavity pressure on a flexible panel designed against flutter, with a mid-chord shock impingement. As Figure 2.32 shows, a high pressure differential results in positive (into the flow) plate deflection, while a low differential causes a negative deflection. With intermediate value, a sinusoidal plate deflection is obtained, where the nature of the deflection depends upon the local value of pressure difference. The nature of deflection at the leading edge has a significant effect on the wall pressure distribution, as depending on whether curvature at the leading edge is towards the flow or the cavity, shock waves or expansion waves are generated at the leading edge. Tripathi et al. (2021) also measured the response of a flexible panel subjected to oblique shock impingement, and found that the interaction length of the SWBLI was a function of both the shock impingement location and the cavity pressure.

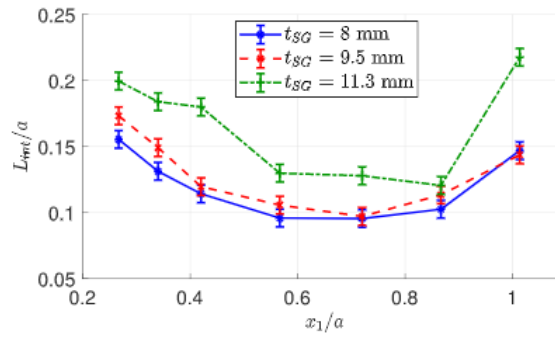


Figure 2.31: SWBLI interaction length vs. shock impingement location from experimental results (Gomez-Vega et al., 2020)

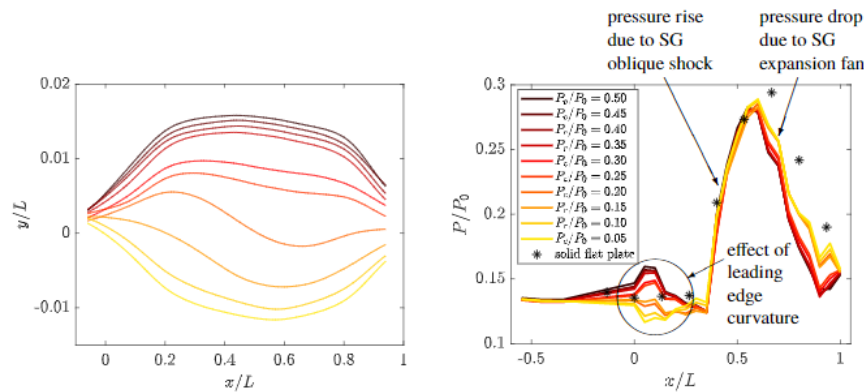


Figure 2.32: Effect of cavity pressure on static deflection and wall pressure (Gramola et al., 2020)

Experiments by Brouwer et al. (2021a) and Brouwer et al. (2021b) attempted to study variation of cavity pressure and hysteresis effects on shock-induced panel flutter. PSD of panel deformation velocity measured using LDV are shown in Figure 2.33. With increasing cavity pressure, higher dominant peaks (at ≈ 260 Hz) are produced, and at a range of higher pressures ($\approx 66 - 71$ kPa), a more periodic response was obtained (essentially, LCO) as indicated by the presence of higher harmonics in the spectra. Eventually, the periodic response dies out after ≈ 71 kPa. When cavity pressure is decreased from the maximum limit, the maximum peak is not obtained at the same values as the ones found with the increasing period of the cycle. In addition, there is an independent temperature differential between the panel and the wind tunnel present (due to different rates of heating), which keeps decreasing throughout the experiment. Hence, it is not clear whether the change in response is because of hysteresis effects related to cavity pressure, or due to the decreasing temperature differential.

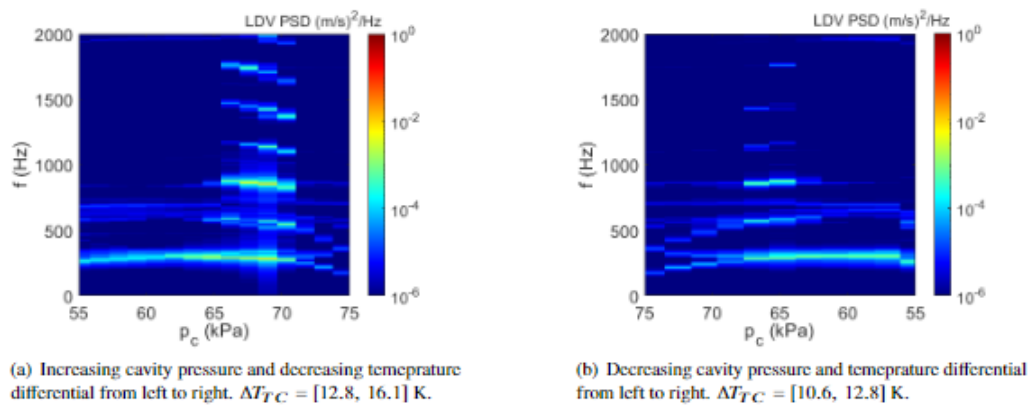


Figure 2.33: Panel velocity PSD for changing cavity pressure and temperature differential (Brouwer et al., 2021a)

2.3.5. Effect of Reynolds Number

Depending on the Reynolds number (Re), flow transition may be triggered by an SWBLI for laminar boundary layers. The simulations by Visbal (2014) of two-dimensional panel flutter with laminar SWBLI showed that with an increase in Re , instantaneous wall pressure fluctuations increased along with a reduction in half of the separation region size. Experiments by Tripathi et al. (2020) confirmed the decrease in separation region length with increase Re per unit length scale, as shown in Figure 2.34. The study by Shinde et al. (2018) found that for a rigid panel, by increasing Re from 1×10^4 to 6×10^4 , separation length increased considerably. When Re was increased to 7×10^4 , triggered transition and also resulted in greater three-dimensionality of the SWBLI, manifested as increased velocity fluctuations in the span-wise direction. Shinde et al. (2019a) extended the study to SWBLIs over flexible panels, and observed an increase in Görtler number, that is attributed to increased vortex instability. Strong vortical structures that are obtained post shock impingement were found to be transmitted in both stream-wise and spanwise directions, unlike the rigid panel. Also, transition was found to occur at lower Re for the flexible panel.

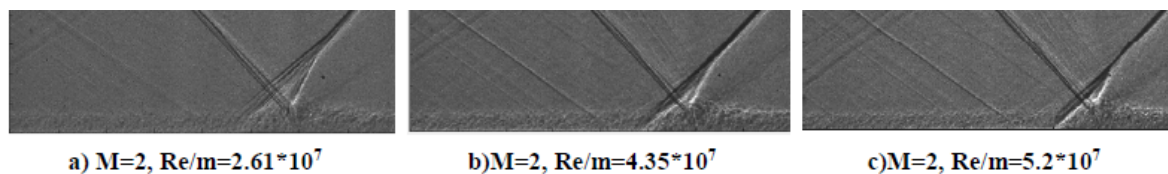


Figure 2.34: Schlieren images of SWBLI over flexible panels for different Re per unit length (Tripathi et al., 2020)

2.3.6. Effect of Geometrical Parameters

Shinde et al. (2019b) conducted an investigation into the influence of structural parameters like panel aspect ratio (b/a), thickness (h/a), dynamic pressure (λ) and mass ratio (m_r) on a transitional SWBLI over a flexible panel using DNS.

Effect of Aspect Ratio

In Figure 2.35, it is seen that the LCO amplitude as well as the time required to establish LCO were higher for $b/a = 4$. The static deflection shapes were found to be slightly different, as shown in Figure 2.36a: $b/a = 4$ had lower deflection upstream of the shock impingement, but higher deflection downstream. Dynamic components of both panel deflections showed sixth order mode shapes, $b/a = 4$ being relatively more negative. The panel deflection spectra at 3/4-chord location showed similar high frequency content for both aspect ratios, however $b/a = 4$ showed a low frequency peak ($St = 0.1$) which was absent for $b/a = 1$.

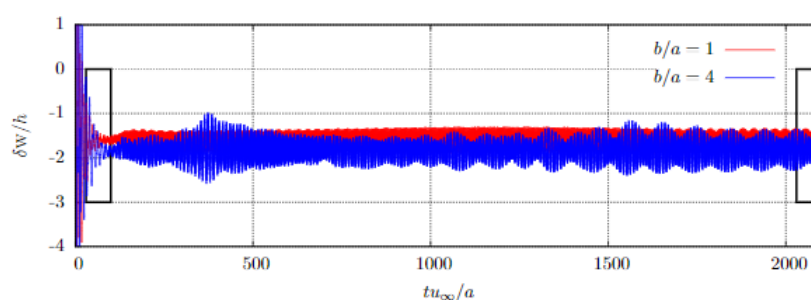


Figure 2.35: Panel deflection over time

Effect of Thickness

In Figure 2.37, it is seen that with increasing thickness the mean peak displacement decreases (in terms of magnitude), with the same trend also observed for the standard deviation (STD). This indicates an increase in stiffness of the panel with increasing thickness. This observation is also confirmed by the mean and fluctuating panel shapes shown in Figure 2.38a, with the thicker panel showing smaller mean and fluctuating deflection all along the chord, while having the same mode shapes. As for the PSD of

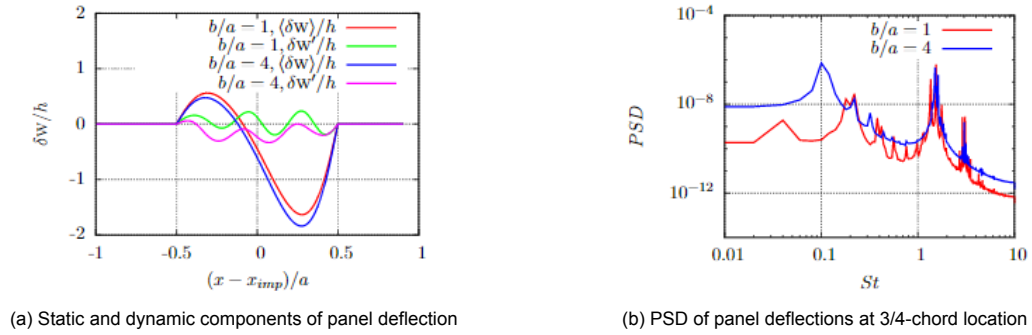


Figure 2.36: Effect of panel aspect ratio (Shinde et al., 2019b)

panel deflections (Figure 2.38b), some low frequency content seen for the two thinner panels that is absent for the other two panels, while the dominant high frequency peak is similar for all panels.

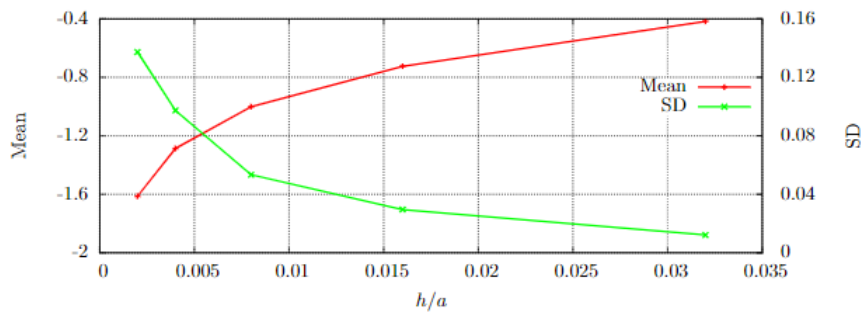


Figure 2.37: Mean and SD of panel deflection at 3/4-chord location for different thicknesses

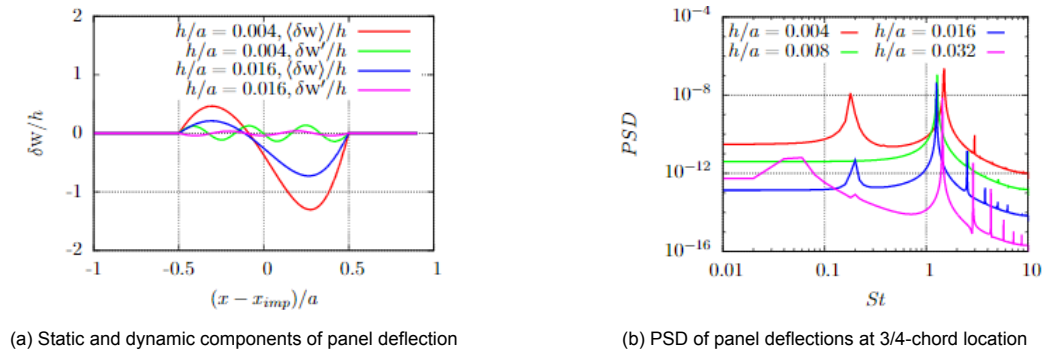


Figure 2.38: Effect of panel thickness (Shinde et al., 2019b)

2.3.7. Three-dimensional Effects

Apart from the three-dimensional effects discussed for coalescent panel flutter, there are conditions unique to SWBLIs that give rise to three dimensional effects in shock-induced panel flutter. Boyer et al. (2018) studied both 2D (semi-infinite) and 3D (square with free side edges) panel configurations with impinging shock and compressible Euler equations and nonlinear von Kármán plate equations. Qualitatively, the centerline behaviour of the 3D configuration was similar to 2D. Quantitatively, flutter boundary was higher while flutter amplitude was lower for 3D panel, indicating increased stiffness. The same study is extended to SWBLI over flexible panels using Navier-Stokes equations by Boyer et al. (2021), and it is observed that while mean deflection is larger, flutter amplitude is smaller for the 3D configuration, in addition to the maximum deflection location being shifted away from the centerline. Shinde et al. (2018, 2019a) in their study of transitional SWBLIs over flexible panels using DNS found

significant span-wise variations due to vortical structures generated by the SWBLI. Thus, mathematically, the condition of cylindrical bending (that happens in the absence of torsion, when span-wise spatial derivatives are zero) is incorrect when studying three-dimensional, viscous shock interactions.

When considering experimental studies, flow interaction with shock generator wedges and wind tunnel side walls often produces bending of shock waves at panel edges, thus inducing three-dimensional behaviour, as reported by [Willems et al. \(2013\)](#). As a result, the shock wave bends at the edges, as seen in [Figure 2.39](#). The edge boundary conditions used play an important role in determining the dominant mode shapes that influence the span-wise variations and three-dimensionality. The experimental studies of [Beberriss et al. \(2011\)](#) and [Spottswood et al. \(2012\)](#) have used fully clamped boundaries at all edges, resulting in mode shapes that exhibit significant spanwise variations (for the latter, see [Figure 2.21a](#)), while [Daub et al. \(2016a,b\)](#) used free side edges in their experiments. The wall pressure distribution from [Spottswood et al. \(2012\)](#) as seen in [Figure 2.40a](#) show significant span-wise variations especially near the edges, while the pressure along the centerline and along a line shifted by 90mm in the span-wise direction for free side edges ([Figure 2.40b](#)) are very similar even for different shock strengths. This indicates that for experiments, taking measures to prevent influence of side walls and ensuring a wide enough shock generator (as done by [Daub et al. \(2016b\)](#), according to suggestions by [Willems et al. \(2013\)](#)) can be sufficient to obtain little or no span-wise variations along large parts of the panel width with free side edges. However, there are other important factors that determine the degree of span-wise variations. The oil flow visualization done by [Tripathi et al. \(2021\)](#) ([Figure 2.41](#)) of a SWBLI over a flexible panel (all edges clamped) show, the cavity pressure that creates a transverse loading, also contributes to the three-dimensionality of the SWBLI, and it is observed that a lower cavity pressure increases the curvature of the SWBLI towards the edges.

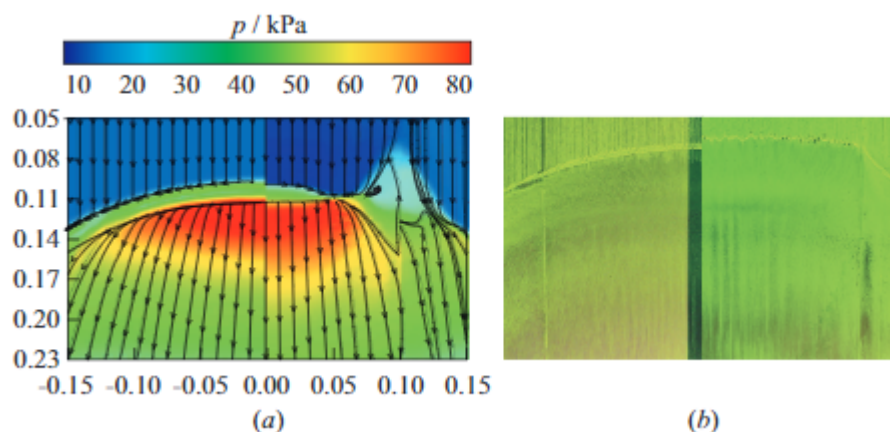


Figure 2.39: Shock shape from (a) 3D simulation and (b) oil-flow image for rigid (left) and flexible panel (right) ([Willems et al., 2013](#))

2.3.8. Techniques to study Shock-induced Panel Flutter

The complex fluid-structure interaction of shock-induced panel flutter arises due to the strong coupling of the SWBLI and flexible panel, resulting in a highly nonlinear phenomenon. Thus, in earlier times when either numerical methods were not sophisticated enough to model the physics with a reasonable degree of accuracy or computing power was not sufficient to provide useful results from the numerical schemes. However, the study of this complex interaction using numerical techniques has been accelerated in recent times due to mitigation of the aforementioned problems. To simulate laminar SWBLIs over flexible panels, [Visbal \(2012\)](#) used compressible Euler equations, while [Visbal \(2014\)](#) extended it to the viscous regime using Navier-Stokes equations. Both studies were limited to two-dimensional panels, the study of [Boyer et al. \(2018\)](#) and [Boyer et al. \(2021\)](#) extended the analysis to three-dimensional panels for inviscid and viscous regimes respectively, using similar methods. [Gogulapati et al. \(2014, 2015\)](#) employed CFD-based surrogate models to simulate turbulent SWBLIs over flexible panels, which, although computationally inexpensive, needed model tuning to improve dynamic behaviour predictions. [Brouwer et al. \(2017\)](#) used Reynolds-averaged Navier Stokes (RANS) to study

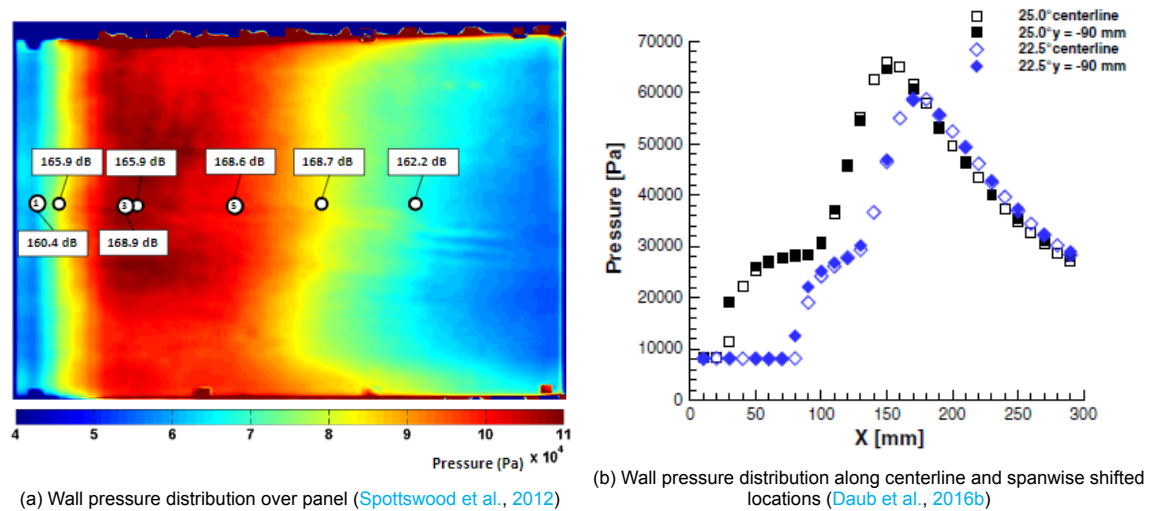


Figure 2.40: Wall pressures for different edge boundary conditions: (a) all edges clamped and (b) free side edges

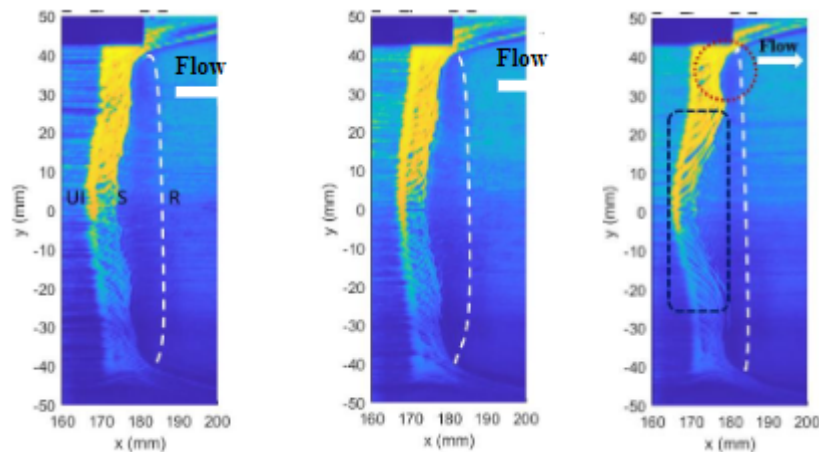


Figure 2.41: Oil flow visualisation of SWBLI surface flow over a flexible panel, cavity pressure decreasing from left to right (Tripathi et al., 2021)

the effect of flexible panels on turbulent SWBLIs, without a coupled fluid-structure interaction. Li et al. (2019) used both Euler equations and RANS to study the effect of laminar boundary layer thickness and suction on dynamics of panel flutter. Brouwer and McNamara (2019, 2020) developed an enriched piston theory that was supplemented by steady state CFD analysis which delivered comparable results at fractional computational cost compared to unsteady RANS. Shinde et al. (2019a) employed DNS to study transitional SWBLIs over finite-span flexible panels, and investigated the modal response of the panel as well as the transitional features of the SWBLI. Zope et al. (2021) used hybrid RANS/LES methods to examine a shock affected by expansion fan due to the construction of the shock generator, impinging on a flexible panel and observed better results compared to RANS and Detached Eddy Simulation (DES). Shinde et al. (2021) used LES to simulate SWBLI over 3D rigid and flexible panels, and to used POD and DMD to extract dominant modes and establish the coupling between flexible panel structural dynamics and SWBLI.

Most prominent experimental investigations of shock-induced panel flutter have been carried out by Spottswood et al. (2012, 2013), Spottswood et al. (2019), Beberniss et al. (2011, 2016), Daub et al. (2016a), who have often employed and developed full-field measurement techniques like DIC, PSP, TSP, IRT to advance the understanding of the physical aspects. Some studies have also been done with combined experimental and numerical techniques: Willems et al. (2013) compared experimen-

tal results with a combined RANS/FEM solver on the effects of Mach number and shock location on shock-induced panel flutter, [Miller et al. \(2012, 2014\)](#) used CFD-based surrogate model to compare results with the measurements of [Spottswood et al. \(2012\)](#), [Pasquariello et al. \(2015\)](#) conducted LES to study the flutter created by an oscillating shock due to a pitching shock generator and compared with experimental results, [Currao et al. \(2019\)](#) used URANS to compare Schlieren and PSP measurements of shock-induced panel flutter on a cantilevered plate, [Brouwer et al. \(2021a\)](#) conducted DIC measurements of full-field deflections of a thermally buckled panel and computed results using enriched piston theory and found reasonable agreement between the two.

To measure the structural dynamics, point-wise techniques such as strain gauges ([Currao et al., 2016](#), [Daub et al., 2016a](#), [Spottswood et al., 2019](#), [Willems et al., 2013](#)), pressure transducers ([Currao et al., 2016](#), [Pasquariello et al., 2015](#), [Willems et al., 2013](#)), and full-field techniques of 3D Digital Image Correlation (DIC) ([Brouwer et al., 2021a](#), [Spottswood et al., 2019, 2013](#)), PSP ([Neet and Austin, 2020](#), [Spottswood et al., 2012](#), [Tripathi et al., 2021](#)) have been used to obtain the panel displacements and wall pressure. The improvement in accuracy of full-field techniques have greatly improved the quality and extent of spatial and temporal data that researchers can now measure. As for measuring the SWBLI, Shadowgraph and Schlieren still remain popular techniques ([Daub et al., 2016a](#), [Neet and Austin, 2020](#), [Tripathi et al., 2020](#), [Willems et al., 2013](#)) due to their relative simplicity, while oil flow visualisation is also employed occasionally as an aid to qualitatively assess the surface flow ([Tan et al., 2019](#), [Tripathi et al., 2020, 2021](#), [Willems et al., 2013](#)). Panel temperature measurements have been carried out using thermocouples ([Brouwer et al., 2021a](#), [Spottswood et al., 2019](#)), TSP ([Beberriss et al., 2011](#), [Spottswood et al., 2019](#)) and Infrared Thermography ([Brouwer et al., 2021a](#), [Daub et al., 2020](#)).

Full-field techniques for measuring panel displacement like DIC are being more often used due to the non-intrusive nature and the superior spatial resolution it offers compared to point-wise techniques. Also, if point-wise measurement is done close to nodal lines then zero displacement would be registered, which is big disadvantage. Techniques like PSP for full-field pressure and TSP, IRT for full-field temperature measurements also offer information with spatial and temporal resolution that was earlier only possible with numerical simulations. However, at the time of writing, only one author has employed PIV for observing the flowfield in shock-induced panel flutter ([Tripathi et al., 2021](#)). Schlieren and Shadowgraphy have been widely used but they still lack the quantitative, quasi-2D/truly 3D nature of measurements that only PIV provides.

Important Experimental Considerations

- Manufacturing imperfections of the panel are inevitable part of experiments, and should be taken into consideration. Additionally, edge support rigidity and fluctuations in ambient conditions are some factors that cannot be fully controlled but something that the researcher should be mindful of when analyzing results.
- As mentioned earlier, [Willems et al. \(2013\)](#) noted that a narrow shock generator used in their experiments caused the shock wave to bend ([Figure 2.39](#)). Thus, care must be taken when designing/choosing shock generators to ensure no unintended three-dimensional effects arise. Also, the length and height of the shock generator must be decided such that the expansion waves generated by its end must not influence the panel specimen or the impinging shock wave unless desired. In the study by [Gomez-Vega et al. \(2020\)](#), the shock generator thickness was intentionally designed to test different shock-expansion wave distances, with both impinging on the panel.
- If no static pressure differential is desired, then a connection is necessary between the flow side and the cavity side to equalize pressures. However, the impinging shock wave still induces a transverse load in case the connection is downstream of the impingement location of the shock. This causes a static deflection of the plate, and is especially important during wind tunnel startup when a strong normal shock passes through the tunnel and could potentially cause structural yield of the panel. Thus, it is recommended to place connection between flow side and cavity upstream of the panel as well ([Daub et al., 2016a](#), [Willems et al., 2013](#)).
- If the panel edges are close to the wind tunnel side walls, then the boundary layer on the latter can considerably influence the flow over the panel, by inducing three-dimensional effects. It is

thus important to maintain sufficient distance between the panel and the walls to mitigate such effects (Daub et al., 2016a).

- Transient thermal gradients affect panel response, and take longer to stabilize than pressure upon wind tunnel startup. Thus, even sampling time may affect the measured dynamics of response, as observed by Beberniss et al. (2011) and shown in Figure 2.42.

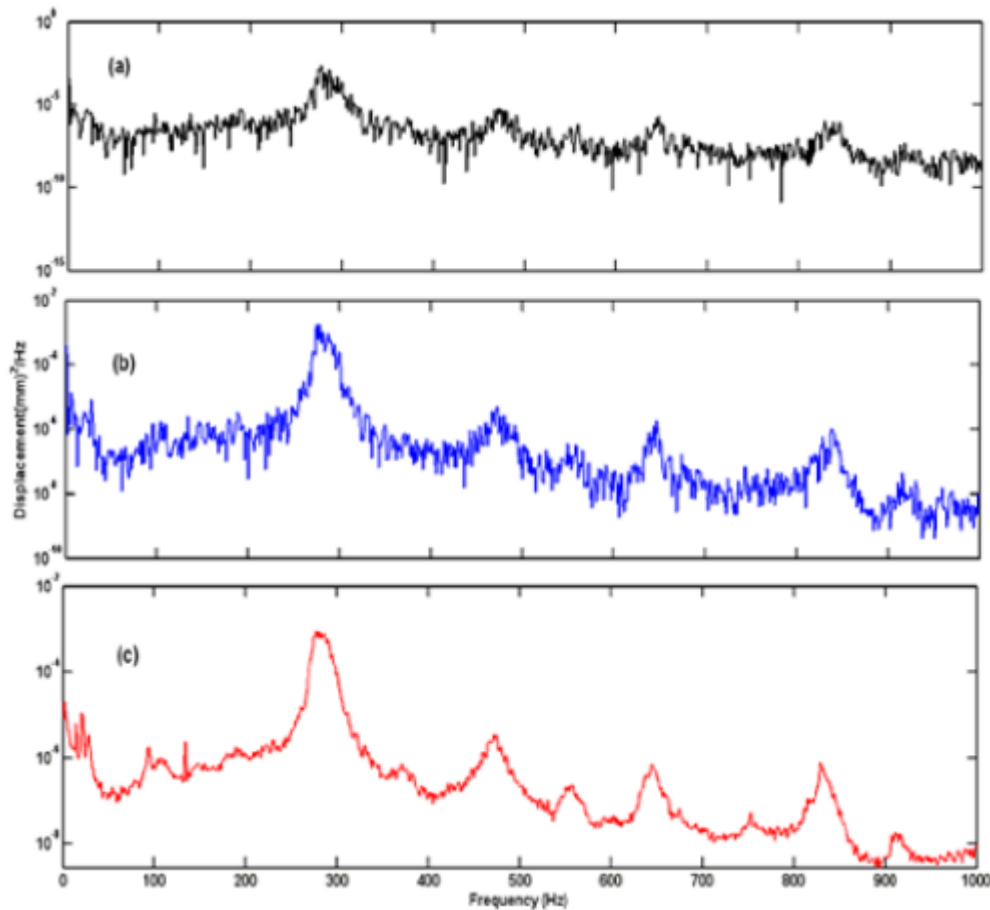


Figure 2.42: DIC displacement PSD from (a) 1 second 5000 frame time record (b) 2 second 10,000 frame time record and (c) 20.8 second 101,661 frame time record (Beberniss et al., 2011)

2.4. Recent Investigation at TU Delft

Allerhand (2020) used simultaneous PIV and DIC to investigate shock-induced panel flutter in the ST-15 supersonic wind tunnel at the Delft University of Technology in which the experiments pertaining to the current study will also be carried out. Thus, it would be useful to look at the techniques used, results obtained, and recommendations made by Allerhand (2020) in order to frame the research questions for the current study.

2.4.1. Experimental Setup

Flow Facility

Located in the High Speed Aerodynamics Laboratory of the Delft University of Technology, the ST-15 is a blowdown type supersonic wind tunnel, driven using dry air stored in a 300 m² pressure vessel using a 6 MW compressor (Allerhand, 2020). Usage of different Mach blocks mounted on the top and bottom of the test section leads to free stream flow of Mach number 1.5, 2, 2.5, 3 in the rectangular test section. Optical access from two sides of the test section allows for usage of non-intrusive optical measurement techniques. To generate shock wave, oblique ramps can be mounted at the top, with the strength of

the shock wave depending on the ramp angle and determined by the $\theta - \beta - M$ relation (Anderson Jr, 2010). The location of the shock generator along the flow direction can also be changed, which allows for choosing a particular shock impingement location.

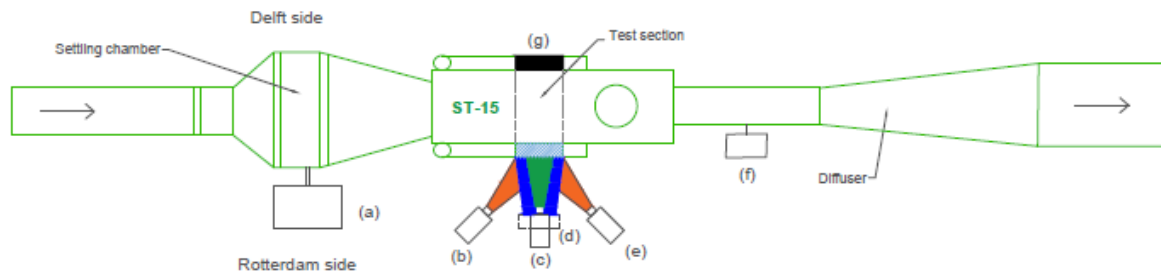


Figure 2.43: Experimental setup used by Allerhand (2020)

A schematic of the setup used is shown in Figure 2.43. Flow driven by the compressor enters through the left and encounters the settling chamber first, where two layers of wire meshes are employed to reduce turbulence levels. In the case of Allerhand (2020), Di-ethyl-hexyl-sebacate (DEHS) particles were used to seed the flow for the PIV cameras, with the particle seeder (item (a) in Figure 2.43) being located right after the meshes in the settling chamber.

PIV

To ensure robustness of measurements as simultaneous PIV-DIC was being attempted for the first time at the facility, Allerhand (2020) opted for a planar-PIV configuration using a single camera (item (c) in Figure 2.43), thus acquiring full-field velocity data in a plane along the chord of the panel located at the midspan. Images were acquired at 5 kHz to ensure capturing of important dynamic features of the flow. A double-pulsed laser (with pulse separation time of $2 \mu\text{s}$ and wavelength $\lambda=532 \text{ nm}$) was mounted downstream of the test section (item (f) in Figure 2.43). Reshaping of the circular laser beam into a thin sheet was done through a series of lenses, and finally a mirror mounted below the test section illuminated it with the laser sheet. However, the positioning of the mirror led to a couple of problems: first, a rocking motion of the mirror due to the high-speed airflow caused the laser sheet to oscillate and occasionally to jump off the bottom wall, and second, contamination of the mirror by DEHS droplets caused the laser sheet to defocus. The latter was resolved to some extent by using lesser number of active nozzles when starting the seeding, and initiating image acquisition within a few seconds post activation of seeding. Later evaluation indicated that while repeatability of PIV measurements was good for the mean values, there were still considerable deviations among different sets of measurements when considering standard deviation field, which was attributed to poor seeding quality. Moreover, the spatial resolution was found to be 32% of the freestream boundary layer thickness $\delta_{99,\infty}$, meaning the boundary layer could be resolved but with poor resolution.

DIC

To measure the out-of-plane panel displacements, two cameras were mounted on the Rotterdam side of the test section (items (b) and (e) in Figure 2.43), as stereographic DIC configuration was required. The speckle pattern on the panels was illuminated using a blue LED (item (d) in Figure 2.43). The speckle pattern is generated using fluorescent paint on top of a matte black paint on the panel, and the blue light from the LED results in the speckle pattern to emit orange colour. The acquisition frequency of both the DIC cameras is again 5 kHz, same as the PIV camera. The DIC measurements showed good repeatability in terms of both mean and standard deviation values. The spatial resolution of DIC measurements was 3.5% of the plate length, meaning that it is good enough to resolve large-scale displacements.

Consideration for simultaneous PIV/DIC

The most important consideration for doing simultaneous PIV/DIC measurements was identified to be avoiding potential optical interference between the illumination systems of both. To do so, a bandpass filter was used on the PIV camera to capture light around the laser wavelength of 532 nm. For illuminating the panel, a blue LED of wavelength lower than the laser used for PIV was used, as reflection of

the blue light by the fluorescent speckle pattern resulted in an orange colour which had a wavelength considerably higher than the laser. Additionally, a longpass filter was attached to both DIC cameras to capture only the orange light reflected by the panel. See Figure 2.44 for a graphical representation of the optical isolation approach used by Allerhand (2020). It was seen that using the longpass filter on the DIC cameras minimized the PIV laser reflections captured, and also resulted in a more homogeneous distribution of intensity of light captured. However, there is a loss in overall intensity captured as a result of the filter, so a lower signal-to-noise ratio can be expected. As for the narrowband filter on the PIV camera, it was observed to drastically reduce the blue and orange light reflections off the panel from polluting the PIV images, especially in regions near the panel.

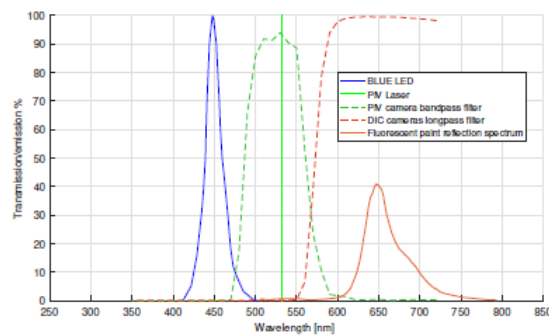


Figure 2.44: Emission/transmission spectra of the employed light sources (Allerhand, 2020)

Also, for truly simultaneous measurements, the image acquisition had to be triggered at the same time, as shown in Figure 2.45. Since two consecutive images are acquired to obtain the velocity field at a given instant using PIV, the image acquisition time of the PIV cameras is set at $100 \mu\text{s}$, and since the laser pulse duration is much smaller ($2 \mu\text{s}$), the laser double pulse is triggered at the end of the exposure of the first PIV image frame. Over the entire interval of $200 \mu\text{s}$ in which the PIV image pair is captured, only one image is required by DIC (since only the absolute displacement is required, not its rate of change at that instant), thus the blue LED is triggered once when the exposure of the second PIV image frame is initiated.

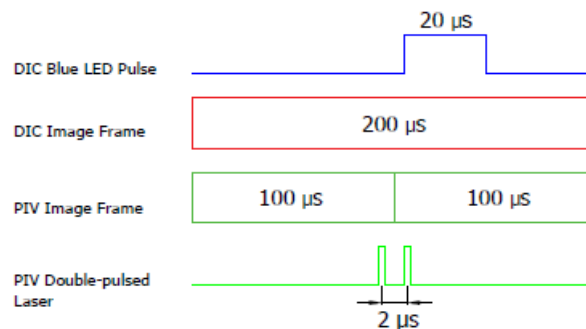


Figure 2.45: Timing diagram of simultaneous PIV/DIC measurements (Allerhand, 2020)

Results are discussed in subsequent sections, and, unless stated otherwise, pertain to flutter of a flexible panel of $a/b=1.5$ with free side edges, with freestream conditions: $M_\infty = 2.0$, $p_0 = 2.5$ bar. The shock generator used has a ramp angle of 11° and the shock impingement location is $x_i/a = 0.55$.

2.4.2. Wind Tunnel Vibrations

Six accelerometers in total were mounted on the sides and top of both Mach block, below the plate, and on the obliques shock generator to determine the influence of wind tunnel vibrations on the fluid-structure interaction. It was found that the most energetic wind tunnel vibrations were present at very high frequencies (>2500 Hz). However, a peak at 576 Hz was found to emerge only at the lower Mach block after the wind tunnel had been continuously run for a long time (see Figure 2.46). Tightening

the lower Mach block to the tunnel helped reduce the energetic content at 576 Hz (see [Figure 2.47](#)). This observed behaviour suggested that the drop in temperature due to continuously running the wind tunnel resulted in contraction of the lower Mach block which lead to the vibrations as the block became "loose". This could be confirmed with temperature measurements. Moreover, this peak only appeared at the lower Mach block when the shock generator was being used, i.e., SWBLI was present on the panel, but was drastically reduced once the shock generator was removed. However, a similar energy peak is not observed in the accelerometer readings at the shock generator. This suggests that the 576 Hz frequency is linked with the SWBLI or other unsteady aerodynamic effects interacting with the lower Mach block rather than the oblique shock or interaction of the shock generator with the flow.

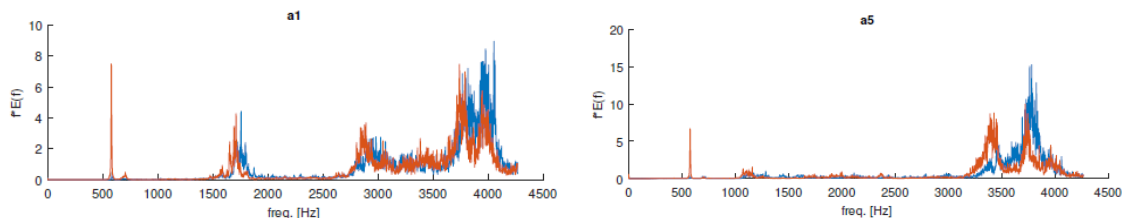


Figure 2.46: Accelerometer readings on lower Mach block for early run (blue) and late run (orange) on the same day ([Allerhand, 2020](#))

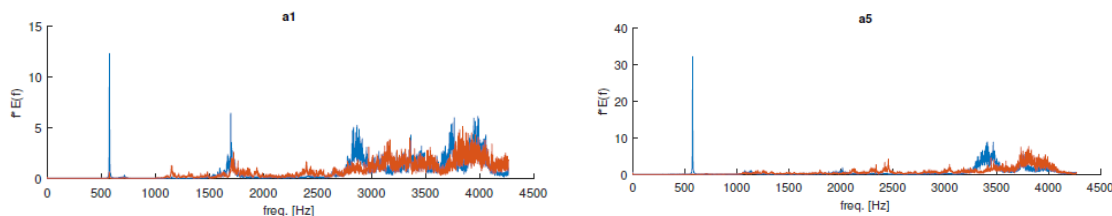


Figure 2.47: Accelerometer readings on lower Mach block before (blue) and after (orange) tightening the lower Mach block ([Allerhand, 2020](#))

2.4.3. Effect of SWBLI on Panel Flutter

- The flutter amplitudes were significantly larger with an impinging shock on the panel than without, confirming the same observations made in literature.
- Then mean panel deflection is of parabolic shape ([Figure 2.48](#)), without an impinging shock, due to cavity pressure differential across the panel thickness. When a shock impinges, the mean deflection changes to a sinusoid ([Figure 2.49](#)), due to the pressure differential created by the SWBLI ([Figure 2.13](#)), and assuming the lowest pressure of the SWBLI is lower in magnitude while the highest pressure is higher in magnitude compared to the cavity pressure differential across the panel thickness.
- The standard deviation of panel displacement at the midspan with an impinging shock are higher than without shock ([Figure 2.49](#) and [Figure 2.48](#), respectively), indicating the exacerbation of flutter due to the SWBLI.
- Without the SWBLI, a broad peak in the spectrum of oscillations (at quarter-chord point on the midspan) is observed at around 731 Hz, with much smaller peaks at 445.4 Hz and 1377.5 Hz. With an impinging shock, much sharper peaks are observed at 423.5 Hz, 1353.8 Hz, 574.9 Hz (in decreasing order of energy). The fact that the latter had significantly less energy content is an indication that the flutter dynamics were not being driven by the lower Mach block vibrations observed at 576 Hz. See [Figure 2.50](#).

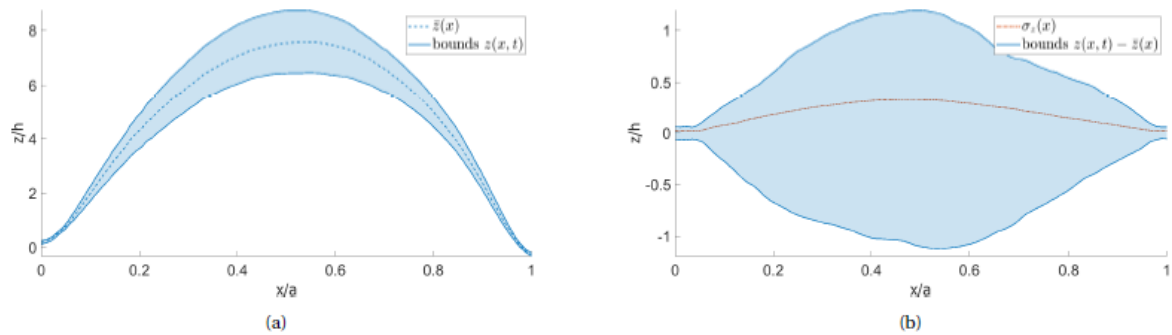


Figure 2.48: (a) Mean and (b) standard deviation of panel displacements at the midspan of the panel without shock impingement (Allerhand, 2020)

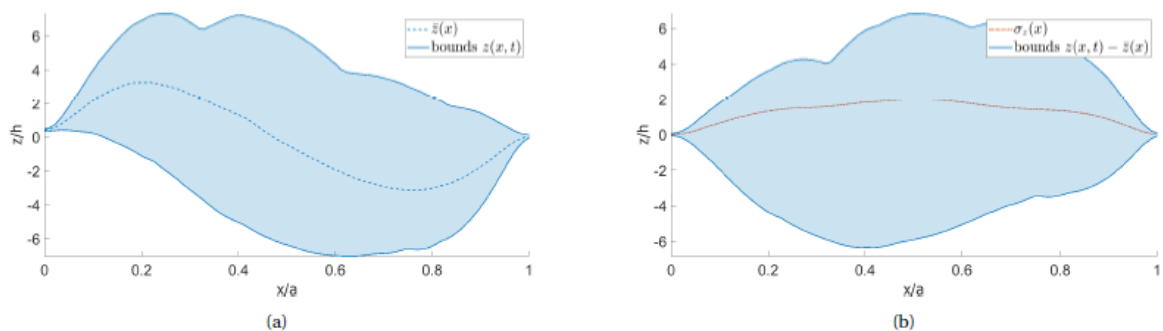


Figure 2.49: (a) Mean and (b) standard deviation of panel displacements at the midspan of the panel with shock impingement (Allerhand, 2020)

2.4.4. Effect of Panel Flexibility on SWBLI

- A leading edge shock of low strength (compared to the impinging shock) was detected in case of a flexible panel, which can be explained by the into-the-flow leading edge curvature.
- Compared to a rigid plate, the mean interaction length of SWBLI increased by 8% in case of flutter. Separation area also significantly increased for a flexible panel. Although these observation clash with results from numerical simulations of Visbal (2014), there is a physical explanation for the observation made in case of experiments: the leading edge shock, although relatively weak, causes the flow to lose stream-wise momentum and thus become more susceptible to separation upon encountering the adverse pressure gradient caused by the SWBLI.
- The reflected (or separation) shock oscillates over a larger spatial region than the impinging shock. This is expected as the latter originates from the shock generator that is fixed, while the latter is sensitive to the unsteady SWBLI and panel motion.
- Moreover, the amplitude of reflected shock oscillations were larger for the flexible panel compared to the rigid plate. No such significant difference found for the impinging shock.
- For rigid panel with impinging shock, no distinct peak in reflected shock energy spectra was observed. For flexible panel with impinging shock, distinct peaks at 424 Hz and 1358 Hz for the reflected shock energy spectra (and a small one at 576 Hz which is linked to the lower Mach block vibrations), same as those found for panel flutter using DIC (Figure 2.50). This is a clear indication of coupling between the dynamics of the flow and structure, with neither being visibly affected by the spurious Mach block vibrations. See Figure 2.51.
- Impinging shock spectra is similar for both rigid and flexible panels, showing multiple peaks over a broad range of high frequencies. Possibly, temporal resolution of PIV is not sufficient to identify the dominant frequencies of the impinging shock as suggested by the spectra.

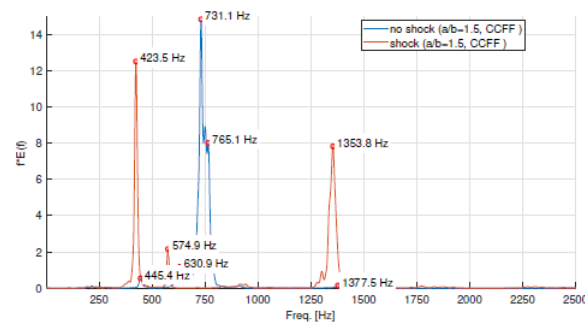


Figure 2.50: Energy spectral density at $x/a = 0.75, y/a = 0.0$ with and without impinging shock (Allerhand, 2020)

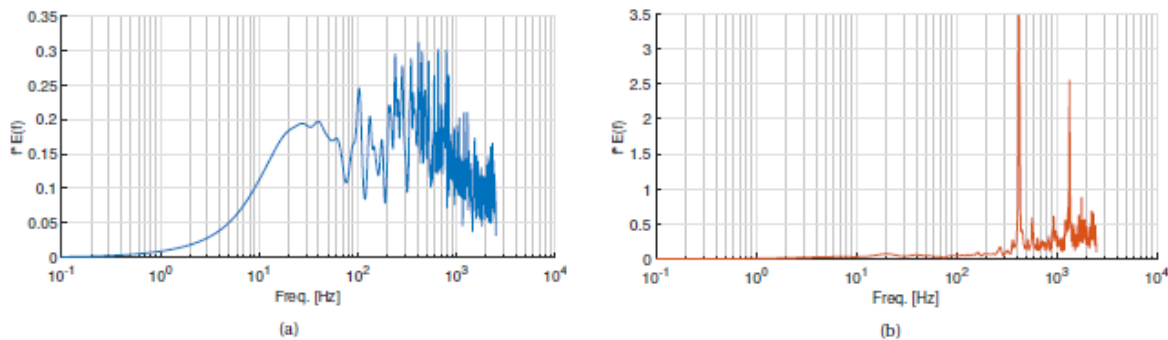


Figure 2.51: Energy spectral density of reflected shock oscillations for (a) rigid plate and (b) flexible panel (Allerhand, 2020)

- Although flow reversal was not detected in the mean flow, it was found to take place intermittently. The occurrences of reversed flow in consecutive frames and total no. of frames was seen to increase for the flexible panel compared to the rigid plate. A weak correlation was also established between the total number of frames with reversed flow and the chord-wise position of reflected shock foot. The correlation was negative because the latter decreases (moves against stream-wise direction, thus forming a larger separation region) when the former is seen to increase (more intermittent flow separation). Also, the magnitude of the correlation value was found to have a higher magnitude for the rigid plate than the flexible panel, which could be because of more resolved vectors near the wall in case of the rigid plate (as unsteady laser reflection hampered near wall measurements for the flexible panel).

2.4.5. Fluid-Structure Correlation

- A lag was observed to exist between the panel deformation at $x/a=0.5$ and the reflected shock motion, estimated at around quarter of a period at 424 Hz, confirmed by cross-correlation of the panel displacement and reflected shock foot position in time. However it was difficult to establish causality, i.e., which is the driver and which is the driven.
- In Figure 2.52, the region enveloped by the leading edge shock and reflected shock is found to have maximum positive correlation at zero time lag between the out-of-plane panel displacement at $x/a = 0.25$ and vertical velocity perturbations, suggesting that this region is where the flow is strongly coupled with panel displacement in an instantaneous sense. Flow downstream of the reflected shock shows lower (and negative) correlation which eventually goes to zero with the panel motion at zero time lag, indicating that it is more strongly coupled with the shock rather than the panel motion.
- With a time lag of 0.6 ms (one phase), at which high correlation was observed between reflected shock foot position and panel deflection, highest (negative) correlation is seen between the out-of-plane panel displacement at $x/a = 0.25$ and vertical velocity perturbations within the range of oscillation of the reflected shock (see Figure 2.53), indicating that when the vertical velocity in this region is high, the panel displacement at $x/a = 0.25$ is nearly zero after a lag of one phase.

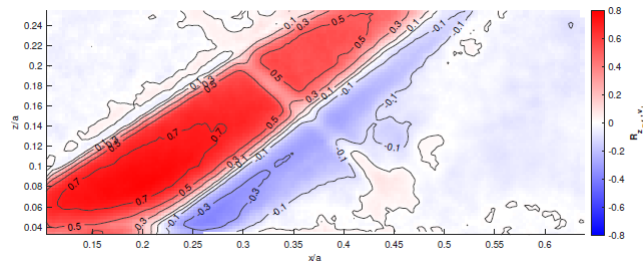


Figure 2.52: Spatial distribution of the zero-lag correlation coefficient between the vertical velocity vector component and the out-of-plane panel displacement at the position $x/a = 0.25$ (Allerhand, 2020)

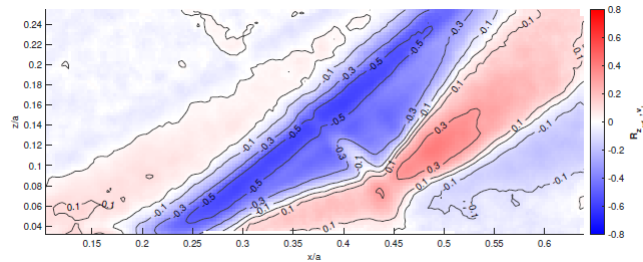


Figure 2.53: Spatial distribution of the correlation coefficient between the vertical velocity vector component and the out-of-plane panel displacement at the position $x/a = 0.25$ with a lag of 0.6 ms (Allerhand, 2020)

2.4.6. Parametric Study

A parametric study was done by using panels with different a/b ratios and different boundary conditions. Specifically, $a/b=1, 1.5, 2$ with CCFF boundaries and CCFF (leading and trailing edges clamped, side edges free) and CCCC (all four clamped) boundaries for $a/b=1, 1.5$ were tested. The following observations and inferences were made:

Effect of length-to-width ratio

- Increased a/b lead to larger maximum mean displacement which is expected because larger length compared to width translates to decreased stiffness to bending. However, increased a/b also lead to a decrease in the maximum standard deviation of the out-of-plane displacement, which was unexpected.
- The mean interaction length of the SWBLI was found to be similar for $a/b=1.5$ and $a/b=2$, whereas the area of separation was found to be considerably larger for $a/b=2$. A possible explanation for the latter could be that 3D structures in the flow are affected by the change in a/b and that is manifested as a change in separation area without affecting the mean interaction length much.
- The frequency of the dominant spectral peak for reflected shock oscillations was seen to increase for $a/b=1$ compared to $a/b=1.5$ and $a/b=2$ (both similar), which was also observed in preliminary FEM analysis owing to the increased stiffness of a square panel. However, the $a/b=1$ panel tested is shorter in length compared to the other two, so it is difficult to conclude whether the increased eigenfrequency is also owing to that reason. Secondly, the frequency with the highest peak for the square panel is 577 Hz, close to the frequency of vibrations of the lower Mach block (576 Hz) which suggests that the vibrations of the lower Mach block are influential in this case (see Figure 2.54).
- The first two dominant modes of $a/b=1$ showed strong span-wise variations, however it could not be concluded whether that is because of additional torsional modes acting or manufacturing imperfections. The $a/b=2$ panel showed a clear torsional mode in its third mode, which could be the reason why separation area increased assuming that torsional motion exacerbates separation. In conclusion, $a/b=1.5$ was seen to have the least span-wise variations in the first mode and could be considered to simulate 2D flutter.

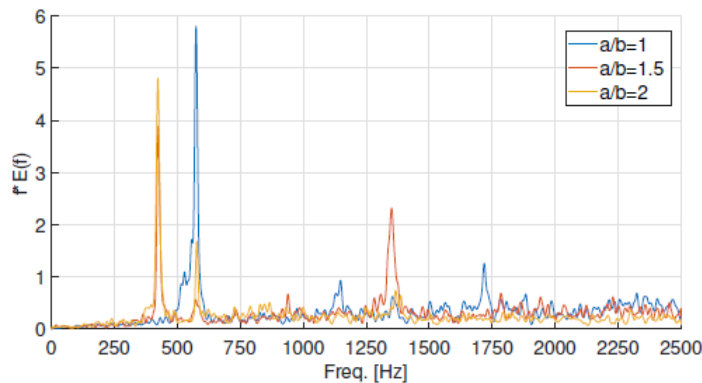


Figure 2.54: PSD of reflected shock oscillations for different a/b and CCF boundaries (Allerhand, 2020)

Effect of boundary conditions

- CCCC and CCF showed similar mean and dynamic deflections. The latter is surprising because CCCC is expected to be stiffer and thus have lesser dynamic deflection (represented by standard deviation).
- For $a/b=1.5$, both mean interaction length and separation area were greater for CCCC than CCF. However, the two cannot be linked as seen earlier when $a/b=2$ had the same interaction length but greater separation area than $a/b=1.5$.
- For $a/b=1.5$, amplitude of oscillation of reflected shock foot position was unaffected by the boundary conditions, but the dominant mode frequency for CCCC was found to be 577 Hz, the frequency of lower Mach block vibrations.
- For $a/b=1$, the maximum standard deviation of the panel displacement is greater by almost one panel thickness in case of CCCC compared to CCF. The opposite was observed in the case of $a/b=1.5$.

2.5. Motivation for Current Study

From the literature survey, multiple open questions and research gaps regarding shock-induced panel flutter were identified. There still exists a disagreement between numerical and experimental studies over the potential of flexible fluttering panels to control shock-induced separation, while the separation zone size has been shown to be a function of the inviscid shock impingement location over statically deformed (flutter-free) flexible panels. However, to the author's knowledge, there is no in-depth study of the effect that shock impingement location has on the SWBLI over fluttering panels, and consequently, over the flutter behaviour itself due to the FSI. This could help answer the question whether an optimum inviscid shock impingement location exists over a fluttering panel for which the separation zone is minimized, or better, lesser in size compared to an SWBLI over a rigid plate.

The study of Allerhand (2020) proved shock-induced panel flutter to be a repeatable phenomenon when simulated in the ST-15 supersonic wind tunnel facility at TU Delft, the same facility in which the current study is conducted. In addition, the study also validated the reliability of DIC to produce reasonably accurate and well-resolved measurements of the unsteady panel motion, paving the way for its continued usage for future studies. However, Allerhand (2020) highlighted some challenges and limitations involved with conducting high-speed FSI investigations in ST-15, especially the problem of vibrations in the test section that appeared to influence the flutter frequency of the flexible panels under certain conditions. A deeper investigation into these vibrations is necessary to possibly eliminate the same for future studies of FSI in the facility.

The research questions that were presented in section 1.3 were formulated based on the aforementioned observations from the literature study.

3

Measurements & Processing

In this chapter, prerequisite knowledge about the whole process of extracting meaningful results from raw measurements will be discussed. This includes the underlying physical principles of the measurement techniques employed in each experimental campaign, practical aspects of conducting the experiments, description of the experimental setup and arrangements, theory behind processing and post-processing techniques that extract quantities of interest from the measured data. This knowledge is imperative to provide context for judging the validity and limitations of the obtained results to answer the research questions that were posed earlier, and will help explain the choices made in the methodology for conducting this study.

Section 3.1 discusses the primary device used to experimentally simulate high-speed flows: a supersonic wind tunnel, including specifications of the ST-15 facility at TU Delft. Next, in section 3.2, the principle of oblique shock generation as used in ST-15 and a description of the panels used for recreating flutter are provided. Three separate experimental campaigns were conducted. The first campaign was aimed at studying wind tunnel vibrations and attempt to relate them to temperature change in the tunnel, using simultaneous use of thermocouples and accelerometers around parts of the test section, relevant information is discussed in section 3.3. The next campaign was focused on capturing the behaviour of the SWBLI using Schlieren imaging, details on which are discussed in section 3.4. The final campaign employed Digital Image Correlation (DIC) to measure the flutter behaviour of the flexible panel, and the system description is provide in section 3.5. The particular values of important flow parameters relevant for the study are listed in section 3.6. A short survey of measurement repeatability for both Schlieren and DIC is done in section 3.7, followed by a brief uncertainty analysis in section 3.8.

3.1. Supersonic Wind Tunnel

As panel flutter only occurs in the presence of supersonic flow, naturally, a wind tunnel that operates in the supersonic regime is desired to carry out the current study. In this section, the general principle of operation of supersonic wind tunnels will be discussed followed by a description of the ST-15 supersonic wind tunnel facility at TU Delft that has been employed for performing the experimental simulations for this study.

3.1.1. Principle of operation

In general, supersonic wind tunnels are part of the broader category of high-speed wind tunnels, which, by definition, operate in the compressible flow regime. As a rule of thumb, the onset of compressibility effects occurs when the flow Mach number crosses 0.3, with Mach number $M = U/a$ where U is the mean flow speed while a is the speed of sound in the particular medium, but usually high-speed wind tunnels operate at higher Mach numbers. High-speed wind tunnels also consist of transonic ($M > 0.8$ & $M < 1$) and hypersonic ($M > 5$) types, but the rest of the discussion will be focused on supersonic wind tunnels ($M > 1$ & $M < 5$) and all the principles discussed hereafter also apply to the aforementioned types. Unlike low-speed wind tunnels which can operate continuously driven by a fan, supersonic wind tunnels are usually constructed to operate in an intermittent manner due to the practical aspects of build-

ing fans large enough to drive flows at such high speeds. Intermittent type supersonic wind tunnels can also be of two types: blowdown type, where stored compressed air is discharged to the atmosphere, or indraft type, where the discharge occurs into a vacuum vessel (Pope and Goin, 1965). In either case, it is the resulting pressure differential created across the storage vessel and atmosphere/vacuum vessel that drives flow through the tunnel.

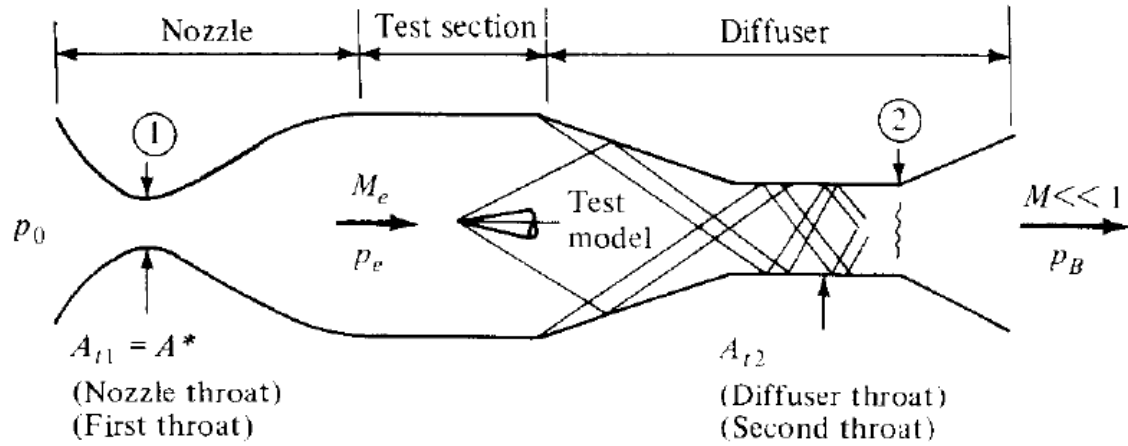


Figure 3.1: General structure of a supersonic wind tunnel (Anderson Jr, 2010)

The general construction of blowdown-type supersonic wind tunnels is shown in Figure 3.1. The stagnant flow in the storage vessel at pressure p_0 accelerates in the converging-diverging nozzle to the required speed in the test section, where the test object is placed, and eventually gets decelerated through the converging-diverging diffuser and discharged to the atmosphere. The shape of the converging-diverging nozzle determines the Mach number achieved at the test section, governed by the area - Mach number relation (Anderson Jr, 2010):

$$\left(\frac{A}{A^*}\right)^2 = \frac{1}{M^2} \left[\frac{2}{\gamma + 1} \left(1 + \frac{\gamma - 1}{2} M^2 \right) \right]^{(\gamma + 1)/(\gamma - 1)} \quad (3.1)$$

Equation 3.1 is derived from isentropic flow relations, where A and M represent local area and Mach numbers at any cross-section while A^* represents the sonic ($M = 1$) throat area (location 1 in Figure 3.1) and γ is the isentropic expansion factor. Mathematically, Equation 3.1 has two solutions: subsonic and supersonic, and there exists a minimum ratio of pressures in the storage vessel and nozzle outlet (just after test section), p_0/p_e , that produces supersonic flow in the test section. Without the diffuser, the nozzle would simply discharge at p_B . If p_B equals atmospheric pressure, then the required stagnation pressure to drive the tunnel would be very high. For this purpose, a diffuser is used to decelerate the supersonic flow gradually and discharge to the atmosphere, such that the pressure at the nozzle exit and entrance of the diffuser, p_e , is much lower than atmospheric pressure at diffuser outlet, p_B , and consequently the pressure storage vessel can be lowered to achieve the required pressure ratio for driving the tunnel, leading to savings in costs and lower operating pressures.

The relation between the two throat areas of a supersonic wind tunnel can be expressed in terms of the respective total pressures as (Anderson Jr, 2010):

$$\frac{A_{t,2}}{A_{t,1}} = \frac{p_{0,1}}{p_{0,2}} \quad (3.2)$$

In ideal isentropic flow, there would be no loss in total pressures across the tunnel, and thus nozzle and diffuser throat areas would be equal. However, shocks occur at the test model and even the entrance of the diffuser which causes a loss in total pressure and increase in entropy. Moreover, the presence of boundary layers is also a source of loss in total pressure and as a result $p_{0,1} > p_{0,2}$, which

means $A_{t,2} > A_{t,1}$, or, the diffuser throat area must be greater than the nozzle throat area to conserve mass flow throughout the tunnel. If this is not the case, a normal shock forms at the end of the nozzle and the tunnel "unstart" occurs, since the same amount of mass flow cannot be sustained at the diffuser throat. This problem of unstart can also occur if the cross-section of the model in the test section is too large and thus must be taken into account.

3.1.2. ST-15

For this purpose, the ST-15 supersonic wind tunnel at the High-Speed Lab (HSL) of the Delft University of Technology is utilized to simulate the flow conditions required. The ST-15 is a blowdown type of supersonic wind tunnel, i.e., supersonic flow in the test section is created by releasing pressurized air stored in a reservoir through a converging-diverging nozzle of specified geometry. The 300 m³ reservoir can store dry air at up to 40 bar of pressure. The total pressure of the flow in the test section can be varied from 2.0 bar till 4.8 bar. The nozzle is built up of two symmetric pieces (called Mach blocks), each installed in the upper and lower sides of the wind tunnel to create a rectangular cross-section converging-diverging profile. The Mach number of flow at the test section can be varied by using different sets of Mach blocks that create different converging-diverging profiles: with this, Mach numbers of 1.5, 2.0, 2.5 and 3.0 can be achieved. For the current work, a freestream Mach number $M_\infty = 2.0$ at a total pressure $p_0 = 2.5$ bar is desired to match the conditions in the study of [Allerhand \(2020\)](#). The achievable test conditions and other properties of the ST-15 are listed in [Table 3.1](#).

In [Figure 3.2](#), the streamwise cross-section of the ST-15 can be seen along with an indication of the flow direction with an arrow (left to right). The settling chamber, indicated by the number 1, is where the incoming flow from the pressure vessel stabilizes and hence stagnation conditions may be assumed. Thus, total pressure and total temperature are measured in the settling chamber itself, following which is a series of wire mesh to impede freestream turbulence. The Mach blocks can be seen on either side of stations 2 and 3, revealing the converging-diverging contour required to accelerate incoming subsonic flow to supersonic speeds. Station 2 indicates the throat of the converging-diverging nozzle, where flow becomes sonic, while station 3 is the test section where the desired flow Mach number is achieved and where the model is placed. Finally, station 4 indicates the throat of the converging-diverging diffuser which is used to decelerate the supersonic flow and also to allow lower pressure in the reservoir by getting the air to exit the test section at a pressure lower than atmospheric pressure at the diffuser outlet, as discussed earlier.

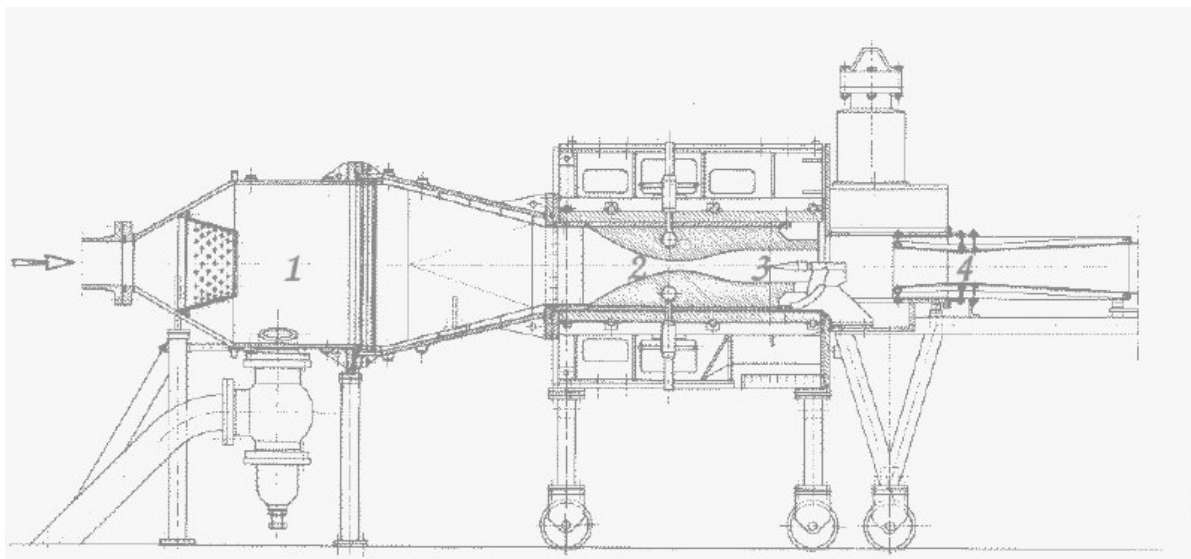


Figure 3.2: Schematic of the ST-15 supersonic wind tunnel at TU Delft ([Sun, 2014](#))

Property	Values
Freestream Mach number, M_∞	1.5, 2.0, 2.5, 3.0
Total pressure, p_0	2.0 - 4.8 bar (for $M_\infty=2.0$)
Total runtime with full reservoir	18 minutes
Test section size (l × w × h)	25 cm × 15 cm × 15 cm

Table 3.1: Properties and achievable test conditions in ST-15

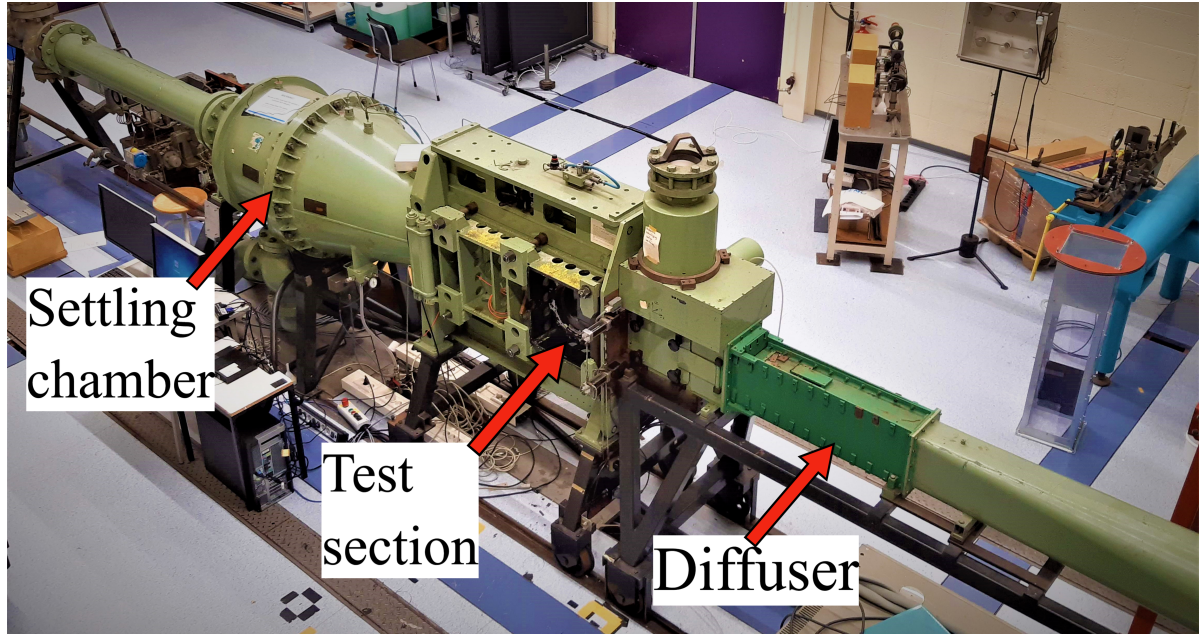


Figure 3.3: Photograph showing the ST15 with different parts labelled

3.2. Test Section Setup

The test section downstream of the converging-diverging nozzle has the dimensions 25 cm × 15 cm × 15 cm in terms of length, width and height, respectively. It has two 250 mm diameter windows on either side to allow optical access for non-intrusive measurement techniques like Schlieren, PIV, DIC. While the Mach blocks are fixed to achieve a particular freestream Mach number, there is provision in the lower Mach block (LMB) to attach a test model which is the panel insert in this case, described in 3.2.2.

3.2.1. Shock Generation

To produce oblique shock waves in the test section, wedge-like ramps of different angles can be mounted on the upper Mach block. The wedge has a sharp leading edge to avoid the formation of detached shocks upstream of it. The shock angle, β can be related to the freestream Mach number, M , and the ramp angle, θ , using the analytical $\theta - \beta - M$ equation (Anderson Jr, 2010):

$$\tan \theta = 2 \cot \beta \frac{M^2 \sin^2 \beta - 1}{M^2(\gamma + \cos 2\beta) + 2} \quad (3.3)$$

$\gamma = 1.4$ usually serves as a good estimate for air. With Equation 3.3, the shock angle can be determined for a given ramp angle and freestream Mach number, and thus the wedge may be positioned with respect to the panel so as to achieve a desired shock impingement location in the streamwise direction. The ramp (also called the shock generator) is attached to the upper Mach block via a pair of guide rails that have long slots. While the shock generator remains fixed with respect to the rails, the latter can be moved in the streamwise direction, thus allowing access to a continuous range of shock impingement locations along the panel length. Since the current study required different shock impingement locations, the horizontal position of the shock generator with respect to the fixed panel for

was calculated for each run based on the shock angle β and the height of the shock generator leading edge from the upper face of the panel, so as to produce the desired inviscid shock impingement location (indicated by x_i in Figure 3.4). For the current work, shock generators with $\theta=12^\circ$ and 15° were chosen to study the effect of shock strength.

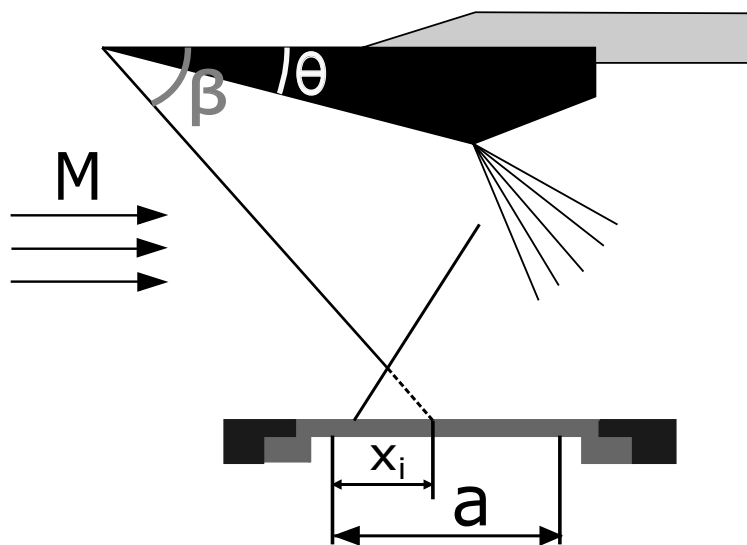


Figure 3.4: Representation of the flow in the test section with a shock generator of ramp angle θ installed, resulting in an oblique shock wave of angle β impinging at location x_i from the leading edge of the panel

3.2.2. Panels

To ensure that panel flutter was observed under the limitations of the wind tunnel operation, numerous design choices had to be made regarding the parameters of the panels: thickness h , length-to-width ratio a/b , material and boundary conditions. Important to note, the design was NOT part of the current work, but was done earlier by [Allerhand \(2020\)](#). For providing some background on the same, some of the important considerations as described in the aforementioned work are briefly discussed here.

- The panel was designed such that flutter occurred at the lowest dynamic pressure possible so as not to run the tunnel near the limits of its operational capability. This translated into the panels having a low h and a high a/b . Concerning the latter, b was limited by the span of the test section, and a was chosen accordingly. For each a/b , panels with clamped leading and trailing edges and free side edges (CCFF) and panels with all edges clamped (CCCC) were manufactured.
- To make sure each panel was able to endure multiple runs without failure, h was fixed at 0.3 mm. Previous experiments had shown that while panels with $h = 0.2$ mm fluttered at a lower dynamic pressure, but encountered structural failure relatively early in terms of number of runs, while thicker panels would require higher dynamic pressure, going against the objective of the previous point.
- It was desired to minimize spanwise variations so as to achieve two-dimensional flutter, which could prove useful for validation of subsequent numerical studies on the same phenomenon.
- While high flexibility of the panels was required to simulate flutter, high yield strength was also necessary to prevent fatigue failure. Thus, Aluminium 7075-T6 was chosen as the material for the panels which showed a good balance of both the aforementioned qualities.

From the investigation of [Allerhand \(2020\)](#), it was concluded that out of all the panels tested, the CCFF panel with $a/b = 1.5$ came closest to exhibiting two-dimensional flutter behaviour. However, the other panel configuration with fully clamped edges and the same aspect ratio (henceforth labelled as CCCC1.5) was not studied in detail. Because of that, and since thin panels with fully clamped edges are more common in applications such as forming the bodies of lightweight high-speed aerial vehicles, the current study aims to focus completely on the flutter of CCCC1.5 panels. [Figure 3.5](#) shows a

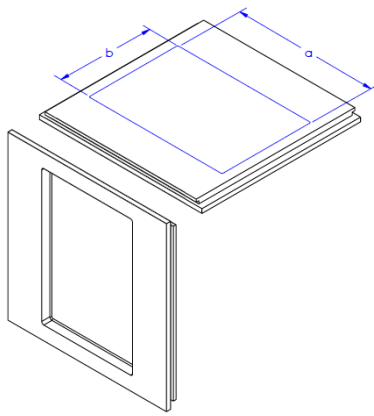


Figure 3.5: Schematic of the designed panel insert, blue lines showing the actual flexible panel cutout (Allerhand, 2020)

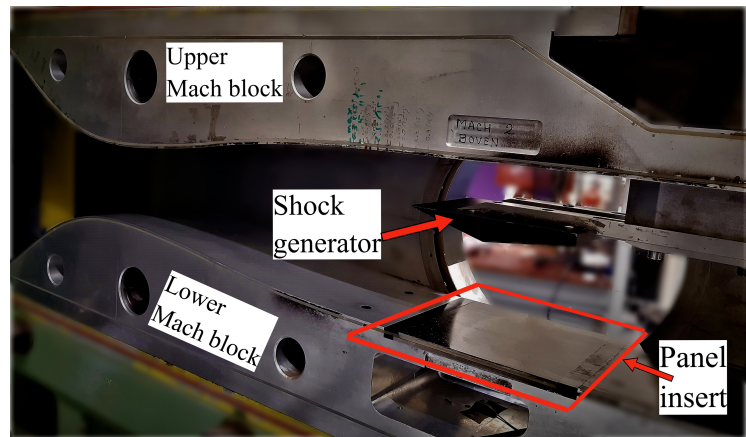


Figure 3.6: Photo of ST-15 showing Mach blocks, shock generator and panel insert

schematic of the panel inserts designed by Allerhand (2020) compatible with the test section of ST-15, where only the area $a \times b$ is the flexible region (0.3mm thick) such that the edge with dimension a is along the streamwise direction of the tunnel. There is also a cavity below the panel that is open at its downstream end and also open to downstream of the test section. The entire test section with the shock generator and panel insert is shown in Figure 3.6. For the interested reader, a more detailed description of the design process of the panels can be found in Allerhand (2020).

3.3. Thermocouples and Accelerometers

Thermal transience is often sidelined when experimentally studying panel flutter, despite the fact that temperature takes longer to stabilize than pressure during wind tunnel startup. Ideally, a non-intrusive method like Infrared Thermography (IRT) would have been used to obtain full-field time-resolved temperature fields over the panel, but practical constraints related to size and geometry of the wind tunnel and special Germanium window (to allow usage of IRT cameras) and the optical properties of the available IR camera made it unfeasible to view the entire panel. Thus, it was decided to obtain temperature measurements around key locations to quantify the thermal transience associated with operating high-speed wind tunnels. Additionally, wind tunnel vibrations could potentially be a source of problems when studying fluid-structure interaction, especially if the unsteady interaction begins to be driven by the vibrations. To measure these vibrations in and around the test section, accelerometers were chosen due to their small size, resulting in easy accessibility, and high accuracy and ruggedness. In this section, the basic principle of operation of both accelerometers and thermocouples will be discussed, followed by a description of the actual arrangement in ST-15.

3.3.1. Principle of operation: Thermocouples

Thermocouples work based upon the Seebeck effect: when two junctions of a closed loop formed with dissimilar metals are kept at different temperatures, a voltage is induced in the loop. The two junctions are called the hot junction, where the temperature is to be measured, and the cold junction, which is maintained at a reference temperature. Before the advent of digital devices, it was common to keep an ice bath as the cold junction (0°C), but that has since been replaced with a digital cold-junction compensator (CJC) that has a known voltage response to temperature. The K-type thermocouple, which is a commonly used type using Chromel (Ni-Cr) and Aluminel (Ni-Al) as the dissimilar conductors and operating in a wide temperature range (-270°C to 1260°C), is used for the current study as its calibration is also easily available.

3.3.2. Principle of operation: Accelerometers

These are devices that utilise the piezoelectric effect, by virtue of which mechanical stress produces an electrical charge in specific materials, to measure acceleration of a vibrating object. The voltage produced by such a piezoelectric material under mechanical stress is proportional to the thickness

Device	Model	Range	Sensitivity	Connection to PC via
Accelerometer	PCB 352A24	0.4 - 12 kHz	10.2 mV/(m/s ²)	NI9234 module
Thermocouple	K-type	-200 - +1300°C	41μV/°C	NI9214 module

Table 3.2: Accelerometer and Thermocouple specifications

of the object on which stress is applied and the value of mechanical pressure itself. As shown in Figure 3.7a, the voltage E measured across the piezoelectric object of thickness t would be $E = \nu t p_x$, where ν is called the voltage sensitivity while p_x is the mechanical pressure. The schematic of a typical accelerometer based on this principle is shown in Figure 3.7b, where a spring-mass combination is installed against piezoelectric crystals. The accelerometer is usually stuck to an object, and the vibration of said object causes the mass to accelerate with respect to the crystal. This results in a change in the stress (which is proportional to force) exerted by the mass on the crystal, and leads to a voltage output from the accelerometer that is proportional to the acceleration of the object.

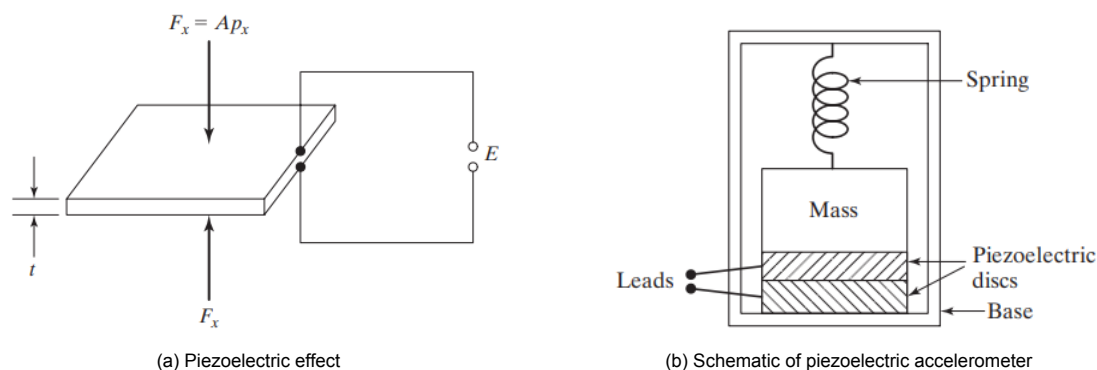


Figure 3.7: From Rao and Yap (2010)

3.3.3. Experimental Setup

The accelerometer and thermocouple arrangement is shown in Figure 3.8. Four regions are marked with purple dots in the test section drawing: Upper Mach block (UMB) top, UMB side, Lower Mach block (LMB) cavity and LMB side. In each of these, one thermocouple and one accelerometer were attached, as shown in the pictures. Additionally, one accelerometer was mounted on the wind tunnel frame instead of the Mach blocks to test whether any Mach block vibrations were "leaking" to the outer structure of the wind tunnel, and one accelerometer was also attached to the top of the shock generator when it was in use. To study the wind tunnel vibrations and thermal loading in isolation from the fluid-structure interaction, a 9 mm thick rigid panel (RP) was used in the test section. Using a rigid plate instead of a flexible one ensured that the vibrations could be observed in isolation without any effects of flutter. Its bottom side (exposed to the LMB cavity rather than flow) was mounted with 9 thermocouples in a 3×3 configuration over the available area, to check if the thermal loading created by the SWBLI could be explicitly captured by looking at the difference in temperature values in both streamwise and spanwise directions. Also, two accelerometers were attached at approximately $x/a=0.25$ and $x/a=0.75$ from the LE of the panel at the midspan location. For fixing the accelerometers, a special wax was sufficient while the thermocouples were stuck using a combination of the same wax and insulating tape to cover the exposed junction. See Table 3.2 for technical specifications of the accelerometers and thermocouples used. Thermocouple measurements were recorded at 50 Hz while accelerometers were used at 8533.33 Hz for a relatively long recording time of ≈ 10 seconds to minimize measurement uncertainty. The acceleration data was then processed using Welch's method (see section 3.5.6) with 8 windows and 50% window overlap to extract the characteristic frequencies from the time-series data.

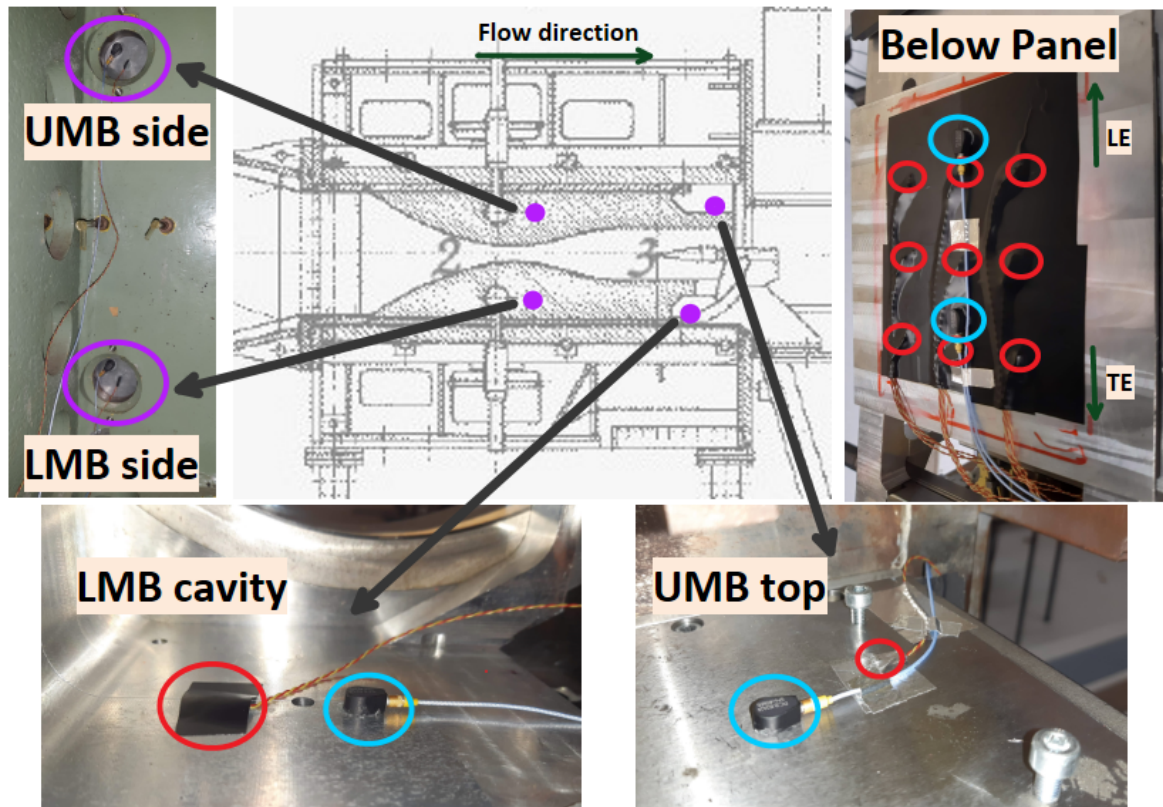


Figure 3.8: Accelerometer (circled in blue) and thermocouple (circled in red) setup around the test section

3.4. Schlieren

Schlieren is a powerful technique for non-intrusive visualization of supersonic flow structures like shocks and expansion waves. It is fast and relatively simple to setup, compared to techniques like PIV and PTV. The only major drawback is that in its most basic form it can only provide qualitative information related to the location of shocks and expansion waves, and no velocity or pressure information like the aforementioned complex techniques. However, Schlieren is sufficient for determining the unsteady behaviour and size of the separation region of an SWBLI. The main quantities of interest that can be extracted from Schlieren images are locations of the impinging shock and separation shock feet, through which the interaction length of the SWBLI can be calculated. If recorded using high-speed cameras, the time-resolved shock foot locations can also give an idea of the spectral content associated with the unsteadiness of the SWBLI. thus fulfilling the basic requirements of flow visualization and Schlieren is therefore deemed sufficient for capturing the flow features in the current study.

3.4.1. Principle

The fundamental underpinning of the Schlieren imaging technique begins with the phenomenon of refraction: how an electromagnetic wave (like visible light) changes its direction of propagation when it encounters a medium with a different density. The optical density is quantitatively characterized by the refractive index, $n = c_0/c$, where c_0 is the speed of light in vacuum while c is the speed of light in the medium. $n \geq 1$ since light travels fastest in vacuum. The deflection of a light ray in the presence of gradient of refractive density is expressed using the ray equation:

$$\frac{\partial}{\partial s} \left(n \frac{\partial x}{\partial s} \right) = \nabla n \quad (3.4)$$

This is illustrated in Figure 3.9, where it is shown how the light path ds deflects towards ∇n . AB and A'B' are the wavefronts to which the instantaneous direction of light propagation is perpendicular. This becomes useful for visualizing compressible flows because the refractive index of a medium is related

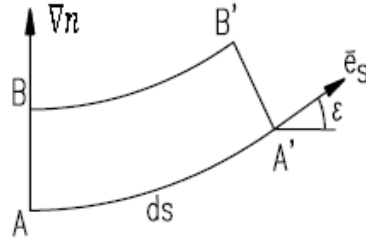


Figure 3.9: Deflection of a light ray in the presence of gradient of refractive index

to its physical density by means of the Gladstone-Dale equation:

$$n = \frac{c_0}{c} = 1 + K\rho \quad (3.5)$$

where K is the Gladstone-Dale constant, equal to $2.25 \text{ m}^3/\text{kg}$ for air. Since there is a linear dependence of n on the local density ρ , the ray deflection can now be expressed in terms of the density gradient. For visualising compressible flow features through a wind tunnel test section, some simple assumptions can be made:

- Assume n to be unity ($n_{air} = 1.000273$)
- Assume small ray deflections such that $ds \approx dz$, z being the spanwise direction of the wind tunnel with total span of the test section W in which any deflections would occur

Using these assumptions and the Gladstone-Dale equation to simplify Figure 3.9, we get:

$$\varepsilon_x = \frac{\partial x}{\partial z} = \int_0^W \frac{\partial n}{\partial x} dz = K \int_0^W \frac{\partial \rho}{\partial x} dz \quad (3.6)$$

Thus, the light deflection in the streamwise direction (x) is directly related to the spanwise integral of the gradient of density in the same direction. The same process can be applied to calculate deflections in the y direction (perpendicular to both streamwise and spanwise direction), ε_y , which can be related to density gradients in the same direction. To get directional sense of the density gradient, a knife-edge filter is placed at the focal length between the focusing lens and the sensor to block part of the incoming light from the wind tunnel to the camera/sensor. The working of a knife-edge filter is illustrated in Figure 3.12. The filter is placed such that downward deflections ($\varepsilon_y < 0$) would be blocked out. Thus, the resulting image would be darker in places where the density gradient is directed downwards, and will be brighter where the opposite is true. If the knife-edge filter as shown above is rotated by 90° , then the Schlieren images will be sensitive to gradients in the x direction. At this point, it is important to realise that Schlieren images are sensitive to the gradient of density, rather than the value of density itself. Thus, regions with constant density will be reproduced as constant intensity regions in the image, only if a density gradient exists will the intensity in the image change. Finally, the change in light intensity due to deflection and the presence of the knife-edge can be expressed as:

$$\frac{\Delta I}{I_0} = \frac{d}{a} = \frac{f \cdot \varepsilon}{a} \quad (3.7)$$

where I_0 is the intensity of light with no deflection, d is the amount of deflection, a is the height/length of the light ray above the knife-edge in $\varepsilon = 0$ condition, and f is the focal length of the lens focusing light on the sensor.

3.4.2. Z-type Schlieren setup in ST-15

There is already a Z-type Schlieren system in place in ST-15, as Schlieren investigations are common in the high-speed tunnel. It consists of a light source, lenses to collimate and converge the light, and pairs of plane and parabolic mirrors to send light through the test section as the source and sensor are placed on either side of the tunnel (see Figure 3.11 for a detailed schematic). In addition, there

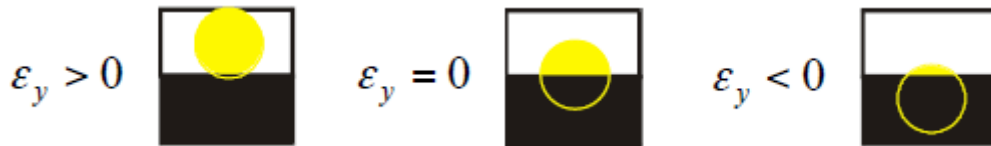


Figure 3.10: Light deflection at the knife-edge filter of a Schlieren system

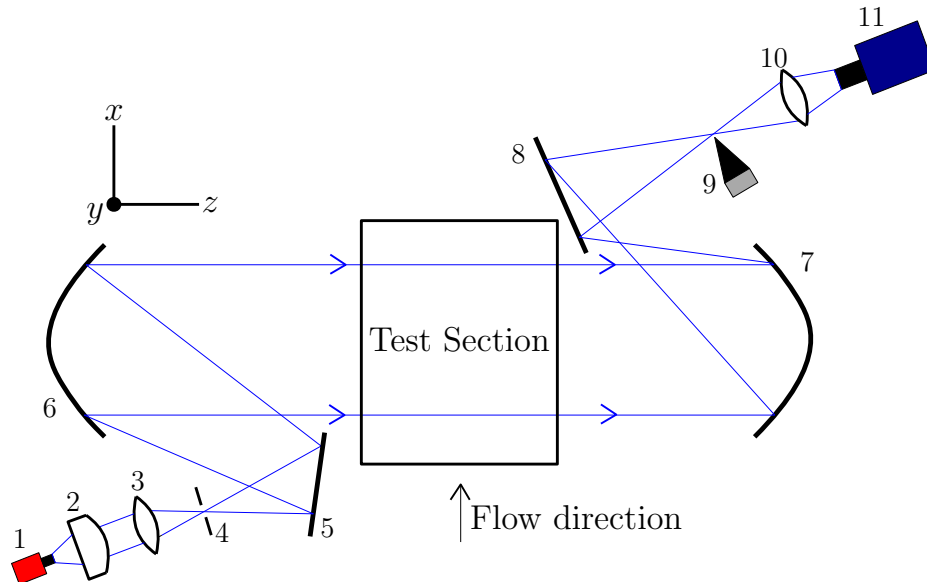


Figure 3.11: Z-type Schlieren system description: 1. Light source 2. Collimating lens 3. Converging lens 4. Pinhole 5. Plane mirror 6. & 7. Parabolic mirrors 8. Plane mirror 9. Knife-edge 10. Converging lens 11. Sensor

is a pinhole on the source side to control the intensity of the collimated light beam, and of course, a knife-edge filter on the sensor side. All components except for the mirrors can be replaced to achieve the desired field-of-view (FOV). The knife-edge is set vertical (as shown in Figure 3.10) such that it is sensitive to density gradients in the streamwise direction. As the light bending towards the streamwise direction is blocked, shocks appear dark and expansion waves appear bright in the resulting Schlieren images. A high-speed camera is advisable as the sensor to resolve the anticipated high-frequency unsteadiness of the separation shock. For the current study, a LaVision ProHS camera was used to record images at a resolution of 1488×1132 pixels and a rate of 2800 Hz, which was the maximum available rate for the given sensor resolution. As per the Nyquist theorem, the rate was sufficient to resolve up to spectral content up to 1400 Hz, which would easily contain any characteristic behaviour at 1200 Hz, the second-most energetic frequency identified by [Allerhand \(2020\)](#) in the shock-induced flutter of CCCC1.5 panels. The lens was exposed for a duration of $9 \mu\text{s}$, long enough to get good image contrast but also short enough to "freeze" the flow structures in time. For each run, 4400-5000 frames were recorded, resulting in a recording time of more than 1.5 seconds. Together with the final converging lens of $f=150\text{mm}$, the FOV achieved was sufficient to capture beyond the entire length of the panel. Details of all components of the Schlieren setup are listed in [Table 3.3](#).

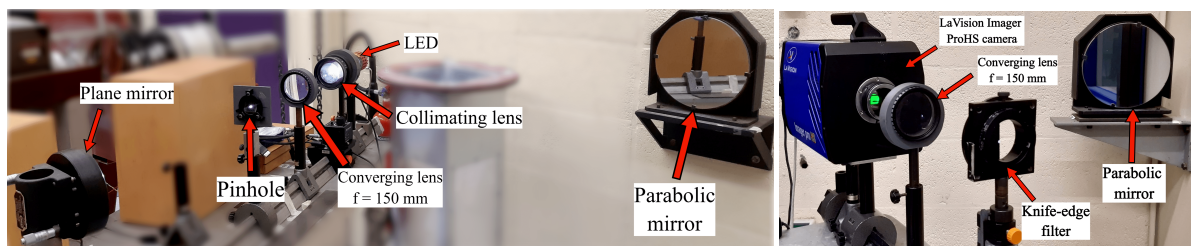


Figure 3.12: Pictures of the Z-type Schlieren setup in ST-15

Label	Item	Description
1	Light source	Thorlabs MCWHL P1 White LED
2	Collimating lens	F2.5 f = 178 mm
3	Converging lens	f = 150 mm
10	Converging lens	f = 150 mm
11	Sensor	LaVision Imager ProHS camera

Table 3.3: Schlieren equipment used (see Figure 3.11)

LaVision Imager ProHS	
Resolution (full)	2016 × 2016 px
Resolution (used)	1488 × 1132 px
Pixel size	11 μm × 11 μm
Acquisition rate (used)	2800 Hz
Exposure	9 μs
Magnification factor	0.08
Spatial resolution	7.28 px/mm

Table 3.4: Schlieren camera technical details

3.4.3. Shock Detection Methodology

The settings used on the Schlieren setup, as mentioned earlier, resulted in images with high-contrast such that shock waves (dark) and expansion waves (white) were clearly visible against the gray background. Thus, any pre-processing of the images was deemed unnecessary. The main objectives of processing the Schlieren images were:

- Detect impinging and separation shocks
- Locate the shock foots at a reference height to calculate the interaction length of the SWBLI
- Verify the inviscid impinging shock location with respect to panel leading edge, which was calculated geometrically using oblique shock relations before running the tunnel

Since the images were recorded using a digital camera, they could essentially be treated as a matrix with each element containing the gray value of the intensity at the corresponding pixel. This made it simple to process the images in MATLAB. First, the panel was located in the images. This was done by placing a marker (a bolt) at the streamwise ends of the panel insert and taking Schlieren images. Next, the leading edge and trailing edge of the flexible panel were located from the ends of the panel insert since the physical dimensions were already known. An intermediary step was to calculate the magnification factor to find the spatial resolution in order to convert the dimensions in pixels to physical dimensions (mm). This was done using the measured length of shock generator, which was simply compared with the length measured in pixels in the images.

Next, because of the objectives of the study, it was required to move the shock generator to generate different impinging shock locations, which meant the shocks were in different places with respect to the camera for each run. Moreover, the flutter of the panel resulted in substantial movement of the separation shock between different frames compared to the steady impinging shock. For these reasons, two steps were taken: first, an average image of the first 200 images was calculated so that the extents of variation of the separation shock could be estimated, and second, 4 points each for the impinging and separation shocks were manually selected on the basis of the average image to mark the regions in which the shock edges would be detected for all frames of the particular set. This is illustrated in Figure 3.13, where the marked regions for detecting the impinging and separation shocks are shown in dashed lines in red and cyan, respectively. Since the impinging shock is steady, the red region only contains the upstream edge of the shock, while the cyan region contains both edges of the separation shock. Also, the panel location is indicated in the same image, marked by LE and TE to represent

the leading and trailing edges, with stations at every 20% of the panel length in between also marked. The top edge of the panel insert is also marked (in white dashed line) as the shock foot reference height.

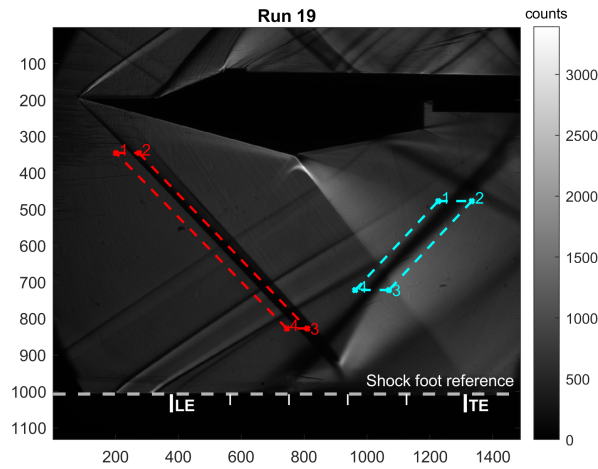


Figure 3.13: Average Schlieren image and definition of shock detection regions for impinging shock (red) and separation shock (cyan)

Shock edges are detected using streamwise gradients of intensity in the marked regions. First, the marked regions are split into a number of equally spaced vertical stations (100 for impinging shock, 300 for separation shock), and the horizontal gradients in intensity are calculated within the horizontal bounds of the respective region corresponding to the vertical height. For the impinging shock, the point of least gradient at each vertical station is chosen as the (upstream) shock edge, while for the separation shock, the point of maximum gradient is picked as the (downstream) shock edge. This choice is an arbitrary convention, as the Schlieren provides a spanwise averaged view of the shock. The important thing is to remain consistent with the convention for all cases to make valid comparisons later. Once the shock edges are known at all vertical stations, a polynomial fit using the least-squares method of order 1 (a straight line) is calculated through the points to represent the complete shock edge. The best-fit lines representing the shock edges can subsequently be extended upto the shock foot reference to calculate the horizontal location of the respective shock feet.

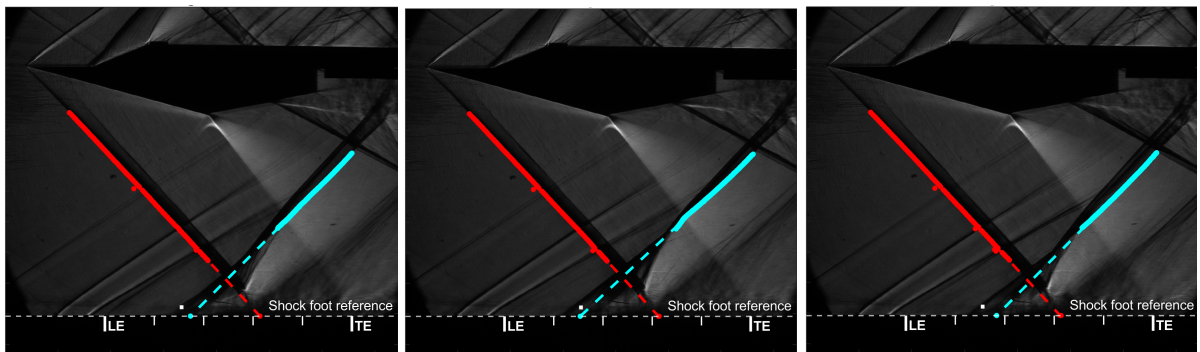


Figure 3.14: Detected shock edges and shock feet from instantaneous Schlieren images

Figure 3.14 shows three consecutive instantaneous frames with the detected shock edges marked and the best fit line (in dashed) extended upto the shock foot reference, with the shock feet marked with points as well. First observation, a couple of points of the detected impinging shock edge (red) seem to be incorrect, this is because of scratches in the Schlieren windows that cause dark regions in the images. However, since 100 points are taken to calculate the best fit line of the impinging shock, such errors become insignificant. The location of the impinging shock foot seems very steady, in comparison to the separation shock foot. Also, the calculated inviscid shock impingement location (in other

words, the impinging shock foot location since the foot reference height is approximately the same as the panel height) for this run (run 19) was at 60% panel length, but from the images it seems a bit downstream of the 60% mark. By calculating from the image, the actual inviscid shock impingement location comes out to be at 62.35%, a relative difference of $\approx 3.4\%$ from the calculated value. Such small differences are to be expected since setting the shock generator in the correct streamwise location was done by hand rather than a more accurate system. The interaction length of the SWBLI is calculated simply as the difference between the two shock feet, and is shown in Figure 3.15. While the change in separation shock foot positions in time can be used to identify the characteristic frequencies of the unsteady SWBLI (using spectral analysis techniques described in 3.5.6), an additional window of 5×5 pixels was also picked manually near the same shock foot (see Figure 3.15), so that the average intensity over the stationary window could be tracked frame by frame and act as another source of information on the unsteady behaviour of the separation shock.

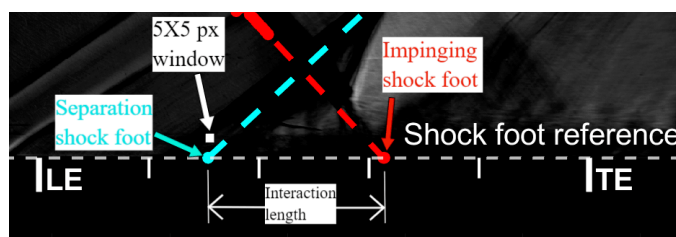


Figure 3.15: Shock feet and definition of interaction length

3.5. Digital Image Correlation

3.5.1. Principle

DIC is an optical measurement technique that is employed to measure displacements of surface marked with optical trackers. Unlike point-based displacement measurement techniques, DIC is non-intrusive and provides full-field information at a desired spatial resolution. For measuring sensitive phenomenon like thin panel flutter, DIC is especially useful since it does not interfere or influence the flutter behaviour directly or indirectly since no part of the equipment comes in physical contact with the model being studied. A typical DIC setup consists of many parts: optical markers on the body of interest, an illumination source to make the markers visible, camera(s) to record image sequences of the motion of the body, and finally processing techniques to extract information such as displacements, strains, velocities, etc. from the recorded image sets by tracking the change in the positions of the markers across consecutive images. Each of these is described in more detail in the following sections.

3.5.2. Optical Markers

In DIC, the goal is to track optical markers through a set of images to determine the deformation. To accurately track the markers, it is crucial to have a high contrast between the markers and the background of the surface. Thus, either the markers should reflect light from the illumination source while the background must absorb the same light, or vice-versa. However, two problems can arise when individual markers are used. First, known as the correspondence problem (Schreier et al., 2009), is that it is practically impossible to track the gray-level intensity values (as captured by the cameras) at the level of a single pixel, since the same gray value can be encountered in many other pixels of the entire image. To resolve this, the typical DIC algorithm relies on tracking the gray values corresponding to a group of markers rather than single pixels. Second, if individual markers are tracked using interrogation windows (representing a single vector) and the displacement of a marker exceeds the respective interrogation window size, then no correlation can be found between the consecutive images. Using smaller markers (called a speckle pattern) and grouping the markers alleviates both problems. As shown by Bebernis et al. (2011), using DIC with speckle patterns leads to a lower noise floor than photogrammetry, which uses individual markers, and thus DIC measurements offer both better spatial resolution and accuracy. Of course, the improvement in accuracy is strongly influenced by the quality of the particular speckle pattern (Reu, 2014b, Roncella et al., 2012), which can be described using the

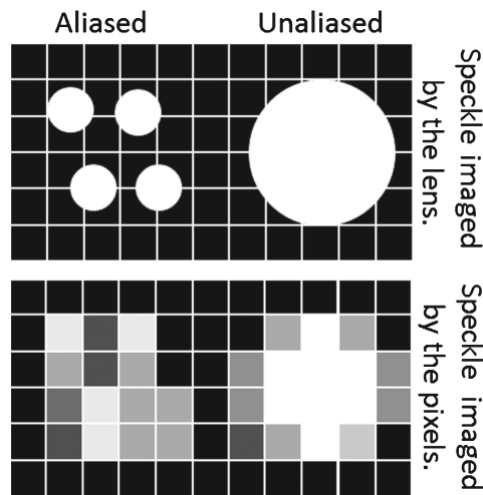


Figure 3.16: The problem of aliasing (Reu, 2014a)

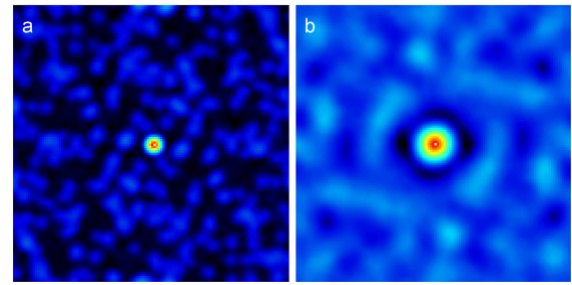


Figure 3.17: Typical correlation function peaks for speckle size of (a) 3 pixels and (b) 8 pixels (Crammond et al., 2013)

following parameters:

Speckle Size

The main challenge associated with determining the size of speckles is avoiding aliasing. If the size of a speckle is equal to or less than one pixel on the camera sensor, then its center cannot be unambiguously determined. In such cases, any sub-pixel motion will not be captured as on the pixel level the speckle would remain in the same position. This is called aliasing or peak locking (see Figure 3.16). It is resolved by ensuring the minimum size of the speckles to be 3 pixels, in which case the center of the speckle can be unambiguously determined. Having larger speckle size also ensures that the speckle pattern is unique, which is important for achieving correlation (Crammond et al., 2013). Another advantage to a larger speckle size is that the correlation function peak is more spread out (see Figure 3.17), meaning that the displacements can be determined to a greater sub-pixel accuracy compared to a more concentrated peak (Crammond et al., 2013). However, there are limits to how large the speckles can be as that also affects other parameters such as speckle density and distribution, thus the optimum size range is 3-5 pixels (Reu, 2014a).

Speckle Density

The number of speckles in each subset (or interrogation window) and the size of speckles determines the speckle density, which influences the accuracy of measurements. As shown in Figure 3.18, the errors in determining the mean tend to reduce when the number of speckles per subset increase and also when the speckle size itself increases (bottom left to top right). These two factors clash for fixed subset sizes, as increasing the speckle size limits the number of speckles that can fit into the subset. In practice, a good rule of thumb is to aim for 50% speckle coverage (ratio of area occupied by speckles to total surface area) to ensure good correlation across the entire surface (Reu, 2015b).

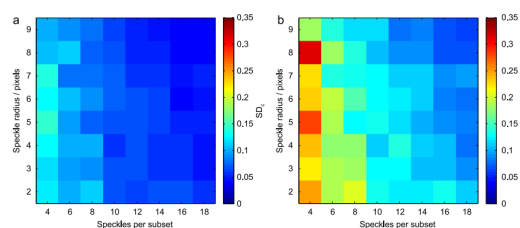


Figure 3.18: Error levels for different speckle patterns at (a) 1% strain and (b) 2% strain (Crammond et al., 2013)

Speckle Shape and Distribution

In general, a speckle pattern must be unique and non-repetitive to minimize errors. For e.g., a bias error may arise due to the repetitive or preferred orientation of a speckle pattern (Schreier et al., 2009).

According to [Crammond et al. \(2013\)](#), the uniqueness resulting from both speckle shape and size leads to reduction in measurement errors.

Image Contrast

When using monochromatic cameras, contrast in case of speckled patterns is simply defined as the difference in intensity counts between speckles and the background. Higher the contrast, lesser the uncertainty in gray value matching procedure. In practice, a contrast of 50-75 counts is considered sufficient for avoiding noise ([Reu, 2015a](#)).

Speckle Edge Sharpness

Having sharply defined speckle edges leads to aliasing in determining the speckle edge in pixels. In short, the gradient of contrast at the speckle edges must be gradual, i.e., the transition from speckle to background must be represented by a higher number of pixels to avoid the bias error produced due to aliasing. In practice, most speckle generation techniques tend to produce softer edges while sharper edges can also be fixed during post-processing ([Reu, 2015c](#)).

3.5.3. Subset Size

In the previous section, it was discussed that increasing both number of speckles per subset and size of the speckles leads to reduction in measurement uncertainties. Of course, if the subset size is fixed, then increasing both will lead to a compromise on other requirements such as contrast and speckle distribution. However, the other option is to increase the size of the subsets used for cross-correlation (see [3.5.6](#)). For the same speckle pattern, larger subsets will automatically have an increased number of markers and thus lesser uncertainties. This is shown by [Pan et al. \(2008\)](#) (see [Figure 3.19](#)), as for different speckle patterns (represented by different coloured lines), a consistent drop in standard deviation of in-plane displacement measurements can be seen when subset sizes are increased. [Marimon Giovannetti \(2017\)](#) also found the same trend with errors, and also observed an increase in computational efficiency with increase in subset size. This is expected, as higher subset sizes corresponds to a lower spatial resolution of the calculated vector field. Thus, a compromise has to be made when deciding between better spatial resolution and reduced measurement errors while choosing the optimum subset size.

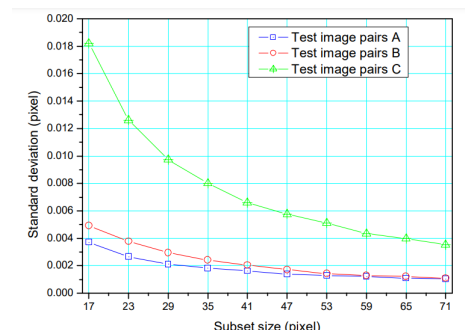


Figure 3.19: Standard deviation of in-plane displacement for different subset sizes ([Pan et al., 2008](#))

3.5.4. Illumination

As described by [Reu \(2013\)](#), an ideal light source for DIC must have the following features: flat and uniform, i.e., it must be diffuse and not produce highlights, and must also provide adequate lighting. The type of paint used to create speckles and background also affects lighting considerations; matte paint is usually preferred to minimize spurious reflections. However, using a very powerful illumination source can also lead to heat waves and heating of the specimen that can produce optical distortions and hence significant errors in measurements. Thus, it is important to optimize the intensity of the light relative to the camera setup so that proper illumination can be achieved, i.e., high contrast and low noise, while avoiding the problems posed by heat waves.

In practice, LEDs are considered to be the ideal source of illumination for DIC, as they provide high amounts of light without incurring the same heat problem compared to other diffuse sources like halogen

lamps (Reu, 2013). Also, lasers are never used as their coherent nature produces laser speckles on surfaces, which interfere with the actual speckle pattern required for DIC (Reu, 2013).

3.5.5. Recording

To perform DIC, it is possible to arrange the cameras in either planar configuration, i.e., where the sensor plane of the camera(s) is parallel to the plane in which displacements are to be measured, or stereographic configuration, where two cameras are set at different angles to the surface of interest and with the proper calibration and geometric reconstruction it becomes possible to extract all three displacement components, including the out-of-plane displacements (Schreier et al., 2009). Since panel flutter is characterized by the out-of-plane panel displacements, it is evident that the stereographic configuration is preferred. Additionally, an angle of 45° between the two cameras in stereographic configuration is deemed best for minimizing uncertainties in the out-of-plane displacement measurements.

As flutter motion of a thin panel is composed of a number of high-frequency periodic oscillations, that depend on the flow conditions and the geometric and structural properties of the panel, it is also desirable to conduct DIC measurements using high-speed cameras. There also exists an interesting trade-off between acquisition frequency, camera resolution, and recording time, as discussed by Bebernis et al. (2011). The camera resolution, which is also dictated by the lens choice and desired field-of-view (FOV), is limited by the desired acquisition frequency, as increasing either leads to sacrificing the other. Moreover, a higher recording time is also preferred to reduce measurement uncertainties, but is limited by the capacity of the storage. Thus, if a higher acquisition frequency is used, it reduces the available recording time for a fixed storage memory. These three parameters have to be optimized to achieve such that the measurements have the correct FOV and are able to resolve up to the required frequencies (dictated by the Nyquist theorem) with enough recorded samples to achieve low uncertainties.

3.5.6. Processing and Evaluation

In this section, the various algorithms that are employed to extract information from recorded images are discussed. These include the cross-correlation function used to calculate the displacement fields in DIC from comparing consecutive frames, Fourier transform and its variant, Welch's method, which are general-purpose functions to extract dominant frequencies from a time-resolved signal, and Proper Orthogonal Decomposition, which is used to separate a spatio-temporal dataset into mutually orthogonal spatial modes and their corresponding time coefficients.

Cross-correlation

Cross-correlation is a statistical technique that is usually used to find displacement vectors from consecutive images of markers in the area of interest. In DIC, the markers are the speckles on a high-contrast background. Displacements in DIC can be processed either relative to one image (to calculate total deformation) or relative to the last image. In either case, the same cross-correlation is used between two images. First, the entire image is divided into subsets or interrogation windows of $M \times N$ pixels, each subset representing a single displacement vector and containing a group of markers. Next, each subset of the second image is displaced by a defined $\vec{d}(m, n)$ with respect to the corresponding subset of the first image, and the product of their intensity fields are calculated:

$$\phi(m, n) = \frac{\sum_{i=1}^I \sum_{j=1}^J [I_1(i, j) - \bar{I}_1] \cdot [I_2(i, j) - \bar{I}_2]}{\sqrt{\sum_{i=1}^I \sum_{j=1}^J [I_1(i, j) - \bar{I}_1]^2} \sqrt{\sum_{i=1}^I \sum_{j=1}^J [I_2(i, j) - \bar{I}_2]^2}} \quad (3.8)$$

where I_1, I_2 are the intensity field of the first and second subsets, and the resulting normalized cross-correlation coefficient, $\phi(m, n)$, is a function of the second subset displacement $\vec{d}(m, n)$, while the denominator is simply a product of the standard deviations of the two intensity fields. Finally, a correlation peak is obtained when $\phi(m, n)$ is plotted as a function of $\vec{d}(m, n)$, as shown in Figure 3.20. The peak represents the most probable displacement of the subset between the two images, and displacement vectors all across the second image with respect to the first are obtained.

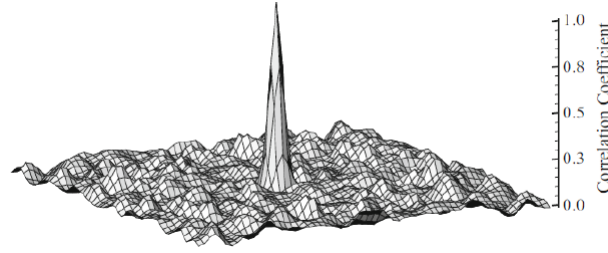


Figure 3.20: A typical correlation map from the cross-correlation operation (Raffel et al., 2018)

Spectral Analysis

Spectral analysis is an important cornerstone of the study of unsteady phenomena, as it helps in determining the dominant characteristic frequencies that make up a specific signal. In the current study, it was crucial to capture the dominant characteristic frequencies from all three experimental campaigns: accelerometer, Schlieren, and DIC. Knowing the characteristic frequencies in each case is required to determine the influence of the wind tunnel vibrations (measured using accelerometers) and characterize the fluid-structure interaction by the unsteady behaviour of the separation shock motion and panel flutter.

The Fourier transform is a popular method to convert a signal from the time domain to the frequency domain, by representing the signal as a sum of sinusoidal waves with respective weighting coefficients, as:

$$X(f) = \int_{-\infty}^{\infty} x(t)e^{-j \cdot 2\pi f \cdot t} dt \quad (3.9)$$

where f is frequency in cycles per unit time, while $x(t)$ is the signal in the time domain. However, use of modern digital computers means the measured signals are also digital in nature, and they can only be represented in a discrete fashion. Thus, for such signals, the Discrete Fourier Transform (DFT) is employed, which is represented mathematically as:

$$X(f) = \sum_{n=1}^N x(n)e^{-j \cdot 2\pi f \cdot n} \quad (3.10)$$

where N is the number of data samples recorded at a constant sampling rate. In case the obtained data is free of noise, then a DFT suffices; however, if there is noise and random effects in the data, which their inevitably is in real-world measurements, then the Power Spectral Density (PSD) needs to be calculated using a periodogram function for a finite sample size (Solomon Jr, 1991):

$$P_{xx}(f) = \frac{1}{N} \left| \sum_{n=1}^N x_w(n)e^{-j \cdot 2\pi f \cdot n} \right|^2 \quad (3.11)$$

where $x_w(n) = w(n)x(n)$ represents the windowed signal using the window function $w(n)$ of the periodogram. Welch's method is another form of the periodogram function, where multiple smaller overlapping windows over the entire finite signal are taken and the average of all the PSDs from the smaller windows is used to represent the spectral content of the entire signal (Solomon Jr, 1991). Mathematically,

$$P_{xx,Welch}(f) = \frac{1}{L} \sum_{l=1}^L P_{xx,l} \quad (3.12)$$

where L is the total number of windows. An interesting trade-off takes place because a smaller number of windows (i.e., a smaller total number of windows) is more effective in suppressing noise but leads to a poorer frequency resolution. Also, increasing the size of overlap between consecutive windows decreases the variance and improves frequency resolution, but only upto a limit.

Throughout this study, Welch's method is employed to convert time-resolved data into spectral space to extract characteristic frequencies. Unless stated otherwise, 8 windows with 50% window overlap are used, and the obtained PSD is normalized with the standard deviation of the signal.

Proper Orthogonal Decomposition

Proper Orthogonal Decomposition (POD) is a popular technique to decompose complex data into its coherent and dominant modes without compromising on time-dependency. It is especially useful for Reduced-order modelling (ROM) of higher-order systems. The main idea behind employing POD for analysis of complex spatio-temporal data (such as displacement field of a fluttering panel or velocity field of an unsteady flow) is to use the Fourier splitting technique to decompose the original data into a linear combination of spatial modes ($\phi(r)$) and time coefficients ($a(t)$) (Cordier, 2008):

$$u(r, t) \approx \sum_{k=1}^K a^k(t) \phi^k(r) \quad (3.13)$$

As $K \rightarrow \infty$, the series approaches the exact solution. However, there is no unique combination of functions that satisfy this. Instead, POD tries to determine modes that are orthonormal to each other, so that each can be investigated separately; this holds true automatically for the time coefficients as well. There are two variations of POD that are popularly used: Singular Value Decomposition (SVD) and the Snapshot-POD (SPOD). A comparison by Arányi et al. (2013) shows that both methods produce similar results, as they both essentially use the same procedure except for a few steps, and the choice between them comes down computational efficiency requirements: if the number of snapshots (measurement points in time), N_t , are significantly less than the number of spatial points of measurement, M , then SPOD is more efficient. In this discussion, only SVD will be described as the conditions of the current study warrant its usage over SPOD.

In SVD, the original data is arranged into a matrix $A \in M \times N_t$ such that each column represents a snapshot in time. Then, the SVD is calculated as:

$$A = U \Sigma V^T \quad (3.14)$$

where $U^k \in M \times M$ and $V^T \in N_t \times N_t$ represent the left and right singular vectors of A while Σ is a diagonal matrix containing the singular values of A arranged in descending order. The spatial modes can now be calculated as:

$$\phi^k = U^k \quad (3.15)$$

while the time coefficients can be written as:

$$a_i^k = \Sigma_k^k \cdot V_i^k \quad (3.16)$$

Also, Σ_k^k is an indication of the energy contribution of the k^{th} mode, thus, the SVD extracts modes in order of the largest contribution to the total energy of the system.

POD is universal in nature since it only requires data that can either come from numerical calculations or experimental measurements irrespective of the phenomenon being modelled or measured, making it a versatile tool. The main purpose of introducing POD in this study is to extract the dominant modes of the panel flutter behaviour. Xie and Xu (2013) numerically modelled a simply supported two-dimensional plate undergoing flutter. After solving the governing equations using the Galerkin method, solutions at certain time steps were used as input to the POD, which produced a ROM of the non-linear flutter. Upon comparison of both solutions, it was found that the ROM generated by the much more efficient POD technique was able to match the expensive Galerkin solution to a high degree of accuracy with fewer number of modes. Moreover, the POD mode shapes were similar to the actual physical modes of the flutter. Xie et al. (2014) extended the study to include different flutter responses: buckled, LCOs, chaotic. In all cases, POD was found to be accurate with much less computational expense compared to the Galerkin approach. For shock-induced panel flutter, Shinde et al. (2019b) employed POD to find dominant spatial modes on a dataset generated by DNS on the Navier-Stokes equations, while Spottswood et al. (2013) extracted POD modes from PSP measurements over the fluttering panel.

3.5.7. Experimental Setup and Pre-Processing

The DIC measurements were conducted separately from the Schlieren, although accelerometers were still attached in the lower Mach block to detect wind tunnel vibrations. For recording, two Photron FAST-CAM SA1.1 cameras were used in a stereographic configuration, which, as discussed earlier, was the proper choice for measuring out-of-plane panel deflections. The cameras were mounted much higher than the panel to create an angle that was as normal as possible to the panel plane. The angle between the cameras was roughly 41° , very close to the optimum angle of 45° as suggested in literature.

The lenses used on the cameras had a focal length of 60mm and provided a wider FOV compared to [Allerhand \(2020\)](#) which used 105 mm lenses. The wider FOV meant that the image had to be cropped to a resolution of 892×512 pixels from its full resolution of 1024×1024 pixels so that only the panel was in view, which lead to a higher achievable acquisition frequency and/or higher recording time (compared to [Allerhand \(2020\)](#)) due to the resultant memory savings. It was decided to keep the acquisition frequency the same as [Allerhand \(2020\)](#) at 5000 Hz as the resolved spectral analysis in that case was sufficient to characterise the flutter motion, but recording time was increased to 1.6 seconds to further reduce uncertainties in the measurements.

The main advantage of conducting DIC separate from another optical technique was that filters on camera lenses to capture light from a particular illumination source were not required anymore. This meant that a great depth-of-field (DOF) could be achieved by increasing the $f_\#$ (which decreases the lens aperture and allows lesser light into the sensor) as the SNR without any lens filters was much higher. Thus, an $f_\#$ of 16 was used on the lenses and the resulting DOF was wide enough to avoid the usage of additional Schiempflug adapters (which make the camera focal plane parallel to the panel surface), as the speckle pattern was always within the DOF throughout its motion.

The illumination source used was the LaVision LED-Flashlight 300, which is an array of 72 white LEDs that could be connected to trigger at the same time as the cameras. While the exposure time of the cameras was $200\mu\text{s}$, the LED pulse duration was only $20\mu\text{s}$, making the effective camera exposure $20\mu\text{s}$ as well to "freeze" the panel at the given time instant. The camera and LED setup is shown in [Figure 3.21](#). The synchronisation of the LED and camera triggers happened through the LaVision High-speed Controller (HSC), which got the trigger input from the acquisition PC (through the software DaVis, more on that later) during recording. All the technical details discussed are summarized in [Table 3.5](#).

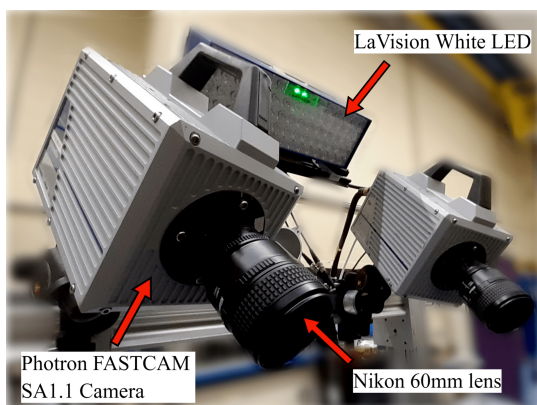


Figure 3.21: Camera, lens and LED arrangement for DIC

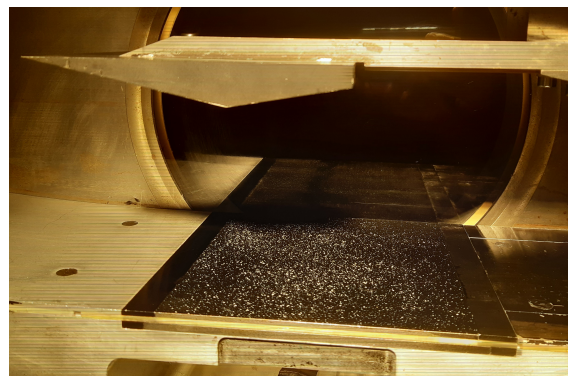


Figure 3.22: Test section showing shock generator and speckle pattern on panel

To make the panel motion visible to the cameras, it was painted using an airbrush with a white speckle pattern on a matte black background to achieve high contrast. Due to the high contrast, the light from the LED reflected off of the painted speckle pattern while most of it was absorbed by the black background, thus resulting in the speckle pattern being clearly captured by the cameras. With a little trial-and-error, the speckle pattern generated had most speckles in the range of 3 to 8 pixels, enough to avoid aliasing. An image of the panel with the speckle pattern can be seen in [Figure 3.22](#).

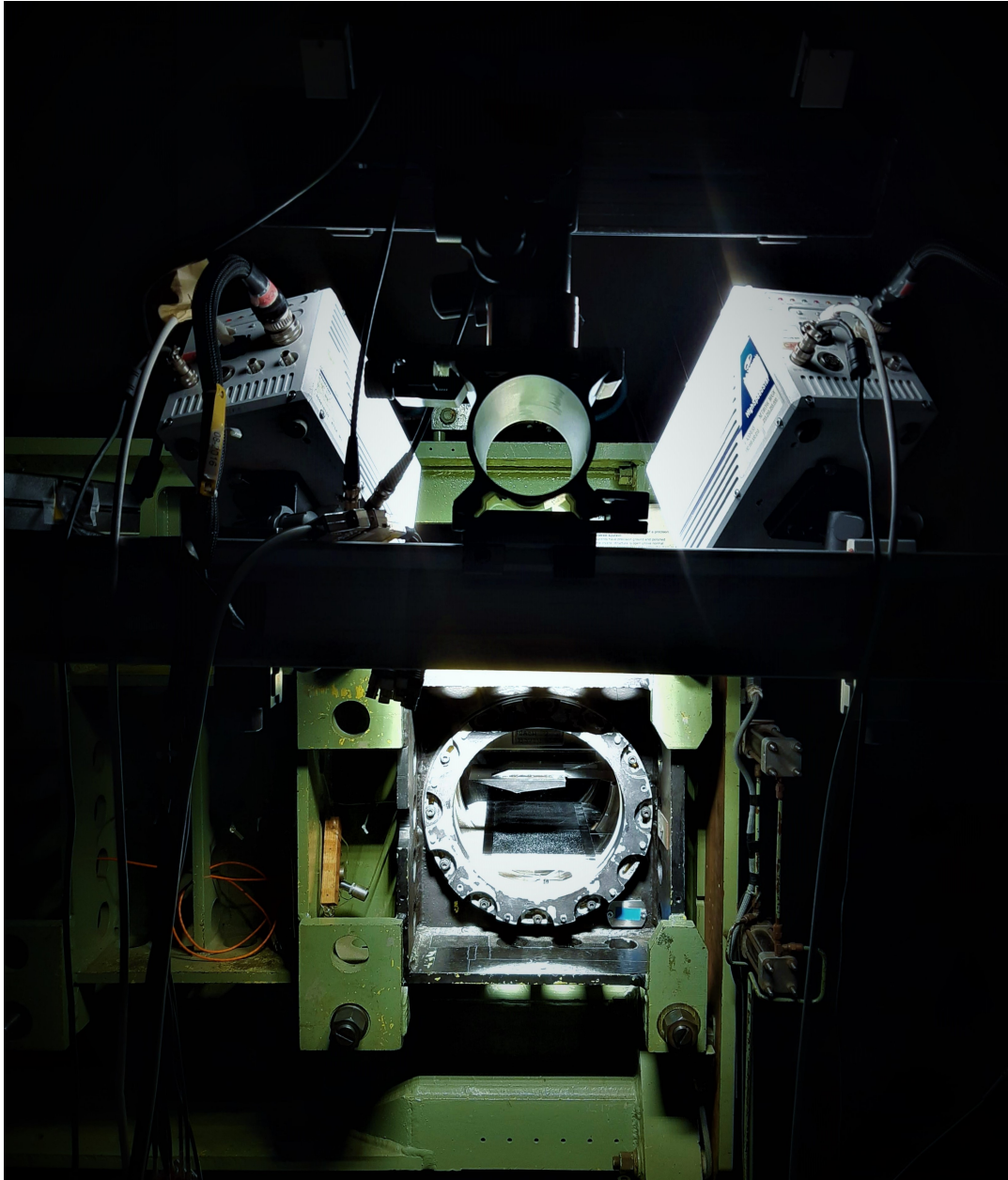


Figure 3.23: Illuminated test section during DIC

DIC equipment	
Camera	2 × Photron FASTCAM SA1.1
Resolution (full)	1024 × 1024 px
Resolution (used)	896 × 512 px
Pixel size	20 μm × 20 μm
Acquisition rate (used)	5000 Hz
Acquisition time	1.6 sec
Lens	Nikon 60mm
$f_{\#}$	16
Magnification factor	0.09
Spatial resolution	4.78 px/mm
Illumination	LaVision LED-Flashlight 300 (White)
LED pulse duration	20 μs

Table 3.5: Technical details of DIC equipment used

Processing of raw DIC images

For processing raw images, the software LaVision DaVis 10.0.4 was used. Before recording images for DIC, calibration to determine the exact camera positions with respect to each other and the panel inside the test section had to be performed. This was done by capturing images of a Type-10 calibration target which was kept inside the test section. The in-built calibration feature in DaVis then processed the images of the calibration target and calculated the orientation of the cameras as well as the magnification factor, which enabled the subsequent recordings to be calibrated in the actual physical scale of mm rather than just pixels. After calibration and before running the tunnel, 100 images of the initial static panel were captured to serve as a reference for cross-correlation. After recording images during the tunnel run, cross-correlation calculations were run on DaVis using a subset size of 27×27 pixels with an overlap of 9 pixels. During cross-correlation, each frame captured during the run was compared with an average image of the 100 images captured before the run, representing the initial displacement of the panel. Thus, the calculated displacement fields were relative to the initial panel position. Additionally, a second-order shape function was also used during cross-correlation to allow for a more accurate estimation of the actual panel deformation.

3.6. Test Conditions

Finally, the main test conditions for the three experimental campaigns are listed in Table 3.6. The shock impingement location was varied in steps of $0.1x/a$ for both Schlieren and DIC measurements, but was kept fixed at $x_i/a=0.5$ for the first campaign with simultaneous temperature and acceleration measurements (section 3.3). The specific dimensions of the test section and the available panel and shock generators limited the minimum impingement locations to 30% and 40% of the panel length for the 15° and 12° shock generators, respectively. As mentioned before, the flowfield measurements using Schlieren and structural measurements using DIC were conducted separately, as the conditions used by Allerhand (2020) showed shock-induced panel flutter in ST-15 was repeatable and periodic. Conducting Schlieren and DIC separately allowed more freedom and flexibility in designing the setup for each. For e.g., for simultaneous PIV-DIC measurements of Allerhand (2020), both techniques used completely different illumination sources (green laser for the former, blue LED for the latter), which meant special filters had to be used on the camera lenses to minimize noise due to light from the other source. Also, usage of space for the setup had to be carefully planned to avoid interference between different equipment, which is not a trivial task considering the limited size of the optical access window in ST-15 (or any other high-speed facility, for that matter).

Parameter	Value
Freestream Mach number, M_∞	2.0
Total pressure, p_0	2.5 bar
Freestream dynamic pressure, q_∞	0.89 bar
Freestream boundary layer thickness, $\delta_{99,\infty}$ (measured by Giepman et al. (2018))	5.2 mm
Freestream Reynolds number, Re_∞/L	$3.33 \times 10^7 \text{ m}^{-1}$
Shock generator ramp angles, θ_{SG}	12° & 15°
Shock impingement locations, x_i/a	$\theta_{SG}=12^\circ$: 0.4-0.8 $\theta_{SG}=15^\circ$: 0.3-0.8

Table 3.6: Governing parameters of tests

3.7. Measurement Repeatability

The phenomenon of shock-induced flutter simulated in ST-15 was already shown to be a repeatable one by Allerhand (2020). However, any measurement technique always carries inherent limitations due to which noise gets added to the measured signal and the measurements differ from what the actual phenomenon. The difference is also exacerbated by inevitable human error and minute changes in test setup conditions when conducting experiments. The two primary techniques employed in this study, Schlieren and DIC, are checked for the repeatability in their measurements under the same test conditions.

3.7.1. Repeatability of Schlieren

Schlieren does not produce any quantitative data, but only images. The code for detecting shock positions from the Schlieren images was self-developed, and the repeatability is measured by comparing values of the SWBLI interaction lengths calculated using the shock detection methodology described in section 3.4.3 for two separate runs done on different days under the same conditions: $\theta_{SG}=12^\circ$ and $x_i/a=0.6$ with the CCCC1.5 flexible panel. The results are shown in Table 3.7. The mean interaction lengths show a relative error of $\approx 7\%$ while the STD of the interaction lengths differ by almost 21%. The error happen because the shock generator is not in the exact same position with respect to the panel between the same runs, as it was setup manually, and thus is susceptible to human error. Moreover, there are errors involved in detecting the exact shock edge because of scratches on the windows and other noise elements in the Schlieren frames, and the unsteady nature of the separation shock coupled with the panel motion also adds to the errors. Last, but not the least, ambient conditions like the temperature, humidity, etc. can also increase the errors since the runs were done on different days.

	mean(L_{int})	std(L_{int})
Run 9	38.55 mm	4.29 mm
Run 14	41.24 mm	3.55 mm
Relative Error	7%	21%

Table 3.7: Comparison of interaction lengths calculated from Schlieren of a CCCC1.5 panel with $\theta_{SG}=12^\circ$ and $x_i/a=0.6$

3.7.2. Repeatability of DIC

The displacement fields are obtained through the software DaVis, which uses its internal calculations to process the recorded stereo-image pairs. Comparison of two runs under the same conditions: $\theta_{SG}=12^\circ$ and $x_i/a=0.6$, done two days apart, is made with the help of mean and STD of the obtained out-of-plane displacements from DIC. From a visual inspection of the mean displacements in Figure 3.24b, slight differences can already be observed (both use the same colorbar limits): the upstream crest (dark red) and the bottom right trough (dark blue) extents look different. In quantitative terms, the relative error between the mean displacement fields comes out to be 2.5%.

The STD displacement fields are compared in Figure 3.25, also on the same colorbar limits. From a visual standpoint, the shapes of the crest are a little different, with run 9 (Figure 3.25a) showing a

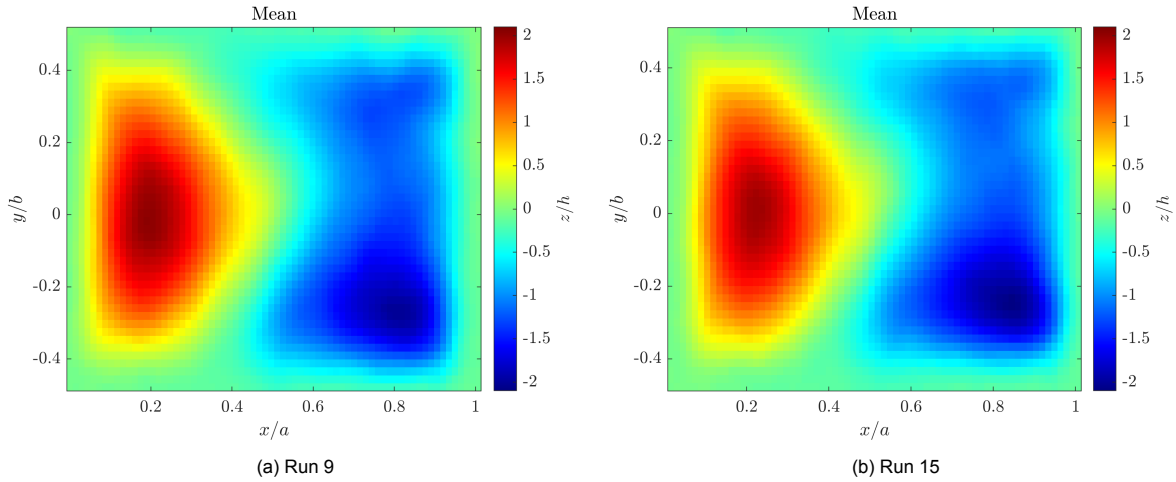


Figure 3.24: Comparison of mean displacement fields between different runs for a CCCC1.5 panel with $\theta_{SG}=12^\circ$ and $x_i/a=0.6$

crest (dark red) that is larger in the spanwise direction, but less extensive in the streamwise direction. Quantitatively, the STD displacement fields shown differ by 6.3%. The errors in both mean and STD displacement fields can be due to change in ambient conditions between different days, change in local conditions inside test section, the added noise from vibrations of the camera or setup, among other sources.

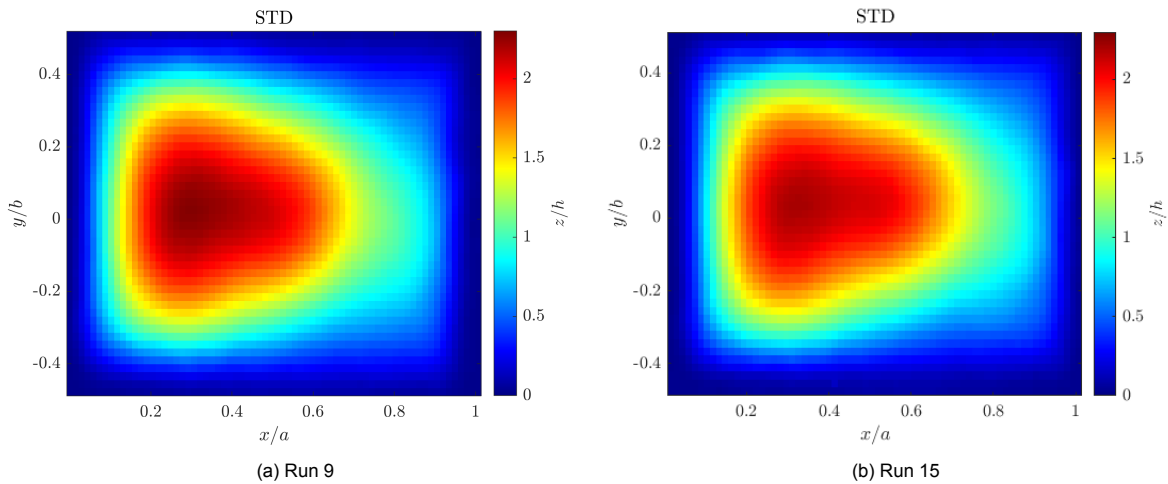


Figure 3.25: Comparison of STD displacement fields between different runs for a CCCC1.5 panel with $\theta_{SG}=12^\circ$ and $x_i/a=0.6$

3.8. Uncertainty Analysis

To ensure that the measurements represent the actual trends of phenomena being measured, the precision of the measurements are quantified through uncertainty analysis. The main quantifiable uncertainty recognized is statistical uncertainty, which is related to random variations resulting from various error sources, and is defined as follows:

$$\varepsilon = \frac{\sigma}{\sqrt{N}} \quad (3.17)$$

where σ is the standard deviation of the measurement and N is the number of recorded samples. Statistical uncertainty is mainly associated with the mean of the measured quantity. Larger the number of samples, lesser is the statistical uncertainty and hence, closer is the mean of the measurements to the true value.

Schlieren did not directly make any quantitative measurements directly, but the recorded images were still used to extract quantitative data like interaction lengths. To check for the statistical uncertainty associated with measuring the interaction lengths using Schlieren, the case of a rigid plate with $\theta_{SG} = 12^\circ$, $x_i/a = 0.5$ is chosen as there is no flutter-associated motion of the shock waves. As it turns out, the maximum statistical uncertainty in calculating interaction lengths is $\approx 0.3\mu\text{m}$, as given in [page 64](#).

Finally, with DIC, the case of the rigid panel $\theta_{SG} = 12^\circ$, $x_i/a = 0.5$ is again chosen as there is no influence of the flutter motion. The displacements measured at the midchord, midspan point are chosen for calculations, and the maximum statistical uncertainty comes out to be $0.155\mu\text{m}$, or, when normalized with the flexible panel thickness h , merely 0.05%. With DIC, another major source of uncertainty is identified as the spatial resolution. It is mainly related to the resolution of the vector field obtained from DIC, which is done by running the cross-correlation function using a subset size of 27 pixels, hence, each displacement vector corresponds to an area of 27×27 pixels in the image. This results in a spatial resolution of 5.72 mm, which is 4.47% of the panel length. Thus, the spatial resolution of the DIC measurements is deemed more than sufficient to resolve the large-scale panel motion of interest. Both uncertainty values are listed in [Table 3.8](#).

Technique	Source	Value
Schlieren	Statistical, ε_L	$< 2.89 \times 10^{-2}$ mm
DIC	Statistical, ε_z	$< 1.55 \times 10^{-4}$ mm
DIC	Spatial resolution, Δ_x	< 5.72 mm

Table 3.8: Uncertainty values from various sources in different measurements

4

Investigation of Wind Tunnel Vibrations

In the previous chapter, all aspects related to acquiring data through measurements were discussed. This provided a background on the principles behind the techniques used for measurements, so that the interpretation of the data can be understood clearly. In this chapter, the focus of the discussion will be on the wind tunnel vibration measurements. In section 4.2, the results obtained from the first campaign in which accelerations and temperatures around the test section were measured will be analyzed. Following that, section 4.3 will discuss the relation between vibrations measured in different parts of the flowfield measured using Schlieren and vibrations in the test section. Also, the link between flutter captured by DIC and the vibrations in the test section will be presented in section 4.4. Finally, section 4.5 will discuss the existence of fluid-structure interaction in the current study in context of the detected vibrations in the wind tunnel test section.

4.1. Previous Investigation in ST-15

Any study of fluid-structure interactions in an experimental setting can be susceptible to spurious vibrations caused by external sources. Thus, it becomes important to be aware of any such external vibrations that may affect the recreation of the desired phenomenon. [Allerhand \(2020\)](#) observed the presence of external vibrations in the lower Mach block in ST-15 that were close in terms of characteristic frequencies to the designed panels that are used for this study too. In particular, a ≈ 576 Hz frequency slowly emerged in the lower Mach block (measured using accelerometers) after the tunnel had been run for an extended period of time. [Allerhand \(2020\)](#) attributed this to contraction of the lower Mach block due to rapid cooling caused by the high-speed air flowing through the tunnel, which expanded the gaps between the Mach block and the tunnel doors/walls, and they seemed to become less energetic when the Mach block was tightened to the wind tunnel wall. Another interesting observation made was that the said characteristic frequency only occurred in the accelerometer readings when the shock generator was installed. In the end, there was not much clarity on the origin of these spurious vibrations and whether they were repeatable or random. This section will be dedicated to the results related to wind tunnel vibrations obtained during the current study. First, the observations from the first campaign involving simultaneous temperature and vibration measurements will be discussed, followed by a discussion on the presence of the vibrations during subsequent campaigns and their influence on the flutter and SWBLI dynamics. The vibrations are characterized by calculating the PSD (see section 3.5.6) of the accelerometer readings. However, PSD ($E(f)$) is not a direct indicator of total energy, which is found by multiplying the PSD with the frequency f at each point (since PSD gives energy per unit frequency). Ideally, $f \cdot E(f)$ should be plotted with the log of f such that the area under the curve is proportional to the energy content at each point. However, in this chapter, $E(f)$ versus f is plotted so that the frequency axis has a linear scale for more clarity in identifying the frequencies of interest caused by the wind tunnel vibrations.

4.2. Relation to Temperature Change

As mentioned before, there was a strong suspicion that contraction of the Mach block due to cooling was leading to the "extra" vibrations at ≈ 576 Hz when a shock generator was installed ([Allerhand,](#)

2020), as tightening the bolts between the Mach block and the tunnel caused a dip in the energy content around the particular frequency. To test this hypothesis, the first campaign involved simultaneous measurements of the temperature and accelerations at various locations around the test section (see section 3.3). The temperature measurements were also meant to provide an estimate of the thermal transience during tunnel startup and shutdown. The entire first campaign was done using a rigid plate, as any spurious vibrations that occurred could be isolated from flutter of the panel and easily attributed to the wind tunnel test section as the plate itself would not flutter.

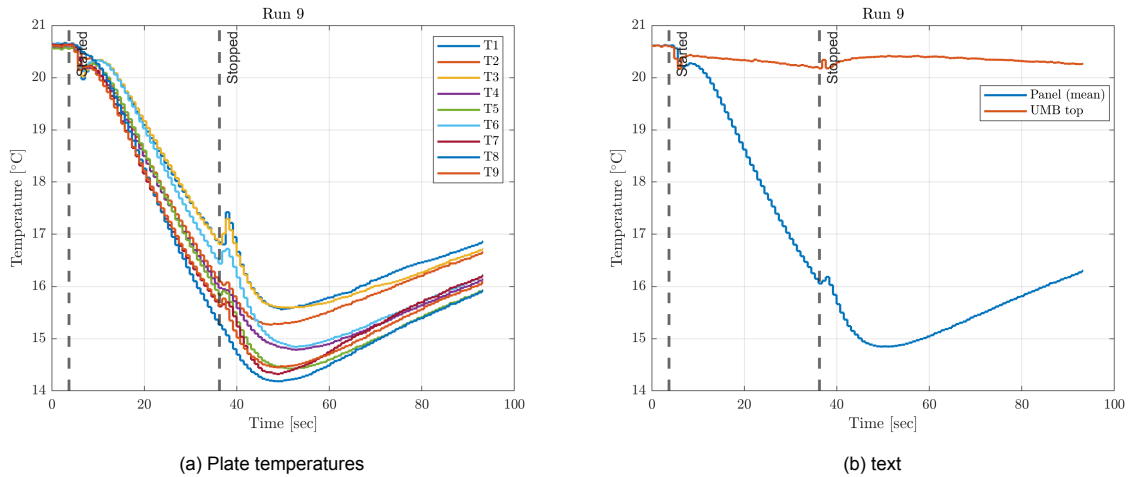


Figure 4.1: Temperature variation in various parts of the test section during tunnel run

In Figure 4.1a, temperatures at the bottom of the panel are plotted with time during a tunnel run where the rigid plate was installed along with a 12° shock generator such that the inviscid shock would impinge at 50% of the plate chord. The times at which the tunnel is started and stopped are marked using dashed lines. Although there is variation in temperature between the different thermocouples, the variation was not found to correlate with the respective locations of the thermocouples on the panel (see section 3.3). These differences could be because of variation in local properties not directly relevant for the current study and since all the thermocouple show the same trend (discussed in detail later), from here on only the mean temperature of the panel is shown. Figure 4.1b shows the mean panel temperature variations (blue) for the same run. It can be clearly observed that before starting the tunnel (marked with a dashed vertical line and labelled "Started"), the mean temperature was equal to $\approx 20.5^\circ\text{C}$ and as soon as the tunnel starts and the compressed air rushes into the test section, a short period of instability exists where temperatures seem to sharply dip, but then recover quickly. As the run progresses, the mean panel temperature consistently drops, as the thermocouples on the panel are closest to the flow in the tunnel compared to the other location: top of the Upper Mach block (UMB top). The UMB top temperature drops very slightly (practically constant) compared to the significant decrease in panel temperature simply because of larger separation from the flow side (and hence greater thermal inertia). While there was a thermocouple installed inside the LMB cavity too, it appeared to malfunction resulting in non-physical temperature rise in the readings. Also, there were thermocouples on the UMB side and LMB side but they did not register much significant change from the ambient temperature, and hence are not shown. Right after the tunnel is stopped (marked with the vertical dashed line labelled "Stopped"), a momentary jump in temperatures can be seen, again an instability caused by the sudden change in conditions. Subsequently, the LMB cavity temperature starts to fall while the UMB top temperature begins to rise in order to reach equilibrium with the ambient conditions. Interestingly, the mean panel temperature continues to fall for an extended period of time even after the tunnel is turned off and starts to recover after ≈ 10 -15 seconds. This is attributed to the thermal inertia of the panel itself. The important takeaway from this result is that any measurements of the flowfield (such as PIV/Schlieren) must be started after at least a period of 5 seconds after the tunnel is started, so as to avoid the initial thermal instability. Also, the temperature recovery takes longer than the time of the run, but can be expedited by opening the tunnel doors completely.

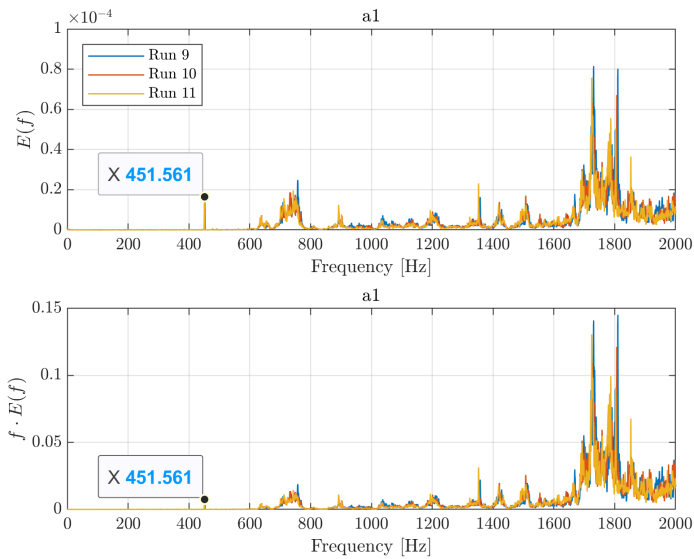


Figure 4.2: Distinction between PSD and total energy

Run Nos.	Figure	Shock generator	Comments
5,6	4.3	None	LMB and UMB bolts tightened
9,10,11	4.5	12°	No changes in between runs
12,13,14	4.7	12°	No changes in between runs
18,19	4.8	12°	LMB and UMB bolts tightened

Table 4.1: Test conditions for particular runs in the first campaign. For some runs, no changes were made in between to the setup to allow for drastic change in temperatures. In others, bolts were tightened to try and eliminate vibrations.

Before proceeding with showing the accelerometer responses, there is an important distinction to be made clear between power spectral density (PSD, denoted as $E(f)$) from FFT/Welch’s method and the total energy content of a periodic phenomenon. PSD, as the name suggests is the power density per unit frequency at a particular frequency. PSD obtained from a FFT indicates dominant frequencies, but is not indicative of the total energy carried by the vibrations at a certain frequency. The quantity, $f \cdot E(f)$, which is simply the PSD pre-multiplied by the frequency, is indicative of the total energy of the vibrations. Thus, the magnitude of PSD should not be taken at face value when it comes to comparing relative energies of different characteristic frequencies. In the current chapter, the accelerometer responses are presented in terms of the PSD, because it allows better clarity in recognizing lower magnitude frequencies of interest. As an illustration of the aforementioned differences, Figure 4.2 shows both $E(f)$ and $f \cdot E(f)$ for the same set of measurements. Compared to $E(f)$, it is clear how the total energy content shrinks for the lower frequencies while it expands for the higher frequencies in a relative sense. This is important as the following results will be presented using PSD to clearly distinguish the lower frequencies that might exist in different parts of the test section, but at the same time it should be clear that the energy contribution from the lower frequencies will be relatively smaller compared to the PSD.

Label	a1	a2	a3	a4	a5	a6	a7	a8
Location	LMB cavity	UMB top	Panel x/a≈0.25	Panel x/a≈0.75	LMB side	UMB side	Wind tunnel outer wall	Shock generator

Table 4.2: Accelerometer locations for Figures 4.3, 4.5, 4.7, 4.8. See Figure 3.8 for more details.

4.2.1. Without Shock Generator

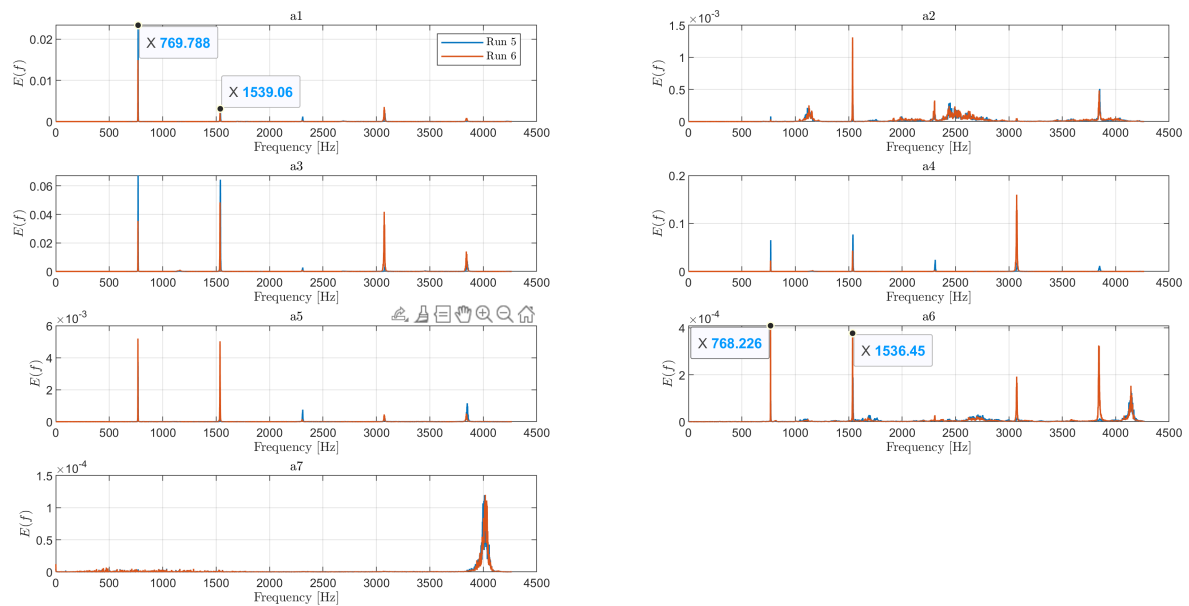


Figure 4.3: Wind tunnel vibrations with no shock generator in test section. See Table 4.2 for accelerometer locations.

The first few tunnel runs were done with no shock generator installed in the test section, and the accelerometer responses for runs 5 and 6 are shown in Figure 4.3. There was no significant change in the frequency response with cooling of the wind tunnel, so the temperature readings are not presented. The characteristic frequency peaks are distinct and sharp, showing that their energy content is much higher compared to other sources of vibrations (as seen later in section 4.2.2). The characteristic frequency exists at around 768-770 Hz (slightly different between the two runs) and is highly energetic in the LMB cavity (a1), LMB side (a5), panel upstream location (a3) while also present with lower energy in the UMB side (a6) and panel downstream (a4). A second characteristic frequency is also observed at 1537-1540 Hz, representing the second harmonic, present in all locations except the wind tunnel wall (a7), which is expected since the outer wind tunnel is clamped to the ground). These frequencies are most energetic at the panel (a3 and a4), and also at the LMB cavity and side (a1 and a5). These are also present in the UMB side (a6), although the energy content in is significantly lower compared to the other two. An important point to note here is that these two runs (5 and 6) were not carried out in quick succession, but rather were done on different days. When the 769 Hz peak was detected in run 5 (and its previous run), it was decided to tighten the horizontal and vertical clamping bolts that connect the Mach blocks to the wind tunnel walls to try and eliminate any vibrations that were occurring due to small gaps between the two. This strategy was found to be useful in the case of Allerhand (2020) in minimizing the 576 Hz frequency of the LMB, albeit in that case there was a shock generator installed. However, despite further tightening both Mach blocks to the wind tunnel walls, the damping of the spurious vibrations was not as significant as desired. Looking at the LMB cavity (a1) and both panel locations (a3 and a4), the tightening does seem to have some effect in controlling the vibrations as clearly the blue peaks (representing the previous run, i.e., run 5) are higher than the orange peaks (representing the run after tightening, i.e., run 6) for these three locations. However, on the LMB side (a5), tightening the bolts appears to result in an increase in the energy content at both 768 and 1537 Hz. The same occurs at the UMB side (a6), as clearly the orange peaks overshadow the blue ones. Lastly, the frequencies at the wind tunnel side (a7) are unchanged between the runs, as expected.

4.2.2. With Shock Generator

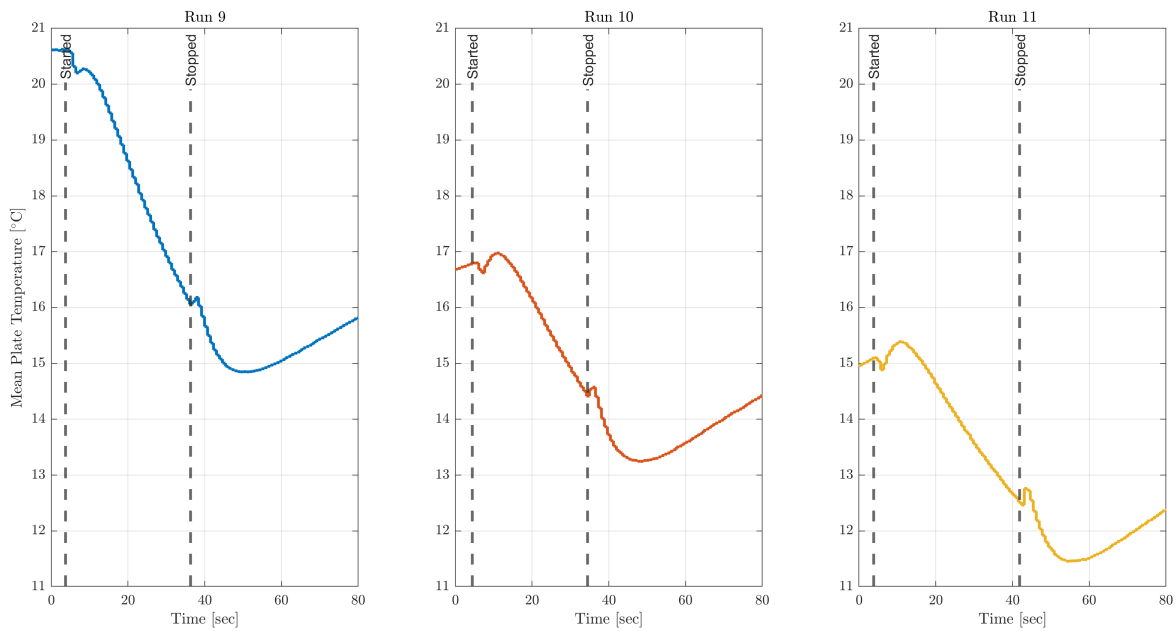


Figure 4.4: Mean plate temperature variation for runs 9 to 11

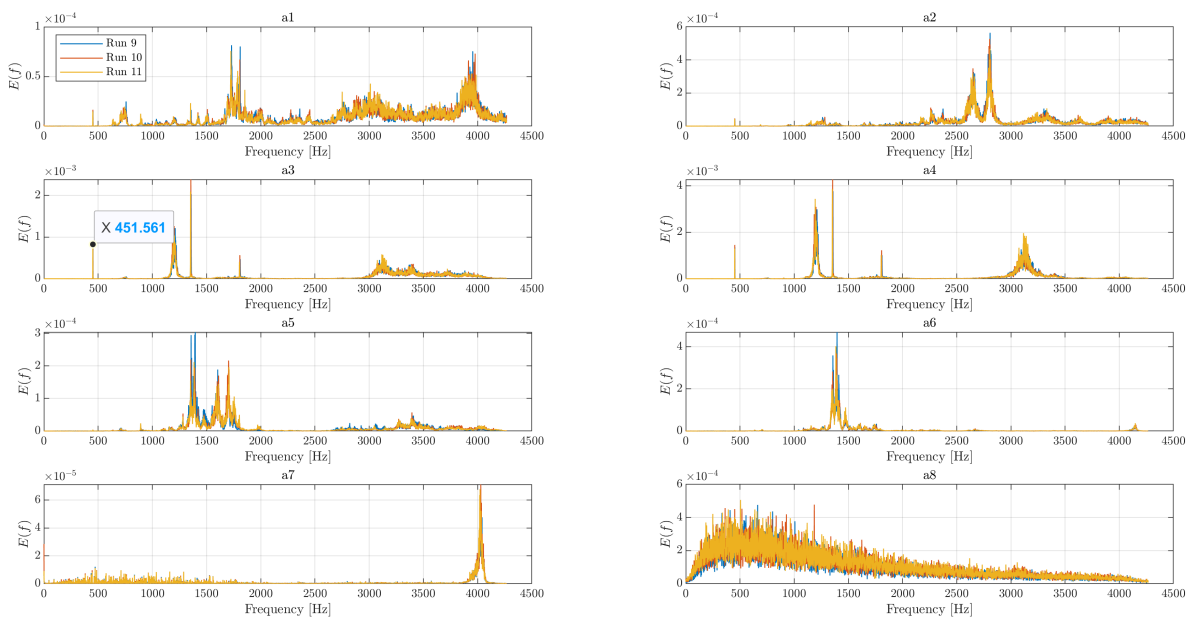


Figure 4.5: Accelerometer response for runs 9 to 11. See Table 4.2 for accelerometer locations.

In an attempt to test the contraction hypothesis proposed by [Allerhand \(2020\)](#) to explain the lower Mach block (LMB) vibrations, the tunnel was run consecutively to cool down quickly so that it could reproduce the same vibrations. The test section was setup with the same 9 mm thick rigid plate with a 12° shock generator and the tunnel was run three times in quick succession, as shown in [Figure 4.4](#). As shown, the temperature below the panel had reached $\approx 12.5^\circ\text{C}$ by the end of the third run from $\approx 20.6^\circ\text{C}$ at the start of the first run. In between the runs, no changes were made to the setup. The accelerations recorded for each of the runs are presented in [Figure 4.5](#), and the particular location of each accelerometer can be identified with the help of [Table 4.2](#) and [Figure 3.8](#). Overall, the frequency

responses across all 3 runs in Figure 4.5 are very similar, and no distinct characteristic frequency can be seen emerging as the tunnel cools down from run 9 to run 11. Some interesting observations can be made regarding the general trends. In the LMB cavity (a1) and UMB top (a2), most energetic vibrations are at higher frequencies: >3800 Hz and between 2500-3000 Hz, respectively. The LMB cavity (a1) does show energies at lower frequencies of 451 Hz and an array of peaks around 630-750 Hz, but the energy content is also very low. The rigid panel (a3 and a4) does respond to the 451 Hz frequency, although again the energy is relatively low compared to that of the frequencies between 1000-1500 Hz detected. The 451 Hz peak is also present in the UMB top (a2) with very low energy. The direction of these particular measured vibrations are along the out-of-plane displacement vector of the panel (or along the height of the test section), given how the accelerometers are attached. On the LMB side (a5) and UMB side (a6), the most energetic frequencies are in 1300-1800 Hz and 1300-1500 Hz, respectively, with the direction of measured vibration being along the test section width. The wind tunnel wall (a7) shows one distinct characteristic frequency of ≈ 4000 Hz, while the shock generator (a8) response is noisy with no characteristic frequencies (which could also be a result of improper attachment since a8 was exposed to the oncoming flow). Finally, the accelerometers on the panel (a3 and a4) apart from 451 Hz also show energetic peaks at ≈ 1200 , 1350, 1800 and >3000 Hz. These could either be due to the panel not being properly tightened to the LMB, or due to vibrations of the upper part of the LMB itself. In any case, the characteristic frequencies below 1000 Hz observed in the Mach blocks and the panel were significantly less energetic (in terms of $f \cdot E(f)$) than the characteristic frequencies found beyond 1000 Hz.

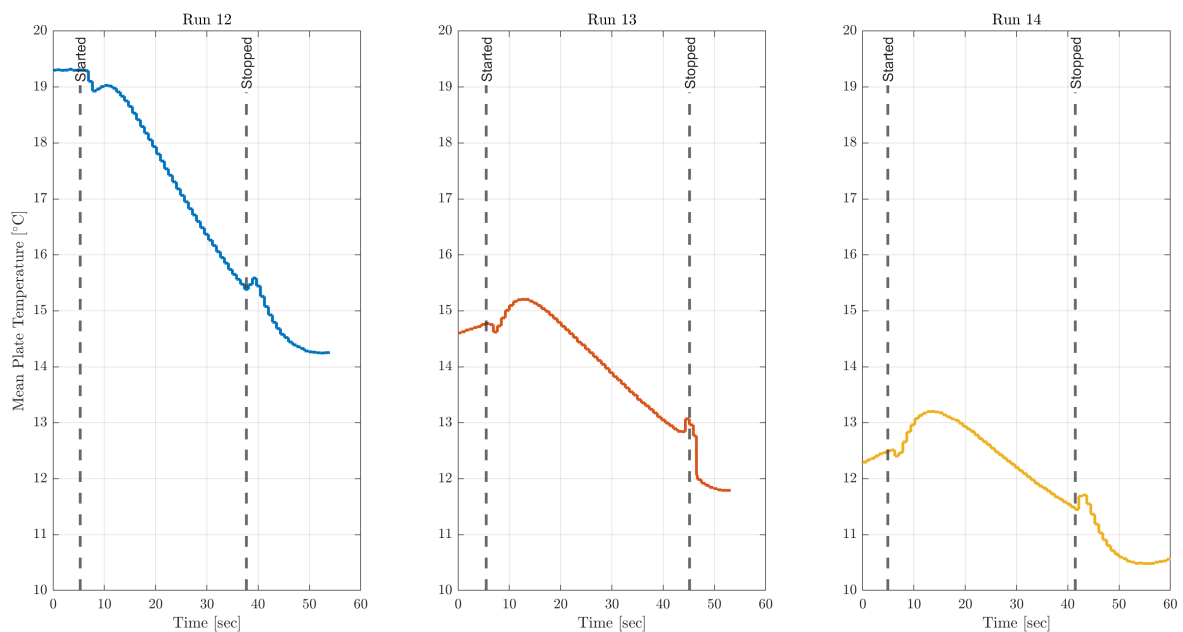


Figure 4.6: Mean plate temperature variation for runs 12 to 14

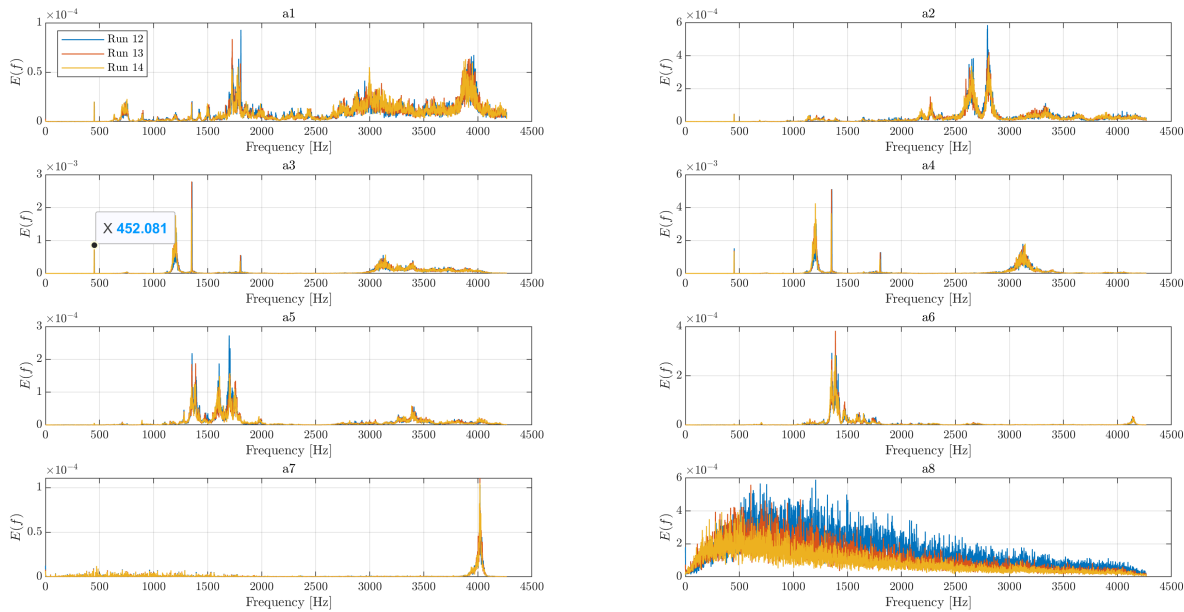


Figure 4.7: Accelerometer response for runs 12 to 14. See Table 4.2 for accelerometer locations.

Of course, the Mach block being massive has a large thermal inertia too, and any contraction of the whole block should not be expected to occur immediately after the first set of runs, as also confirmed by [Allerhand \(2020\)](#). Runs 9-11 were the first runs of the day, and several more runs were carried out throughout the whole day to give time for the LMB to cool down and contract. The next set of runs were carried out one hour later after run 11 in a similar fashion: three runs in quick succession. By this time the panel temperature had recovered since run 11 to $\approx 19.4^\circ\text{C}$ as seen at the start of run 12 in [Figure 4.6](#), and by the end of run 14 had gone down to $\approx 11.4^\circ\text{C}$. Comparing [Figure 4.7](#) with [Figure 4.5](#), the vibrations in all parts of the tunnel show quite similar trends: the characteristic frequencies with the most energy are beyond 1000 Hz in the upper and lower Mach blocks. The LMB cavity and side (a1 and a5, respectively) still have energies spread out in the range 630-750 Hz, but its energy content is insignificant compared to the higher frequencies, which was also observed in [Figure 4.5](#). This time, there is a peak at 452 Hz appearing in the LMB cavity (a1) as well as the panel accelerometers (a3 and a4) but the PSD is too low compared to that at higher frequencies, so total energy content can be expected to be even lower. As mentioned earlier, the higher frequencies are not of much interest or concern as the dominant natural panel frequencies are designed to be below 500 Hz ([Allerhand, 2020](#)), thus the higher characteristic frequencies observed in the test section can only influence low energy panel modes that occur at nearby higher frequencies. Only the shock generator response (a8) is distinct in this set of runs compared to runs 9-11, as the vibrations seem to become less energetic from run 12 to 14.

Finally, after several more runs under similar conditions, the final two runs (18-19) happened 5 hours after the very first runs of the day (runs 9-11). Similar to before, these were done in quick successions, and the frequency responses of the accelerometers are shown in [Figure 4.8](#). Here, although the most energetic peaks are observed at similar frequency regions as the previous two sets ([Figure 4.5](#) and [Figure 4.7](#)) in each of the locations around the test section, there is one interesting peak at 632 Hz present in the LMB cavity, LMB side and UMB side (a1, a5 and a6, respectively). Between runs 18 and 19, the bolts connecting the LMB and UMB to the wind tunnel were tightened, to see if it would have any effect on the vibrations. The 632 Hz peak in the panel response (a3) does seem to slightly reduce (the orange peak is shorter than the blue one), but the energy itself is very low at the frequency. In the other locations, there is no significant difference in the energy around the 632 Hz peak between the two runs. As observed before, the energy content of the 632 Hz peak is significantly smaller than the other distinct peaks beyond 1000 Hz, however, the interesting point is that the peak is much sharper compared to the small spread-out peaks found at around 630-750 Hz in the previous sets. There also seems to be another sharp yet smaller peak close to 900 Hz in a1 and a5. These were the last runs

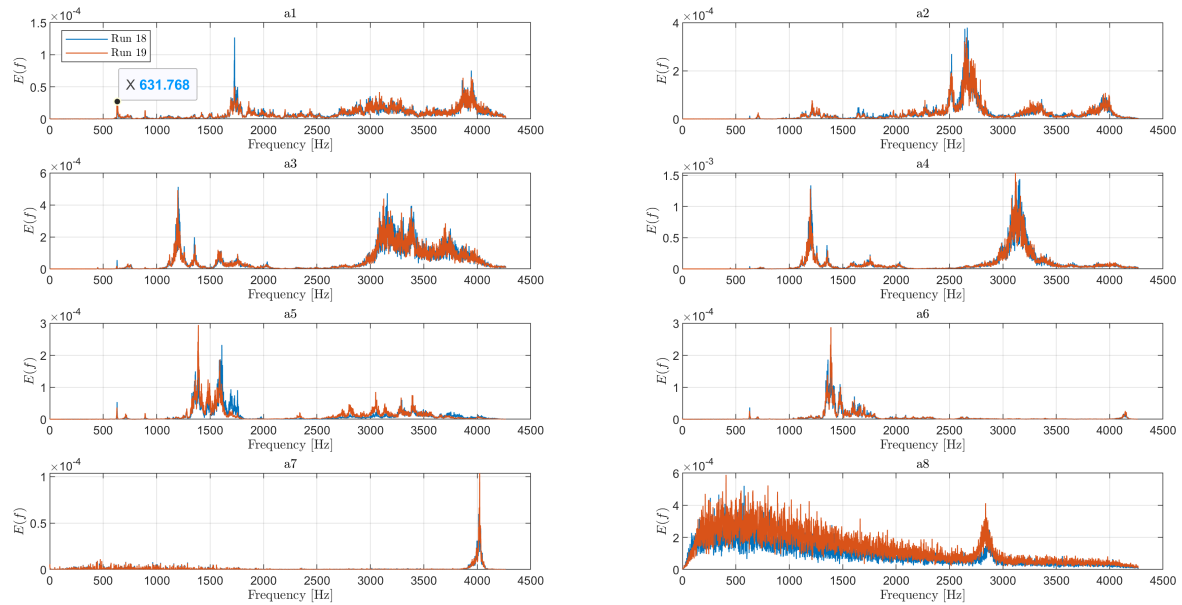


Figure 4.8: Wind tunnel vibrations during the last runs of the day. See Table 4.2 for accelerometer locations.

of the day, and despite the tunnel being run several times (11, to be exact) on the same day, and also several other times on the previous two days, the same highly energetic vibrations around 576 Hz that were observed by [Allerhand \(2020\)](#) were not found in the lower Mach block, instead a small but sharp peak at 632 Hz was observed which could not be completely eliminated despite efforts to make the LMB and UMB stiffer by tightening connecting bolts. Although some potentially problematic frequencies below 1000 Hz could be seen, they were orders in magnitude smaller in terms of energy content when compared to the higher characteristic frequencies.

Overall, from the results of the first campaign involving simultaneous temperature and acceleration measurements, the most interesting find was the highly energetic vibrations in the LMB at 768-769 Hz when the tunnel is run without a shock generator. Tightening the bolt connecting the LMB of the wind tunnel was not found to be a remedy for eliminating the particular characteristic frequency, as it seemed to persist even when tests were done on separate days. These vibrations also appear periodic in nature, with clear 2nd and 4th harmonics observed in the frequency plots. However, when a shock generator is installed, such periodic and highly energetic vibrations do not appear any more, instead low-energy vibrations were observed at around 632 Hz after running the tunnel multiple times throughout the day, suggesting that some unsteady aerodynamic phenomenon might be playing a role in determining the frequency and energy content of the LMB and UMB vibrations. The source of these vibrations is difficult to ascertain in the scope of this work, since nothing much could be done beyond tightening the bolts from a practical perspective. With the temperature measurements, the test section was found to cool rapidly due to the high-speed flow, however, the effects of this rapid cooling varied to different extents due to the high thermal inertia of the Mach blocks. No direct correlation was obtained between low tunnel temperatures and increase in energy of vibrations at ≈ 576 Hz, as the latter was not observed despite multiple runs of the tunnel over several days, and the hypothesis of [Allerhand \(2020\)](#) on contraction of LMB due to cooling causing the aforementioned vibrations could not be directly confirmed.

4.3. Schlieren with Accelerometers

From the first campaign, it was inconclusive whether vibrations occurring below 700 Hz with a shock generator installed could influence the flutter of the flexible panel, since they were found to have very low energy. Without a shock generator, it was clear that a 768 Hz peak existed in the LMB which could not be completely eliminated. To keep in check any problematic vibrations which were most energetic

in the LMB, the accelerometers attached to the LMB cavity and side remained in place for some runs of the Schlieren campaign and all runs of the DIC campaign. In this section, the response of the accelerometers will be compared with characteristic frequencies extracted from the Schlieren images to show how the LMB vibrations play a pivotal role in determining the frequency of flutter and the pressure waves in the open cavity below the panel.

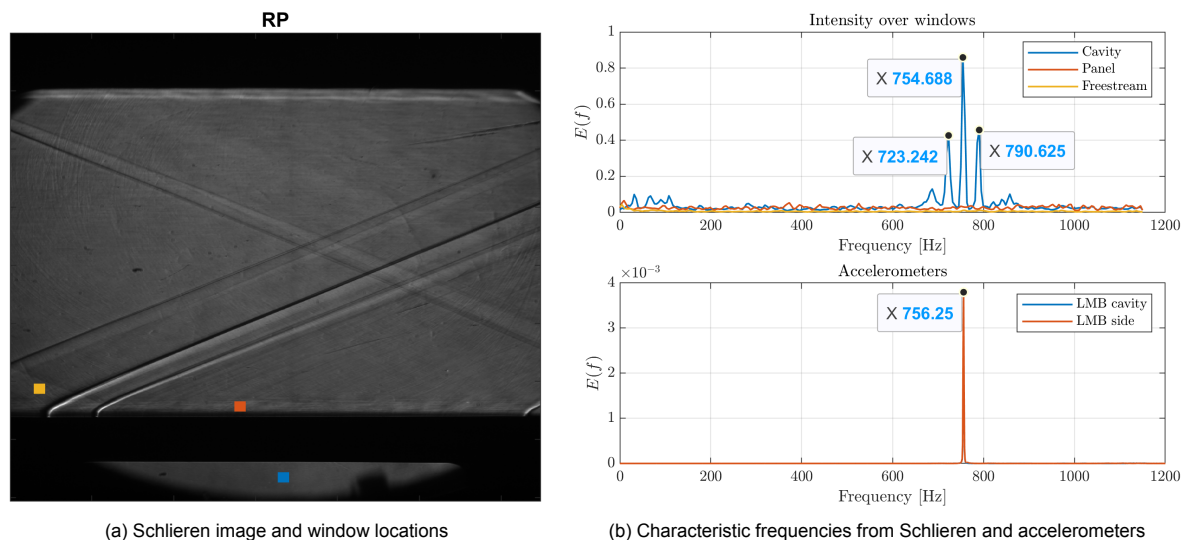


Figure 4.9: Wind tunnel vibrations for a rigid plate with no shock generator

First, Schlieren recordings of a rigid panel without a shock generator were made at an acquisition frequency of 2300 Hz for a recording time exceeding 2 seconds, alongside simultaneous accelerometer measurements in the LMB. To analyze the characteristic frequencies of different locations in the flow-field from Schlieren images, an 11×11 pixel window was defined manually in three locations of interest: the cavity (in blue), boundary layer on top of the panel (in orange), and in the freestream (in yellow), as seen in Figure 4.9a. The idea is that any periodic phenomenon in the region can be captured by tracking the change in mean intensity count over a particular window through the frames. Larger the window size, lesser is the noise, but if the window is too large such that the periodic wave remains inside it for too long can lead to incorrect results. Two shock-expansion waves (dark line followed by a bright line) can be seen in between the yellow and orange windows. These are caused by small gaps in between the panel insert/LMB and the clamping pieces that hold the panel in place. These are unavoidable due to the imperfections in manufacturing and assembly, and slightly lower the flow Mach number received by the panel, as shown by the PIV measurements of Allerhand (2020). In Figure 4.9b, the frequency responses from the Schlieren and accelerometer recordings are shown, and at first glance it is clear that the wind tunnel vibrations detected in the LMB side at ≈ 756 Hz match the peak frequency of pressure waves in the cavity, at ≈ 755 Hz. Although, the exact frequency values between the two differ slightly, that may be attributed to noise in the measurements but for practical purposes they can be considered the same. Interestingly, around the 755 Hz peak in the cavity pressure waves, there are secondary peaks (lesser in energy) on both sides at ≈ 723 Hz and ≈ 790 Hz in symmetric fashion. These symmetric peaks in the cavity are only found in case of no shock generator installed, as will be seen in a later result. It is unclear as to why this happens, as the complex interactions within the cavity are not investigated in more detail in the current thesis. As for the windows over the panel and in the freestream, it is clear they do not have any sharp characteristic frequency compared to the cavity pressure waves, which shows that 756 Hz peak is not coming from the freestream and since a rigid panel is used, the panel and hence the boundary-layer over it does not respond to the LMB vibrations. However, there is still not sufficient information to ascertain causality between the pressure waves in the cavity and the LMB vibrations, i.e., it is unclear whether the LMB vibrations cause the pressure waves or vice-versa.

Next, the same measurements are made with a rigid panel but this time with a 12° shock gen-

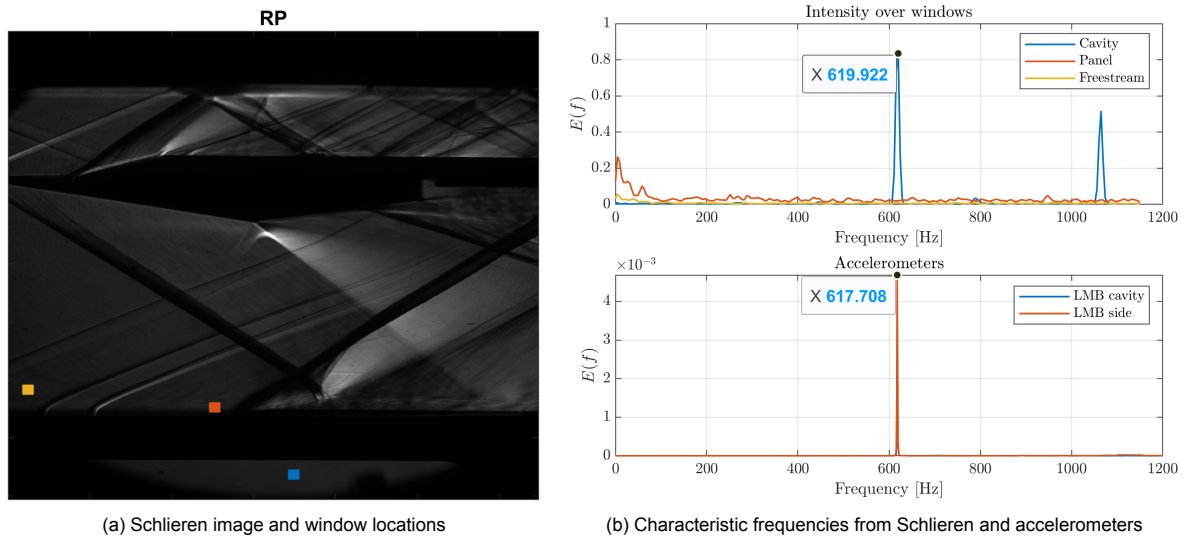


Figure 4.10: Wind tunnel vibrations for a SWBLI over a rigid plate

erator installed with an inviscid shock impingement location of 50% of the panel length. As seen in Figure 4.10a, the resulting SWBLI is clear with the impinging and separation shocks visible. Again, three windows are manually selected in similar positions: inside cavity (blue), over panel (orange), and in the freestream (yellow). This time, as shown in Figure 4.10b, the characteristic frequency of the LMB vibration shifts to ≈ 618 Hz, again more energetic at the LMB side than the LMB cavity but very similar in terms of energy content to the case without a shock generator (Figure 4.9b). And again, the cavity pressure waves show practically the same frequency as the LMB vibrations, at 620 Hz, while no such characteristic frequencies are found in the freestream or right above the panel. The latter again makes sense because the rigid panel does not flutter and hence even the separation shock motion does not have a distinct characteristic frequency.

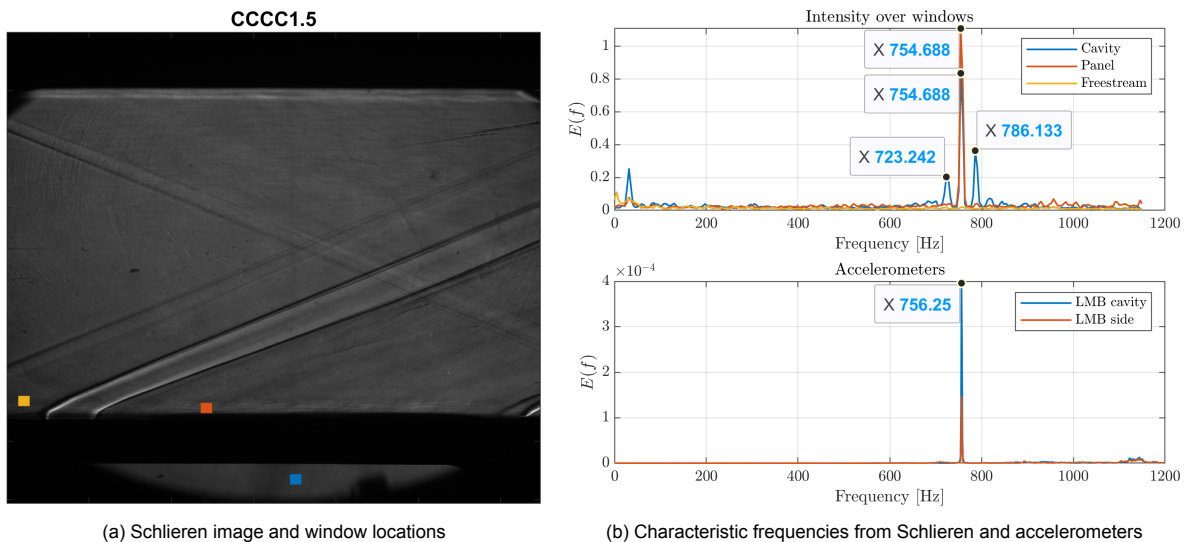


Figure 4.11: Wind tunnel vibrations in free flutter of a CCCC1.5 flexible panel

Having established from previous results with the rigid plate that the LMB vibrations are an inherent problem with ST-15 as they occur even without a fluttering panel installed, it was checked how an actual fluttering panel was affected by these vibrations. First, the flexible CCCC1.5 panel was installed with no shock generator and the Schlieren recording were made alongside accelerometer readings. On the Schlieren image (Figure 4.11a), windows in similar locations as before were picked to determine fre-

quency response in different parts as shown. The corresponding frequency responses are presented in Figure 4.11b, and the first notable feature is the emergence of a characteristic frequency for the panel window (orange) too, which was not there earlier when the rigid plate was in place. This is clearly because of the flutter of the flexible panel itself, and the frequency matches that of the cavity pressure waves (blue) exactly at 755 Hz, albeit the former is more energetic. The freestream response is, as expected, just noise with no distinct energetic frequencies. The LMB cavity and side accelerometers again pick up the 756 Hz frequency, exactly the same as in the case with the rigid panel (Figure 4.9b). These results show that without a shock generator, the LMB vibrations exist regardless of which panel is installed, and in fact drive the vibrations of the fluttering panel at the same frequency.

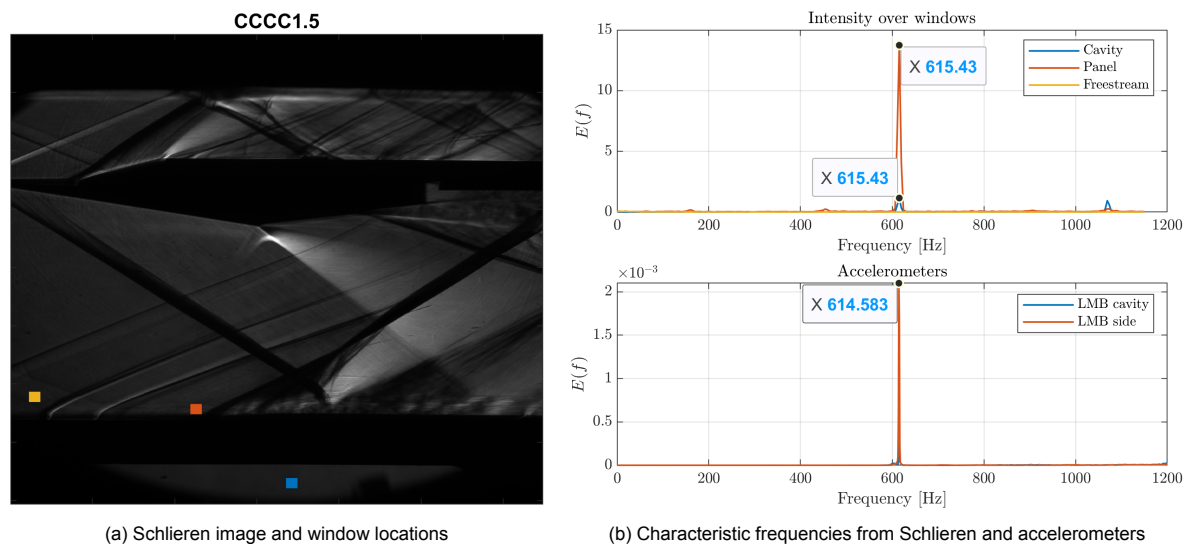


Figure 4.12: Wind tunnel vibrations in shock-induced flutter of a CCCC1.5 flexible panel

Finally, the same test is done on the shock-induced panel flutter of the CCCC1.5 panel with a 12° shock generator with an inviscid shock impingement location of 50% chord length. With the LMB vibrations, the same observation is made as with the case of the rigid plate: the characteristic frequency of the LMB vibrations shifts to a lower value with the shock generator installed, 614 Hz in this particular case (Figure 4.12b). The response from the Schlieren confirms that the same frequency (615 Hz) is also detected in the flutter of the panel (orange) as well as inside the cavity (blue). Essentially, the LMB vibrations seem to drive the frequency of the flutter even in the shock-induced case.

In conclusion, with simultaneous Schlieren and accelerometer measurements it is shown that the LMB vibrations are unavoidable in ST-15, and appear to drive the flutter frequency of flexible panels too. Without any shock generator installed in the test section, the vibrations were manifested at a frequency of ≈ 756 Hz but when a shock generator was in place, that frequency dropped to ≈ 614 -618 Hz. Within the scope of the work, no further efforts were made to completely eliminate these vibrations apart from ensuring that the connecting bolts between the LMB/UMB and the wind tunnel were firmly tightened before each run, although it did not have the desired effect and the vibrations persisted.

4.4. DIC with Accelerometers

Since DIC was done separately from Schlieren, accelerometers were used throughout the DIC campaign to check for LMB vibrations.

For the case of free flutter of a CCCC1.5 panel (no impinging shock), the frequency response extracted from out-of-plane panel displacements at the location where standard deviation (STD) is maximum (representing the most energetic flutter location) is compared to the accelerometer response in Figure 4.13a. While the accelerometers show characteristic frequencies of ≈ 754 Hz along with its

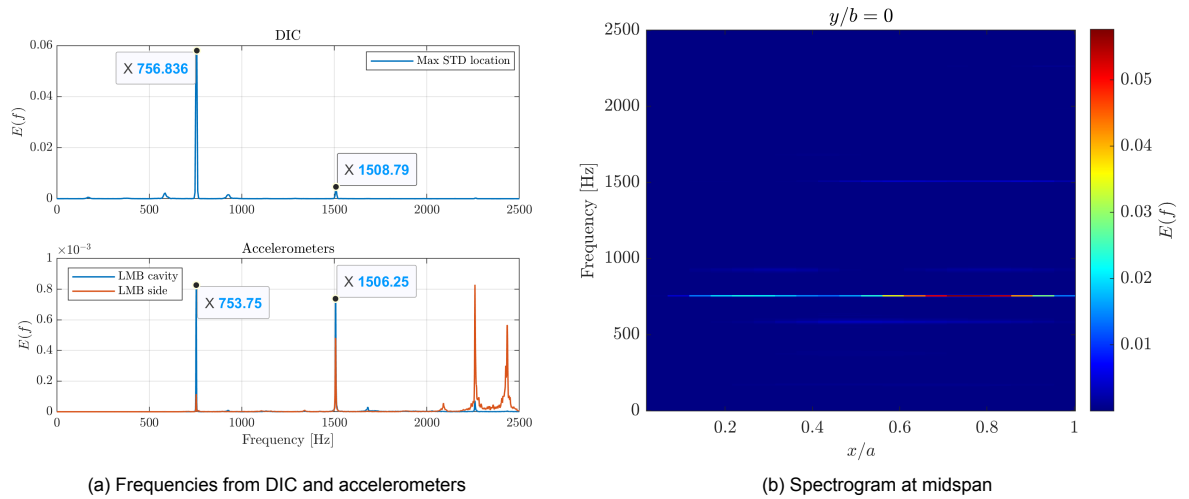


Figure 4.13: Wind tunnel vibrations with DIC measurements in free flutter of a CCCC1.5 flexible panel

second harmonic at ≈ 1507 Hz (both in LMB cavity and side), the response of the displacements as measured by DIC has peaks at ≈ 757 Hz and ≈ 1509 Hz. Again, as discussed before, these are close enough to be considered the same for all practical considerations, and again it is shown that the frequencies of LMB vibrations and the panel flutter are linked. The spectrogram in Figure 4.13b shows the frequency response across the length of the panel at the midspan location, and the 757 Hz along with the less energetic 1509 Hz peaks can be clearly seen, the former especially sharp after $x_i/a=0.7$, i.e., 70% chord length of the panel.

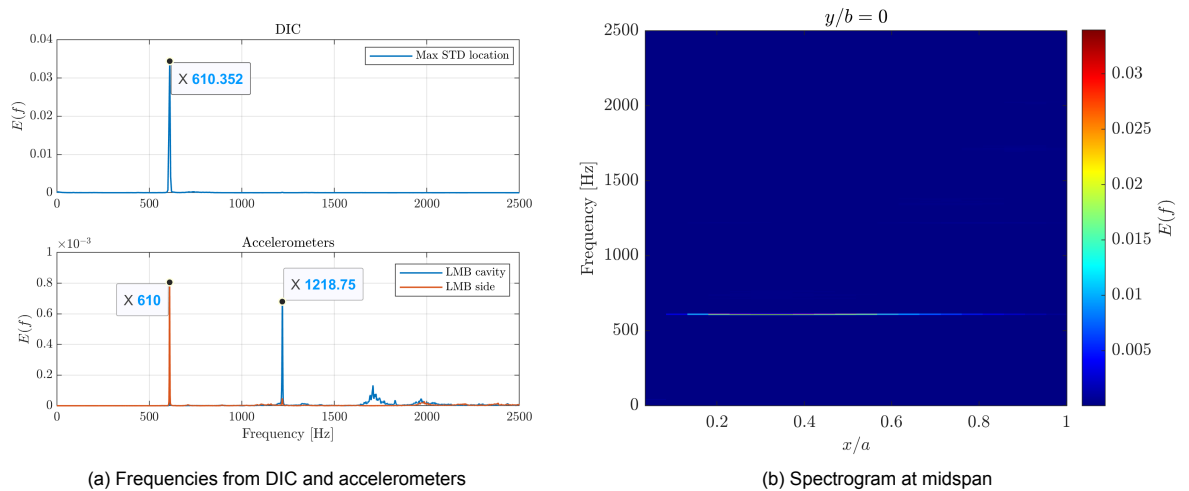


Figure 4.14: Wind tunnel vibrations with DIC measurements in shock-induced flutter of a CCCC1.5 flexible panel

In the case of shock-induced flutter of the same CCCC1.5 panel with a 12° shock generator and an inviscid shock location at 50% of panel chord length, the displacement measurement at the maximum standard deviation location of the panel has a characteristic frequency of 610 Hz, which is matched by the accelerometers with their peak at almost the same frequency (Figure 4.14a). There is a distinct secondary peak in the LMB cavity at 1219 Hz, which is not present in the DIC at all. Looking at the spectrogram in Figure 4.14b, this time the maximum energy carried by the 610 Hz frequency lies between $x_i/a=0.2$ and 0.5 , much upstream than in the case of free flutter (Figure 4.13b). When looked at closely, very faint traces of the ≈ 1219 Hz frequency can be observed between $x_i/a=0.2-0.4$ and beyond 0.6 .

Finally, DIC measurements were also done over a rigid panel, to quantify the noise arising from

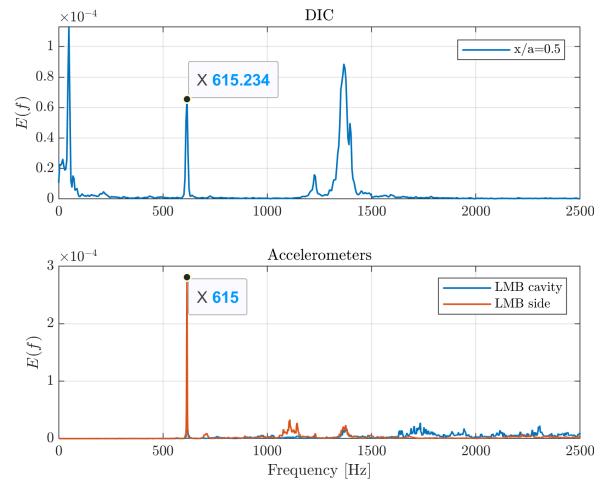


Figure 4.15: Wind tunnel vibrations with DIC measurements for SWBLI on rigid panel

different sources such as camera shaking, ground vibrations, etc. The accelerometers still pick up vibrations in the LMB at 615 Hz, as shown in Figure 4.15. The DIC response too shows a characteristic frequency of 615 Hz, which is a testament to the sensitivity of DIC as the panel is not fluttering but simply shaking with the LMB at that frequency. Some lower (≈ 40 Hz) and higher frequencies are also detected by the DIC, which are not present in the accelerometer readings, which could belong to noise not inherent to the physical setup, such as shaking of the camera setup.

4.5. Note on Fluid-Structure Interaction

In the simultaneous PIV-DIC measurements of Allerhand (2020) on shock-induced flutter of flexible CCFF1.5 panels, a basic check to confirm the existence of flow-structure interaction was to compare the frequencies of the separation shock foot motion from PIV and flutter frequency at a point on the panel from DIC. This was confirmed successfully in the work and the interlinked frequencies of both were also distinct from the accelerometer frequency of 576 Hz.

For the case of the current study, Schlieren (flow) and DIC (structural) measurements were made separately, as the phenomenon of shock-induced panel flutter was shown to be both repeatable and periodic by Allerhand (2020). However, through all the DIC and Schlieren runs, wind tunnel vibrations of 605–640 Hz were found to drive the flutter frequency. Just as a confirmation, the frequency of the separation shock motion from Schlieren recordings (see section 3.4.3 and Figure 3.15 for the methodology and definitions used) was compared with the characteristic frequency obtained from DIC measurements under the same shock generator and shock impingement location, and both were found to agree to a reasonable degree, given that the Schlieren and DIC campaigns were conducted several weeks apart. Thus, it is safe to say that fluid-structure interaction was indeed observed in the current study, although the characteristic frequency were driven by the wind tunnel vibrations.

The example of shock-induced flutter of a CCCC1.5 panel with the 12° shock generator causing an inviscid shock impingement at 50% of panel chord is once again used for demonstration. As seen in Figure 4.16a, the separation shock is unsteady in nature with a characteristic frequency of 615 Hz (dictated by the LMB vibrations which were not measured for this run), as found from both the location of the shock foot and a stationary window near the shock foot (see Figure 3.15). In contrast, the frequency of the maximum STD location on the fluttering panel is 610 Hz, same as the LMB vibration frequency. As long as both the separation shock motion and the DIC produce similar characteristic frequencies, it is sufficient to confirm fluid-structure interaction. Of course, the matter of separation shock displaying a distinct frequency of motion is also subject to the shock generator used and the shock impingement location, as will be explored in the next chapter.

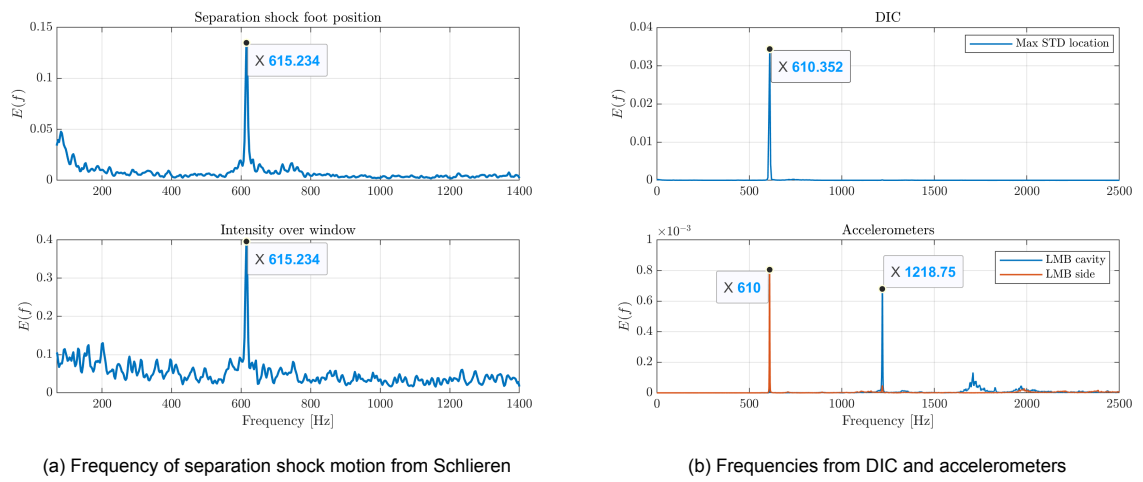


Figure 4.16: Comparison of frequencies for shock-induced flutter of a CCCC1.5 panel with 12° shock generator and inviscid shock location of $x_i/a=0.5$

5

Effect of Shock Strength and Shock Location

In this chapter, the role of the impinging shock strength and location in influencing the SWBLI and panel flutter characteristics will be analyzed. In section 5.1, the SWBLI on CCCC1.5 flexible panels will be studied with the help of Schlieren for the two different shock strengths used, with emphasis on the change in the interaction lengths and characteristic frequencies of the shock motion. Comparisons are also made with canonical SWBLIs on rigid panels. Next, the influence of shock strength on panel flutter will be looked at in section 5.2, through the mean and STD shapes of the panel, displacement-vs-time history, correlation maps, characteristic frequencies, and POD modes. A short discussion on how panel shape affects the SWBLI structure is presented in section 5.3. Following that, in section 5.4, the focus will be on the influence of varying the shock impingement location on the SWBLI on a flexible panel, in terms of the interaction lengths, characteristic frequencies, and energies associated with the unsteady motion of the separation shock. Finally, section 5.5 will discuss the effect of shock location on the flutter of the panel, through an exploration of mean and STD shapes at midspan, the characteristic frequencies (and respective energies), spectrograms along the chord, and variation in POD mode relative energies.

5.1. Effect of Shock Strength on SWBLI

While generating oblique shocks, a higher ramp angle results in a stronger shock (Anderson Jr, 2010), i.e., for the same freestream static pressure, the pressure downstream of the shock will be higher when the shock generating ramp has a greater inclination. In a canonical oblique SWBLI (on a flat, rigid plate), an increase in shock strength translates into an increase in the separated flow region (in case it was already separated before), or the onset of a separation region (in case there was no separation before). By recalling the mechanism by which shock-induced boundary-layer separation occurs (as explained in section 2.2), this can be understood simply as the stronger shock causing a more adverse pressure gradient experienced by the subsonic part of the boundary layer, which results in boundary layer separation occurring more upstream than in the case with a weaker shock. In this section, two cases are chosen for comparison: $\theta_{SG}=12^\circ$, $x_i/a=0.6$ and $\theta_{SG}=15^\circ$, $x_i/a=0.6$. The choice of the particular impingement location will become clear later on.

5.1.1. SWBLI Interaction Length

In Figure 5.1, the average Schlieren images (calculated as a simple average of all instantaneous frames recorded) are presented for both reference cases. It is clearly seen that separation does indeed happen much more upstream with $\theta_{SG}=15^\circ$, as expected, with the separation shock foot varying between the leading edge and $x_i/a=0.2$, compared to between $x_i/a=0.3-0.4$ for $\theta_{SG}=12^\circ$. In both cases, the interaction lengths (an indicator of the extent of separated flow) are also calculated from each instantaneous frame (the definition and methodology is described in section 3.4.3), and the mean values are tabulated in Table 5.1. While the expected jump in the interaction length is observed for both the flexible and rigid panels when θ_{SG} is increased, it is also seen that for the same θ_{SG} , the SWBLI on the

flexible panel has a higher interaction length. The latter observation shows that at the given shock impingement location, using a flexible panel instead of a rigid plate leads to an increased shock-induced flow separation, as also observed in various other experimental studies including [Allerhand \(2020\)](#) and [Daub et al. \(2016a\)](#). For $\theta_{SG}=12^\circ$, the difference in mean L_{int} between the rigid and flexible panels is $\approx 0.5\delta_{99,\infty}$ and for $\theta_{SG}=15^\circ$, it is $\approx 0.4\delta_{99,\infty}$.

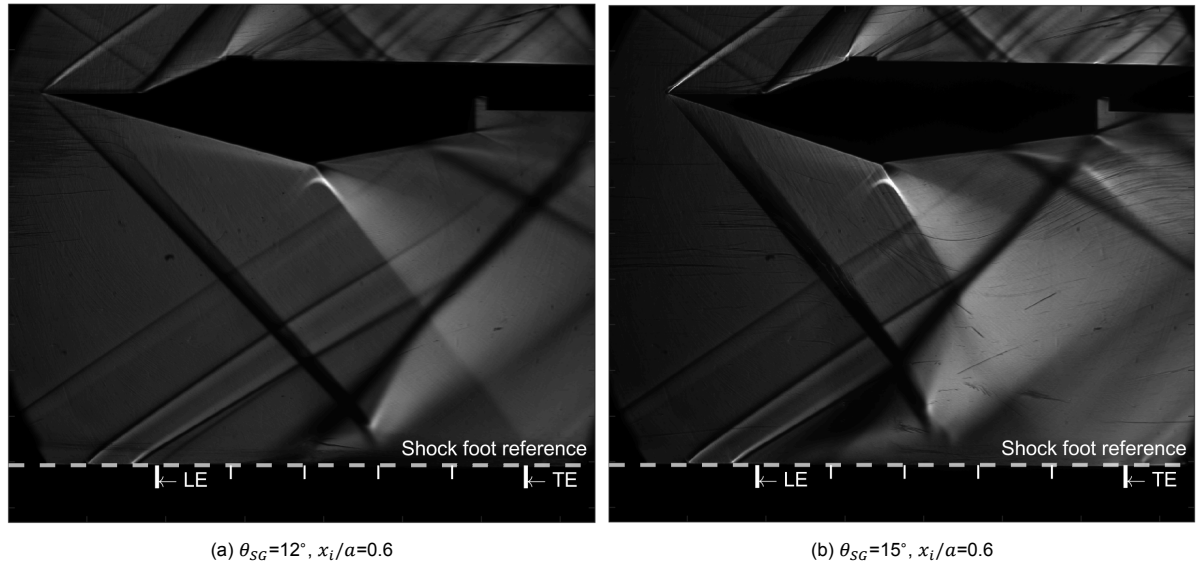


Figure 5.1: Average Schlieren images for different shock strengths

	$\theta_{SG}=12^\circ$		$\theta_{SG}=15^\circ$	
	L_{int} [mm]	$L_{int}/\delta_{99,0}$	L_{int} [mm]	$L_{int}/\delta_{99,0}$
CCCC1.5 flexible panel	38.54	7.41	59.39	11.42
Rigid plate	35.90	6.90	57.35	11.03

Table 5.1: Mean SWBLI interaction lengths for different cases

5.1.2. SWBLI Characteristic Frequencies

By tracking the positions of the impinging shock foot and separation shock foot in time, it was possible to process the signals using Welch's method to extract the dominant frequencies of their unsteady motion. The results for the flexible panel with both shock generators is presented in [Figure 5.2](#). This time, the spectrum is shown in terms of the total energy, $f \cdot E(f)$, which is normalized with the standard deviation of the time-resolved signal. As mentioned before, the sampling rate of the Schlieren was 2800 Hz, which results in a maximum resolved frequency of 1400 Hz in accordance with the Nyquist theorem. Since the impinging shock originates at the shock generator and is not influenced by the panel flutter, no sharp peaks can be noticed in its spectrum, in either case. The separation shock is generated due to thickening of the boundary layer, and is clearly influenced by the flutter of the flexible panel and hence the separation shock foot demonstrates dominant peaks in its spectrum: 623.4 Hz (along with a second harmonic) for $\theta_{SG}=12^\circ$, and 609.8 Hz for $\theta_{SG}=15^\circ$. While no accelerometer measurements in the LMB were done during either of the runs, the value of the dominant frequencies is most likely from the vibrations of the LMB, which are seen to be driving the flutter of the panel and consequently the separation shock motion as well. Due to the significant influence of the LMB vibrations in determining the frequency of panel flutter, it is inconclusive whether a change in shock strength results in a change in the dominant frequencies of the separation shock motion as well.

Schlieren was also conducted with both shock generators and a rigid panel, and the same procedure of tracking both impinging and separation shock feet was employed to check for distinct frequencies in their motion, shown in [Figure 5.3](#). Since there is no periodic fluttering motion of the rigid plate, neither

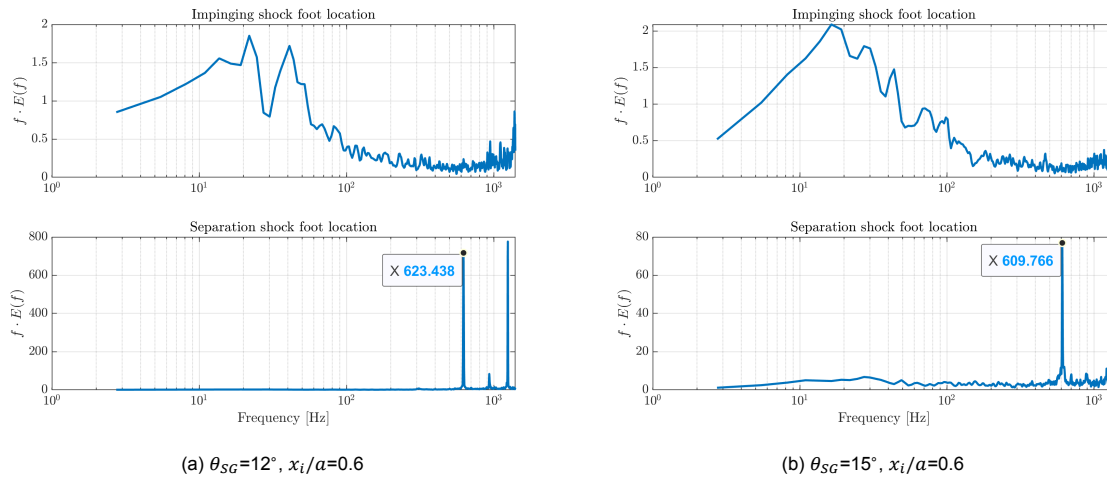


Figure 5.2: Frequency response of impinging and separation shock foot locations for CCCC1.5 flexible panel

the impinging nor the separation shock display any distinct characteristic frequencies.

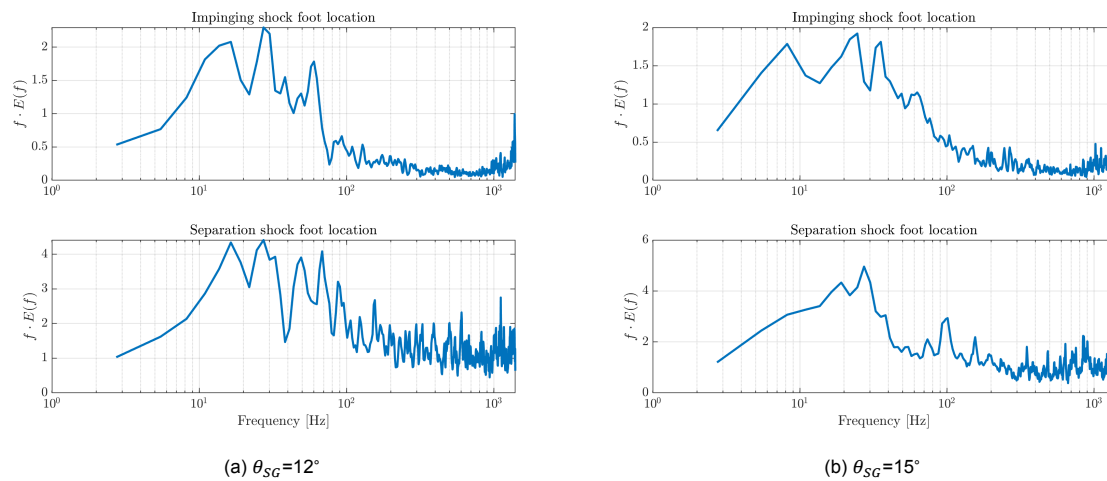


Figure 5.3: Frequency response of impinging and separation shock foot locations for rigid plate

5.2. Effect of Shock Strength on Panel Flutter

As shown in the previous section, increasing the impinging shock strength directly leads to a larger area of flow separation. The effect of this on the flutter characteristics of a CCCC1.5 flexible panel are explored in the current section. Similar to the previous section, $\theta_{SG}=12^\circ$, $x_i/a=0.6$ and $\theta_{SG}=15^\circ$, $x_i/a=0.6$ are chosen, along with the no shock generator (SG) case as well to illustrate the differences between shock-induced and free flutter.

5.2.1. Panel Shapes

The panel response is first studied using mean and STD of the out-of-plane displacement fields. In Figure 5.4, the mean shapes based on z/h , where h is the panel thickness and z is the out-of-plane displacement, for three cases are plotted: free flutter (no SG), $\theta_{SG}=12^\circ$, $x_i/a=0.6$ and $\theta_{SG}=15^\circ$, $x_i/a=0.6$ using the same scale for better clarity on the differences. In the No SG case, the mean shape is similar to an upward bump, and also has the highest peak among the three cases. With $\theta_{SG}=12^\circ$, the mean shape has both a crest (upstream) and a trough (downstream), separated by an angled node ($z=0$) which is upstream towards the edges and downstream towards the middle. The amplitudes of the peaks are noticeably smaller than the peak amplitude of the no SG case. The mean shape resulting

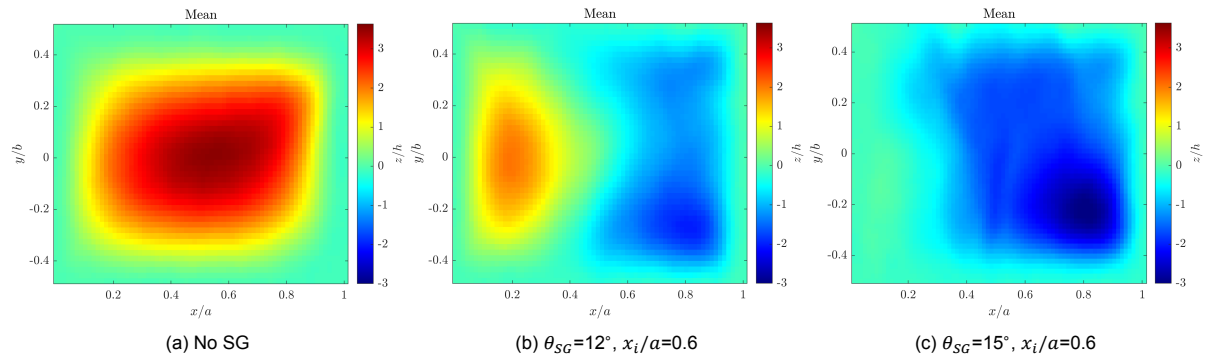


Figure 5.4: Mean panel shapes for different shock strengths

from $\theta_{SG}=15^\circ$ looks similar to the $\theta_{SG}=12^\circ$ case, but is different in proportions: the downstream trough is deeper, the upstream crest is barely higher than $z/h=0$ while the node is even more upstream for the former. The differences among the aforementioned cases can also be appreciated by looking at the mean shapes at the midspan, as shown in Figure 5.6a. The contrast in mean shapes across the three cases can be explained by considering the structure of the SWBLI. Without a shock generator, the mean shape here resembles the classical shape of free flutter: an upward convex bump. In the presence of a shock, pressure across it varies, and is much higher downstream of the shock. This causes the downstream trough in the shock-induced flutter cases, while the crest remains in the upstream region where pressure is lower (and same as the pressure in the no SG case). The shock is stronger with $\theta_{SG}=15^\circ$ which leads to a higher pressure jump downstream of the shock, leading to the deeper trough. The stronger shock also results in a larger separation region. Hence, for the same impingement location, a panel exposed to a stronger shock will experience a post-shock high-pressure region that extends more upstream compared to the case with a weaker shock. It is also important to note that control of the cavity pressure below the panel can lead to drastically different results.

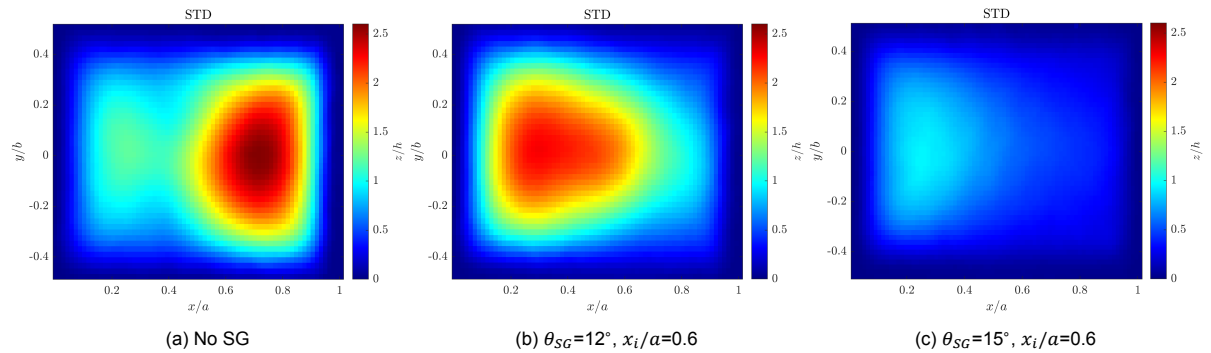


Figure 5.5: STD panel shapes for different shock strengths

The extent of fluctuations about the mean are indicated by plots of standard deviation (STD) of the out-of-plane displacements, scaled by the panel thickness h and shown in Figure 5.5, while the same shapes at the midspan of the panels is shown in Figure 5.6b. Again, the STD values are scaled using the global maxima of the three cases, and from a glance it is clear that the No SG case has the maximum STD value of all. The maximum STD location represents the point on the panel that is most energetic. Theoretically, the maximum STD location for free flutter of thin panels occurs at the 3/4th chord point: $x/a=0.75$ (Meng et al., 2020), and the maximum STD location in the current investigation for the No SG case is observed to be very close to that value ($x_i/a \approx 0.72$). In comparison, the maximum STD point is located more upstream for both shock-induced flutter cases. The free flutter case also shows the maximum STD amplitude among the three, followed by $\theta_{SG}=12^\circ$ and $\theta_{SG}=15^\circ$. This trend seems specific to the CCCC boundary condition of the panel, as Allerhand (2020) observed that in case of a CCFF1.5 (free side edges) panel, free flutter had a lower amplitude than shock-induced flutter. Between the two shock-induced cases investigated in this study, the higher post-shock pres-

sure of $\theta_{SG}=15^\circ$ seems to lead to a more suppressed flutter with significantly lower mean and STD amplitudes compared to $\theta_{SG}=12^\circ$.

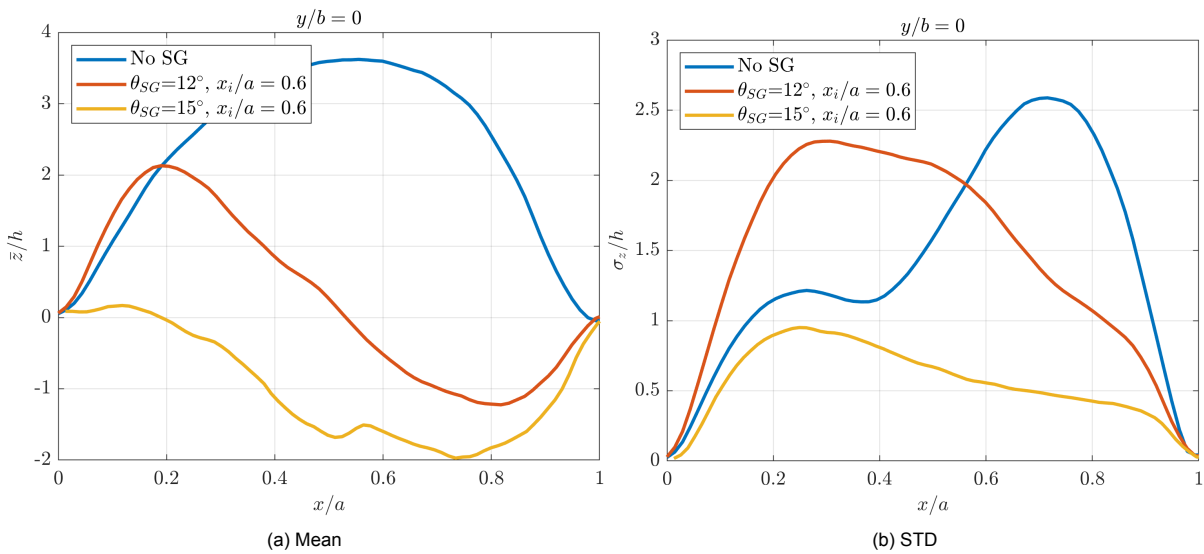


Figure 5.6: Mean and STD shapes at midspan of the CCCC1.5 flexible panel

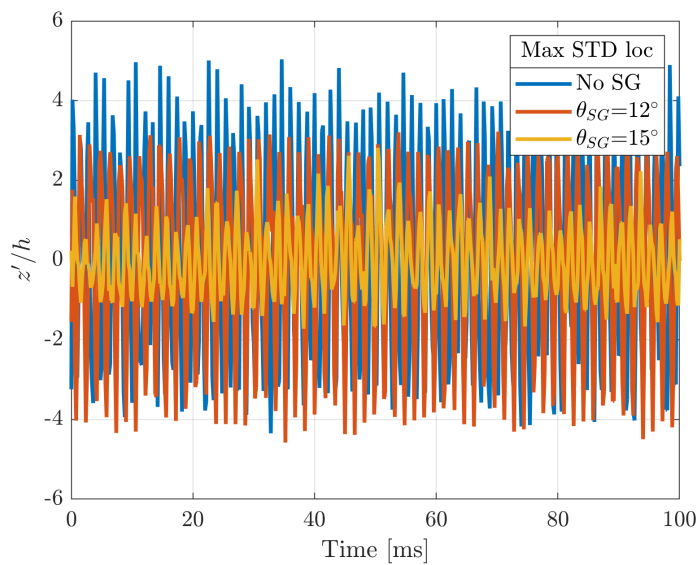


Figure 5.7: Displacements about the mean at the maximum STD locations

The difference in flutter amplitudes is also analyzed with the help of displacement-time graphs, as shown in Figure 5.7. The displacements are shown as fluctuations about the mean ($z' = z - \bar{z}$) scaled by the panel thickness h over a time period of 100 ms. As a rule of thumb, flutter limits are considered as $z'/h=1$, and it is clear that all cases surpass that limit. Among the three cases, shock-induced flutter with $\theta_{SG}=15^\circ$ has the lowest amplitude, reiterating the earlier observation of a more "suppressed" flutter with a stronger impinging shock when compared to the other two cases for a CCCC panel.

A crude method to investigate the phase relationship between different parts of the fluttering panel is to build cross-correlation maps over the panel. This has been done by picking the displacement over the maximum STD location as a reference signal for performing cross-correlation with the displacement signal over every other point on the panel, and the plots of the resulting correlation coefficients

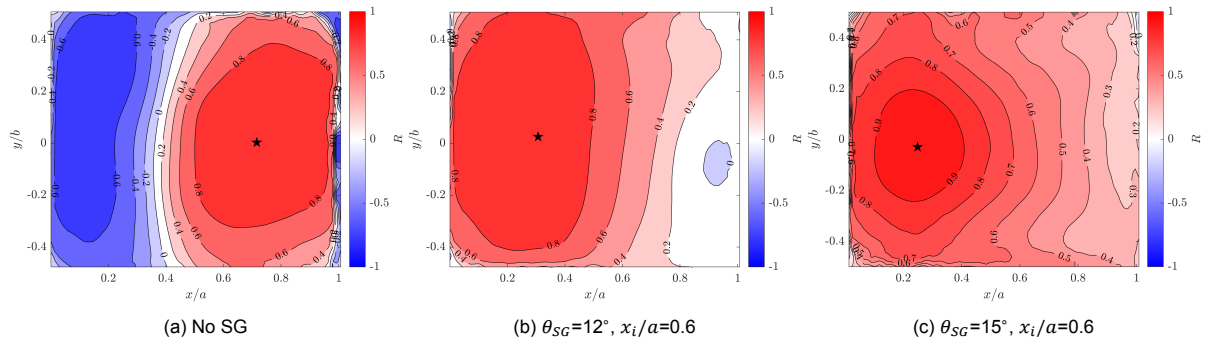


Figure 5.8: Correlation maps with respect to displacement at maximum STD location for different shock strengths

are shown in Figure 5.8. The maximum STD locations are marked with a black star. For the no shock case (Figure 5.8a), the maximum STD location is at $\approx 0.72a$, and two distinct regions of the flutter can be seen: the red region downstream, representing positive correlation coefficients, i.e., the region where the displacements are in phase with the displacement at the maximum STD location, and the blue region representing negative correlation coefficients, which denote displacements that are out-of-phase with respect to the maximum STD location. This means that during any instant of the free flutter, the upstream region of the panel is displaced oppositely to the downstream region. Deeper the colour, more intense the phase relationship. A zero-correlation region is also observed at $\approx 0.4a$ for the no SG case. In contrast, neither of the two shock-induced cases show an out-of-phase region with respect to the maximum STD location, which is at $\approx 0.3a$ and $\approx 0.24a$ for $\theta_{SG}=12^\circ$ and $\theta_{SG}=15^\circ$, respectively. With no negatively correlated regions, it means that during shock-induced flutter, the entire panel displaces in the same sense, i.e., either upwards or downwards.

To conclude, the differences in panel shapes between free and shock-induced flutter were illustrated, and it was seen that for a CCCC panel, shock-induced flutter has lower amplitudes, owing to the post-shock pressure jump which suppresses the panel. Another key difference between the two was that there were no out-of-phase regions observed in shock-induced flutter. Between the two shock-induced flutter cases, it was seen that an increase in shock strength mainly resulted in further suppression of the flutter amplitude, leading to lower mean and STD amplitudes.

5.2.2. Flutter Characteristic Frequencies

The displacement-vs-time signal at any point on the panel is sufficient to extract characteristic frequencies of the flutter motion. In the results presented in this section, two points on the panel were selected: the maximum STD location and the midspan, midchord ($x/a=0.5, y/b=0$) in the coordinate system used) point. The DIC images were recorded at a rate of 5000 Hz, thus frequencies upto 2500 Hz are resolved. Simultaneous accelerometer readings were also taken in the LMB at an acquisition rate of 8533.34 Hz to compare the LMB vibrations with the flutter. In Figure 5.9, the spectra of the DIC measurements are plotted as PSD alongside the response of the accelerometers, for three cases: no SG, $\theta_{SG}=12^\circ, x_i/a=0.6$ and $\theta_{SG}=15^\circ, x_i/a=0.6$.

From the DIC of the no SG case, the clear dominant peak is at 757 Hz, matched by a peak of 754 Hz in the LMB cavity and side. As discussed in the previous chapter, the frequency of LMB vibrations drives the flutter frequency. There is also the second harmonic at 1506 Hz in the LMB that leads to 1509 Hz appearing in the DIC, but none of the other higher frequency peaks in the LMB result in a response in the flutter. Interestingly, a couple of peaks at 586 Hz and 928 Hz appear in the DIC, albeit with significantly lower energies compared to the 757 Hz and 1509 Hz peaks. It is possible that these are a natural response of the panel rather than influenced by the LMB vibrations.

In case of shock-induced flutter with $\theta_{SG}=12^\circ$, a 610 Hz peak is observed at both DIC locations with a lower PSD peak at 1226 Hz. Both frequencies are clearly excited by the 614 Hz and its second harmonic at 1226 Hz found from the LMB accelerometer readings. Even the separation shock position spectra in Figure 5.9b shows both first (623 Hz) and second (1245 Hz) harmonics. For the $\theta_{SG}=15^\circ$

case, the most dominant peak from both DIC locations is found at 605 Hz, which seems to be driven by a 604 Hz peak in the LMB. The second harmonic in the LMB at 1207 Hz also excites a response in the panel at 1206 Hz. However, for the same SG the separation shock does not show a second harmonic in [Figure 5.9c](#), but only a dominant peak at 610 Hz.

The observations made from the frequency responses of the DIC are similar to what was seen from the motion of the separation shock from Schlieren: the flutter, and consequently, the separation shock unsteadiness, are both driven by the LMB vibrations, which seem to be practically independent of the impinging shock strength (in terms of frequency value). Thus, it is not clear whether the panel response frequencies would get altered because of a change in shock strength or not.

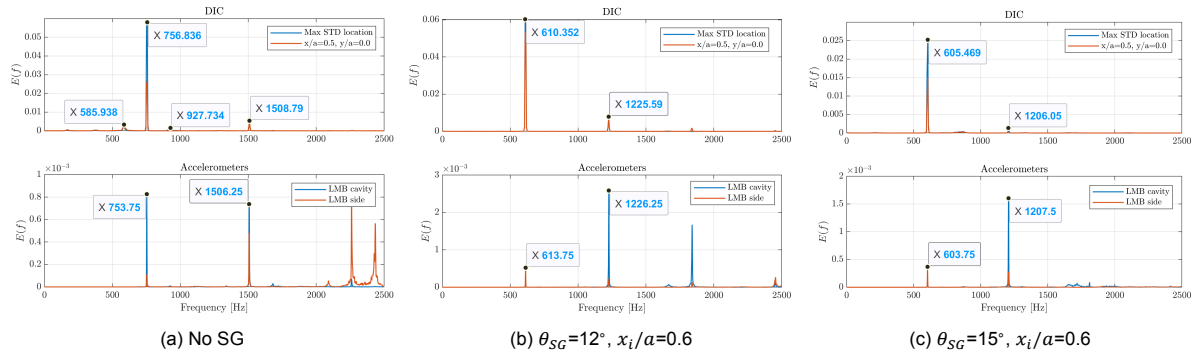


Figure 5.9: Characteristic frequencies from DIC and accelerometers

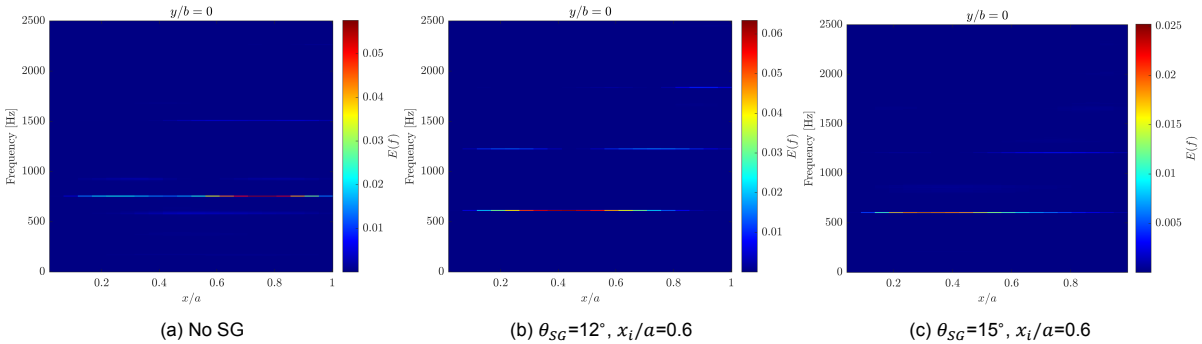


Figure 5.10: Spectrograms along panel chord from DIC along panel midspan ($y/b=0$)

The extent to which the characteristic frequencies exist over the panel are studied by plotting spectrograms, which as shown in [Figure 5.10](#) are along the midspan ($y=0$ in the current coordinate system) of the panel. The dominant frequencies in each case, as already recorded in [Figure 5.9](#), are seen to be present across the entire length of the panel (except very near to the leading and trailing edge, which being fixed do not show any unsteadiness anyway). The trend in change of the maximum PSD location of the characteristic frequencies in the spectrograms among the three cases seems similar to the trend observed in the change of maximum STD location, previously discussed in [Figure 5.8](#). For the no SG case, the maximum PSD of the dominant frequency (757 Hz) occurs at $\approx 0.8a$ while its maximum STD location was at $\approx 0.72a$. In case of $\theta_{SG}=12^\circ$, the maximum PSD of the dominant frequency (610 Hz) shifts to $\approx 0.45a$ when its maximum STD location was at $\approx 0.3a$, while for $\theta_{SG}=15^\circ$ the maximum PSD location (of the dominant frequency of 605 Hz) shifts upstream to $\approx 0.3a$ and its maximum STD location changes to $\approx 0.24a$. This shows that the maximum STD location is indeed a rough indicator of the location which contains the greatest vibrational energy.

Also, the second harmonic at 1508 Hz as observed for the no SG case in [Figure 5.9a](#) is seen to exist only beyond $x/a=0.4$ in the spectrogram ([Figure 5.10a](#)). Traces of both the 586 Hz and 928 Hz seen in [Figure 5.9a](#) are also observed in various streamwise extents. As for the $\theta_{SG}=12^\circ$ case, second

harmonic of the dominant frequency at 1226 Hz is also observed across various extents of the panel excluding the max STD location, while a third harmonic can also be distinguished beyond $x/a=0.7$. Finally, with $\theta_{SG}=15^\circ$, the second harmonic can be seen in $x/a < 0.4$ & $x/a > 0.6$.

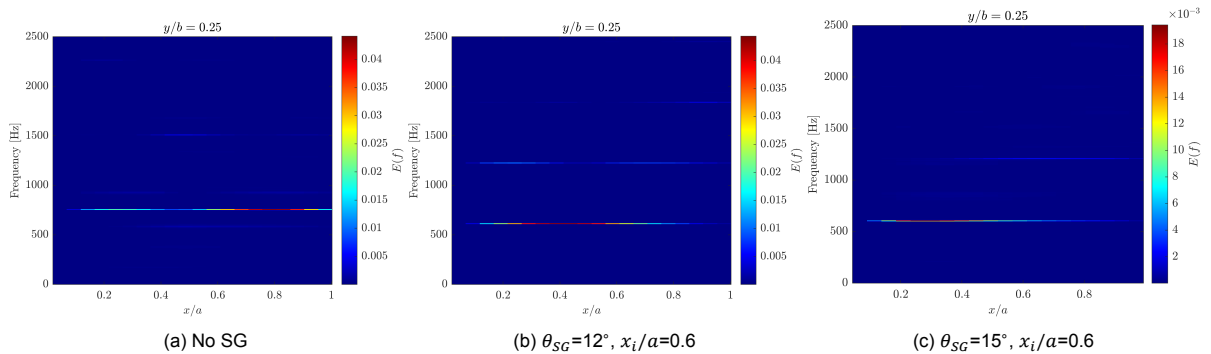


Figure 5.11: Spectrograms along panel chord from DIC away from panel midspan ($y/b=0.25$)

Spectrograms are also plotted at an off midspan location at $y/b=0.25$ in Figure 5.11 to compare with the midspan spectrograms. The first clear distinction between $y/b=0$ and $y/b=0.25$ spectrograms is the decrease in PSD, as indicated by the colourbar limits. Thus, towards the edges, flutter is less energetic when compared to the midspan. While the primary dominant frequencies in each of the cases remain similar in chordwise extents between both spanwise locations, the second harmonics of the same frequencies differ in their extents. The same observations were also made for spectrograms at $y/b=-0.25$, which are not shown here.

5.2.3. Flutter POD Modes

For investigating the mode shapes that dominate the flutter of the panel in a particular condition, POD is employed on the spatio-temporal dataset obtained using DIC. As discussed before, the particular algorithm used is the Singular Value Decomposition (SVD), which processes the initial data to reveal spatial modes, their energies (Σ) and corresponding time coefficients. The SVD algorithm is run on fluctuations about the mean of displacements, such that only the dynamics of flutter are resolved without including the time-average (or mean) shape. The spatial modes produced by the SVD are in order of their relative energy content, i.e., mode 1 has the highest energy, mode 2 has the second highest energy, and so on. Relative energies, calculated as $\Sigma/\text{sum}(\Sigma)$, are also plotted for the first 10 modes. The time coefficients are processed using Welch's method to extract dominant frequencies of each spatial mode. The POD mode shapes shown in the section have been normalized with respect to the maximum displacement value of each mode, and for comparison, it is only required to observe the phase relationship between different regions in a mode shape, rather than the magnitudes or exact sense (positive or negative) of displacement. The modes are identified using a simple and commonly employed naming convention for study of flutter (also used by Brouwer et al. (2021b)), where each mode is associated with an integer pair, (m, n) , such that m denotes the numbers of peaks (or valleys) the shape exhibits along the spanwise direction of the panel, while n corresponds to the number of peaks/valleys in the streamwise direction. The usage will become clear in the subsequent discussion.

The first three POD mode shapes for free flutter of the CCCC1.5 panel are shown in Figure 5.12a, along with the relative energies of the first 10 POD modes. The first, and the most energetic, POD mode shows a (1,2) shape, i.e., a single peak in the spanwise and two peaks in the streamwise direction exist. Again, it should be noted that the positive or negative sense of the displacements as indicated by the colour mapping is unimportant, only the number of peaks/valleys are considered for unique identification. The second POD mode shape is also a (1,2) shape, with only one peak in the spanwise extent and two peaks in the streamwise direction. Both peaks in each of the mode shapes are out-of-phase with each other, and the proportions are slightly different between the two shapes, which is not unexpected from experimental data. The first two modes also exhibit spanwise symmetry, an indication that there is no torsional contribution to either mode, only bending. The third POD mode has a (3,1) shape, with alternating phases across the span. Next, the relative energies show that the

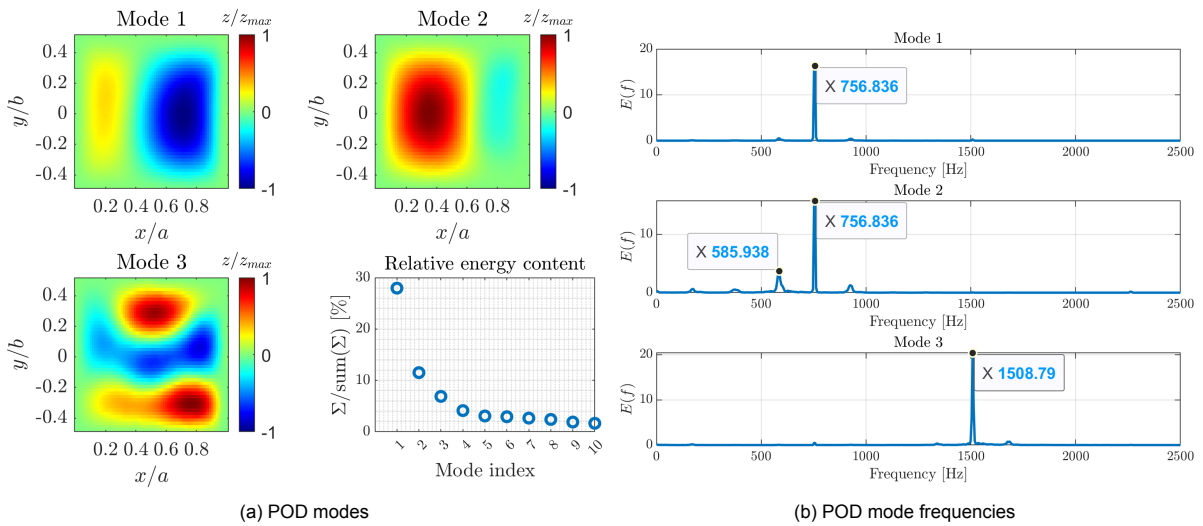


Figure 5.12: (a) POD modes and (b) corresponding frequencies for flexible panel with no SG

first two POD modes contribute close to 40% of the total flutter energy, while the third mode onward each contributes less than 8% to the energy. This asymptomatic nature in the variation of POD mode energies is typical, and only serves to help in identifying how many of the first few modes contribute significantly to determining the flutter. In this case, the first two modes are the most significant given the difference in relative energies with the third mode onward. Finally, the dominant frequencies of the first three modes are shown in Figure 5.12b, and it is evident that the LMB vibrations for the free flutter case at 754 Hz (seen in Figure 5.9a) influence the flutter and consequently the characteristic frequency of the most energetic mode at 757 Hz is also driven by the same frequency, while the second POD mode also shows the 757 Hz frequency with a high PSD, alongside a 586 Hz peak with much lower PSD. The dominant frequency of the third mode is at 1509 Hz, which is also detected in the LMB at a slightly different yet practically equal 1506 Hz (see Figure 4.13a).

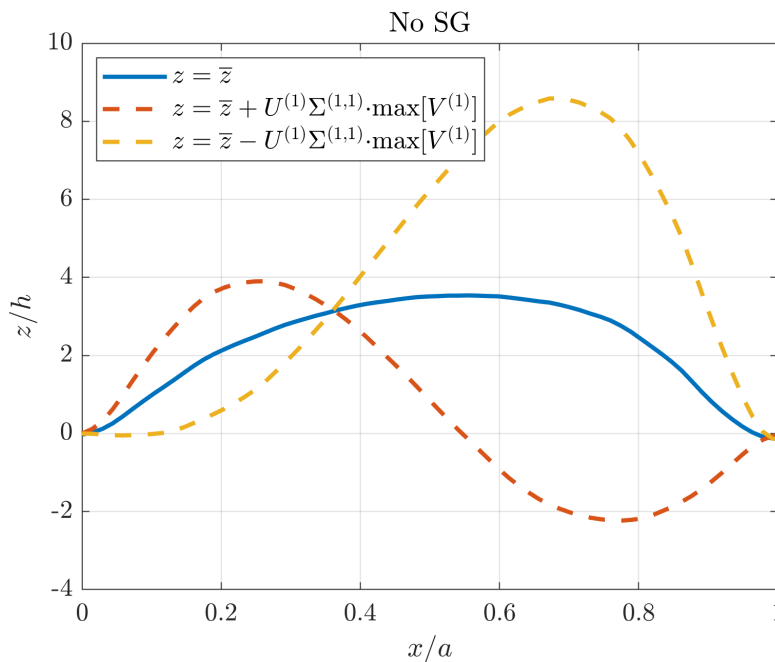


Figure 5.13: Effect of POD mode 1 on the mean shape at midspan of CCCC1.5 flexible panel with no SG

For the free flutter case, the influence of the first POD mode (shown in Figure 5.12a) on the mean panel shape (shown in Figure 5.4a) is investigated. Since both the mean and POD mode 1 shapes are largely spanwise symmetric, it is valid to limit the analysis only to the panel midspan. To do this, the first POD spatial mode ($U^{(1)}$) is multiplied with its corresponding mode energy value ($\Sigma^{(1,1)}$) and the maximum value of the corresponding time coefficient ($\max[V^{(1)}]$), to obtain the mode shape when its most energetic. The terms used for constructing the POD mode are explained in section 3.5.6. Then, the mode shape is added to and subtracted from the mean shape of the panel. All three shapes are shown in Figure 5.13. While the mean shape (solid blue line) is an upward bump (a solitary peak), the first POD mode was shown to be a (1,2) shape, i.e. with two out-of-phase peaks in the streamwise direction. Thus, when the first mode is added to the mean (red dashed line), it leads to a fall in the upstream shape (without a negative trough) accompanied by a rise in the downstream shape. When the first mode is subtracted from the mean, then the upstream part rises while the downstream portion form a trough with negative displacement. It is also clear from the difference in shapes between adding and subtracting the first POD mode that the magnitude of the upstream peak of the mode is lesser than that of the downstream peak, as was also seen in Figure 5.12a.

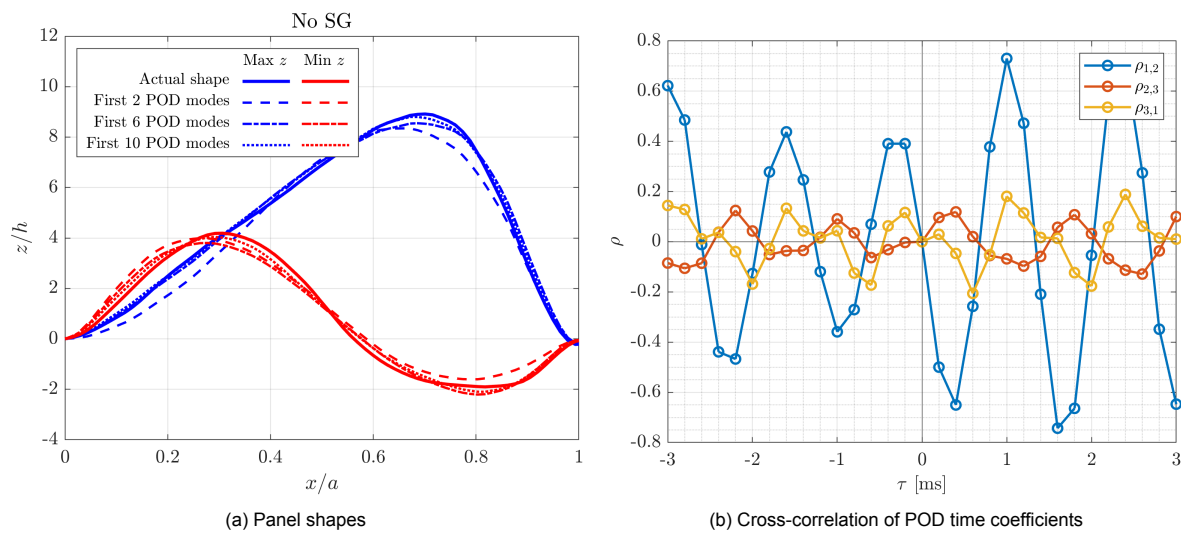


Figure 5.14: (a) Actual panel shapes (solid lines) at time instants when displacement at max STD location is maximum (blue) and minimum (red) compared to shapes predicted using first k POD modes: $k=2$ (dashed lines), $k=6$ (long dash-short dash lines), $k=10$ (dotted lines) and (b) cross-correlation between pairs of first 3 POD time coefficients for flexible panel with no SG

Splitting up the space and time-resolved DIC measurements using POD into constitutive spatial modes and temporal coefficients is useful for developing a reduced-order model (ROM) of the panel flutter using only the first few modes which carry the majority of flutter energy to see how well the actual panel shape can be approximated with a limited number of modes. The approximate shape using the first two (dashed), six (short-dash/long-dash) and 10 (dotted) POD modes are compared to the actual instantaneous shapes (solid) obtained from DIC measurements at the panel midspan when the out-of-plane displacement at the maximum STD location on the panel ($x/a=0.72$ for this case) is maximum (blue) and minimum (red) for the no SG flutter case in Figure 5.14a. With only 2 POD modes, which contain 39.5% of total energy, at maximum displacement (blue), the ROM predicts a good match with the actual shape in $x/a=0.4-0.6$ and $x/a > 0.85$, but under-predicts the displacements at other locations, including the maximum peak value, whereas for minimum displacement (red) it consistently deviates from the actual shape. When 6 POD modes are used, which contain 56.4% of total energy, a clear improvement is visible in both predictions over just 2 modes used. With 10 modes, containing 65% of total energy, a much better prediction of the peaks is achieved, except for the trough in the minimum displacement case, which is still over-predicted in magnitude. In Figure 5.14b, cross-correlation is calculated between pairs of the first 3 POD modes in an attempt to understand their relationship. At first glance, all 3 cross-correlation coefficients, $\rho_{1,2}$, $\rho_{2,3}$, $\rho_{3,1}$, show periodicity, confirming that all 3 POD modes are periodic in nature and also correlated. Also, all three ρ 's are also zero at zero time lag ($\tau=0$), confirming the mutually orthogonal nature of POD modes. The first two POD modes appear to

be the most strongly correlated in this case, as suggested by the large amplitude of $\rho_{1,2}$ at $\tau=0.4$ ms, although the negative magnitude shows that the modes are out-of-phase. In contrast, the second and third mode seem to be in-phase with a weaker maximum correlation at the same time lag. Finally, the first and third POD modes are also out-of-phase, which is expected from looking at the previous two correlations, and have a maximum amplitude at a time lag of 0.6 ms.

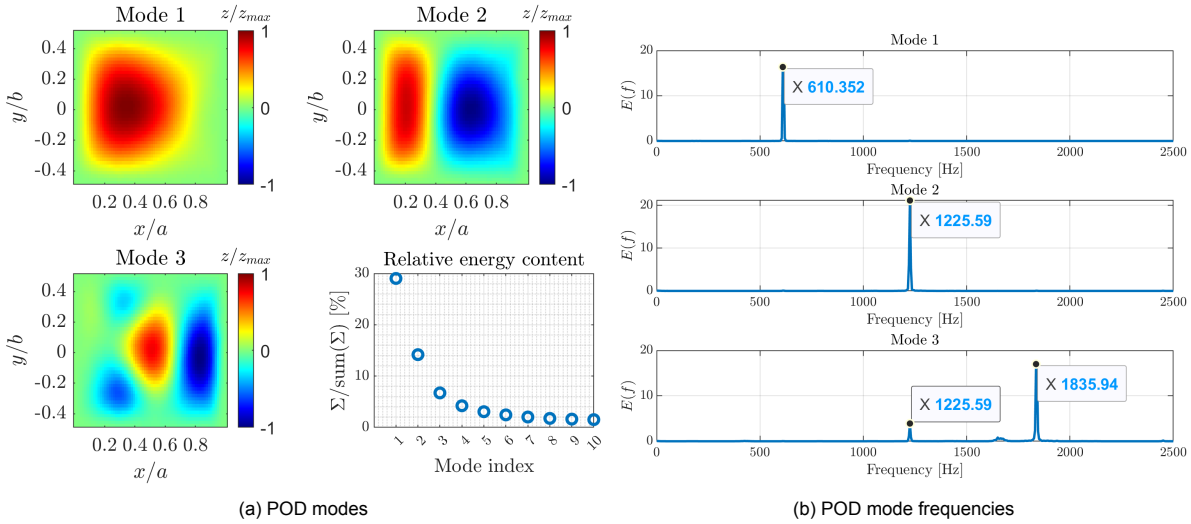


Figure 5.15: (a) POD modes and (b) corresponding frequencies for flexible panel with $\theta_{SG}=12^\circ$, $x_i/a=0.6$

From the POD of the $\theta_{SG}=12^\circ$, $x_i/a=0.6$ case, the mode shapes are shown in Figure 5.15a. For this case, the first and most energetic POD mode shows a (1,1) shape, i.e., a solitary peak over the entire panel. The second POD mode turns out in a (1,2) shape with two out-of-phase antinodes in the streamwise direction, while the third mode appears complex yet resembles a (1,4) shape with four peaks of alternating phase in the streamwise direction. The first two modes again exhibit spanwise symmetry, confirming the absence of any torsional contribution. These are, of course, very different from the POD mode shapes seen for the no SG case. The relative energy of the first mode is approximately at 30% while the second mode has a relative energy content of almost 14%, and the third mode contributes just above 7% to the overall energy of flutter. Contributions of fourth mode onward is increasingly less than 4%, and hence much less significant. In terms of frequency content of the various modes, as shown in Figure 5.15b, they are again influenced by the LMB vibrations at 614 Hz and its second and third harmonics at 1226 Hz and 1840 Hz (see Figure 5.9b). The first POD modes shows a characteristic frequency of 610 Hz, the second shows 1226 Hz, and the third mode contains both 1226 Hz as well as 1836 Hz.

The POD mode shapes from the higher shock strength case of $\theta_{SG}=15^\circ$, $x_i/a=0.6$ are shown in Figure 5.16a. Similar to the previous case with lower shock strength, mode 1 remains a (1,1) shape, although with a more pronounced upstream bias in the location of the solitary peak. The second POD mode also remains a (1,2) shape with out-of-phase peaks, similar to the previous case. The third POD mode exhibits an approximate (2,1) shape, with two peaks along the spanwise direction extending throughout the streamwise direction, in contrast to the (1,3) shape shown by the third mode of the previous case with $\theta_{SG}=12^\circ$, $x_i/a=0.6$. The relative energies with the stronger shock are seen to be much lower, with the first mode contributing only around 20% and the second mode approximately 7%. In comparison, the contribution of the rest of the modes does not drop as drastically as the first two modes, with the third mode still contributing almost 5%. This shows that for the same shock impingement location, a stronger shock, which results in a larger extent of the panel to be affected by the flow separation, excites a flutter response in which the higher modes (in terms of mode index, with relatively low energies) contribute in a larger proportion to the total flutter energy. In terms of frequencies of the POD modes, the first modes shows a characteristic frequency of 605 Hz, which is practically the same as the primary frequency of the LMB vibrations at 604 Hz (see Figure 5.9c), while the second mode resonates with the second harmonic of the LMB vibrations at 1206 Hz. The third mode also shows a

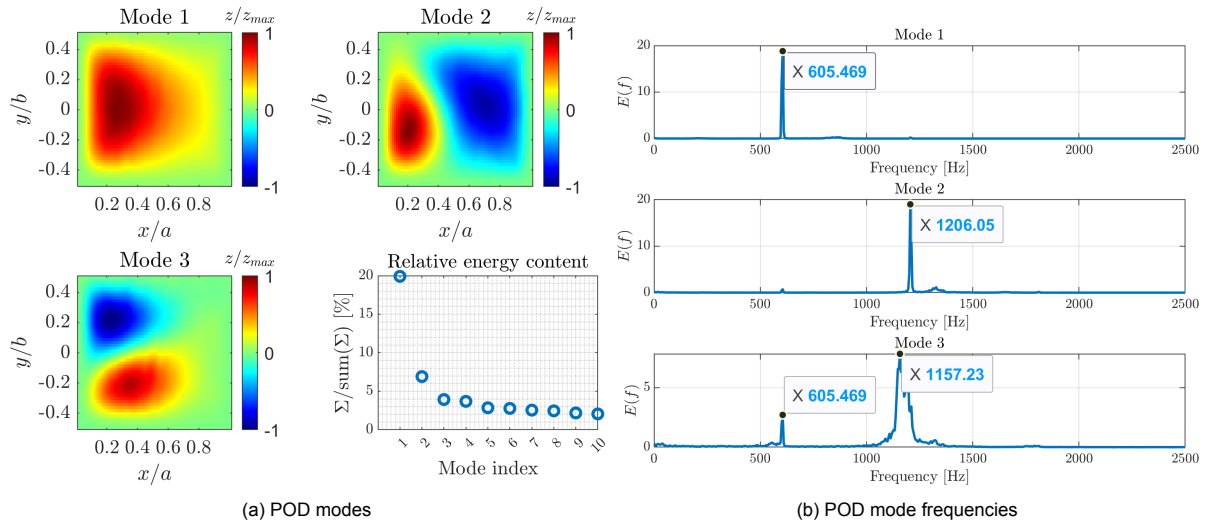


Figure 5.16: (a) POD modes and (b) corresponding frequencies for flexible panel with $\theta_{SG}=15^\circ$, $x_i/a=0.6$

605 Hz peak, along with a broad range of peaks in the 1127-1210 Hz range, indicating a more chaotic, less periodic response.

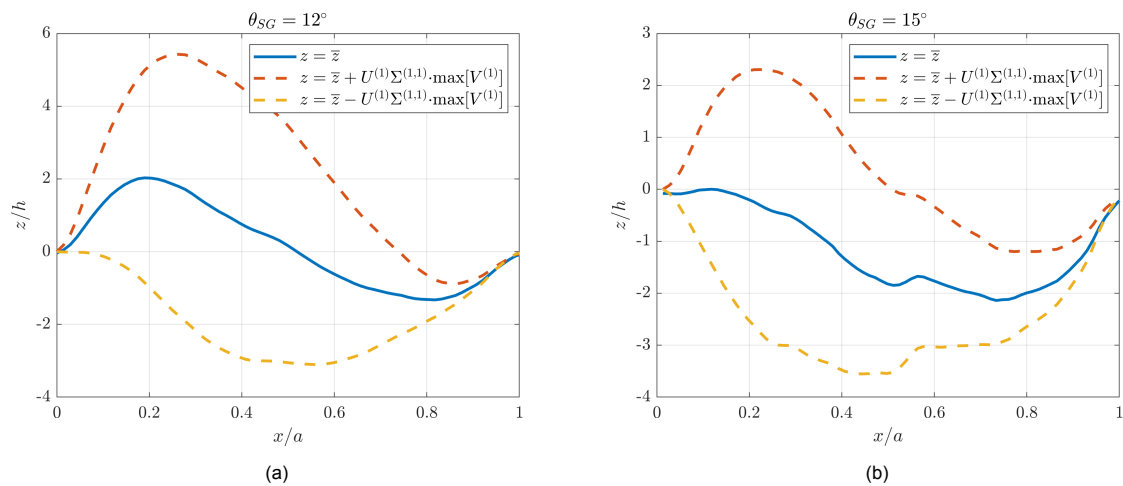


Figure 5.17: Effect of POD mode 1 on the mean flutter shape at midspan of CCCC1.5 flexible panel with (a) $\theta_{SG}=12^\circ$, $x_i/a=0.6$ and (b) $\theta_{SG}=15^\circ$, $x_i/a=0.6$

Similar to the analysis done in Figure 5.13, the effect of the first POD mode on the mean panel shape in case of shock-induced flutter is also investigated. In general, the mean shape for shock-induced flutter is a (1,2) shape with a positively displaced crest upstream and a negatively displaced trough downstream, as already seen in Figure 5.6a. The shock strength simply modifies the extent of the positive/negative displacement of the peaks. At the same time, the first POD modes in case of shock-induced flutter exhibited a (1,1) shape, i.e., with a solitary peak that was incidentally displaced upstream. Thus, the effect of the first POD mode on the mean shape in case of shock-induced flutter becomes clear from Figure 5.17: it simply raises or drags down the mean shape at once, to varying degrees across the span. As shown in Figure 5.17a, with $\theta_{SG}=12^\circ$, $x_i/a=0.6$, adding the first POD mode to the mean (solid blue line) leads to a more pronounced crest and a subdued trough (dashed red line), while subtracting the mode from the mean leads to no crest and only a downward peak (yellow dashed line). In case of $\theta_{SG}=15^\circ$, $x_i/a=0.6$, shown in shown in Figure 5.17b, the mean shape (solid blue line) did not have a pronounced crest, but adding the first POD mode to it creates the crest (dashed red line), whereas subtracting the mode leads to a more severe downward buckled shape (dashed yellow

line).

Since the first POD mode is a representation of the most energetic dynamics of panel flutter, crudely, it is also representative of how the panel motion is distributed across the panel in terms of phase relationships between different points and regions. A similar concept was explored with the correlation maps in Figure 5.8, where cross-correlation between the panel motion at the location of maximum STD (and hence, most energetic) and all other locations was calculated, leading to maps that revealed in-phase and out-of-phase regions. In hindsight, the correlation map for the free flutter case was similar in shape to the first POD mode of the same case, i.e., a (1,2) shape with out-of-phase peaks. This can be clearly seen by comparing Figure 5.8a and Mode 1 in Figure 5.12a, and it is also clear that in both, the magnitude of the upstream peak is lower than that of the downstream peak. Further, a (1,1) shape is also consistent between the correlation maps of the shock-induced flutter cases (Figure 5.8b and Figure 5.8c) and their corresponding POD Mode 1 shapes (Figure 5.15a and Figure 5.16a). This observation simply serves as validation of the POD method employed.

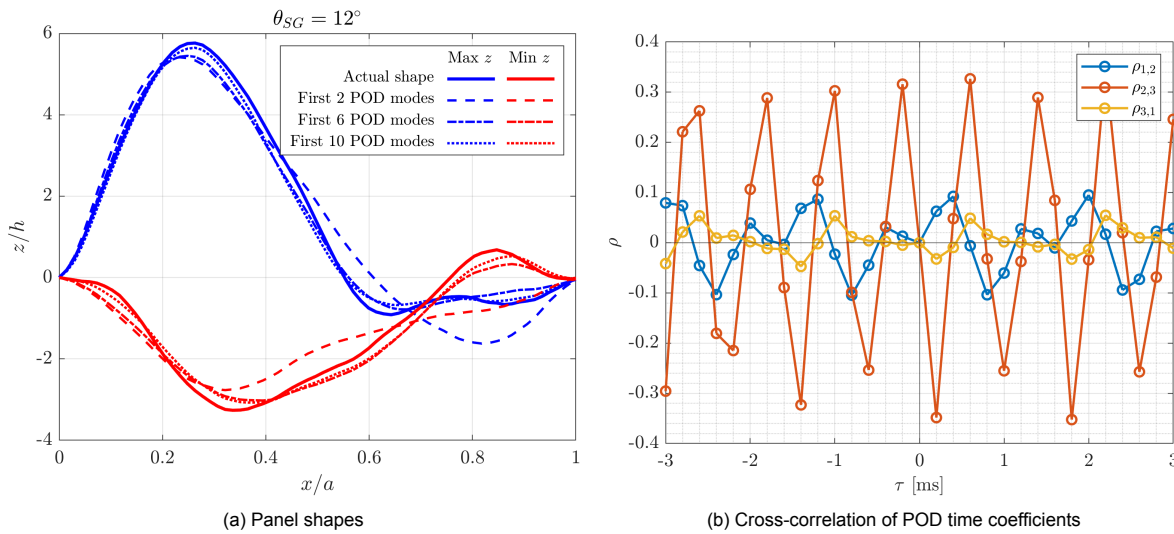


Figure 5.18: (a) Actual panel shapes (solid lines) at time instants when displacement at max STD location is maximum (blue) and minimum (red) compared to shapes predicted using first k POD modes: $k=2$ (dashed lines), $k=6$ (long dash-short dash lines), $k=10$ (dotted lines) and (b) cross-correlation between pairs of first 3 POD time coefficients for flexible panel with $\theta_{SG}=12^\circ$, $x_i/a=0.6$

The ROM with 2, 6 and 10 POD modes is tested on shock-induced panel flutter in a similar fashion as shown earlier in Figure 5.14a, for $\theta_{SG}=12^\circ$ in Figure 5.18a. When the displacement at the max STD location ($x/a=0.3$ for this case) is maximum (blue), using only 2 modes (dashed), which contain 43.2% of overall energy, grossly over-predicts the displacements (in magnitude) at the downstream half of the panel, while also under-predicting the crest amplitude. Large deviations between the actual shape and the shape calculated using 2 POD modes exists in the minimum displacement case (red) too, over almost the entire panel length. Using 6 modes (containing 59.6% of total energy) instead results in a significant improvement for both maximum and minimum cases, especially in the tricky shape beyond $x/a=0.6$ which the 2 mode model struggled with, and using 10 modes, which contain 66.5% of total energy, helps fill in the finer details compared to the 6 mode model. Looking at the cross-correlations between the first 3 POD modes in Figure 5.18b, where periodicity in time is confirmed, modes 2 and 3 seem most strongly correlated, in the negative sense with a time lag of 2 ms, whereas the first 2 modes are positively correlated with a time lag of 0.4 ms. Modes 1 and 3 show a negative correlation at $\tau=0.2$ ms, and all three modes are uncorrelated at zero time lag, as prescribed by the orthogonality between all POD modes.

Finally, the ROM is attempted for $\theta_{SG}=15^\circ$ and is shown in Figure 5.19a. In the case of maximum displacement at maximum STD location (blue), the crest and troughs are under-predicted in value by using only 2 modes (which contain merely 26.8% of the total energy, compared to more than 40% with $\theta_{SG}=12^\circ$), and surprisingly, even using 6 modes (40% of total energy) and 10 modes (49% of overall

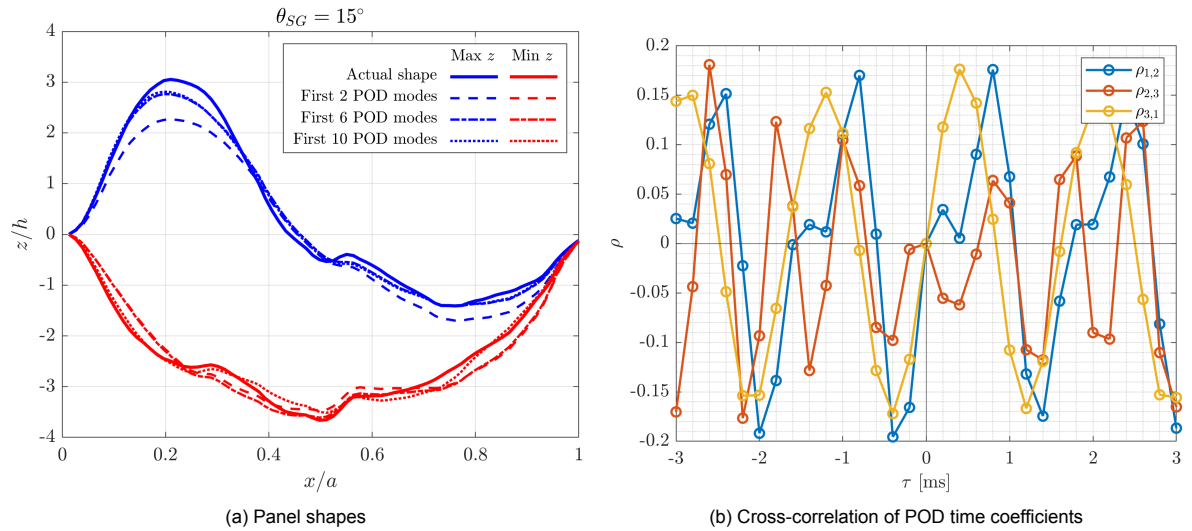


Figure 5.19: (a) Actual panel shapes (solid lines) at time instants when displacement at max STD location is maximum (blue) and minimum (red) compared to shapes predicted using first k POD modes: $k=2$ (dashed), $k=6$ (large dash-small dash), $k=10$ (dotted) and (b) cross-correlation between pairs of first 3 POD time coefficients for flexible panel with $\theta_{SG}=15^\circ$, $x_i/a=0.6$

energy) struggle to match the crest amplitude, but the latter two do offer improvements in other regions over the 2 mode model. When the displacement at the maximum STD location is minimum (red), the panel shape appears like a "bowl", and even using 10 modes is not sufficient to capture all the complexities of the instantaneous shape. Unlike the previous cases (Figure 5.14a and Figure 5.18a), where using 10 POD modes provided a very close match with the instantaneous shapes, in this case the predictions are seen to be lackluster. This is possibly due to a lower contribution of the first 10 modes to the total energy compared to the previous cases, and hence more modes may be required to approximate the shape with better accuracy. From the correlation between time coefficients shown in Figure 5.19b, both $\rho_{1,2}$ and $\rho_{3,1}$ show periodicity and high positive correlation at time lags of 0.8 ms and 0.4 ms, respectively. Even though $\rho_{2,3}$ appears periodic at first glance, the correlation amplitudes seem to vary significantly.

5.3. Coupling of Panel and Separation Shock Motion

As the flow and structural measurements were done separately and with different sampling rates, it is not possible to directly link the motion of the separation shock and the panel motion without knowing the phase relationship, i.e., which part of its motion cycle the panel is in at a particular time instant of the flow measurement. This was done by Allerhand (2020) with the simultaneous PIV/DIC measurements, and it was seen the SWBLI motion lagged behind the panel motion. However, it is still possible to qualitatively assess how panel motion drives changes in the flowfield through mutual coupling with the separation shock.

From the Schlieren measurements of the SWBLI formed over the CCCC1.5 flexible panel using $\theta_{SG}=12^\circ$ at $x_i/a=0.6$, two frames are picked out in which the separation shock foot (calculated as described in section 3.4.3) is downstream (Figure 5.20a) and upstream (Figure 5.20b) in a relative sense, the approximate location of the shock foot being marked with colored triangles in each figure. The horizontal dashed line indicates the zero-height of the LMB, and in Figure 5.20a the upward deflection of the panel upstream of the separation shock foot (blue triangle) relative to the dashed line can be seen. Due to the same upward deflection of the panel, a relatively strong leading-edge shock is also seen in the same figure (marked with a red arrow), which is expected as the upward deflection at the leading edge forces the flow to turn into itself, resulting in compression waves that quickly coalesce into a shock wave at the LE. In turn, the LE shock decreases the Mach number from its freestream value, which means the flow experiences a lower pressure ratio across the impinging shock due to the lower incoming Mach number. At the same time, the presence of the LE shock also raises the static pressure of the flow downstream of it, thus, not only is the flow at a higher pressure due to the LE shock

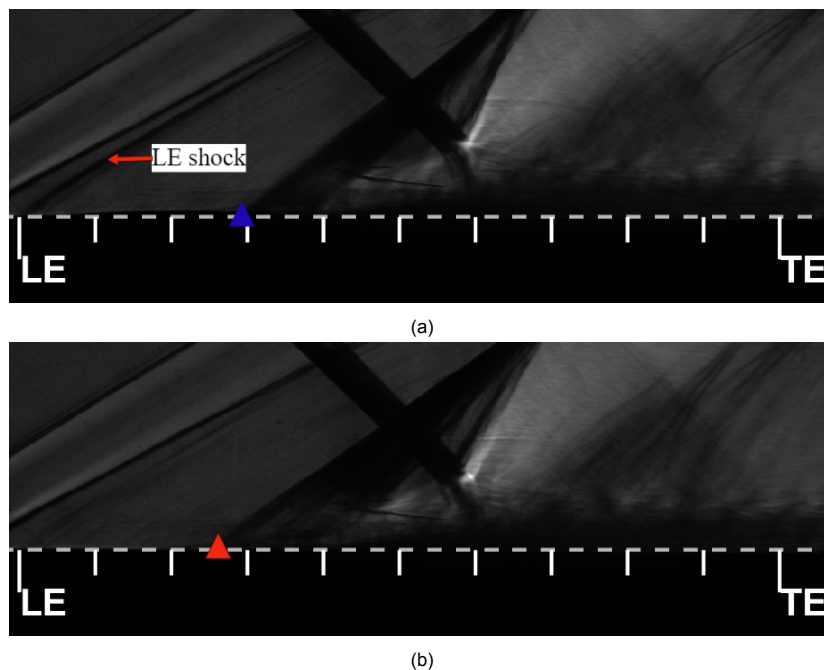


Figure 5.20: SWBLI organization at different time instances when separation shock originates (a) more downstream and (b) more upstream for flexible panel with $\theta_{SG}=12^\circ$, $x_i/a=0.6$

but it also experiences a lower pressure ratio across the impinging shock, which leads to a diminished adverse pressure gradient that the subsonic part of the boundary layer experiences. The effect of the lower adverse pressure gradient manifests into a more downstream origin of the separation shock.

In comparison, when the upward deflection of the panel at the leading edge is not as high, as seen in Figure 5.20b, the resulting leading edge shock is not prominent (i.e., weaker) and the separation shock is seen to originate even more upstream because the adverse pressure gradient due to the impinging shock is stronger when compared to the case with a high panel deflection and a strong LE shock. Unfortunately, the exact panel shapes at the given time instants cannot be determined, and it is also not possible to determine whether any time lag exists between the most upstream/downstream separation shock foot locations and most upwards/downwards panel deflections, as the flow and structural measurements are not synchronized in terms of phase of panel motion.

5.4. Effect of Shock Location on SWBLI

In the previous two sections of the chapter, the influence of shock strength in determining the behaviour of the SWBLI and panel flutter was investigated. In this section, the effect of varying the inviscid shock impingement location on the SWBLI characteristics will be explored. Of primary interest will be the effect on interaction lengths on a flexible panel, to determine whether there exists a particular impingement location such that the interaction length is minimum or less than the interaction length on a rigid plate, indicating a successful control strategy for shock-induced separation can be devised using flexible panels. Also, despite the knowledge that LMB vibrations determine the frequency of flutter and hence also the frequency of the separation shock motion, an analysis of the separation shock unsteadiness with varying shock impingement location will also be included.

It was already discussed that the placement of the shock generator inside the test section so as to achieve the desired shock impingement location was done manually after running calculations using inviscid oblique shock relations, since there was no high-precision system in place to vary the streamwise location of the shock generator. Thus, it was also important to know the actual shock impingement location achieved in practice and how much it deviated from the targeted ideal locations. Using the shock detection technique (described in section 3.4.3), it was possible to calculate the actual

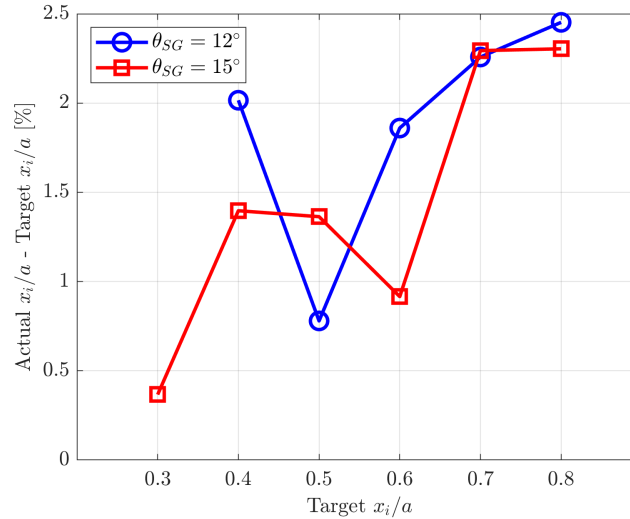


Figure 5.21: Errors in shock impingement location values achieved in practice for both $\theta_{SG}=12^\circ$ (in blue) and $\theta_{SG}=15^\circ$ (in red)

inviscid shock impingement location on the panel, and the errors between the target (ideal) x_i/a and actual x_i/a for different shock impingement locations is shown in Figure 5.21. It is seen that in most cases the error is limited to lower than 2% of chord length, only breaching the limit to a maximum of $\approx 2.5\%$ for $x_i/a=0.7, 0.8$. Since the variation in the impingement locations is desired to be 10% of chord length, the errors are considered to be acceptable. A combination of human error and deviation from the calculated impingement location from isentropic flow relations leads to the error.

The mean location of the separation shock foot (determined at approximately the height of the panel) is plotted for both the shock generators at different (actual) shock impingement locations, as a fraction of the chord in Figure 5.22. Between $\theta_{SG}=12^\circ$ and $\theta_{SG}=15^\circ$ for the same impingement locations, the separation shock foot is more upstream for the latter by at least $0.1a$, as the separated flow region is much higher with the stronger shock. In fact, at the two most upstream shock impingement locations, $x_i/a \approx 0.3$ and $x_i/a \approx 0.4$, the separation shock foot is even upstream of the leading edge of the panel ($x/a=0$).

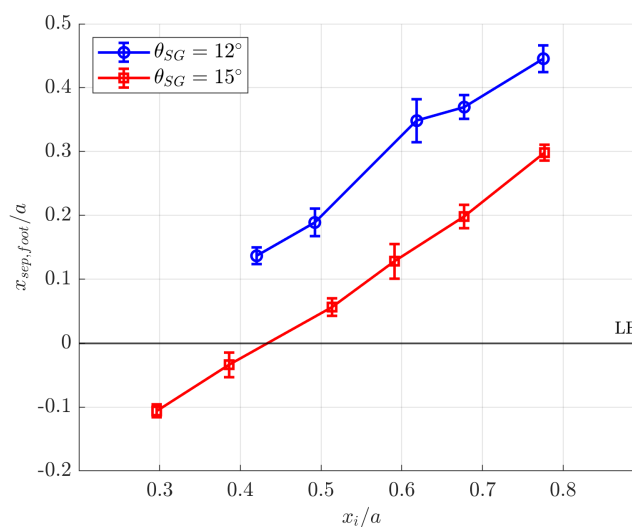


Figure 5.22: Mean location of separation shock foot at panel height for different shock impingement locations, for both $\theta_{SG}=12^\circ$ (in blue) and $\theta_{SG}=15^\circ$ (in red)

5.4.1. SWBLI Interaction Lengths

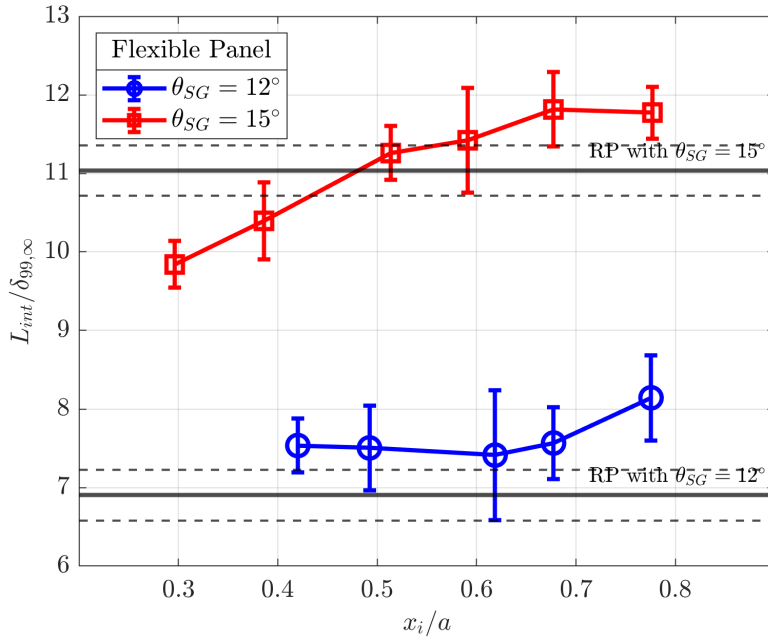


Figure 5.23: Mean interaction lengths on flexible and rigid panels at different shock impingement locations for both $\theta_{SG}=12^\circ$ (in blue) and $\theta_{SG}=15^\circ$ (in red)

The SWBLI interaction lengths, calculated from Schlieren images using the method described in section 3.4.3 and Figure 3.15, which serve as a measure of the extent of shock-induced flow separation, are plotted against the actual inviscid shock impingement locations for both $\theta_{SG}=12^\circ$ and $\theta_{SG}=15^\circ$ on the CCCC1.5 flexible panel. Interaction lengths are also calculated on the rigid plate with both shock generators, but since the rigid plate does not flutter, the interaction length is the same regardless of the shock impingement location. The interaction lengths are normalized with the freestream boundary layer thickness, $\delta_{99,\infty}$.

First of all, interaction lengths increase between $\theta_{SG}=12^\circ$ and $\theta_{SG}=15^\circ$ regardless of whether the rigid plate or flexible panel is used. With $\theta_{SG}=12^\circ$, the rigid plate has an interaction length of $\approx 7\delta_{99,\infty}$, as indicated by the solid black line marked "RP with $\theta_{SG}=12^\circ$ ", while the STD for the same are indicated with dashed black lines on either side. The flexible panel with the same shock generator shows a mean SWBLI interaction length clearly above that of the rigid plate for all inviscid shock impingement locations. In fact, there is very little change in the interaction length for $\theta_{SG}=12^\circ$, $x_i/a \approx 0.4-0.7$, and it only increases for $x_i/a \approx 0.8$, showing that a fluttering panel exacerbates shock-induced separation compared to a rigid plate.

For $\theta_{SG}=15^\circ$, the rigid plate shows an interaction length of $\approx 11\delta_{99,\infty}$, also indicated by a solid black line marked as "RP with $\theta_{SG}=15^\circ$ " along with the corresponding STD by dashed black lines on either side. Interestingly, the two most upstream shock impingement locations, $x_i/a \approx 0.3$ & 0.4 , on the flexible panel with the same shock generator, $\theta_{SG}=15^\circ$, seem to result in a shorter mean interaction length. It is important to recall that for both these shock impingement locations with $\theta_{SG}=15^\circ$, the separation shock is not coupled with the fluttering motion of the panel because the foot falls upstream of the panel leading edge, as seen in Figure 5.22. At the next shock impingement location, $x_i/a \approx 0.5$, the mean interaction length on the flexible panel becomes greater than that corresponding to the rigid plate, but still lies within the upper STD limit of the latter. The mean interaction length on the flexible panel continues increasing as the shock impingement location goes to $x_i/a \approx 0.6$ and 0.7 , and slightly decreases at $x_i/a \approx 0.8$ but still remains clear of the mean+STD interaction length on the rigid plate.

In conclusion, a fluttering flexible panel is not an effective shock-induced separation control method

when the separation shock is coupled with panel motion, regardless of the inviscid shock impingement location. With fluttering panels, an upward curvature of the fixed leading edge results in a leading edge shock, which reduces the freestream Mach number that the flow just above the panel experiences. Thus, the flow near the panel that encounters the oblique impinging shock becomes more susceptible by virtue of the loss in streamwise momentum that the leading edge shock causes, and, as a result, the separation region can be expected to be larger than for SWBLIs over flat, rigid panels. However, when the particular combination of the shock generator ramp angle and the inviscid shock impingement location results in the separation shock foot originating upstream of the flexible panel leading edge such that its dynamics are no longer coupled with the panel motion, it does lead to a reduction in the interaction length of the SWBLI compared with that on a rigid plate.

5.4.2. SWBLI Characteristic Frequencies

The dominant frequencies of separation shock motion over the flexible panel at different shock impingement locations is listed in Table 5.2. The frequencies were detected by processing the fluctuations about the mean separation shock foot location from Schlieren using Welch's method. Frequencies up to 1400 Hz are resolved as the Schlieren images are recorded at a rate of 2800 Hz. The "first peak" and "second peak" in Table 5.2 refer to the first and second clearly distinguishable peaks in terms of ascending order of frequency values, not in terms of PSD/total energy, although the total energy, $f \cdot E(f)$, was used to identify the frequencies.

	$\theta_{SG}=12^\circ$		$\theta_{SG}=15^\circ$	
	First peak	Second peak	First peak	Second peak
$x_i/a \approx 0.3$	NA	NA	-	-
0.4	-	-	-	-
0.5	615.2	-	-	-
0.6	623.4	1246.8	609.7	-
0.7	634.4	1268.8	623.4	-
0.8	-	-	639.8	-

Table 5.2: Characteristic frequencies (in Hz) detected in separation shock foot motion from Schlieren based on $f \cdot E(f)$

Looking at the $\theta_{SG}=12^\circ$ case first, the most upstream ($x_i/a \approx 0.4$) and most downstream ($x_i/a \approx 0.8$) impingement locations do not show any dominant frequencies in the separation shock motion. When the shock impinges at $x/a \approx 0.5, 0.6, 0.7$, the separation shock motion appears coupled with the flutter of the panel and shows distinct characteristic frequencies increasing from 615 to 635 Hz. For the latter two locations, even a second harmonic is detected in the separation shock motion. While no accelerometer measurements were made during these particular Schlieren runs, previous observations and the values of the dominant frequencies clearly indicate that the fluid-structure interaction is resonating with the LMB vibrations.

For the $\theta_{SG}=15^\circ$ case, the three most upstream impingement locations of $x/a \approx 0.3, 0.4, 0.5$ do not exhibit any characteristic frequencies in the separation shock motion. For $x_i/a \approx 0.3$ and 0.4, it was already observed that the separation shock foot lies upstream of the flexible panel leading edge (in Figure 5.22) on a rigid portion of the LMB, thus it is acceptable that its motion does not show any distinct periodicity. The three most downstream impingement location, $x/a \approx 0.6, 0.7, 0.8$ only display a single characteristic frequency, increasing from 609 to 623 to 640 Hz as the impingement shifts downstream.

As the separation shock motion does not show any characteristic frequencies for $\theta_{SG}=12^\circ$, $x_i/a=0.4$ and $\theta_{SG}=15^\circ$, $x_i/a \approx 0.5$ even when the shock foot lies downstream of the panel leading edge (as seen in Figure 5.22), it shows that there is a particular location on the flexible panel beyond which the coupling between the separation shock and the flutter takes place. Possibly, if the separation shock foot is too close to the leading edge, the rigidity of the clamped boundary condition prevents this coupling as the flutter at that location is not strong enough. The slight increase in dominant frequency value with the impingement location shifting downstream for both shock generators cannot be declared universal, because the frequency is driven by the LMB vibrations, the exact physics of which are unexplored

within the scope of the work. Moreover, the characteristic frequencies of the panel flutter from DIC measurements do not show the same trend, as will be presented later in Table 5.3 and Table 5.4. The absence of a distinct dominant frequency for $\theta_{SG}=12^\circ$, $x_i/a \approx 0.8$ could also be the indication of a maximum downstream location on the fluttering panel, such that if the separation shock foot is located downstream of it, its motion does not couple with the flutter due to increased rigidity near the panel TE. For $x_i/a \approx 0.8$, the separation shock foot is much more upstream for $\theta_{SG}=15^\circ$, and thus shows a distinct characteristic frequency.

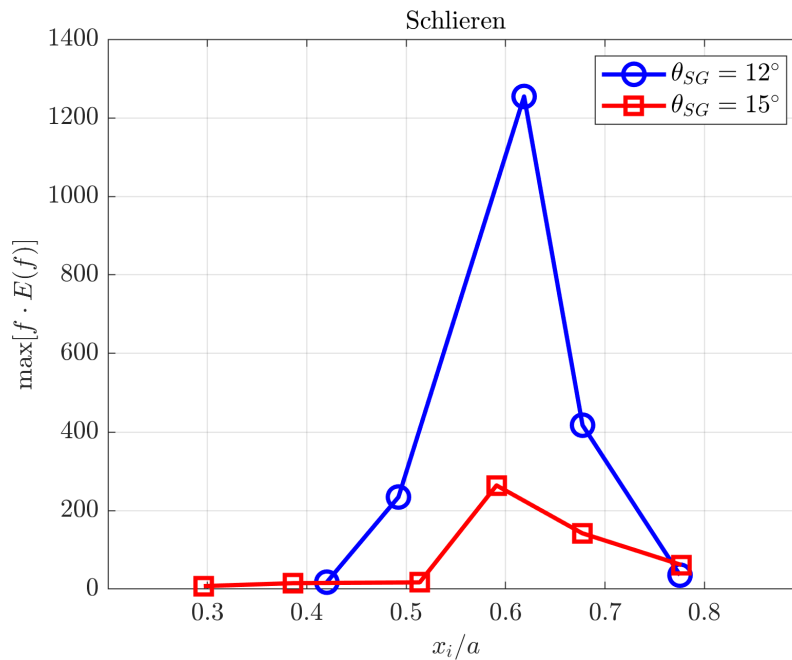


Figure 5.24: Energy of separation shock characteristic frequency bandpassed at 620 ± 20 Hz at different shock impingement locations for both $\theta_{SG}=12^\circ$ (in blue) and $\theta_{SG}=15^\circ$ (in red)

The time-resolved separation shock foot location signal obtained from Schlieren is bandpass filtered at 620 ± 20 Hz, which is the range in which the LMB vibration-driven flutter and separation shock motion frequencies are detected. The peak total energy of the bandpass filtered processed through Welch's method is then plotted against the impingement locations in Figure 5.24. The total energies of the particular combinations of θ_{SG} and x_i/a that did not show distinct characteristic frequencies in Table 5.2 are comparatively insignificant than the other cases, as expected. For both $\theta_{SG}=12^\circ$ and $\theta_{SG}=15^\circ$, the maximum energy is contained in the separation shock motion when $x_i/a \approx 0.6$, and for the same x_i/a , the energy with $\theta_{SG}=12^\circ$ is significantly higher. The flutter with the greater shock strength was already shown to be more "suppressed", and as a result even the coupled separation shock motion appears to be less energetic. It is valid to compare energies between $\theta_{SG}=12^\circ$ and $\theta_{SG}=15^\circ$ because the fluctuations about mean of separation shock foot location are used for calculations, thus the absolute values of the mean impingement locations being different does not influence the results shown in Figure 5.24.

5.5. Effect of Shock Location on Panel Flutter

Having seen how varying the shock impingement location affects the SWBLI on a fluttering panel in the previous section, the current section will focus on the flutter characteristics with changing shock impingement locations. Mainly, the mean and STD panel shapes, characteristic frequencies of flutter, and POD modes will be discussed. The shock impingement values used in this section are the ideal values, not actual ones, mainly because the actual ones could not be measured since DIC was done separately from Schlieren. Given a maximum relative error of 2.5% between the actual and ideal impingement locations as seen from the Schlieren (see Figure 5.21), usage of the actual values is deemed acceptable.

5.5.1. Panel Shapes

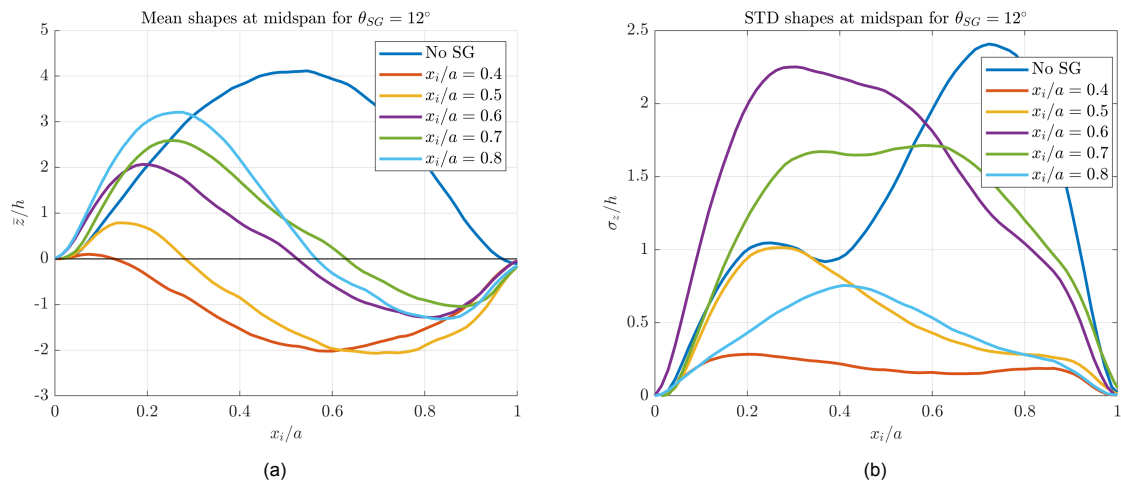


Figure 5.25: (a) Mean and (b) STD panel shapes based on out-of-plane displacements for $\theta_{SG}=12^\circ$ at different inviscid shock impingement locations

The mean shapes at the panel midspan ($y/b=0$) for $\theta_{SG}=12^\circ$ at different shock impingement locations are shown in Figure 5.25a. The mean shape of free flutter (no SG) is also shown for reference. The displacements are normalized by the panel thickness h . While the free flutter shape is the classic upward bump, the shock-induced flutter mean shape has some general characteristics: a crest upstream and a trough downstream, separated by a node. The amplitude of the crest increases as the inviscid impingement location shifts downstream, while the amplitude of the trough does not show a similar monotonic variation, owing to it being influenced by the chaotic separation region. As already discussed in section 5.2.1, the mean surface pressure variation caused by the SWBLI determines the mean shape of the panel. Since post-shock pressure is higher than the freestream pressure ahead of the shock, it results in an upstream crest followed by a downstream trough. As the shock impingement location shifts downstream, a larger upstream extent of the panel experiences the freestream pressure, and consequently the crest rises while the node shifts downstream. The peak of the crest is also seen to shift downstream along with shock impingement location. However, the greatest amplitude is still that of the free flutter case.

The STD (σ_z/h) panel shapes (normalized by panel thickness) at midspan, as shown in Figure 5.25b for $\theta_{SG}=12^\circ$, do not follow such a monotonic variation with change in the shock impingement location. For the most upstream shock impingement ($x_i/a=0.4$), the STD is roughly uniform over the entire chord of the panel, except near the LE and TE ($x/a=0$ and $x/a=1$, respectively) where it is zero since the both edges are clamped. The separation shock foot in this case is located at $x/a=0.13$ (see Figure 5.22), which means that over 85% of the panel is affected by the separated (and eventually reattached) flow, leading to very little variation in the displacement STD over the chord. When the impingement location is changed to $x/a=0.5$ and 0.6 , the maximum STD amplitude steadily increases, but decreases when the impingement location moves further downstream to $x/a=0.7$ and 0.8 . Since STD of panel displacements is treated as a measure of the energy of the flutter, it is seen that for $\theta_{SG}=12^\circ$, a shock impingement at 60% of panel chord results in the most energetic flutter of the panel. However, the free flutter has a greater STD amplitude than any of the shock-induced cases.

Similar observation in trends regarding the mean shapes when shock impingement locations are changed can be made when a higher shock strength with $\theta_{SG}=15^\circ$ occurs, as shown in Figure 5.26a. The stronger shock due to $\theta_{SG}=15^\circ$ results in a higher post-shock pressure compared to $\theta_{SG}=12^\circ$, and the effects are manifested in the mean displacement of the panel being pushed downwards of the no-flow panel height ($z/h=0$) completely when the impingement locations are upstream ($x_i/a=0.3, 0.4, 0.5$). For $x_i/a=0.6$, an upstream crest can finally be seen to develop, and eventually grow in amplitude as x_i/a goes to 0.7 and 0.8 . Due to the higher post-shock pressure, the crest amplitudes in this case are much lower than the $\theta_{SG}=12^\circ$ case at each x_i/a . At the most downstream location ($x_i/a=0.8$ for

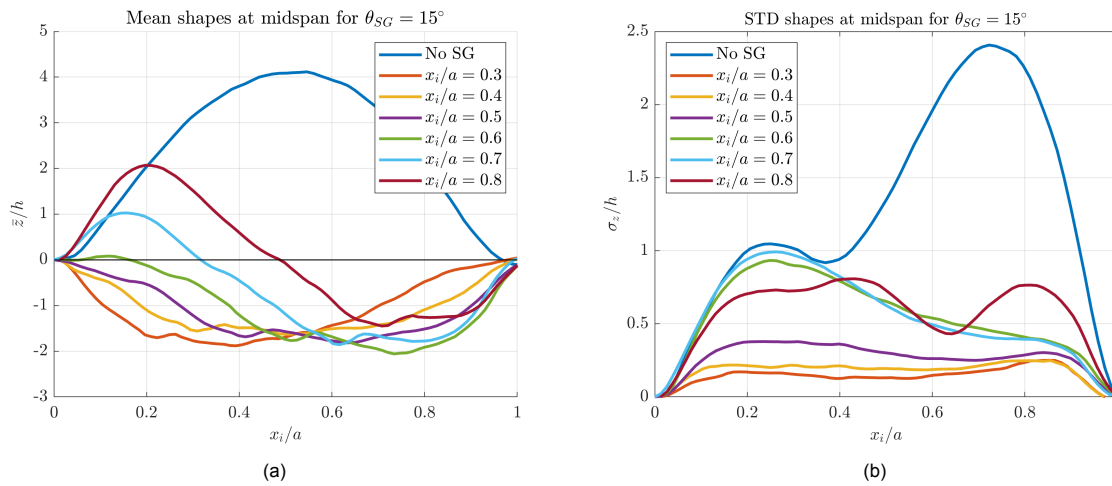


Figure 5.26: (a) Mean and (b) STD panel shapes based on out-of-plane displacements for $\theta_{SG}=15^\circ$ at different inviscid shock impingement locations

both), where the crest is at its highest, for $\theta_{SG}=12^\circ$ the crest height is $\approx 3.3h$ while with $\theta_{SG}=15^\circ$ it is $\approx 2h$.

The STD shapes with $\theta_{SG}=15^\circ$, shown in Figure 5.26b are also much lower in amplitude compared to $\theta_{SG}=12^\circ$. For $\theta_{SG}=15^\circ$ and $x_i/a=0.3,0.4,0.5$, the STD shapes are very similar to that observed for $\theta_{SG}=12^\circ$, $x_i/a=0.3$ (see Figure 5.25b) and have a roughly uniform STD value across the entire panel except for the edges, although the value increases with a shift in x_i/a downstream. Clearly, the post-separation shock boundary layer and its chaotic nature leads an approximately constant distribution of energy over the flutter rather than a distinct location with highest energy. The STD amplitudes increase when x_i/a goes to 0.6 and 0.7, although the difference between the two is relatively low. At the most downstream $x_i/a=0.8$, the STD amplitude again becomes smaller, indicating the $x_i/a=0.7$ causes the most energetic flutter when $\theta_{SG}=15^\circ$ is used, although the case of $x_i/a=0.6$ is very close too.

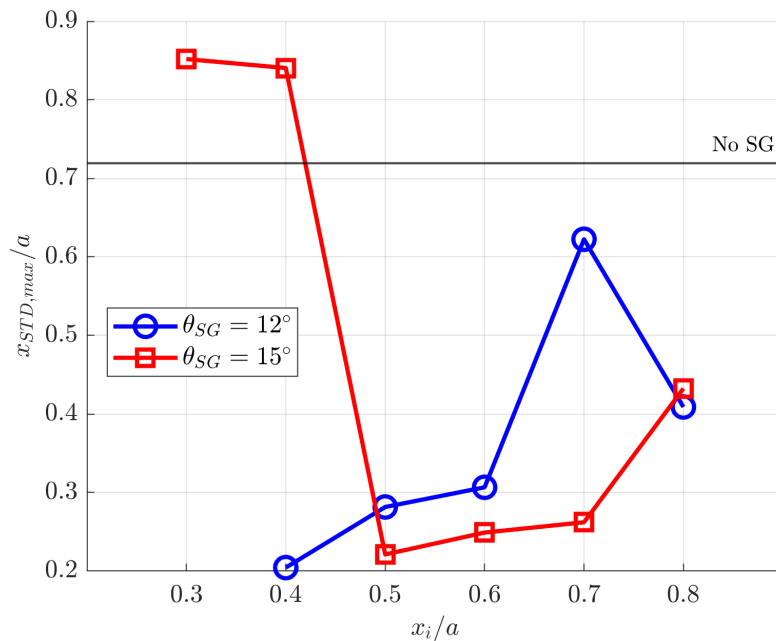


Figure 5.27: Variation in location of maximum STD point of panel flutter at different shock impingement locations for both $\theta_{SG}=12^\circ$ (in blue) and $\theta_{SG}=15^\circ$ (in red)

The trends in the STD of displacements at the midspan of the CCCC1.5 panels with both shock generators is summarized in terms of the maximum STD locations in Figure 5.27 and amplitudes in Figure 5.28. Only when the separation shock foot lies upstream of the flexible panel itself, which happens for $\theta_{SG}=15^\circ$ and $x_i/a=0.3$ and 0.4 (see Figure 5.22), the streamwise location of maximum STD (also the point of maximum energy of flutter) lies downstream of even the maximum STD location in free flutter (solid black line marked as "No SG"), as shown in Figure 5.27. When that is not the case, the maximum STD location for shock-induced flutter is always upstream compared to the free flutter. Panel displacements at the same maximum STD locations for each combination of θ_{SG} and x_i/a are used to build reference signals and extract characteristic frequencies of the panel flutter presented in Figure 4.13a, Figure 4.14a, Figure 4.15, Figure 5.9, Table 5.3, Table 5.4.

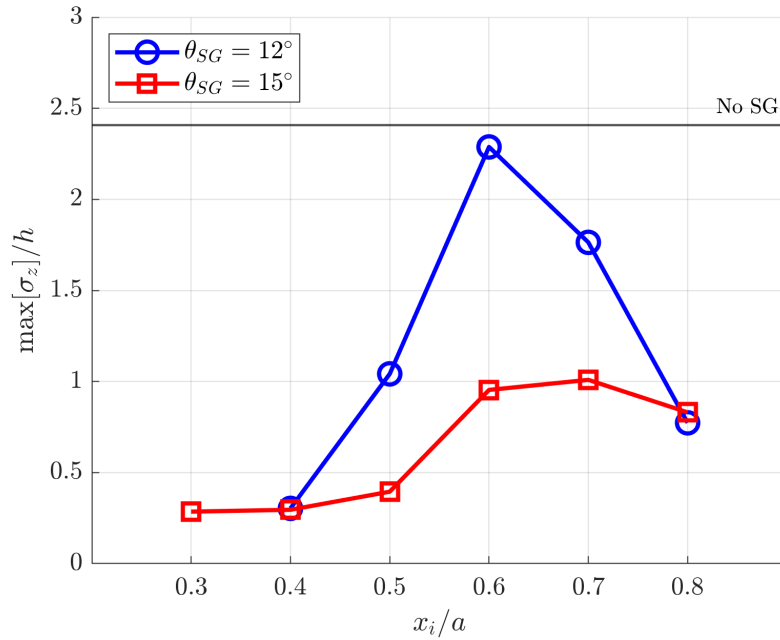


Figure 5.28: Variation in amplitude of maximum STD point of panel flutter at different shock impingement locations for both $\theta_{SG}=12^\circ$ (in blue) and $\theta_{SG}=15^\circ$ (in red)

The trend in variation of STD amplitude was already discussed earlier in this section, and is reiterated with the help of Figure 5.28: the maximum energy (interchangeably used with maximum STD) of flutter occurs at $x_i/a=0.6$ for $\theta_{SG}=12^\circ$ and at $x_i/a=0.7$ for $\theta_{SG}=15^\circ$ (although the difference in maximum STD values between $x_i/a=0.6$ and $x_i/a=0.7$ for $\theta_{SG}=12^\circ$ is less than 5%). Also, the maximum STD values of shock-induced flutter are always less than that of free flutter (no SG).

5.5.2. Flutter Characteristic Frequencies

Accelerometer recordings were made alongside the DIC measurements to confirm for the existence of LMB vibrations and its influence on the flutter. The characteristic frequencies detected using the panel displacements at the maximum STD location and midchord, midspan ($x/a=0.5$, $y/b=0$) of the panel (both locations always exhibit the same frequencies) are compiled along with the frequency response from the accelerometers mounted in the LMB in Table 5.3 and Table 5.4. The "first peak" and "second peak" refer to the first and second clearly distinguishable total energy peaks, calculated as $f \cdot E(f)$, in terms of ascending order of frequency values and not the magnitude of total energy.

As tabulated in Table 5.3, for $\theta_{SG}=12^\circ$, at all shock impingement locations except for $x/a=0.8$, the first peak frequency exists in the range 610-630 Hz from both, the accelerometers and DIC, and the value is a confirmation of the existence of resonance between the flutter frequency and LMB vibrations. For $x_i/a=0.5, 0.6, 0.7$ the LMB vibrations also display the second harmonic of the first peak frequency, but only for $x_i/a=0.6, 0.7$ the same are seen in the panel flutter. There is no discernible trend or correlation

	$\theta_{SG}=12^\circ$			
	Accelerometers		DIC	
	First peak	Second peak	First peak	Second peak
$x_i/a=0.4$	617.5	-	615.2	-
0.5	610	1218.8	610.3	-
0.6	613.8	1226.2	610.3	1225.6
0.7	630	1261.2	629.9	1259.8
0.8	745	-	439.4	639.6

Table 5.3: Characteristic frequencies (in Hz) detected at the maximum STD location of panel from DIC and accelerometers in LMB based on $f \cdot E(f)$ for $\theta_{SG}=12^\circ$ at different inviscid shock impingement locations

between the change in first peak frequency as x_i/a increases (shock impinges more downstream), unlike that in the case of Schlieren (see Table 5.2). An interesting anomaly is observed when $x_i/a=0.8$ for $\theta_{SG}=12^\circ$, when the accelerometers detect a peak at only 745 Hz, significantly distinct from the 620 ± 20 Hz range associated with the LMB vibrations during shock-induced flutter. For the same conditions, the panel flutter exhibits frequencies at 439 Hz and 640 Hz from DIC measurements, the former suspiciously close to the eigenfrequency of 460 Hz associated with the second eigenmode of the CCCC1.5 panel, as observed by Allerhand (2020) using an FEM solver to solve for the flutter of the panel during its design phase. It is possible that the particular combination of $\theta_{SG}=12^\circ$ and $x_i/a=0.8$ changes the conditions of the pressure waves in the cavity and affects the LMB vibrations, leading to a jump in its frequency and consequently the emergence of the panel natural frequency.

	$\theta_{SG}=15^\circ$			
	Accelerometers		DIC	
	First peak	Second peak	First peak	Second peak
$x_i/a=0.3$	621.2	-	620.1	1245.1
0.4	618.8	-	620.1	1582
0.5	612.5	895	610.3	908.2
0.6	603.8	1207.5	605.5	1206
0.7	616.2	-	615.2	-
0.8	1641.2	-	625	1645.5

Table 5.4: Characteristic frequencies (in Hz) detected at the maximum STD location of panel from DIC and accelerometers on LMB based on $f \cdot E(f)$ for $\theta_{SG}=15^\circ$ at different inviscid shock impingement locations

With $\theta_{SG}=15^\circ$, the accelerometer and DIC frequency responses are shown in Table 5.4. Similar to the case with the other SG, all shock impingement locations result in LMB vibrations detected by the accelerometers in the range of 603-621 Hz, except for $x_i/a=0.8$, which exhibits a peak at 1641 Hz. A second harmonic of the LMB vibration frequency is only detected for $x_i/a=0.6$. The first peak of the panel response frequencies also match the first frequency of LMB vibrations for each x_i/a , except $x_i/a=0.8$. The second dominant frequencies detected from the DIC measurements are usually not second harmonics of the first peaks, except for $x_i/a=0.6$, neither do they appear in the LMB accelerometers. This could again be a sign of natural panel frequencies being excited. For $x_i/a=0.8$, the only peak of the LMB vibrations exists at 1641 Hz, but the panel for the same conditions shows its first peak at 625 Hz and a second peak at 1645 Hz which, in all probability, is excited by the LMB vibrations. However, it is still not conclusive enough to claim the 625 Hz in the panel flutter originates from its natural response rather than being driven by the LMB vibrations by virtue of the frequency value. It might be possible that the 625 Hz frequency still exists in the LMB with a very low energy that is still sufficient to cause the panel to resonate at the same frequency.

At this point, it is worth revisiting the separation shock frequencies tabulated in Table 5.2, especially two particular cases: $\theta_{SG}=12^\circ$, $x_i/a=0.4$ and $\theta_{SG}=15^\circ$, $x_i/a=0.5$, for which although the separation shock foot was located on the flexible panel (as seen in Figure 5.22) and yet the separation shock did not show characteristic frequencies in its motion. On the other hand, for both those cases, the panel

did show resonance with the LMB vibrations and hence equal characteristic frequencies, as noted in Table 5.3 and Table 5.4. The DIC was also used to measure spurious vibrations of a rigid plate and was found to be sensitive enough to pick up the isolated LMB vibrations that appeared as noise in the same measurements (since the rigid plate was not fluttering), as already shown in Figure 4.15. This raises the question whether the frequencies detected using DIC at 615.2 Hz and 610.3 Hz for $\theta_{SG}=12^\circ$, $x_i/a=0.4$ and $\theta_{SG}=15^\circ$, $x_i/a=0.5$, respectively, are actually present in the flutter of the panel or are simply picked up by the DIC due to shaking of the entire LMB, since the separation shock does not exhibit the same frequencies despite being located on the flexible panel. To check the same, DIC signal at rigid points beside the flexible region of the CCCC1.5 panel insert are processed using Welch's method to extract frequencies, and compared to frequency response of the flexible panel as well as the accelerometer responses.

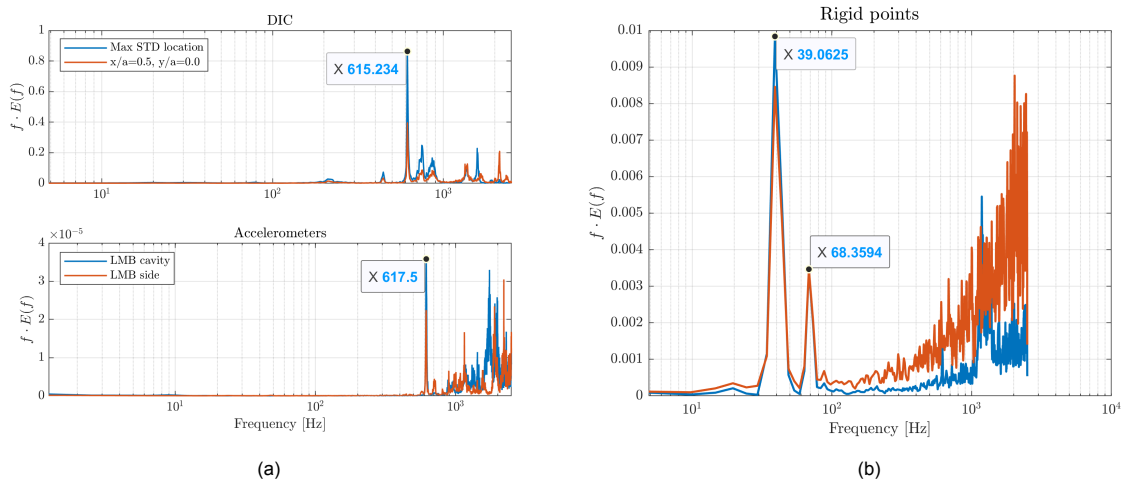


Figure 5.29: Comparison of frequency responses from (a) DIC measurements on the flexible panel and accelerometers (b) DIC measurements on rigid points beside the flexible panel for $\theta_{SG}=12^\circ$ and $x_i/a=0.4$

For $\theta_{SG}=12^\circ$, $x_i/a=0.4$, the comparison is shown in Figure 5.29a and Figure 5.29b. The total energy spectra are used for clearly identifying the relative energies. From the DIC measurements over the flexible panel at its maximum STD location and midspan, midchord location, a clear characteristic frequency is observed at 615.2 Hz, while the accelerometer shows a frequency of 617.5 Hz. From the same DIC run, two rigid points are chosen on either side (in the spanwise direction) of the flexible panel, and the corresponding spectra in Figure 5.29b only show clear characteristic frequencies at 39 Hz and 68 Hz. Since the 615 Hz frequency is dominant over the flexible region but has even lesser energy than low frequency noise detected in the rigid portion of the panel, it conclusively shows that the panel is indeed fluttering at 615 Hz frequency and the same frequency is not picked up by the DIC over points on the flexible panel simply because the LMB is shaking.

A similar analysis is repeated with $\theta_{SG}=15^\circ$, $x_i/a=0.5$. The DIC measurements at the flexible panel's maximum STD location and its midspan, midchord location in Figure 5.30a show a response at 610.3 Hz considerably large in energy, which is clearly due to the LMB vibrational frequency of 612.5 Hz as detected by the accelerometers. In contrast, the response at rigid points beside the flexible region of the CCCC1.5 panel insert show no clear characteristic frequencies, as seen from Figure 5.30b. Thus, the 610 Hz measured by the DIC over the flexible panel is again proven to be due to the physical flutter of the panel, rather than shaking of the entire LMB, otherwise the same frequency would have been dominant over the rigid points on the panel insert as well.

With this comparison of the difference in frequency responses between the flexible panel and rigid points on the same panel, it is conclusively shown that the flexible panel actually flutters for the cases $\theta_{SG}=12^\circ$, $x_i/a=0.4$ and $\theta_{SG}=15^\circ$, $x_i/a=0.5$, so the fact that the separation shock does not exhibit the same frequencies as the fluttering panel (and hence is not coupled with the flutter despite lying within the flexible region) could be because of the reasons discussed earlier in section 5.4.2: the panel is

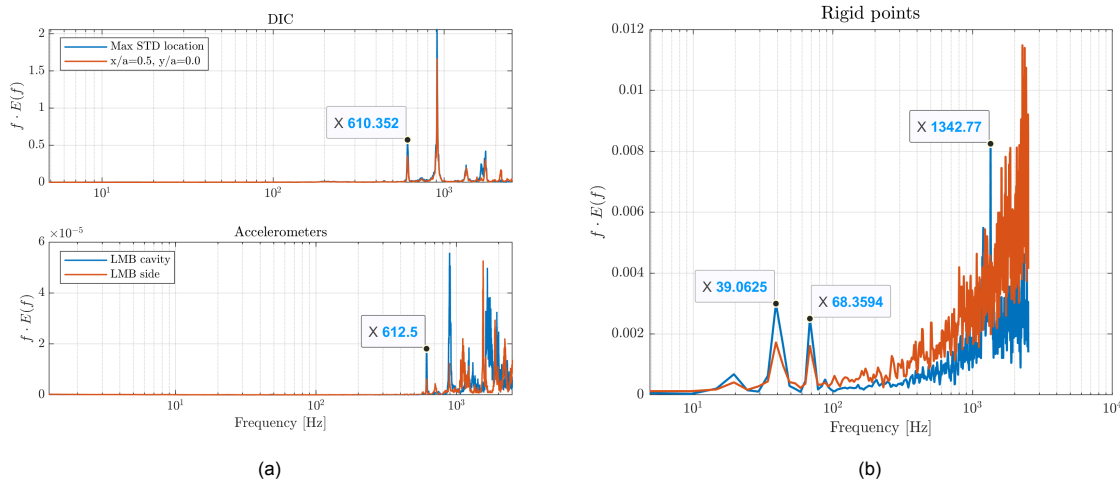


Figure 5.30: Comparison of frequency responses from (a) DIC measurements on the flexible panel and accelerometers (b) DIC measurements on rigid points beside the flexible panel for $\theta_{SG}=15^\circ$ and $x_i/a=0.5$

more rigid towards the clamped leading edge and thus the flutter is not as energetic, so if the separation shock foot falls too near the edge then its motion does not couple with the flutter.

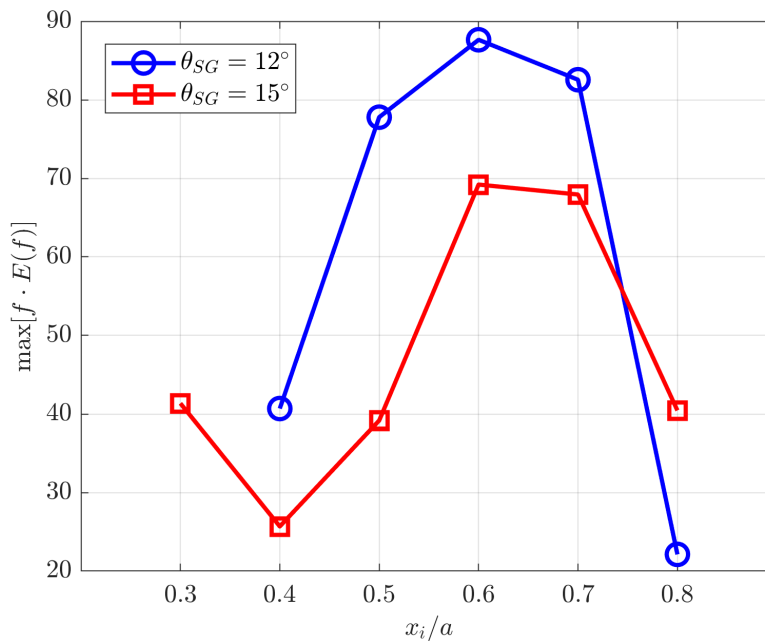


Figure 5.31: Energy of flutter characteristic frequency at maximum STD location on panel, bandpassed at 620 ± 20 Hz for different shock impingement locations for both $\theta_{SG}=12^\circ$ (in blue) and $\theta_{SG}=15^\circ$ (in red)

The frequency response of the panel displacements at the maximum STD locations at various shock impingement locations are bandpass filtered at 620 ± 20 Hz, the frequency range in which the LMB vibrations are detected (except for $x_i/a=0.8$ for both shock generators). Then, the total energy of the filtered signals is calculated using Welch’s method to check for the variation with shock impingement locations, and is shown in Figure 5.31. For both $\theta_{SG}=12^\circ$ and $\theta_{SG}=15^\circ$, the energy is maximum at $x_i/a=0.6$. This is analogous to a similar analysis done on the separation shock motion as calculated from a separate set of experiments using Schlieren, discussed earlier and shown in Figure 5.24, where, again, $x_i/a=0.6$ is seen to be the shock impingement location that results in maximum energy of the separation shock motion (that is coupled with the panel flutter) at 620 ± 20 Hz for both shock genera-

tors. These results serve as a link between the Schlieren and DIC measurements that were carried out separately, and also serves as a third confirmation (after energies of separation shock motion in Figure 5.24 and maximum STD value of panel flutter at midspan in Figure 5.28 show the same trends) of $x_i/a=0.6$ being the location where the flutter, and consequently, the fluid-structure interaction is most energetic for the given geometry and flow conditions: $M_\infty=2.0$, $p_0=2.5$ bar, $\theta_{SG}=12^\circ$. With $\theta_{SG}=15^\circ$, such a conclusion cannot be unequivocally drawn, as cases with $x_i/a=0.6$ and $x_i/a=0.7$ are very close in terms of both: the maximum STD value of flutter at midspan (Figure 5.28) and the total energy from Welch's method applied on panel displacements at the maximum STD locations (Figure 5.31), showing them to be also close in terms of flutter energy. Possibly, the actual location of maximum energy with $\theta_{SG}=15^\circ$ could be located closer to the middle of $x_i/a=0.6$ and 0.7 rather than the ends.

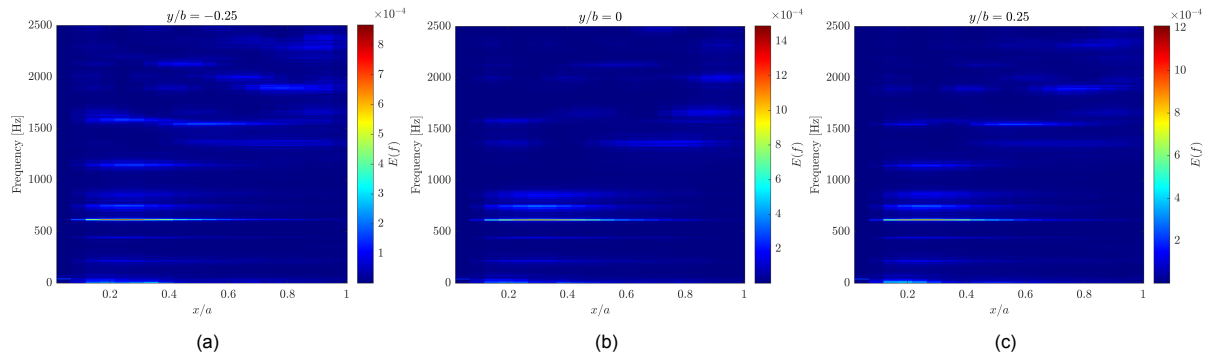


Figure 5.32: Spectrograms over panel length at different spanwise locations: (a) $y/b=-0.25$, (b) $y/b=0$, (c) $y/b=0.25$ for $\theta_{SG}=12^\circ$, $x_i/a=0.4$

In a crude sense, changing the shock impingement location simply changes the extents to which the panel surface experiences freestream pressure and post-shock higher pressure and flow separation. To see how that affects the panel frequency response, spectrograms are plotted across the chord of the panel at different spanwise locations: midspan ($y/b=0$) as well as two off-midspan locations, $y/b = \pm 0.25$. First, the case of $\theta_{SG}=12^\circ$, $x_i/a=0.4$ is seen in Figure 5.32. The separation shock foot is located at $x/a \approx 0.13$ (see Figure 5.22) and does not show coupling with the flutter (see Table 5.2), and thus more than 85% of the panel is affected by the shock-induced flow separation and subsequent reattachment. In the spectrograms, a distinguishably high PSD can be seen at ≈ 616 Hz (from Table 5.3) across most of the panel chord for all three spanwise posts. However, a variety of frequencies also crop up at a higher range, as well as some of lower magnitudes. Also, these other frequencies show variation in PSD with change in spanwise location. Overall, the frequency response for this condition of shock generator and shock impingement location can be termed as "chaotic", with multiple, non-correlated frequency responses detected across the length of the panel with spanwise variation.

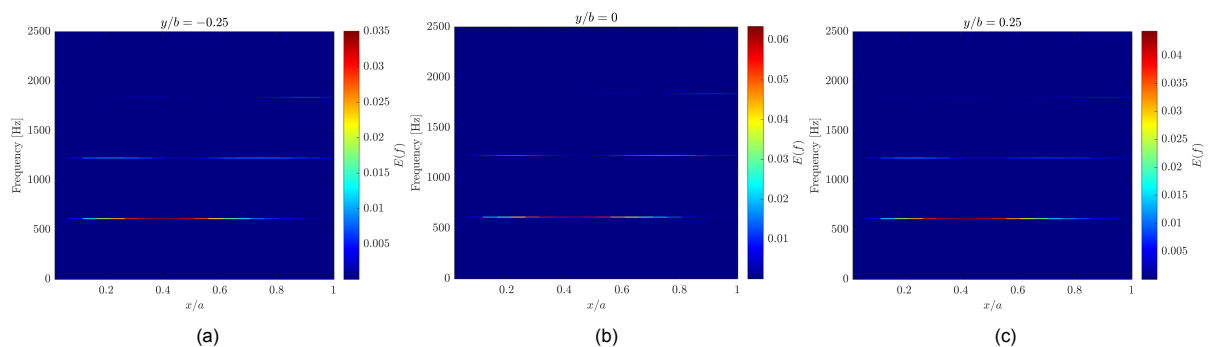


Figure 5.33: Spectrograms over panel length at different spanwise locations: (a) $y/b=-0.25$, (b) $y/b=0$, (c) $y/b=0.25$ for $\theta_{SG}=12^\circ$, $x_i/a=0.6$

In contrast, when spectrograms at the same locations are plotted for $\theta_{SG}=12^\circ$, $x_i/a=0.6$, a combination for which the separation shock foot does show coupling with the panel flutter (see Table 5.2) unlike the previous case, a more periodic response can be observed in Figure 5.33. The peak PSD is seen at ≈ 614 Hz for all three spanwise stations, and the next peak exists at 1226 Hz, the second harmonic. Even the third harmonic can be observed in the second half of the panel chord. Also, no significant spanwise variation is observed in the spectrograms. Thus, the response of the panel when the separation shock foot is coupled with its flutter is seen to be more periodic, compared to the chaotic nature in the previous case.

This observation holds even for the case when $\theta_{SG}=12^\circ$, $x_i/a=0.5$, as the separation shock motion appears coupled with the flutter (from Table 5.2) while the spectrogram at the midspan, already shown in Figure 4.14b while discussing wind tunnel vibrations in chapter 4, shows a clean, periodic response of the panel flutter with a clear dominant frequency at 610 Hz.

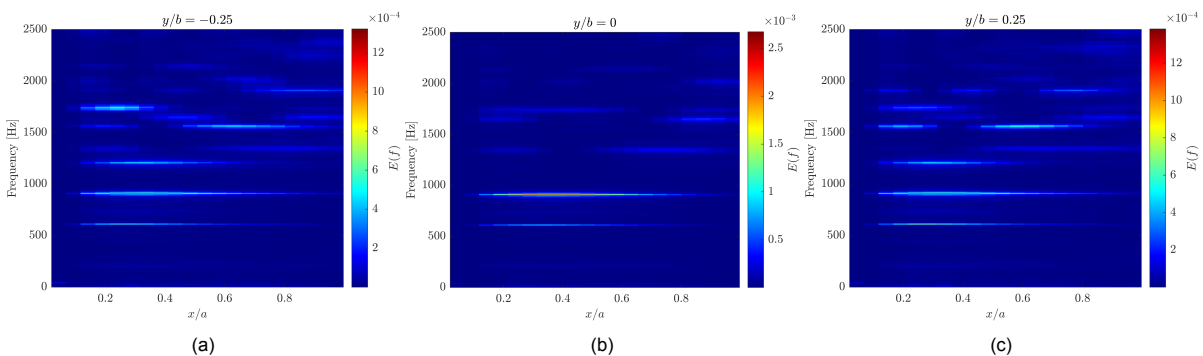


Figure 5.34: Spectrograms over panel length at different spanwise locations: (a) $y/b=-0.25$, (b) $y/b=0$, (c) $y/b=0.25$ for $\theta_{SG}=15^\circ$, $x_i/a=0.5$

The very same relationship between the coupling of separation shock motion with the panel flutter and the nature of panel response (chaotic or periodic) is also observed with the higher shock strength using $\theta_{SG}=15^\circ$. When the shock impinges at $x/a=0.5$ for $\theta_{SG}=15^\circ$, the separation shock foot does not show coupling with the flutter motion (see Table 5.2), and the spectrograms show a chaotic flutter response consisting of a myriad of frequencies (including the primary flutter frequency driven by the LMB vibrations at 610 Hz) across the panel chord, as presented in Figure 5.34. Again, a considerable variation in the spectral content is observed when the spanwise stations are changed.

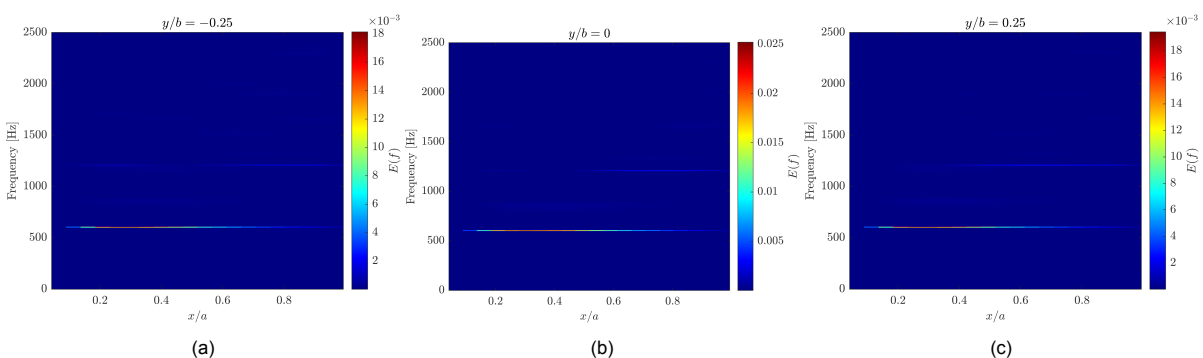


Figure 5.35: Spectrograms over panel length at different spanwise locations: (a) $y/b=-0.25$, (b) $y/b=0$, (c) $y/b=0.25$ for $\theta_{SG}=15^\circ$, $x_i/a=0.6$

With $\theta_{SG}=15^\circ$ and $x_i/a=0.6$, the separation shock motion is coupled with the panel flutter as it shows (practically) the same primary frequency as the flutter (see Table 5.2 and Table 5.4), and the flutter spectrograms reveal a more periodic response across all spanwise stations in Figure 5.35, with the primary PSD peak at ≈ 605 Hz along with the presence of its second and third harmonics at various streamwise

extents. There still are other non-harmonic frequencies present, but their relative energies are significantly lower than that of the primary peak, unlike the previous case.

Causality cannot be assigned to the phenomenon of fluid-structure interaction, i.e., it cannot be determined whether the panel flutter drives the separation shock motion or vice-versa. Consequently, the observation made in the current discussion - only when the separation shock motion is coupled with the panel flutter (determined simply when both show roughly the same primary frequencies), the flutter response is clean and periodic, otherwise chaotic - cannot be assigned causality either.

5.5.3. Flutter POD Modes

The background on POD has already been described in section 3.5.6 and section 5.2.3. In the current section, the effect of changing shock impingement locations on the POD mode shapes and energies extracted from the panel flutter measurements using DIC will be explored.

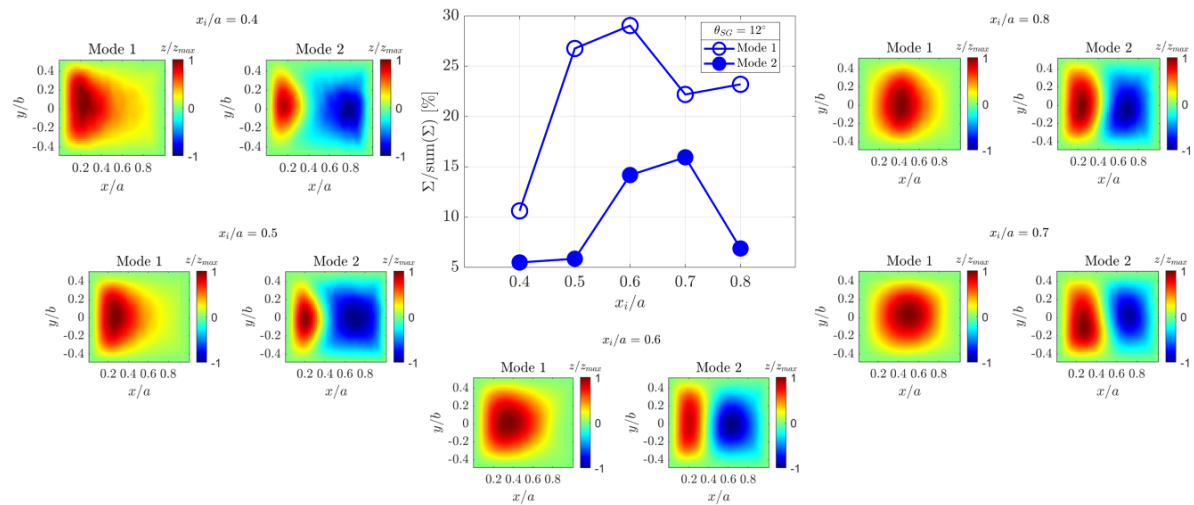


Figure 5.36: First two POD mode shapes and corresponding relative energies at different shock impingement locations for $\theta_{SG}=12^\circ$

POD mode shapes are plotted alongside the relative energies of the first two modes at different shock impingement locations for $\theta_{SG}=12^\circ$ in Figure 5.36. As per the POD technique, the first mode contains the highest energy (Σ), followed by the second mode. The relative energies in each case are calculated as a fraction of the total energy, $\text{sum}(\Sigma)$. First of all, both the first and second modes are consistent in their shape: the first mode is always a (1,1) shape while the second mode is always in (1,2) shape. Thus, shock impingement location does not seem to affect the topology of the two most energetic POD modes of the flutter, limited to the range of impingement locations tested: $x_i/a=0.4$ to 0.8. For the most upstream shock impingement, $x_i/a=0.4$, the relative energy of the first mode is shockingly low: just above 10%, while the second mode contributes around 5%. For this impingement location, the separation shock motion was not coupled with the flutter, as the former did not show any characteristic frequencies at all (in Table 5.2) while the latter did (in Table 5.3). Since the separation shock foot is at its most upstream, the panel is severely affected by the flow separation and its chaotic nature. Hence, the energy of the flutter is built up without one or two significantly dominant modes, but many modes contribute to it and hence the relative energy of the most energetic mode is around 10%. This is characteristic of a chaotic panel response, as with periodic responses there are clearly identifiable dominant modes. Essentially, this is another confirmation of the chaotic panel response when the shock impingement happens too upstream, as also see earlier with the spectrogram (Figure 5.32) for the same case.

When the shock impinges at the next downstream location, $x_i/a = 0.5$, the energy contribution of the first mode jumps up to over 25%, while the second mode contribution only rises slightly closer to 6%. At this impingement location for $\theta_{SG}=12^\circ$, the separation shock is coupled with the flutter motion (as

	$\theta_{SG}=12^\circ$	
	Mode 1	Mode 2
$x_i/a=0.4$	615.2	1337.9
0.5	610.3	1220.7
0.6	610.3	1225.6
0.7	629.9	1259.8
0.8	439.4	1342.8

Table 5.5: Characteristic frequencies (in Hz) detected from the time coefficients of the first two POD modes based on $f \cdot E(f)$ for $\theta_{SG}=12^\circ$ at different inviscid shock impingement locations

seen in Table 5.2), and the panel response is also periodic (see spectrogram in Figure 4.14a), hence the first mode is seen to be more dominant in terms of relative energy than the more upstream shock impingement case.

At $x_i/a=0.6$, the share of energy contribution of the first mode is at its maximum: 29%, among other x_i/a for $\theta_{SG}=12^\circ$. At the same time, the contribution from the second mode also sees a significant jump to almost 15% from around 6% previously. Thus, the first two modes grow in dominance compared to the other modes at $x_i/a=0.6$, which is also the shock impingement location at which the fluid-structure interaction is at its most energetic for ($\theta_{SG}=12^\circ$), as seen from the energy of separation shock motion (Figure 5.24) and energy of flutter at the maximum STD point on the panel (Figure 5.31).

For $x_i/a=0.7$, the first mode energy drops to around 22% of overall energy, while the second mode contribution increases to over 15%. At this x_i/a , the energies of the two modes are the closest. At the most downstream shock impingement location, $x_i/a=0.8$, the first mode energy contribution slightly increases to over 23% but the second mode energy contribution drastically drops to nearly 7%. For $x_i/a=0.8$, the panel flutter exhibits a characteristic frequency at 439.4 Hz, which is close to the 460 Hz natural frequency of the (1,2) mode calculated using an FEM solver by Allerhand (2020). and not in the 620 ± 20 Hz range in which the LMB vibrations occur. However, in this case, the first mode, which is a (1,1) shape, shows the frequency of 439.4 Hz as noted in Table 5.5.

The frequencies of the first two POD modes for different shock impingement locations and $\theta_{SG}=12^\circ$ are listed in Table 5.5, calculated from the corresponding POD time coefficients. While the first modes show the same frequencies as the first dominant peaks found from the DIC measurements (tabulated in Table 5.3), which are also equal to the frequency of LMB vibrations in the 620 ± 20 Hz range except for $x_i/a=0.8$, only the second POD modes for $x_i/a=0.5, 0.6, 0.7$ show a frequency equal to the second harmonic of the LMB vibration frequency (in the 1220-1269) Hz. The most upstream and downstream shock impingement locations, i.e., $x_i/a=0.4$ and 0.8, show second POD mode frequencies unrelated to the first mode, at 1338 Hz and 1343 Hz, respectively.

A similar plot is created for $\theta_{SG}=15^\circ$ and is shown in Figure 5.37. While the first POD mode shape can be approximated as a (1,1) at all different impingement locations, for the two most upstream location, i.e., $x_i/a=0.3$ and 0.4, the solitary peak appears to be smeared out across the entire panel, indicating how the separation influenced flutter does not seem to have a preferred or sharp peak due to the chaotic nature of the surface pressure experienced by the panel. As the shock impingement location shifts more downstream to $x_i/a=0.6, 0.7$, the shape of the first mode eventually begins to resemble the first POD mode shapes of $\theta_{SG}=12^\circ$ with $x_i/a=0.4, 0.5$, i.e., a (1,1) shape with the peak located more upstream. In fact, the similarity holds true even for the corresponding second POD modes. This similarity in the both first and second mode shapes across the two different shock generators appears to be related to the fact that the separation shock foot in case of $\theta_{SG}=12^\circ$, $x_i/a \approx 0.4$ and $\theta_{SG}=15^\circ$, $x_i/a \approx 0.6$ are very close, and the same holds true for $\theta_{SG}=12^\circ$, $x_i/a \approx 0.5$ and $\theta_{SG}=15^\circ$, $x_i/a \approx 0.7$, as shown in Figure 5.22, even though extents of separated flow are different due to the different shock strengths. At the most downstream shock impingement, $x_i/a=0.8$, the mode shape does not appear to exactly be a (1,1) shape, it looks more of a (1,2) shape with an in-phase pair of peaks across the streamwise direction. The second POD modes with $\theta_{SG}=15^\circ$ in Figure 5.37 consistently demonstrate a (2,1) shape,

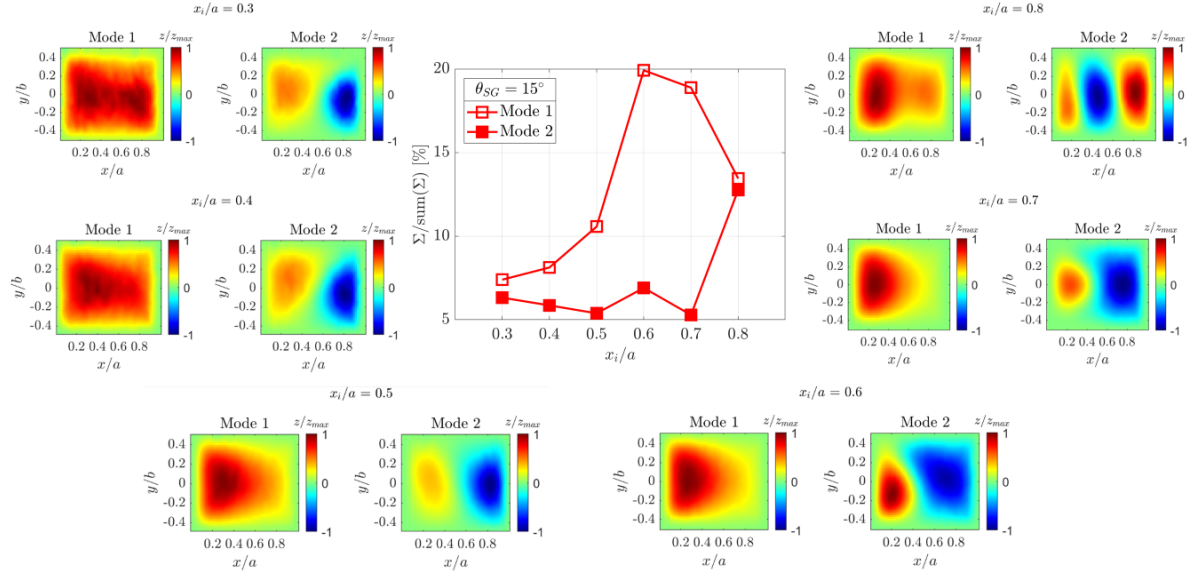


Figure 5.37: First two POD mode shapes and corresponding relative energies at different shock impingement locations for $\theta_{SG}=15^\circ$

a trend similar to what was observed with $\theta_{SG}=12^\circ$ in Figure 5.36. However, the trend with is bucked for $x_i/a=0.8$, when the second POD mode changes to a (1,3) shape for $\theta_{SG}=15^\circ$.

The trend in relative energies shows very low contributions from the first POD mode for the three upstream shock impingement locations, $x_i/a=0.3, 0.4, 0.5$ at 7%, 8% and 11%, respectively. All three shock impingement locations result in separation-dominated flutter (thus chaotic, as seen in the spectrogram for the latter x_i/a in Figure 5.34) where the higher order modes contribute more significantly. As the shock impingement location shifts downstream from 0.3 to 0.5, the second mode contribution to energy decreases while that of the first mode increases, showing a growing dominance of the the latter over determining the flutter compared to all other modes as the extent of panel exposed to separated flow decreases. The contribution of the first mode quickly jumps to 20% at $x_i/a=0.6$, which is also the maximum among all shock impingement locations for $\theta_{SG}=15^\circ$. While $x_i/a=0.6$ was also the location for which the first mode made its maximum contribution with $\theta_{SG}=12^\circ$, the value was higher at 29%. Thus, the stronger shock which causes a larger separation also leads to higher order POD modes to contribute more to the flutter energy, for the same shock impingement locations. At $x_i/a=0.7$ for $\theta_{SG}=15^\circ$, contributions from both first and second mode drops from $x_i/a=0.6$. Interestingly, the first mode contribution drastically drops to 13.5% while the second mode contribution shoots up to 12.5% when the shock impinges at its most downstream location of $x_i/a=0.8$. This is also accompanied by a change in the shapes of both modes to (1,2) and (1,3), as discussed earlier. This sudden shift in trends is not further explored.

	$\theta_{SG}=15^\circ$	
	Mode 1	Mode 2
$x_i/a=0.3$	620.1	1245.1
0.4	620.1, 966.9	1298, 1582
0.5	610.3, 908.2	1342.7, 1655.3
0.6	605.5	1206.2
0.7	615.2	1230.4, 1679.7
0.8	625, 727.5	1645.5

Table 5.6: Characteristic frequencies (in Hz) detected from the time coefficients of the first two POD modes based on $f \cdot E(f)$ for $\theta_{SG}=15^\circ$ at different inviscid shock impingement locations

Table 5.6 shows the frequencies of the POD modes for $\theta_{SG}=15^\circ$ at different x_i/a . The first POD modes always contain the frequency of the LMB vibrations, in the 605-625 Hz. At some locations, a secondary frequency is also associated with the first POD mode, such as $x_i/a=0.4$ and 0.5 , which result in a chaotic flutter response, show secondary frequencies of 967 Hz and 908 Hz, respectively. The most downstream impingement at $x_i/a=0.8$ also shows a secondary frequency in its first POD mode, at 727.5 Hz. The frequencies of the second POD modes are always higher than those of the first modes, and with $x_i/a=0.3, 0.6, 0.7$, the second POD modes contain the second harmonic of the LMB vibrations at 1206-1245 Hz.

The first and second POD modes across different impingement locations for both $\theta_{SG}=12^\circ$ and $\theta_{SG}=15^\circ$ showed similarity in shapes, except for the $\theta_{SG}=15^\circ$, $x_i/a=0.8$ case. The specific proportion of the shapes appears to be influenced by the shock impingement location but the phase relationships remain the same. In terms of relative energies, the first mode was found to be most dominant at $x_i/a=0.6$ for both SGs. However, it was not clear within the limits of the current investigation as to why that is the case.

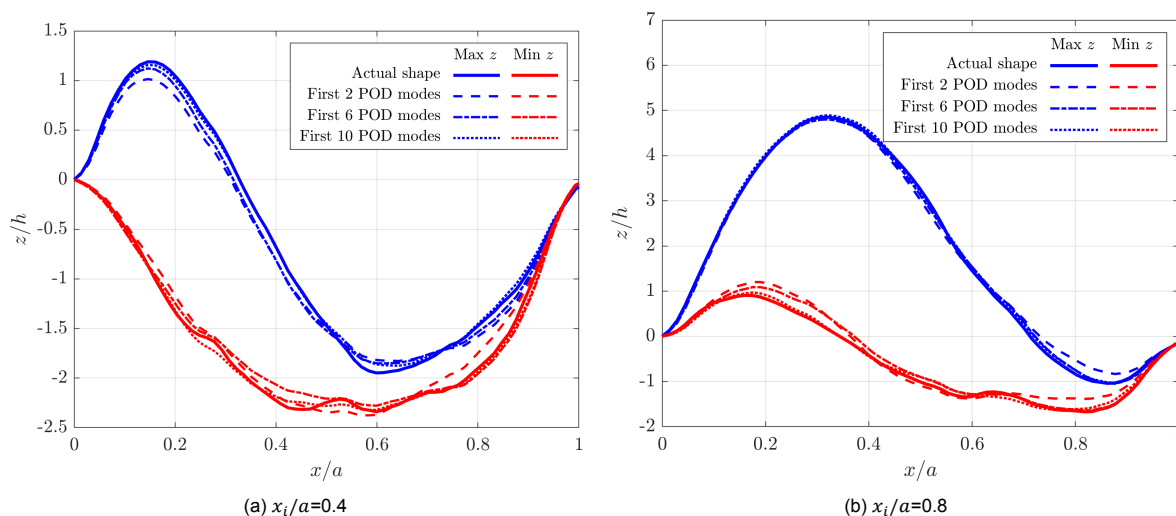


Figure 5.38: Comparison of instantaneous panel shapes (solid lines) with predicted shapes from first k POD modes: $k=2$ (dashed lines), $k=6$ (long dash-short dash lines), $k=10$ (dotted lines) at (a) most upstream and (b) most downstream shock impingement locations for flexible panel with $\theta_{SG}=12^\circ$

Reduced-order modelling of the panel flutter shapes have already been presented for $\theta_{SG}=12^\circ$, $x_i/a=0.6$ in Figure 5.18a, where it was noted that only using the first 2 modes to represent the actual shape showed significant deviations even though they contributed 43% of the total energy but improved drastically when 10 modes were used which contained 66.5% of the overall energy. Now, for $\theta_{SG}=12^\circ$, the same process is repeated with the most upstream (Figure 5.38a) and most downstream (Figure 5.38b) shock impingement locations, and the most startling observation for both is that even using the first 2 POD modes provides an excellent match with the actual panel shape. This is surprising because for $x_i/a=0.4$, the first two modes only contain 16% of the total energy, while for $x_i/a=0.8$, that contribution rises to 30% (check Figure 5.36 for relative energy contents), but still remains well short of the 43% contribution of the first 2 modes in case of $x_i/a=0.6$, in which using only 2 modes resulted in large deviations (Figure 5.18a). The explanation to this puzzle lies in the trend of total flutter energies for different shock impingement locations, as shown in Figure 5.31. The flutter is most energetic (higher fluctuations about mean) at $x_i/a=0.6$ when $\theta_{SG}=12^\circ$ is used, while the energies for $x_i/a=0.4$ and $x_i/a=0.8$ are much less than even half of the former (thus, lesser fluctuations about mean). The fact that using only 2 modes does not create as good a representation of the actual shape when the total flutter energy is high (for $x_i/a=0.6$) even though the contribution of the first 2 modes to that energy is also relatively high (43%), compared to when the total flutter energy is low ($x_i/a=0.4, 0.8$) and the 2-mode ROM is able to provide much better approximations even if the two modes contribute lesser energy to the overall flutter (16%, 30%), goes to show that a high relative energy contribution of the first k POD modes by itself does not lead to a good ROM, it also depends on how energetic the actual flutter is.

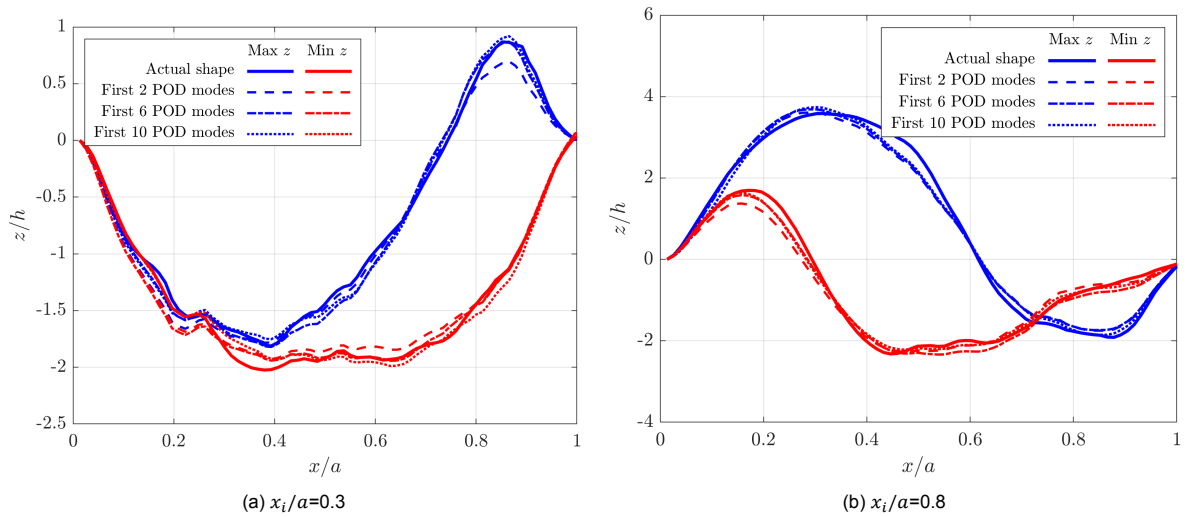


Figure 5.39: Comparison of instantaneous panel shapes (solid lines) with predicted shapes from first k POD modes: $k=2$ (dashed lines), $k=6$ (long dash-short dash lines), $k=10$ (dotted lines) at (a) most upstream and (b) most downstream shock impingement locations for flexible panel with $\theta_{SG}=15^\circ$

Similar observation as before are made for $\theta_{SG}=15^\circ$. Using only 2 modes provides an excellent match with the actual shapes and is only slightly improved by using 10 modes for the most upstream ($x_i/a=0.3$ in Figure 5.39a) and most downstream ($x_i/a=0.8$ in Figure 5.39b) shock impingement locations, compared to the shock impingement location which produces the most energetic flutter response in the panel ($x_i/a=0.6$, as seen in Figure 5.31) for which using only 2 POD modes results in much larger deviations from the actual shape (as seen in Figure 5.19a). Again, comparing the relative energy contributions of the first two modes for $\theta_{SG}=15^\circ$ at $x_i/a=0.3, 0.6, 0.8$ gives 13.7%, 26.8%, 26.2% respectively, and even with lower relative energies for the first and last cases, a better prediction is achieved using only 2 modes as the flutter itself is significantly less energetic than $x_i/a=0.6$. If the overall flutter itself is low in energy, it means that the fluctuations are low and fewer number of modes can still provide a decent match with the actual shapes. It is possible that more factors are also involved in this determination, but for the current study, it is sufficient to note that when comparing the accuracy of ROMs using POD modes for different cases, only taking into account the relative energy content of the modes is not enough.

6

Conclusions and Recommendations

6.1. Conclusions of Current Study

An experimental study of shock-induced panel flutter was conducted in the ST-15 supersonic wind tunnel facility at the High-speed Aerodynamics Laboratory of the Delft University of Technology. The study was designed by building upon the knowledge of problems and limitations of the facility investigated by previous studies of [Allerhand \(2020\)](#) and [Mathijssen \(2022\)](#). The aforementioned studies, being some of the first-of-their-kind in the ST-15 facility, deemed it necessary to conduct the flow and structural measurements involved simultaneously in order to successfully establish the existence of fluid-structure interaction. This meant simultaneous use of different optical techniques for measuring the flow and structural aspect, with completely different illumination sources and cameras, which involved considerable practical challenges to avoid optical interference and lead to decreased SNR of the measurements. However, the successful simultaneous measurements confirmed that shock-induced flutter was indeed a repeatable and periodic phenomenon when experimentally simulated in the ST-15 facility. This observation helped inform the decision to conduct flow and structural measurements non-simultaneously in completely separate campaigns in the current study, mainly to alleviate the problem of optical interference effects and that of accommodating different equipment related to different techniques in a tight space around the test section. [Allerhand \(2020\)](#) had conducted an extensive study using CCFF1.5 flexible panels, which were clamped at the leading and trailing edges but free on the sides and had an aspect ratio of 1.5, and found the particular aspect ratio to produce the most two-dimensional characteristics of flutter at the panel centerline, compared to aspect ratios of 1 and 2. However, CCCC (clamped on all edges) flexible panels were not studied in-depth for shock-induced flutter, even though the configuration is the most common in forming bodies of high-speed aerial vehicles. For this reason, the current study focused on the flutter of CCCC1.5 flexible panels, while measurements were also done on a rigid plate for comparison. The tests were conducted at $M_\infty=2.0$ and $p_0=2.5$ bar.

It was desired to gain a better insight into the origin of spurious vibrations detected in the lower Mach block (LMB) at 576 Hz of the test section by [Allerhand \(2020\)](#) only when the shock generator was installed in the test section. These vibrations were observed to cause the frequency of flutter in certain cases to resonate with the same frequency, and their energy seemed to grow throughout the same day as more and more wind tunnel runs were conducted. This was hypothesized to be a result of the gradual contraction of the LMB throughout the day as tunnel cooled by convection due to the high-speed air flow inside. It was aimed to test the repeatability of the same spurious vibrations with accelerometer measurements around various locations in the test section and simultaneous temperature measurements at the same locations were also made using K-type thermocouples in an attempt to link the temperature variations with the emergence of spurious vibrations. The rigid plate was used for the tests so as not to include any vibrations caused by the fluttering panel, and a 12° shock generator was installed in the test section. With three consecutive runs of the tunnel in quick succession, on two different occasions, in which the temperature was found to drop by $\approx 10^\circ\text{C}$ by the end of the last runs from an initial ambient temperature of $\approx 20^\circ\text{C}$, some vibrations were detected in the LMB in the range

630-750 Hz along with another peak at 451 Hz, but all of them had significantly lower energy than other high frequency vibrations >1500 Hz. Because the thermal inertia of the LMB was very large, more runs were carried out on the same day to allow for it to contract, but even towards the last run of the day, energy of vibrations below 1000 Hz were still very low in relative terms, unlike what [Allerhand \(2020\)](#) had observed with the 576 Hz peak becoming the singular dominant peak in the entire spectra. However, in the last two runs, an almost singular lower frequency peak was observed at 632 Hz in the LMB. In fact, before the last run, the LMB was tightened to the wind tunnel walls via tightening the bolts between the two, a strategy that had resulted in reduction in energy of the 576 Hz peak in LMB for [Allerhand \(2020\)](#), but the last run in the current case showed no drastic changes in energy at 632 Hz in the LMB despite tightening. Thus, no direct link could be established between long-term cooling of the test section and a drastic increase in energy of specific low-frequency vibrations in the LMB or any other parts of the wind tunnel test section. Also, runs on the rigid panel were carried out without the shock generator installed, and this resulted in very high energy dominant peaks at 770 Hz in the LMB, along with its second harmonic at 1540 Hz. Despite attempting to tighten the bolts connecting both Mach blocks to the wind tunnel walls, the energy at these frequencies did not show a significant change, always remaining the dominant ones. This frequency detected in the LMB without the shock generator installed is actually the same as the flutter frequency of 770 Hz detected by [Mathijssen \(2022\)](#) in the study of supersonic panel flutter (without an impinging shock), who also hypothesized that a lock-in resonance effect might be taking place between the panel flutter and wind tunnel vibrations due to which all panels of different geometries and boundary conditions showed the same flutter frequency, which was also considerably different from the respective eigenfrequencies. The current measurements prove this hypothesis to be true.

In the second campaign, flow measurements were done using Schlieren imaging, employing the existing Z-type Schlieren setup in ST-15. The images were recorded with a high-speed camera at 2800 Hz, to resolve periodicity up to 1400 Hz, which was observed by [Allerhand \(2020\)](#) as the highest dominant frequency in magnitude when studying CCC1.5 panels. Variation in impinging shock strength was done by using shock generators of 12° and 15° . For both shock generators, recordings were made with different shock impingement locations, varied in steps of $\approx 10\%$ of the panel chord length, with a 0.5-2.5% error observed in the actual impingement locations versus the targeted locations, in terms of chord length. For $\theta_{SG}=12^\circ$, x_i/a ranged from 0.4 to 0.8 and for $\theta_{SG}=15^\circ$, x_i/a ranged from 0.3 to 0.8. To calculate the SWBLI interaction lengths for the varied conditions, a shock detection methodology was devised to detect the impinging and separation shock edges from the Schlieren images, and extend the detected edge to the panel height in order to locate the corresponding shock foots. By processing the obtained shock foot motion using Welch's method, it was also possible to detect characteristic frequencies of its motion. The impinging shock foot motion did not show any clear dominant frequencies, as should be expected as it originates at the shock generator which remains fixed in position for any particular run. The separation shock is expected to couple with the flutter of the panel, and thus show the same characteristic frequencies. For the cases of $\theta_{SG}=12^\circ$, $x_i/a=0.4$ (most upstream), 0.8 (most downstream) and $\theta_{SG}=15^\circ$, $x_i/a=0.3, 0.4, 0.5$, the separation shock did not show any characteristic frequencies. While for $\theta_{SG}=15^\circ$, $x_i/a=0.3, 0.4$ it was found that the separation shock foot was actually located upstream of the flexible panel leading edge and hence could not couple with the flutter, for the other cases it was hypothesized that the separation shock being too close to the clamped edges, where the flutter was suppressed and less energetic due to additional rigidity, resulted in no coupling between the shock and panel motion. Apart from the aforementioned exceptional cases, a characteristic frequency in the range of 620 ± 20 Hz was detected for the rest of the $\theta_{SG}, x_i/a$ combinations. Interestingly, the frequency of 620 ± 20 Hz was found to be most energetic for $x_i/a=0.6$, for both shock generators. This frequency was also found to be suspiciously close to the 632 Hz detected in the LMB from the first campaign, and additional Schlieren recordings were made with simultaneous accelerometer measurements in the LMB. Without any shock generator installed, a frequency of 755 Hz was detected from the Schlieren image intensity variation over a small window inside the LMB cavity below the panel, which was matched by a 756 Hz peak from the LMB accelerometers. The same frequency was also found just above the flexible panel from Schlieren, proving resonance between the flutter and LMB vibrations, as hypothesized by [Mathijssen \(2022\)](#). Since the 755 Hz frequency existed in both Schlieren (inside the cavity) and the LMB vibrations even when the flexible panel was replaced with a rigid plate, it was proven that the frequency was not linked to the flutter of the flexible panel,

rather it was inherent to some other phenomenon linked to pressure waves inside the open cavity. Similar observations were made when simultaneous Schlieren and accelerometer (in LMB) readings were done with a 12° shock generator for both rigid and flexible panels, except that the resonant frequency linking the LMB vibrations and the cavity pressure waves shifted to 615 Hz. The flexible panel showed the same flutter frequency, showing that it was driven by the LMB vibrations. The issue could not be remedied in the current setup, despite trying to tighten the LMB to the wind tunnel wall, so the study was carried forward by treating the resonance in frequencies of flutter and LMB vibrations as a boundary condition for the specific facility/setup. The SWBLI interaction lengths were calculated as the difference between the extrapolated impinging shock and separation shock foots, and it was found that the interaction length associated with shock-induced flutter was consistently greater than the interaction length of a canonical SWBLI over a rigid panel. With an increase in impinging shock strength, the interaction length increased, because the stronger shock encourages larger flow separation and hence the separation shock shifts more upstream when compared to an SWBLI with a weaker shock. Only for $\theta_{SG}=15^\circ$, $x_i/a=0.3,0.4$, the interaction lengths over the flexible panels were found to be smaller than the case of rigid plate, but the separation shock was not coupled with the flutter in these cases as its foot was upstream of the leading edge. No distinct trend could be differentiated in the variation of interaction length with changing shock impingement location.

The third campaign involved simultaneous DIC and accelerometer measurements. Based on the recommendations of previous DIC measurements in ST-15, the setup involved two high-speed cameras in a stereographic configuration with a 41° stereo angle, and a white LED for illumination, and the same combinations of θ_{SG} and x_i/a were used. The resulting spatial resolution came out to be 4.47% of the panel length, sufficient enough to resolve large-scale panel motion of interest. In the case without a shock generator installed, the panel demonstrated a mean shape resembling the classic free flutter shape of an upward bump, while the point with the maximum STD was located at $x/a=0.72$, very close to the theoretical point of maximum STD which lies at $x/a=0.75$. With a shock generator installed, the mean shape of the panel changed to an upstream crest-downstream trough shape, and the maximum STD location shifted upstream. As the shock impingement location moved downstream, the upstream crest rose in amplitude while the trough became less defined, because the post-shock high pressure region became less influential while the lower freestream pressure increased in prominence. However, even at the most downstream impingement location, $x_i/a=0.8$, the crest amplitude was considerably less than the amplitude in case of free flutter. The shapes for $\theta_{SG}=15^\circ$ were more suppressed than $\theta_{SG}=12^\circ$ for the same impingement locations, mainly because the post-shock pressure jump is much higher for the stronger shock. The maximum amplitude of the STD shapes occurs when $x_i/a=0.6$. Characteristic frequencies of the flutter for all combinations of θ_{SG} and x_i/a are calculated at the maximum STD and the midspan, midchord locations on the panel, always resulting in a dominant frequency in the range 620 ± 20 Hz, which are matched by the frequency of the LMB vibrations from simultaneous accelerometer measurements. A single exception exists to this: $\theta_{SG}=12^\circ$ at $x_i/a=0.8$, which shows a characteristic frequency of 439 Hz from the DIC and a dominant frequency of 745 Hz in the LMB. It is possible that only for this condition, the pressure waves in the cavity are somehow affected and do not show the 620 ± 20 Hz, allowing the panel to flutter at its natural frequency, as the observed frequency of 439 Hz is close to the second eigenfrequency at 460 Hz of the CCCC1.5 panel. Using spectrograms that denote the spread of dominant frequencies across the panel length, it is observed that when the separation shock is not coupled with the panel motion despite the foot lying beyond the panel leading edge ($\theta_{SG}=12^\circ$, $x_i/a=0.4$ and $\theta_{SG}=15^\circ$, $x_i/a=0.5$), the panel response appears chaotic, with lots of excited frequencies across the spectrum. As soon as the separation shock foot appears coupled with the flutter ($\theta_{SG}=12^\circ$, $x_i/a=0.5$ and $\theta_{SG}=15^\circ$, $x_i/a=0.6$), the response becomes periodic, with the primary frequency of 620 ± 20 Hz showing up along with its harmonics. POD of the fluctuations about mean of out-of-plane panel displacements revealed that the most energetic mode shape (representative of the most energetic dynamics of motion) for free flutter possesses a (1,2) form, i.e., with two alternating peaks in the streamwise direction. In contrast, shock-induced flutter has a (1,1) shape (a solitary peak) of its first POD mode, for all combinations of θ_{SG} and x_i/a except $\theta_{SG}=15^\circ$, $x_i/a=0.8$, which has an approximate (1,2) shape. With change in inviscid shock impingement locations, the mode shapes only change in the relative proportions but not identity, i.e., first mode remains (1,1) for shock-induced flutter and (1,2) for free flutter. The relative energy of the first POD mode is very low when the shock impingement is too upstream, possibly because of the chaotic nature of flutter for those impingement

locations that results in higher order modes excited by the chaotic nature of separated flow contributing more significantly. The first order mode is at its most energetic in relation to other modes at $x_i/a=0.6$ for both shock generators, and its contribution decreases once again as the impinging shock moves further downstream. In terms of frequencies of the POD modes, the first mode is always dominated by the 620 ± 20 Hz frequency of the flutter, while the second mode exhibits the second harmonic of the flutter or some other higher frequency, depending the particular combination of θ_{SG} and x_i/a .

6.2. Recommendations for Future Studies

The problem of LMB vibrations observed in the current study (see [chapter 4](#)) which causes resonance of flutter frequency of CCCC1.5 flexible panels was not resolved within the scope of the work, and is a crucial area which needs a deeper investigation in future studies. Without a shock generator, the LMB vibrations existed at 756-770 Hz, and carried more energy than vibrations in case with shock generators at 620 ± 20 Hz. Since pressure waves detected in Schlieren recordings in the cavity (which is open to the downstream end of the test section) below the panel fixture displayed the same frequency as the LMB vibrations, the simplest way to reduce the vibrations could be to close the cavity. In case the flow at the downstream end of the LMB is a primary influence in creating these pressure waves, then closing the cavity would at least reduce the effect of the pressure waves on the flexible panel. However, if the source of the LMB vibrations is not linked to leakage of flow at the downstream end, then closing the cavity might have little to no effect on the resonance between LMB vibrations and panel flutter. That is why it is also important to characterize the vibrational behaviour of the entire LMB itself, which could be done with the help of a simplified CAD model and a FEM solver. Causality could not be assigned between the existence of cavity pressure waves and vibrations of the LMB, and for an exceptional case in the current study ($\theta_{SG}=12^\circ$, $x_i/a=0.8$), the LMB vibrations in 620 ± 20 Hz were not detected and the panel appeared to flutter at one of its eigenfrequencies. The repeatability of this observation should be confirmed and other edge cases with different flow conditions should also be checked, before proceeding with verifying if panels of different geometry and/or boundary conditions also result in the same LMB vibrations and resonance with the panel flutter.

Another important parameter that could be measured and controlled is the cavity pressure itself. With the current setup, the open cavity is expected to result in pressure equalization between the post-shock pressure and the cavity pressure, however, this has not yet been demonstrated by any of the panel flutter studies so far in ST-15, including the current study. In literature, the transverse pressure differential (pressure difference across the thickness of the panel) has been shown to have a profound impact on the flutter behaviour of thin panels, as it can result in an initial static deformation of the panel. Thus, it is also important to study the flutter under varied conditions of the transverse pressure differential, for which the cavity could be sealed and fitted with either an air compressor or a vacuum pump, depending on the desired configuration.

An SWBLI is unsteady even in the thermal aspect, and that has not yet been investigated in-depth for shock-induced panel flutter in ST-15. While thermocouples were used in the test section in the current study, they were only useful for forming an approximate idea of cooling in the test section caused by convection due to the high-speed air flow. The main drawback was that the thermocouples could not provide a direct measure of the flow side temperatures in the tunnel, instead having to be attached below the panel. With flexible panels that fluttered, the thermocouples could not stay attached to the bottom of the panel for long (this was attempted multiple times), while their mere presence would have modified the panel response anyway. To get an idea of the unsteady temperature field over a shock-induced panel flutter, it is imperative to use a non-intrusive technique, like IRT. The full-field nature of IRT measurements will also be useful to reveal the three-dimensionality of the effects of an SWBLI. Preliminary calculations had revealed that the CCCC1.5 panels used in the current study were too wide to be captured by the available IRT camera and lens combination, which could also not be modified to change the field-of-view. Thus, to capture the full extent of the panel with the IR camera, new panels with a shorter span will be required.

While POD was employed on DIC data to extract the most important modes of the panel under different flow conditions, the same can also be done on the flow aspect if measurements are done with

PIV which yields quantitative flowfield information, unlike Schlieren. This will reveal the dominant flow structures and how they are affected by the flexibility of the panel. Further, PIV could be done using low-speed cameras, which offer better spatial resolution, to resolve the boundary layer properly. If DIC and PIV measurements are conducted separately, which would result in a less cumbersome setup and better SNR compared to simultaneous measurements, it would also be useful to have a laser vibrometer below the panel to record the displacements at a certain location on the panel simultaneously with the PIV, so that phases of the panel motion can be directly linked to the dominant flow structures and form a complete picture of the FSI even if the measurements are separate. In fact, with separate flow and structure measurements, it will also be possible to conduct tomographic-PIV and obtain flowfield information over the entire volume of flow above the panel, leading to a deeper understanding of the physical mechanisms involved in shock-induced flutter. A small practical suggestion when conducting non-simultaneous flow and structural measurements is to keep the acquisition rates as integral multiples in case the rates are different for the two, this would allow the downsampling of the signal acquired at a higher frequency to the lower frequency for a direct comparison at the same time instances.

Bibliography

- Allerhand, P. Q. An experimental investigation of shock-induced panel flutter using simultaneous PIV and DIC. Master's thesis, 2020.
- Amirzadegan, S. and Dowell, E. H. Correlation of experimental and computational results for flutter of streamwise curved plate. *AIAA Journal*, 57(8):3556–3561, 2019.
- Anderson, W. J. Experiments on the flutter of flat and slightly curved panels at mach number 2.81. Technical report, CALIFORNIA INST OF TECH PASADENA GRADUATE AERONAUTICAL LABS, 1962.
- Anderson Jr, J. D. *Fundamentals of aerodynamics*. Tata McGraw-Hill Education, 2010.
- Arányi, P., Janiga, G., Zähringer, K., and Thévenin, D. Analysis of different pod methods for piv-measurements in complex unsteady flows. *International journal of heat and fluid flow*, 43:204–211, 2013.
- Babinsky, H. and Harvey, J. K. *Shock wave-boundary-layer interactions*, volume 32. Cambridge University Press, 2011.
- Baidya, R., Scharnowski, S., Bross, M., and Kähler, C. Interactions between a shock and turbulent features in a mach 2 compressible boundary layer. *Journal of Fluid Mechanics*, 893, 2020.
- Beberniss, T., Spottswood, M., and Eason, T. High-speed digital image correlation measurements of random nonlinear dynamic response. In *Experimental and Applied Mechanics, Volume 6*, pages 171–186. Springer, 2011.
- Beberniss, T. J. Nonlinear response of a thin panel subjected to a shockwave impingement and thermal buckling. In *33rd AIAA Aerodynamic Measurement Technology and Ground Testing Conference*, page 3555, 2017.
- Beberniss, T., Spottswood, S., Perez, R., and Eason, T. Nonlinear response of a thin panel in a multi-discipline environment: Part i—experimental results. In *Nonlinear Dynamics, Volume 1*, pages 237–248. Springer, 2016.
- Beresh, S., Clemens, N., and Dolling, D. Relationship between upstream turbulent boundary-layer velocity fluctuations and separation shock unsteadiness. *AIAA journal*, 40(12):2412–2422, 2002.
- Bohon, H. L. and Dixon, S. C. Some recent developments in flutter of flat panels. *Journal of Aircraft*, 1(5):280–288, 1964.
- Bohon, H. L., Anderson, M. S., and Heard, W. L. *Flutter design of stiffened-skin panels for hypersonic aircraft*. National Aeronautics and Space Administration, 1969.
- Boyer, N. R., McNamara, J., Gaitonde, D., Barnes, C. J., and Visbal, M. R. Features of shock-induced panel flutter in three-dimensional inviscid flow. *Journal of Fluids and Structures*, 83:490–506, 2018.
- Boyer, N. R., McNamara, J., Gaitonde, D., Barnes, C. J., and Visbal, M. R. Features of panel flutter response to shock boundary layer interactions. *Journal of Fluids and Structures*, 101:103207, 2021.
- Brouwer, K. R. and McNamara, J. J. Enriched piston theory for expedient aeroelastic loads prediction in the presence of shock impingements. *AIAA Journal*, 57(3):1288–1302, 2019.
- Brouwer, K. R. and McNamara, J. J. Surrogate-based aeroelastic loads prediction in the presence of shock-induced separation. *Journal of Fluids and Structures*, 93:102838, 2020.

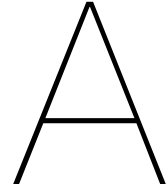
- Brouwer, K. R., Gogulapati, A., and McNamara, J. J. Interplay of surface deformation and shock-induced separation in shock/boundary-layer interactions. *AIAA Journal*, 55(12):4258–4273, 2017.
- Brouwer, K. R., Perez, R., Beberniss, T. J., Spottswood, S. M., and Ehrhardt, D. A. Fluid-structure interaction on a thin panel including shock impingement effects. In *AIAA Scitech 2021 Forum*, page 0910, 2021a.
- Brouwer, K. R., Perez, R. A., Beberniss, T. J., Spottswood, S. M., and Ehrhardt, D. A. Experiments on a thin panel excited by turbulent flow and shock/boundary-layer interactions. *AIAA Journal*, pages 1–16, 2021b.
- Bruce, P., Burton, D., Titchener, N., and Babinsky, H. Corner effect and separation in transonic channel flows. *Journal of Fluid Mechanics*, 679:247, 2011.
- Clemens, N. T. and Narayanaswamy, V. Low-frequency unsteadiness of shock wave/turbulent boundary layer interactions. *Annual Review of Fluid Mechanics*, 46:469–492, 2014.
- Cordier, L. Proper orthogonal decomposition: an overview. 2008.
- Crammond, G., Boyd, S., and Dulieu-Barton, J. Speckle pattern quality assessment for digital image correlation. *Optics and Lasers in Engineering*, 51(12):1368–1378, 2013.
- Cunningham, H. Flutter analysis of flat rectangular panels based on three-dimensional supersonic potential flow. *AIAA journal*, 1(8):1795–1801, 1963.
- Currao, G., Neely, A. J., Buttsworth, D. R., and Choudhury, R. Measurement and simulation of hypersonic fluid-structural interaction on a cantilevered plate in a mach 6 flow. In *15th Dynamics Specialists Conference*, page 1088, 2016.
- Currao, G. M., Neely, A. J., Kennell, C. M., Gai, S. L., and Buttsworth, D. R. Hypersonic fluid–structure interaction on a cantilevered plate with shock impingement. *AIAA Journal*, 57(11):4819–4834, 2019.
- Daub, D., Willems, S., Esser, B., and Gülhan, A. Experiments on elastic aerothermal fluid/structure interaction in supersonic flows. *SFB/TRR40 Annual Report*, pages 277–290, 2019.
- Daub, D., Willems, S., and Gülhan, A. Experiments on the interaction of a fast-moving shock with an elastic panel. *AIAA Journal*, 54(2):670–678, 2016a. doi: 10.2514/1.J054233.
- Daub, D., Willems, S., and Gülhan, A. Experimental results on unsteady shock-wave/boundary-layer interaction induced by an impinging shock. *CEAS Space Journal*, 8(1):3–12, 2016b.
- Daub, D., Esser, B., and Gülhan, A. Experiments on high-temperature hypersonic fluid–structure interaction with plastic deformation. *AIAA Journal*, 58(4):1423–1431, 2020.
- Délery, J. and Dussauge, J.-P. Some physical aspects of shock wave/boundary layer interactions. *Shock waves*, 19(6):453, 2009.
- Dolling, D. S. Fifty years of shock-wave/boundary-layer interaction research: what next? *AIAA journal*, 39(8):1517–1531, 2001.
- Dowell, E. H. Panel flutter—a review of the aeroelastic stability of plates and shells. *AIAA journal*, 8(3): 385–399, 1970.
- Dowell, E. H. *Aeroelasticity of plates and shells*, volume 1. Springer Science & Business Media, 1974.
- Dowell, E. H. and Bendiksen, O. Panel flutter. *Encyclopedia of Aerospace Engineering*, 2010.
- Dowell, E. H. and Voss, H. Theoretical and experimental panel flutter studies in the mach number range 1.0 to 5.0. *AIAA Journal*, 3(12):2292–2304, 1965.
- Dugundji, J. Theoretical considerations of panel flutter at high supersonic mach numbers. *AIAA journal*, 4(7):1257–1266, 1966.

- Dupont, P., Haddad, C., Ardissonne, J., and Debieve, J. Space and time organisation of a shock wave/turbulent boundary layer interaction. *Aerospace science and technology*, 9(7):561–572, 2005.
- Dussauge, J.-P., Dupont, P., and Debiève, J.-F. Unsteadiness in shock wave boundary layer interactions with separation. *Aerospace Science and Technology*, 10(2):85–91, 2006.
- Estruch, D., Lawson, N. J., MacManus, D. G., Garry, K. P., and Stollery, J. Measurement of shock wave unsteadiness using a high-speed schlieren system and digital image processing. *Review of Scientific Instruments*, 79(12):126108, 2008.
- Fung, Y. Some recent contributions to panel flutter research. *AIAA journal*, 1(4):898–909, 1963.
- Gaitonde, D. V. Progress in shock wave/boundary layer interactions. *Progress in Aerospace Sciences*, 72:80–99, 2015.
- Gaspers, P. A. *Further experimental results on the influence of the turbulent boundary layer on panel flutter*. National Aeronautics and Space Administration, 1970.
- Génin, F. and Menon, S. Studies of shock/turbulent shear layer interaction using large-eddy simulation. *Computers & Fluids*, 39(5):800–819, 2010.
- Gibbs, S. C., Wang, I., and Dowell, E. Theory and experiment for flutter of a rectangular plate with a fixed leading edge in three-dimensional axial flow. *Journal of Fluids and Structures*, 34:68–83, 2012.
- Giepmans, R., Schrijer, F., and Van Oudheusden, B. A parametric study of laminar and transitional oblique shock wave reflections. *Journal of Fluid Mechanics*, 844:187–215, 2018.
- Gogulapati, A., Deshmukh, R., Crowell, A., McNamara, J., Vyas, V., Wang, X., Mignolet, M., Beberniss, T., Spottswood, S., and Eason, T. Response of a panel to shock impingement: modeling and comparison with experiments. In *55th AIAA/ASME/ASCE/AHS/SC Structures, Structural Dynamics, and Materials Conference-SciTech Forum and Exposition 2014*, 2014.
- Gogulapati, A., Deshmukh, R., McNamara, J. J., Vyas, V., Wang, X., Mignolet, M. P., Beberniss, T., Spottswood, S. M., and Eason, T. Response of a panel to shock impingement: Modeling and comparison with experiments—part 2. In *56th AIAA/ASCE/AHS/ASC Structures, Structural Dynamics, and Materials Conference*, page 0685, 2015.
- Gomez-Vega, N., Gramola, M., and Bruce, P. J. Oblique shock control with steady flexible panels. *AIAA Journal*, 58(5):2109–2121, 2020.
- Gordnier, R. E. and Visbal, M. R. Development of a three-dimensional viscous aeroelastic solver for nonlinear panel flutter. *Journal of fluids and structures*, 16(4):497–527, 2002.
- Gramola, M., Bruce, P. J., and Santer, M. J. Response of a 3d flexible panel to shock impingement with control of cavity pressure. In *AIAA Scitech 2020 Forum*, page 0314, 2020.
- Gray, C. E., Mei, C., and Shore, C. Finite element method for large-amplitude two-dimensional panel flutter at hypersonic speeds. *AIAA journal*, 29(2):290–298, 1991.
- Gray Jr, C. E. and Mei, C. Large-amplitude finite element flutter analysis of composite panels in hypersonic flow. *AIAA journal*, 31(6):1090–1099, 1993.
- Hashimoto, A., Aoyama, T., and Nakamura, Y. Effects of turbulent boundary layer on panel flutter. *AIAA journal*, 47(12):2785–2791, 2009.
- Hedgepeth, J. M. Flutter of rectangular simply supported panels at high supersonic speeds. *Journal of the Aeronautical Sciences*, 24(8):563–573, 1957.
- Hoy, J. F. and Bermejo-Moreno, I. Numerical study of stbli on flexible panels with wall-modeled les. In *AIAA Scitech 2021 Forum*, page 0250, 2021.
- Humble, R., Scarano, F., and Van Oudheusden, B. Particle image velocimetry measurements of a shock wave/turbulent boundary layer interaction. *Experiments in Fluids*, 43(2):173–183, 2007.

- Humble, R., Elsinga, G., Scarano, F., and Van Oudheusden, B. Three-dimensional instantaneous structure of a shock wave/turbulent boundary layer interaction. *Journal of Fluid Mechanics*, 622:33, 2009.
- Jerri, A. J. The shannon sampling theorem—its various extensions and applications: A tutorial review. *Proceedings of the IEEE*, 65(11):1565–1596, 1977.
- Kobett, D. Flutter of multiple-streamwise bay rectangular panels at low supersonic mach number. 1966.
- Kordes, E. E., Tuovila, W. J., and Guy, L. D. *Flutter research on skin panels*, volume 451. National Aeronautics and Space Administration, 1960.
- Li, Y., Luo, H., Chen, X., and Xu, J. Laminar boundary layer separation over a fluttering panel induced by an oblique shock wave. *Journal of Fluids and Structures*, 90:90–109, 2019.
- Ligrani, P. M., McNabb, E. S., Collopy, H., Anderson, M., and Marko, S. M. Recent investigations of shock wave effects and interactions. *Advances in Aerodynamics*, 2(1):4, 2020.
- Maestrello, L. and Linden, T. Measurements of the response of a panel excited by shock boundary-layer interaction. *Journal of Sound and Vibration*, 16(3):385–391, 1971.
- Marimon Giovannetti, L. *Fluid structure interaction testing, modelling and development of passive adaptive composite foils*. PhD thesis, University of Southampton, 2017.
- Mathijssen, L. C. M. J. An experimental study on supersonic panel flutter using simultaneous digital image correlation schlieren. Master's thesis, 2022.
- Mei, C. A finite-element approach for nonlinear panel flutter. *AIAA Journal*, 15(8):1107–1110, 1977.
- Mei, C., Abdel-Motagaly, K., and Chen, R. Review of nonlinear panel flutter at supersonic and hypersonic speeds. 1999.
- Meng, X., Ye, Z., Ye, K., and Liu, C. Analysis on location of maximum vibration amplitude in panel flutter. *Proceedings of the Institution of Mechanical Engineers, Part G: Journal of Aerospace Engineering*, 234(2):457–469, 2020.
- Miller, B., Crowell, A., and McNamara, J. Modeling and analysis of shock impingements on thermo-mechanically compliant surface panels. In *53rd AIAA/ASME/ASCE/AHS/ASC Structures, Structural Dynamics and Materials Conference 20th AIAA/ASME/AHS Adaptive Structures Conference 14th AIAA*, page 1548, 2012.
- Miller, B. A., Crowell, A. R., Deshmukh, R., Gogulapati, A., McNamara, J. J., Vyas, V., Wang, X., and Mignolet, M. P. Response of a panel to shock impingement: Modeling and comparison with experiments. In *55th AIAA/ASMe/ASCE/AHS/SC Structures, Structural Dynamics, and Materials Conference*, page 0148, 2014.
- Morgan, B., Duraisamy, K., Nguyen, N., Kawai, S., and Lele, S. Flow physics and RANS modelling of oblique shock/turbulent boundary layer interaction. *Journal of Fluid Mechanics*, 729:231, 2013.
- Muhlstein, L. *An experimental study of the influence of the turbulent boundary layer on panel flutter*. National Aeronautics and Space Administration, 1968.
- Neet, M. C. and Austin, J. M. Effects of surface compliance on shock boundary layer interaction in the caltech mach 4 ludwig tube. In *AIAA Scitech 2020 forum*, page 0816, 2020.
- Olson, M. D. and Fung, Y. Comparing theory and experiment for the supersonic flutter of circular cylindrical shells. *AIAA Journal*, 5(10):1849–1856, 1967.
- Oyibo, G. A. Flutter of orthotropic panels in supersonic flow using affine transformations. *AIAA Journal*, 21(2):283–289, 1983.
- Pan, B., Xie, H., Wang, Z., Qian, K., and Wang, Z. Study on subset size selection in digital image correlation for speckle patterns. *Optics express*, 16(10):7037–7048, 2008.

- Pasha, A. A. and Sinha, K. Simulation of hypersonic shock/turbulent boundary-layer interactions using shock-unsteadiness model. *Journal of Propulsion and Power*, 28(1):46–60, 2012.
- Pasquariello, V., Hickel, S., Adams, N., Hammerl, G., Wall, W., Daub, D., Willems, S., and Gülhan, A. Coupled simulation of shock-wave/turbulent boundary-layer interaction over a flexible panel. 2015.
- Pasquariello, V., Hickel, S., and Adams, N. A. Unsteady effects of strong shock-wave/boundary-layer interaction at high reynolds number. *J. Fluid Mech*, 823(617):014602–19, 2017.
- Pirozzoli, S. and Grasso, F. Direct numerical simulation of impinging shock wave/turbulent boundary layer interaction at $m = 2.25$. *Physics of Fluids*, 18(6):065113, 2006.
- Pope, A. and Goin, K. L. *High-Speed Wind Tunnel Testing*. Wiley Sons, 1965.
- Priebe, S., Wu, M., and Martin, M. Direct numerical simulation of a reflected-shock-wave/turbulent-boundary-layer interaction. *AIAA journal*, 47(5):1173–1185, 2009.
- Quan, L. H., Hung, N. P., Long, V. N., et al. Analysis and design of a scramjet engine inlet operating from mach 5 to mach 10. *International Journal of Mechanical Engineering and Applications*, 4(1):11, 2016.
- Raffel, M., Willert, C. E., Scarano, F., Kähler, C. J., Wereley, S. T., and Kompenhans, J. *Particle image velocimetry: a practical guide*. Springer, 2018.
- Rao, S. S. and Yap, F. F. *Mechanical vibrations*, 5th eddition, 2010.
- Reu, P. Stereo-rig design: lighting—part 5. *Experimental Techniques*, 37(3):1–2, 2013.
- Reu, P. All about speckles: aliasing. *Experimental Techniques*, 38(5):1–3, 2014a.
- Reu, P. Speckles and their relationship to the digital camera. *Experimental Techniques*, 38(4):1–2, 2014b.
- Reu, P. All about speckles: contrast. *Experimental Techniques*, 39(1):1–2, 2015a.
- Reu, P. All about speckles: speckle density. *Experimental Techniques*, 39(3):1–2, 2015b.
- Reu, P. All about speckles: edge sharpness. *Experimental Techniques*, 39(2):1–2, 2015c.
- Roncella, R., Romeo, E., Barazzetti, L., Gianinetto, M., and Scaioni, M. Comparative analysis of digital image correlation techniques for in-plane displacement measurements. In *2012 5th International Congress on Image and Signal Processing*, pages 721–726. IEEE, 2012.
- Schreier, H., Orteu, J.-J., and Sutton, M. A. *Image correlation for shape, motion and deformation measurements*. Springer US, 2009.
- Shinde, V., McNamara, J. J., Gaitonde, D. V., Barnes, C. J., and Visbal, M. R. Panel flutter induced by transitional shock wave boundary layer interaction. In *2018 Fluid Dynamics Conference*, page 3548, 2018.
- Shinde, V., McNamara, J., Gaitonde, D., Barnes, C., and Visbal, M. Transitional shock wave boundary layer interaction over a flexible panel. *Journal of Fluids and Structures*, 90:263–285, 2019a.
- Shinde, V. J., McNamara, J. J., and Gaitonde, D. V. Effect of structural parameters on shock wave boundary layer induced panel flutter. In *AIAA Aviation 2019 Forum*, page 3716, 2019b.
- Shinde, V. J., McNamara, J. J., and Gaitonde, D. V. Shock wave turbulent boundary layer interaction over a flexible panel. In *AIAA Scitech 2021 Forum*, page 0488, 2021.
- Shitov, S. and Vedeneev, V. Flutter of rectangular simply supported plates at low supersonic speeds. *Journal of fluids and structures*, 69:154–173, 2017.
- Solomon Jr, O. M. Psd computations using welch’s method.[power spectral density (psd)]. Technical report, Sandia National Labs., Albuquerque, NM (United States), 1991.

- Souverein, L. J., Dupont, P., Debieve, J.-F., Dussauge, J.-P., Van Oudheusden, B. W., and Scarano, F. Effect of interaction strength on unsteadiness in shock-wave-induced separations. *AIAA journal*, 48(7):1480–1493, 2010.
- Spottswood, S., Eason, T., and Bebernis, T. Influence of shock-boundary layer interactions on the dynamic response of a flexible panel. *Proceedings of the ISMA-2012*, pages 17–19, 2012.
- Spottswood, S. M., Bebernis, T. J., Eason, T. G., Perez, R. A., Donbar, J. M., Ehrhardt, D. A., and Riley, Z. B. Exploring the response of a thin, flexible panel to shock-turbulent boundary-layer interactions. *Journal of Sound and Vibration*, 443:74–89, 2019.
- Spottswood, S. M., Eason, T., and Bebernis, T. Full-field, dynamic pressure and displacement measurements of a panel excited by shock boundary-layer interaction. In *19th AIAA/CEAS aeroacoustics conference*, page 2016, 2013.
- Sun, Z. Micro ramps in supersonic turbulent boundary layers. 2014.
- Sun, Z., Gan, T., and Wu, Y. Shock-wave/boundary-layer interactions at compression ramps studied by high-speed schlieren. *AIAA Journal*, 58(4):1681–1688, 2020.
- Tan, S. S., Bruce, P. J., and Gramola, M. Oblique shockwave boundary layer interaction on a flexible surface. In *AIAA Scitech 2019 Forum*, page 0097, 2019.
- Tripathi, A., Mears, L., Shoele, K., and Kumar, R. Oblique shockwave boundary layer interactions on a flexible panel at mach 2. In *AIAA Scitech 2020 Forum*, page 0568, 2020.
- Tripathi, A., Gustavsson, J., Shoele, K., and Kumar, R. Response of a compliant panel to shock boundary layer interaction at mach 2. In *AIAA Scitech 2021 Forum*, page 0489, 2021.
- van Oudheusden, B., Flinkerbusch, A., and Schrijer, F. Velocity and pressure fields of swblis on porous plates. In *Proceedings of the 13th International Symposium on Particle Image Velocimetry*, 2019.
- Van Oudheusden, B., Jöbsis, A., Scarano, F., and Souverein, L. Investigation of the unsteadiness of a shock-reflection interaction with time-resolved particle image velocimetry. *Shock Waves*, 21(5):397–409, 2011.
- Ventres, C. and Dowell, E. Comparison of theory and experiment for nonlinear flutter of loaded plates. *AIAA Journal*, 8(11):2022–2030, 1970.
- Visbal, M. Viscous and inviscid interactions of an oblique shock with a flexible panel. *Journal of Fluids and Structures*, 48:27–45, 2014.
- Visbal, M. On the interaction of an oblique shock with a flexible panel. *Journal of Fluids and structures*, 30:219–225, 2012.
- Willems, S., Gülhan, A., and Esser, B. Shock induced fluid-structure interaction on a flexible wall in supersonic turbulent flow. *Progress in Flight Physics*, 5:285–308, 2013.
- Xie, D. and Xu, M. A simple proper orthogonal decomposition method for von karman plate undergoing supersonic flow. *Comput. Model. Eng. Sci*, 93(5):377–409, 2013.
- Xie, D., Xu, M., and Dowell, E. H. Proper orthogonal decomposition reduced-order model for nonlinear aeroelastic oscillations. *AIAA journal*, 52(2):229–241, 2014.
- Zope, A., Horner, C., Collins, E. M., Bhushan, S., and Bhatia, M. Investigation of flexible panel dynamic response induced by coherent turbulent vortical structures. In *AIAA Scitech 2021 Forum*, page 0251, 2021.



Experimental Campaign Test Matrices

Campaign 1: Thermocouples and Accelerometers

Run No.	Date & Time	θ_{SG} [°]	x_i/a	LMB/UMB tightened before run
1	28/07/21 & 1122	NA	NA	No
2	28/07/21 & 1123	NA	NA	No
3	02/08/21 & 1541	NA	NA	No
4	02/08/21 & 1615	NA	NA	No
5	02/08/21 & 1618	NA	NA	No
6	03/08/21 & 1135	NA	NA	Yes
7	03/08/21 & 1458	NA	NA	Yes
8	03/08/21 & 1650	12	0.5	No
9	04/08/21 & 1116	12	0.5	No
10	04/08/21 & 1118	12	0.5	No
11	04/08/21 & 1120	12	0.5	No
12	04/08/21 & 1232	12	0.5	No
13	04/08/21 & 1233	12	0.5	No
14	04/08/21 & 1234	12	0.5	No
15	04/08/21 & 1438	12	0.5	No
16	04/08/21 & 1439	17	0.5	No
17	04/08/21 & 1441	17	0.5	No
18	04/08/21 & 1600	12	0.5	No
19	04/08/21 & 1602	12	0.5	Yes

Table A.1: All runs using rigid plate. θ_{SG} = shock generator angle. x_i/a = inviscid shock impingement location as fraction of chord.

Campaign 2: Schlieren

Run No.	Date & Time	Panel type	θ_{SG} [°]	x_i/a	Accelerometer used
1	22/09/21 & 1051	CCCC1.5	15	0.6	No
2	22/09/21 & 1115	CCCC1.5	15	0.5	No
3	22/09/21 & 1139	CCCC1.5	15	0.4	No
4	22/09/21 & 1515	CCCC1.5	15	0.3	No
5	22/09/21 & 1540	CCCC1.5	15	0.7	No
6	22/09/21 & 1630	CCCC1.5	15	0.8	No
7	23/09/21 & 1115	CCCC1.5	12	0.4	No
8	23/09/21 & 1218	CCCC1.5	12	0.5	No
9	23/09/21 & 1527	CCCC1.5	12	0.6	No
10	23/09/21 & 1545	CCCC1.5	12	0.7	No
11	23/09/21 & 1630	CCCC1.5	12	0.8	No
12	24/09/21 & 1436	RP	12	0.5	No
13	24/09/21 & 1525	RP	15	0.5	No
14	27/10/21 & 1130	CCCC1.5	12	0.6	Yes
15	27/10/21 & 1205	CCCC1.5	12	0.5	Yes
16	28/10/21 & 1030	CCCC1.5	NA	NA	Yes
17	28/10/21 & 1105	RP	NA	NA	Yes
18	28/10/21 & 1400	RP	12	0.5	Yes

Table A.2: θ_{SG} = shock generator angle. x_i/a = inviscid shock impingement location as fraction of chord. RP = rigid plate. CCCC1.5 = fully clamped flexible panel of aspect ratio 1.5.

Campaign 3: Digital Image Correlation

Run No.	Date & Time	Panel type	θ_{SG} [°]	x_i/a	T_{amb} [°C]
1	04/11/21 & 1615	CCCC1.5	NA	NA	15.7
2	04/11/21 & 1643	CCCC1.5	15	0.3	15.2
3	04/11/21 & 1731	CCCC1.5	15	0.4	14.2
4	05/11/21 & 1410	CCCC1.5	15	0.5	16
5	05/11/21 & 1505	CCCC1.5	15	0.6	15.5
6	05/11/21 & 1552	CCCC1.5	15	0.7	15.3
7	05/11/21 & 1648	CCCC1.5	12	0.8	15.1
8	08/11/21 & 1020	CCCC1.5	NA	NA	15.6
9	08/11/21 & 1055	CCCC1.5	12	0.6	15.2
10	08/11/21 & 1130	CCCC1.5	12	0.4	15.1
11	08/11/21 & 1154	CCCC1.5	12	0.8	15.2
12	08/11/21 & 1232	CCCC1.5	12	0.5	14.9
13	08/11/21 & 1454	CCCC1.5	12	0.7	16.6
14	08/11/21 & 1622	CCCC1.5	12	0.7	15.6
15	10/11/21 & 1318	CCCC1.5	12	0.6	19.2
16	10/11/21 & 1358	CCCC1.5	12	0.4	19.1
17	10/11/21 & 1645	RP	12	0.5	19.5

Table A.3: θ_{SG} = shock generator angle. x_i/a = inviscid shock impingement location as fraction of chord. RP = rigid plate. CCCC1.5 = fully clamped flexible panel of aspect ratio 1.5. T_{amb} = ambient temperature.

B

Technical Drawing

